PULSES IN THE SAND: LONG RANGE AND HIGH DATA RATE COMMUNICATION TECHNIQUES FOR NEXT GENERATION WIRELESS UNDERGROUND NETWORKS

by

Abdul Salam

A DISSERTATION

Presented to the Faculty of

The Graduate College at the University of Nebraska

In Partial Fulfilment of Requirements

For the Degree of Doctor of Philosophy

Major: Engineering

Under the Supervision of Mehmet Can Vuran

Lincoln, Nebraska

August, 2018

PULSES IN THE SAND: LONG RANGE AND HIGH DATA RATE COMMUNICATION TECHNIQUES FOR NEXT GENERATION WIRELESS UNDERGROUND NETWORKS

Abdul Salam, Ph.D.

University of Nebraska, 2018

Adviser: Mehmet Can Vuran

The recent emergence of Internet of Underground Things (IOUT) in many areas including environment and infrastructure monitoring, border patrol, transportation, and precision agriculture, underscores the importance of wireless underground (UG) communications. Yet, existing solutions are limited by relatively short communication distances and low data rates that prohibit widespread adoption. Extending the communication ranges and increasing data rates in wireless UG communications faces unique challenges because of the interactions between soil and communication components: (1) antenna properties, such as resonance frequency and antenna bandwidth, depend on soil type and varies with changes in soil parameters (e.g., soil moisture). Therefore, an antenna designed for over-the-air communication is no longer matched to the transceiver when buried in soil, and the system bandwidth, which is limited by antenna bandwidth varies in time. (2) Delay spread of the UG channel, which determines its coherence bandwidth, is a time-variant function of the soil parameters. Accordingly, the channel bandwidth varies significantly with physical changes in the environment. (3) The soil-air interface results in fluctuations in both antenna performance and EM wave propagation, which should be considered in system design. Consequently, next generation wireless UG communication solutions should be tailored to deployment parameters such as soil composition and depth while being

robust to variations in environmental parameters.

In this dissertation, the UG channel is characterized and environment-aware, cross-layer communication solutions are developed to achieve high data rate, long range communications. Moreover, applications to agriculture and smart lighting are illustrated. The impulse response of the wireless UG channel is captured and analyzed through extensive experiments. Based on this analysis, multi-carrier modulation and wireless underground channel diversity reception schemes have been developed. Furthermore, based on UG antenna analysis, soil moisture adaptive beamforming using underground antenna arrays is also designed. A wide variety of applications can potentially utilize UG communication solutions with diverse requirements. Among these, smart agriculture solutions that highlight long range and high data rate aspects of UG communications are considered to evaluate the developed solutions. The findings of this research are also evaluated using computational electromagnetics simulations.

DEDICATION

To *Dr. Mehmet C. Vuran*,

as George Bernard Shaw said, "Some men see things as they are and ask "Why?" Others dream things that never were and ask "Why not..."

Indeed, *Dr. Vuran* has a humble home in "Why not..."!

ACKNOWLEDGMENTS

I am highly excited and glad to express my heartfelt gratitude to many people who made this dissertation possible.

I am exceedingly thankful to my advisor and teacher, Dr. Mehmet Can Vuran who encouraged me to work in the area of wireless underground communications. No words can ever fully express my gratitude for his great mentorship. It has been an honor being his student. I am very grateful to have been trained by him. His encouragement has been a great inspiration to achieve excellence. He has not only guided me for the research work in this area, but also gave me the excellent guidance and support that has helped me to secure a faculty position at the Purdue University. I am indebted to Dr. Vuran for everything that I have learnt from him.

I whole heartedly thank Dr. Suat Irmak for his tremendous guidance and support during the design and development of the greenhouse indoor testbed and UNL's South Central Agricultural Laboratory (SCAL) experiments. I am very grateful to him for sharing invaluable scientific expertise and for providing access to these great facilities. This dissertation and the prior work completed at the Internet of Underground Things (IOUT) testbed at Irmak Research Laboratory advanced center pivot irrigation system at SCAL would not have being possible without his support.

I would like to thank Dr. Byrav Ramamurthy for being on my dissertation committee. His invaluable comments have helped me to greatly improve this dissertation. His expertise in next-generation Internet architectures and protocols, design of optical WDM networks; and LAN, MAN and WAN architectures have been a great inspiration for me.

My cordial thanks also extend to Dr. Christos Argyropoulos for sharing his expertise in antenna theory and design. I really enjoyed his electromagnetic theory classes

and working with him. I would also like to thank Dr. Hongfeng Yu for his constant support throughout the dissertation writing.

I am also grateful to my colleagues at the Cyber-Physical Networking Lab for their support. I am especially thankful to Dr. Samil Temel who benefited me with his company during his post-doctoral pursuit at University of Nebrasaka-Lincoln; and also to Dr. Xin Dong, Mohammad Mosiur Rahman Lunar, and Rigoberto Wong for their friendship and support. Time passes, things change, but memories will always stay where they are, in the heart!

This acknowledgment section would not be complete without a heartfelt gratitude to Umbreen, Alizay, Anzalna, and Naba, who have stood by me, through all my hard times, particularly, through the process of leaving my homeland Pakistan to pursue my doctoral education at Nebraska. It is due to their love and prayers, I have the chance to complete this dissertation.

All praise be to Allah, the Sustainer of the creation; and peace be upon His servants whom He has chosen. May Allah sent his salutations on Prophet Muhammad and his family, as He sent salutations on the Ibrahim and his family. By Whose bounty all pious deeds are completed. I ask Him, for beneficial knowledge, good sustenance, and good deeds that are acceptable. Indeed, there is no power and no strength except with Him.

GRANT INFORMATION

This work is partially supported by a NSF CAREER award (CNS-0953900), NSF CNS-1423379, NSF CNS-1247941, CNS-1619285, and a NSF Cyber-Innovation for Sustainability Science and Engineering (CyberSEES) grant (DBI-1331895).

Table of Contents

List of Notations

Notation	Description
k_s	wavenumber in the soil
k_0	wavenumber in the air
λ_s	wavelength in the soil
β_s	phase constant
α_s	attenuation constant
ϵ_s	permittivity of soil
ϵ_s'	real permittivity of soil
ϵ_s''	imaginary permittivity of soil
μ_0	permeability of free space
l	half length of antenna
ω	angular frequency
Z_a	antenna impedance
Z_s	transmission line impedance
E_r	reflected electric field
I_r	reflected current
I_m	current amplitude
Z_r	reflected impedance
Z_0	characteristics impedance
Z_s	transmission line impedance
R_a	radiation resistance
$I_0(\zeta)$	current distribution along the antenna
Z_a	antenna impedance
Z_a^u	soil-air interface adjusted impedance

RL	return Loss
f_r	resonant frequency
f_0	over-the-air frequency
BW	bandwidth
h	burial depth
h_t	transmitter burial depth
h_r	receiver burial depth
η	refractive index
η_a	refractive index of air
η_s	refractive index of soil
m_v	Volumetric water content+
ρ_b	bulk density
ρ_s	particle density
δ, ν' and ν''	empirical constant
$\epsilon_s^{'}$,$\epsilon_s^{''}$	real and imaginary part of permittivity of soil
S and C	sand and clay particle percentage
ϵ_{fw}' and ϵ_{fw}''	relative permittivity of free water real and imaginary
σ_{eff}	effective conductivity of soil
$\epsilon_{w\infty}$,	limit of permittivity of water
ϵ_{w0}	static permittivity of water
τ_w	relaxation time of water
P_t	transmitted power
P_r	received power
PL	path loss
Γ	reflection coefficient

SWR	standing wave ratio
R_a	pure resistance
H	channel transfer function
R	received signal
T	transmitted signal
$h(t)$	impulse response
$h_{ug}(t)$	underground channel impulse response
S	speed of wave in soil
c	speed of wave in air
PDP	power delay profile
$\alpha_l, \alpha_d, \alpha_r$	multipath gain
τ_l, τ_d, τ_r	multipath delay
L, D, R	number of multipaths
G_t	transmitter antenna gain
G_r	receiver antenna gain
τ	mean excess delay
τ_{rms}	root mean square (RMS) delay
H_n	discretized complex channel frequency response
f_{start}	start frequency of the sweep
f_{inc}	increment frequency the sweep
F_{sweep}	sweep frequency range
δ_s	distance travel by wave in soil
δ_a	distance travel by wave in air
δ	dirac delta
θ	phase

γ_L	decay rate
r	length of the reflection path
B_s	system bandwidth
f_m	lowest return loss frequency
f_M	highest return loss frequency
B_{cb}	coherence bandwidth
N_c	number of sub-carriers
R_{ug}	underground channel bit rate
$R_{ug}^{\max}$	maximum bit rate
R_{ug}^{eq}	equal power bit rate
P_{sc_i}	symbol-error probability
P_{sc}^*	target probability of symbol error
$\|H(f)\|^2$	approximated channel transfer function
λ	lagrangian multiplier
D_a	array directivity
d_x	inter-element spacing in x direction
d_y	inter-element spacing in y direction
M x N	planar array dimensions
w_{ij}	element weight
δ_{ij}	phase shift
AF_{bs}	array factor beam steering
AF_{ra}	array factor refrection adjustment
τ_{ij}	beamforming time delay
η_a, η_s	refractive indices of air, and soil
θ_r	refraction angle

θ^*_{UG}	optimum angle
P_{rad}	power radiated
P_{av}	far-field power density
w^i_{sm}	soil moisture adaptive element weight
$P_b(\bar{\gamma}_b)$	average BER probability
γ_b	received per bit SNR
$\bar{\gamma}_b$	average SNR per bit
$P_{e\|\gamma_b}$	conditional AWGN error probability
$p(\gamma_b)$	pdf of SNR
T	sample period
$u(t)$	baseband input
$z(t)$	received signal output waveform
N_0	noise density
h_d, h_l, h_r	separable channel response
ϕ	soil factor
f_{min}	lowest path loss frequency

Chapter 1

Introduction

The World's population will increase by 32 percent in 2050, doubling the need for food. Yet today, up to 70 percent of all water withdrawals are due to food production. This demands novel technologies to produce *more crop for drop*. USDA Agricultural Resource Management Survey (ARMS) is the primary source of information on the financial condition, production practices, and resource use of America's farm businesses and the economic well-being of America's farm households. ARMS data show that *precision agriculture* has become a widespread practice nationwide. In Fig. 1.1, adoption rates of major precision agriculture approaches (bars) along with the total precision agriculture adoption rate (line) are shown for corn for each year of USDA ARMS publication (USDA ARMS 2015 version was under development at the time of this writing). It can be observed that adoption rate of precision agriculture for corn increased from 17.29 percent in 1997 to 72.47 percent in 2010 with similar trends observed for other crops such as soybean and peanuts. Aside from presenting a growing trend in the usage of precision agriculture in corn production, it is evident that as new technologies emerge, they are widely adopted by farmers.

Among the various precision agriculture techniques, crop yield monitoring is the most widely adopted technique (61.4 percent). In addition, guidance and auto-steering system adoption jumped from 5.34 percent in 2001 to 45.16 percent in nine

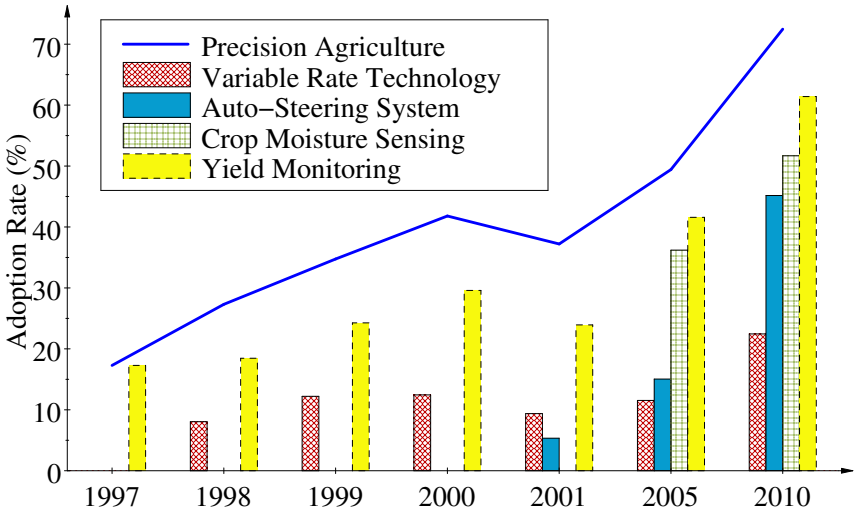

Figure 1.1: Precision agriculture technology adoption in corn production (USDA ARMS Data).

years. Use of equipment and crop location information enables precise control with auto-steering systems which reduce production and maintenance costs and reduces repetitive field work for farmers. Despite the drastic increase in adoption rates of other techniques, variable rate technology (VRT) adoption has been relatively steady, where adoption rate increased from 8.04 percent in 1998 to only 11.54 percent in 2005. Adaptive application of resources like fertilizers, pesticide, and water promises significant gains in crop production but requires accurate and timely information from the field. It can be observed that only after the adoption of recent crop moisture sensing technology, VRT adoption doubled to 22.44 percent in 2010. During the same period, crop moisture sensing adoption increased from 36.21 percent in 2005 to 51.68 percent in 2010.

It is clear that the success and adoption of variable rate technology depends on advancing soil monitoring approaches. Despite being the most recent precision agriculture technology, crop moisture sensing has become one of the most adopted practices. Yet techniques are still limited to manual data collection or limited field coverage.

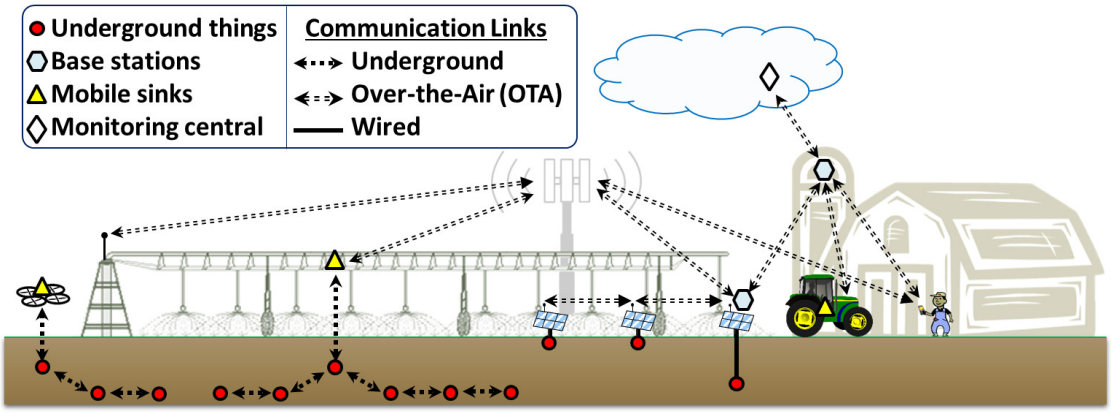

Figure 1.2: IOUT Paradigm in Precision Agriculture.

1.1 Internet of Underground Things

1.1.1 Introduction

Internet of Underground Things (IOUTs) is a type of IoT, which consists of sensors and communication devices, partly or completely buried underground for real-time soil sensing and monitoring. As an extension to Wireless Underground Sensor Networks (WUSNs) [39], [51], [75], [76], [96], [97], [106], [119], [136], [155], [154], [158], [165], [163], [166], [177], [189], [183], [186], [201], IOUT represents autonomous devices that collect any relevant information about the Earth and are interconnected with communication and networking solutions that facilitate sending the information out of fields to the growers and decision mechanisms. IOUT provides seamless access of information collected from agricultural fields through the Internet. IOUT will not only include in-situ soil sensing capabilities (soil moisture, temperature, salinity, etc.), but will also provide the ability to communicate through plants and soil, and can provide real-time information about the environment (wind, rain, solar). When interconnected with existing machinery on the field (seeders, irrigation systems, combines), IOUT will enable complete autonomy on the field and pave the way

for more efficient food production solutions. Due to to the unique requirements of the IOUT applications; i.e., information from soil, operation in remote crop fields, wireless communication through plants and soil, and exposure to elements; existing over-the-air (OTA) wireless communication solutions face significant challenges because they were not designed for these circumstances. As such, IOUT also gives rise to a new type of wireless communications: *wireless underground (UG) communications* [39, 200], where radios are buried in soil and wireless communication is conducted partly through the soil. Integration of UG communications with IOUT will help conserve water resources and improve crop yields [183], [189]. Moreover, advances in IOUT will benefit other applications including landslide monitoring, pipeline assessment, underground mining, and border patrol [40], [76], [155], [158], [200].

Most recently, the need for real-time in-situ information from agricultural fields have given rise to a new type of IoTs: Internet of underground Things (IOUT). IOUT represents autonomous devices that collect any relevant information about the Earth and are interconnected with communication and networking solutions that facilitate *sending the information out of fields* to the growers and decision mechanisms.

IOUT provides seamless access of information collected from agricultural fields through the Internet. IOUT will not only include in-situ soil sensing capabilities (soil moisture, temperature, salinity, etc.), but will also provide the ability to communicate through plants and soil, and can provide real-time information about the environment (wind, rain, solar). When interconnected with existing machinery on the field (seeders, irrigation systems, combines), IOUT will enable complete autonomy on the field and pave the way for more efficient food production solutions.

Due to to the unique requirements of the IOUT applications; i.e., information from soil, operation in remote crop fields, wireless communication through plants and soil, and exposure to elements; existing over-the-air (OTA) wireless communi-

cation solutions face significant challenges because they were not designed for these circumstances. As such, IOUT also gives rise to a new type of wireless communications: *wireless underground (UG) communications* [39, 200], where radios are buried in soil and wireless communication is conducted partly through the soil. Integration of UG communications with IOUT will help conserve water resources and improve crop yields [184], [189]. Moreover, advances in IOUT will benefit other applications including landslide monitoring, pipeline assessment, underground mining, and border patrol [40], [76], [200], [158], [155].

1.1.2 IOUT Architecture

IOUT will consist of interconnected heterogeneous devices tailored to the crop and field operations. Common desirable functionalities of IOUT are:

- *In-situ Sensing:* On board soil moisture, temperature, salinity sensors are required for accurate localized knowledge of the soil. These sensors can be either integrated on the chip along-with other components of the architecture, or they can be used as separate sensors that can be connected to the main components through wires.

- *Wireless Communication in Challenging Environments:* Communication components of IOUT devices are either deployed on the field or within the soil. For OTA communication, solutions should be tailored to the changing environment due to irrigation and crop growth. In addition, any system on the field is exposed to natural elements and should be designed to sustain challenging conditions. Underground communication solutions, while mostly shielded from the environment, require the ability to communicate through soil and adjust its parameters to adapt to dynamic changes in soil.

Table 1.1: Academic IOUT Systems.

Architecture	Sensors	Comm. Tech.	Node Density
Automated Irrigation System [97]	DS1822 (temperature) VH400 (soil moisture)	OTA, ZigBee (ISM)	One node per indoor bed
Soil Scout [189]	TMP122 (temperature) EC-5 (soil moisture)	UG, Custom (ISM)	Eleven scouts on field
Remote Sensing and Irrigation Sys. [119]	TMP107 (temperature) CS616 (soil moisture) CR10 data logger	OTA, Bluetooth (ISM)	Five field stations
Autonomous Precision Agriculture [76]	Watermark 200SS-15 (soil moisture) Data logger	UG, Custom (ISM)	Up to 20 nodes per field
SoilNet [51]	ECHO TE (soil moisture) EC20 TE (soil conductivity)	OTA, ZigBee (ISM)	150 nodes covering 27 ha
MOLES [184]	Magnetic Induction Communications	Magnetic Induction	Indoor Testbed
Irrigation Nodes in Vineyards [31]	Yield NDVI	VRI	140 irrigation nodes
Sensor Network for Irrigation Scheduling [21, 67]	Capacitance (soil moisture) Irromesh	OTA	6 nodes per acre
Cornell's Digital Agriculture [3]	E-Synch, Touch-sensitive soft robots Vineyard mapping technology, RTK	OTA	Field Dependant
Plant Water Status Network [153]	Crop water stress index (CWSI) Modified water stress index (MCWSI)	OTA	Two management zone
Real-Time Leaf Temperature Monitor System [16]	Leaf temperature Ambient temperature Relative humidity and Incident Solar radiation	OTA	Soil and plant monitors,
Thoreau [218]	Temperature, Soil moisture Electric conductivity and Water potential,	OTA	Based on Sigfox,
FarmBeats [197]	Temperature, Soil moisture Orthomosaic and pH,	OTA	Field size of 100 acres
Video-surveillance and Data-monitoring WUSN [87]	Agriculture data monitoring Motion detection, Camera sensor	OTA	In the order of several km
Purdue's Digital Agriculture Initiative [19]	Adaptive weather tower PhenoRover sensor vehicle	OTA	Field Dependant
Pervasive Wireless Sensor Network [204]	Soil Moisture, Camera	OTA	Field Dependant
Pilot Sensor Network [127]	Sensirion SHT75	OTA	100 nodes in a field
SoilBED [81]	Contamination detection	UG	Cross-Well Radar

- *Inter-Connection of Field Machinery, Sensors, Radios, and Cloud:* IOUT architecture should link a diverse multitude of devices on a crop field to the cloud for seamless integration. Accordingly, IOUT architecture will not only provide collected information but will also automate operations on the field based on this information.

Based on these main required functionalities, a representative IOUT architecture is illustrated in Fig. 1.2, with the following components.

- *Underground Things (UTs):* An UT consist of an embedded system with communication and sensing components, where a part of or the entire system resides underground. UTs are protected by weatherproof enclosures and, in un-

Table 1.2: Commercial IOUT Systems.

Architecture	Sensors	Comm. Tech.	Node Density
IRROmesh [13]	200TS (temperature) Watermark 200SS-15 (soil moisture)	OTA, Custom (ISM) OTA, Cellular	Up to 20 nodes network mesh
Field Connect [14]	Leaf wetness Temperature probe Pyranometer Rain gauge Weather station	OTA, Proprietary OTA, Cellular OTA, Satellite	Up to eight nodes per gateway
SapIP Wireless Mesh Network [7]	Plant water use Measure plant stress Soil moisture profile Weather and ET	OTA	25 SapIP nodes.
Automated Irrigation Advisor [29]	Tule Actual ET sensor	OTA	Field Dependant
Internet of Agriculture-BioSense [2]	Machinery auto-steering and automation EC probe & XRF scanner Electrical conductivity map NDVI map Yield map Remote sensing Nano and micro-electronic sensors Big data, and Internet of things	OTA	Field Dependant
EZ-Farm [9]	Water Usage Big data, and Internet of Things Terrain, Soil, Weather Genetics Satellite info Sales	OTA	IBM Bluemix & IoT Foundation
Internet of Food and Farm (IoF2020) [11]	Soil moisture Soil temperature Electrical conductivity and Leaf wetness	OTA	Field Dependant
Cropx Soil Monitoring System [4]	Soil moisture Soil temperature and EC	OTA	Filed Dependant
Plug & Sense Smart Agriculture [17]	Temperature and humidity sensing, Rainfall, Wind speed and direction, Atmospheric pressure, Soil water content, and Leaf wetness	OTA	Field Dependant
Grain Monitor-TempuTech [28]	Grain temperature and Humidity	OTA	Multiple Depths in Grain Elevator
365FarmNet [1]	Mobile device visualization tool for IOUT data	OTA	Field Dependant
SeNet [20]	Sensing and control architecture	OTA	Field Dependant
PrecisionHawk [18]	Drones for sensing Field map generation	OTA	Field Dependant
HereLab [8]	Soil moisture, Drip line psi and rain	OTA	Field Dependant
IntelliFarms [10]	YieldFax Biological BinManager	OTA	Field Dependant
IoT Sensor Platform [12]	IoT/M2M sensors	OTA	Field Dependant
Symphony Link[26]	Long Range Communications	OTA	Field Dependant

derground settings, watertight containers. Buried UTs are protected from the farm equipment and extreme weather conditions. Sensors typically include soil temperature and moisture sensors, but a wide range of other soil- or weather-related phenomena can be monitored. Existing communication scheme include Bluetooth, ZigBee, satellite, cellular, and underground. A UT using Bluetooth

[119] or underground wireless [76] can communicate over 100 meters, commercial products at industrial, scientific and medical (ISM) band can cover three times larger distances, whereas longer-distance connectivity is possible through cellular or satellite. Considering the relatively large field sizes, nodes can be configured to form networks capable of transferring all the sensed information to a collector sink and self-heal in the event that nodes become unreachable (e.g., Irromesh). Nodes are generally powered by a combination of batteries and, if on field, solar panels. Cost of UTs is expected to be relatively inexpensive as they are deployed by the multitude [97].

- *Base stations* are used as gateways to transfer the collected data to the cloud. They are installed in permanent structures such as weather stations or buildings. Base stations are more expensive as they are better safe-guarded and have higher processing powers and communication capabilities [97].

- *Mobile sinks* are installed in equipment that move around the field periodically or as required, such as tractors and irrigation systems [76]. When weather conditions are favorable, turning on an irrigation systems only for data retrieval purpose is expensive. Alternatives unmanned vehicles such as quadrotors or ground robots.

- *Cloud services* are intended to use for permanent storage of the data collected, real-time processing of the field condition, crop related decision making, and integration with other databases (e.g., weather, soil).

A summary of the existing academic and commercial architectures is provided in Table 1.1 and Table 1.2. In most commercial products, OTA wireless communication is utilized, where the UT includes a high-end soil moisture and temperature sensor,

connected to a tower in the field with cellular or satellite communication capabilities. Consequently, measurements generally represent a single point in the field and redeployment of the equipment is needed after planting and before harvest each season to avoid damages by the farming machinery. In addition, commercial products based on OTA wireless mesh networks and academic approaches featuring underground wireless communication have been emerging.

Availability of such a diverse range of communication architectures makes it challenging to form a unified IOUT architecture with the ability to fulfill agricultural requirements seamlessly. This is further complicated due to the lack of standard protocols for sensing and communication tailored to the IOUT. The IOUT communications challenges are discussed in the next section.

1.2 Challenges in IOUT Communications

Unique interactions between soil and communication components in wireless underground communications necessitate revisiting fundamental communication concepts from a different perspective. External factors that directly influence the soil properties also have a great impact over the communication performance of underground communications. The network topology should be designed to be robust to support drastic changes in the channel conditions. The most important soil property to be considered in a IOUT design is the Volumetric Water Content (VWC). Hence, the analysis of the spatio-temporal variation of the VWC in the region where an IOUT application will be deployed is very important. Furthermore, soil composition at a particular location should be carefully investigated to tailor the topology design according to specific characteristics of the underground channel at that location. For instance, different node densities and inter-node distances should be investigated for

the IOUT deployment in a region that presents significant spatial soil composition heterogeneity. Besides the effects of soil type, seasonal changes result in variations of VWC, which significantly affects the communication performance.

We have investigated specific environment parameters through experiments. Insights gathered from the experimental results clearly show the adverse effects of the VWC on the underground communications. Therefore, in the protocol design for IOUT, environment dynamics need to be considered such that operation parameters can be adjusted to the surrounding. Finally, the feasibility of IOUT depends on the investigation of multiple novel factors not considered for traditional terrestrial WSNs. For instance, IOUT must be robust enough to environment parameters, such as VWC and soil composition. To this end, a detailed characterization of the wireless underground channel is necessary. On the other hand, there are several specific positive features of the underground environment, such as the temporal stability, that can be exploited to achieve reliable and energy-efficient communication. Our goal in this research is to develop techniques to achieve high data rate, long range communications, with the ability to adjust operation parameters according to the environment in which such systems are deployed, for a hybrid architecture IOUT design.

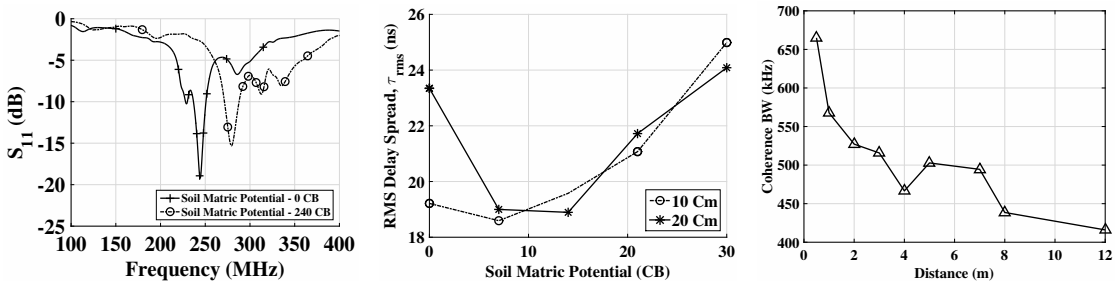

(a) (b) (c)

Figure 1.3: (a) Antenna return loss with change in soil moisture at 40 cm depth in sandy soil [155], (b) RMS delay spread vs. soil moisture at 50 cm distance in silty clay loam soil (greater matric potential values indicate lower soil moisture and zero matric potential represents near saturation condition) [155], (c) Coherence bandwidth as a function of distance at transmitter receiver depth of 20 cm in silty clay loam soil [155].

The ultimate potential of IOUT for high data rate communication depends on the underground channel characteristics, which is not well modeled. Therefore, experimentation is required to characterize its nature. Furthermore, interactions between soil and communication components, including antenna and wireless underground channel, result in unique performance characteristics in IOUT. We provide three distinct examples below and in Figs. 1.3, based on empirical measurements [155], [158], on the effects of soil on antenna bandwidth and coherence bandwidth of the underground channel.

Soil type, soil moisture, burial distance, and depth affect the communication performance [200], leading to dynamic changes in antenna return loss, channel impulse response, and root mean square (RMS) delay spread. In Fig. 1.3(a), empirical antenna return loss with change in soil moisture has been shown at a 40 cm depth in sandy soil. Soil moisture is expressed as soil matric potential (CB); greater matric potential values indicate lower soil moisture and zero matric potential represents near saturation condition. It can be observed that resonant frequency of antenna changes from 244 MHz to 289 MHz when soil matric potential (inversely proportional to soil moisture) increases from 0 CB to 240 CB.

This significant change of 45 MHz necessitates a dynamic change in operation frequency with soil moisture to achieve maximum system bandwidth [74], otherwise, performance degradation will result due to operation frequency going outside of the antenna bandwidth and resonant frequency range. Similarly, with a decrease in soil moisture, antenna bandwidth, defined as the frequency range where the return loss is less than -10 dB, has increased from 14 MHz to 20 MHz. Accordingly, soil moisture also impacts available system bandwidth.

Soil texture is determined from the percentage of the sand, silt and clay in the soil. Particle size distribution and classification of testbed soils is given in Table 1.3.

In Fig. 1.3(b), the change in RMS delay spread with soil moisture is shown at a 50 cm distance, and 10 cm and 20 cm depths in silt loam. It can be observed that RMS delay spread decreases first as soil moisture is decreased from near-saturation (0 CB) to 8 CB. Then, a consistent increase in delay spread is observed. These variations, which may occur within a short span of time due to external impacts such as rain or irrigation, causes the wireless underground channel to be frequency-selective.

The coherence bandwidth statistics (for 90% signal correlation based on root mean square delay spread) are shown as a function of distance in Fig. 1.3(c). It can be observed that the coherence bandwidth ranges from 411 kHz to 678 kHz for distances up to 12 m. This small coherence bandwidth limits the achievable data rates through use of conventional communication techniques in IOUT communications.

Based on this empirical insight, we can classify mainly five types of physical mechanisms that lead to variations in the UG channel statistics, the analyses of which constitutes the major contributions of this research:

Soil Texture and Bulk Density Variations: EM waves exhibit attenuation when incident in soil medium. These variations vary with texture and bulk density of soil. For example, sandy soil holds less bound water, which is the major component in soil that absorbs EM waves. Water holding capacity of medium textured soils (silt loam, fine sandy loam, and silty clay loam) is much higher, because of the small pore size, as compared to coarse soils (sand, sandy loam, loamy sand). Medium textured soils have lower pore size and hence, no aggregation and little resistance against

Table 1.3: Particle Size Distribution and Classification of Testbed Soils.

Textural Class	**%Sand**	**%Silt**	**%Clay**
Sandy Soil	86	11	3
Silt Loam	33	51	16
Silty Clay Loam	13	55	32

gravity [85].

Soil Moisture Variations: The effective permittivity of soil is a complex number. Thus, besides diffusion attenuation, EM waves also suffer from an additional attenuation caused by the absorption of soil water content [75], [76], [165].

Distance and Depth Variations: Received signal strength varies with depth of and distance between transmitter and receiver antennas because different components of EM waves suffer attenuation based on their travel paths. Sensors in WUSN applications are usually buried in topsoil and subsoil layers[1] [163], [166].

Antenna Variations: When an antenna is buried underground, its return loss property changes due to the high permittivity of the soil [74]. Moreover, with the variation in soil moisture and hence soil permittivity, the return loss of the antenna varies as well [74].

Frequency Variations: The path loss caused by the attenuation is frequency dependent [69]. In addition, when EM waves propagate in soil, their wavelength shortens due to higher permittivity of soil than the air. Channel capacity in soil is also function of operation frequency [74].

[1]Topsoil layer (root growth region) consists of top 1 Feet of soil and $2-4$ Feet layer below the topsoil is subsoil.

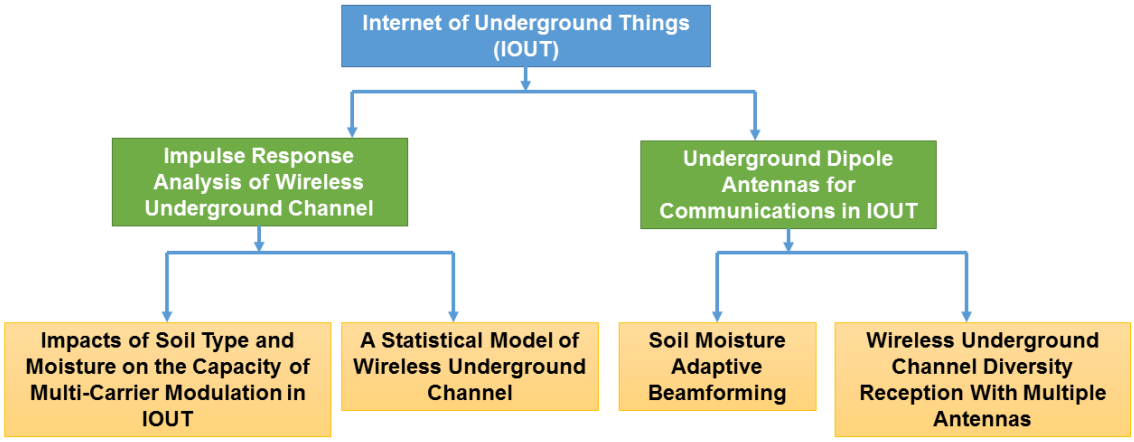

Figure 1.4: The structure of the research.

1.3 Research Objectives and Solutions

The aim of this research is to characterize UG channel; develop environment-aware, cross-layer communication solutions to achieve high data rate, long range communications; and illustrate applications to agriculture. This research also aims to capture and analyze the impulse response of the wireless UG channel through extensive experiments. The components of this research are shown in Fig. 1.4. With IOUT communications at its core, it develops into two sub-branches. First, the impulse response analysis of the wireless underground channel, second, underground dipole antennas for communications in IOUT. The statistical model and multi-carrier modulation are based on the impulse response analysis branch. Antenna analysis branch is further divided into soil moisture adaptive beamforming and wireless underground channel diversity reception.

These findings are evaluated using computational electromagnetic software simulation and proof of concept validations are done using testbed experiments. In the rest of the section, each research objective is introduced in detail.

1.3.1 Impulse Response Analysis of Wireless Underground Channel

In Chapter 4, UG channel impulse response is modeled and validated via extensive experiments in indoor and field testbed settings. Three distinct types of soils are selected with sand and clay contents ranging from 13% to 86% and 3% to 32%, respectively. Impacts of changes in soil texture and soil moisture are investigated with more than 1,200 measurements in a novel UG testbed that allows flexibility in soil moisture control. Time domain characteristics of channel such as RMS delay spread, coherence bandwidth, and multipath power gain are analyzed. The analysis of the power delay profile validates the three main components of the UG channel: direct, reflected, and lateral waves. It is shown that RMS delay spread follows a log-normal distribution. The coherence bandwidth ranges between 650 kHz and $1.15 MHz$ for soil paths of up to 1m and decreases to 418 kHz for distances above 10m. Soil moisture is shown to affect RMS delay spread non-linearly, which provides opportunities for soil moisture-based dynamic adaptation techniques. The model and analysis paves the way for tailored solutions for data harvesting, UG sub-carrier communication, and UG beamforming.

1.3.2 A Statistical Model of Wireless Underground Channel

In Chapter 5, based on the empirical and the statistical analysis, a statistical channel model for the UG channel is developed. The parameters for the statistical tapped-delay-line model are extracted from the measured power delay profiles (PDP). The PDP of the UG channel is represented by the exponential decay of the lateral, direct, and reflected waves. The aim is to develop a statistical model to generate the channel impulse response to precisely predict the UG channel RMS delay spread, coherence bandwidth, and propagation loss characteristics in different conditions. The statistical

model, which is useful for tailored IOUT deployments, will also be compared with the empirical data.

1.3.3 Impacts of Soil Type and Moisture on the Capacity of Multi-Carrier Modulation in Internet of Underground Things

In Chapter 6, capacity profile of wireless underground (UG) channel for multi-carrier transmission techniques is analyzed based on empirical antenna return loss and channel frequency response models in different soil types and moisture values. It is shown that data rates in excess of 124 Mbps are possible for distances up to 12 m. For shorter distances and lower soil moisture conditions, data rates of 362 Mbps can be achieved. It is also shown that due to soil moisture variations, UG channel experiences significant variations in antenna bandwidth and coherence bandwidth, which demands dynamic subcarrier operation. Theoretical analysis based on this empirical data show that by adaption to soil moisture variations, 180% improvement in channel capacity is possible when soil moisture decreases. It is shown that compared to a fixed bandwidth system; soil-based, system and sub-carrier bandwidth adaptation leads to capacity gains of 56%-136%. The analysis is based on indoor and outdoor experiments with more than $1,500$ measurements taken over a period of 10 months. These semi-empirical capacity results provide further evidence on the potential of underground channel as a viable media for high data rate communication and highlight potential improvements in this area.

1.3.4 Soil Moisture Adaptive Beamforming

In Chapter 7, a novel framework for underground beamforming using adaptive antenna arrays are presented to extend communication distances for practical applications. Based on the analysis of propagation in wireless underground channel, a

theoretical model is developed to use soil moisture information to improve wireless underground communications performance. Array element in soil is analyzed empirically and impacts of soil type and soil moisture on return loss (RL) and resonant frequency is investigated. Accordingly, beam patterns is analyzed to communicate with underground and above ground devices. Depending on the incident angle, effects of the refraction from soil-air interface are ascertained. Beam steering to improve UG communications is developed by providing a high-gain lateral wave. To this end, the angle to enhances lateral wave, as a function of dielectric properties of the soil, soil moisture, and soil texture is determined. Accordingly, a soil moisture adaptive beamforming (SMABF) algorithm is developed for planar array structures and evaluations is done with different optimization approaches to improve UG communication performance.

1.3.5 Wireless Underground Channel Diversity Reception With Multiple Antennas

In Chapter 8, the performance of different modulation schemes in IOUT communications is studied through simulations and experiments. The spatial modularity of direct, lateral, and reflected components of the UG channel is exploited by using multiple antennas. First, the achievable bit error rates is determined under normalized delay spreads (τ_d) constraint of the UG channel. Evaluations is conducted through the first software-defined radio-based field experiments for UG channel. Moreover, impacts of equalization on the performance improvement of an IOUT system is determined using multi-tap DFE (decision-feedback equalizer) adaptive equalizer. Then, two novel UG receiver diversity reception designs, namely, 3W-Rake and Lateral-Direct-Reflected (LDR) will developed and analyzed for performance improvement. BER under diversity reception is also analyzed.

1.3.6 Underground Dipole Antennas for Communications in Internet of Underground Things

In Chapter 9, a theoretical model is developed to investigate the the impact of change of soil moisture on the performance of a dipole antennas buried underground. Antenna impedance is determined by taking into account the proximity of burial depth to the topsoil horizon. Experiments are conducted to characterize the effects of soil in an indoor testbed and field testbeds, where antennas are buried at different depths in silty clay loam, sandy and silt loam soil. For different subsurface burial depths (0.1-0.4m), impacts of change in soil moisture on the resonant frequency of the antenna is investigated. Simulations are done to validate the theoretical and measured results. Figures of merit of underground antenna in different soils, under different soil moisture levels at different burial depths are presented to allow system engineer to predict underground antenna resonance and to aid in design an efficient communication system in IOUT.

1.3.7 *In Situ* Real-Time Permittivity Estimation and Soil Moisture Sensing using Wireless Underground Communications

Internet of Underground Things (IOUT) communications have the potential for soil properties estimation and soil moisture monitoring. In Chapter 10, a method has been developed for real-time *in situ* estimation of relative permittivity of soil, and soil moisture, that is determined from the propagation path loss, and velocity of wave propagation of an underground (UG) transmitter and receiver link in wireless underground communications (WUC). The permittivity and soil moisture estimation processes (*Di-Sense*, where *Di-* prefix means *two*) are modeled and validated through an outdoor UG software-defined radio (SDR) testbed, and indoor greenhouse testbed.

SDR experiments are conducted in the frequency range of 100 MHz to 500 MHz, using antennas buried at 10 cm, 20 cm, 30 cm, and 40 cm depths in different soils under different soil moisture levels, by using dipole antennas with over the air (OTA) resonant frequency of 433 MHz. Experiments are conducted in silt loam, silty clay loam, and sandy soils. By using Di-Sense approach, soil moisture and permittivity can be measured with high accuracy in 1 m to 15 m distance range in plant root zone up to depth of 40 cm. The estimated soil parameters have less than 8 % estimation error from the ground truth measurements and semi-empirical dielectric mixing models.

1.4 Thesis Organization

This thesis is organized as the following. In Chapter 2, the existing work related to wireless underground channel is discussed. UG testbed design, experiment methodology, and empirical results are presented in Chapter 3. The impulse response model of the wireless underground channel, indoor testbed design and development and impulse response parameters of the wireless underground channel in different soils at different depths and distances and soil moisture levels is discussed in Chapter 4. A statistical channel model for the UG channel based on the empirical and the statistical analysis is presented in Chapter 5. In Chapter 6, UG multi-carrier modulation capacity model has been presented for high data rate communications in wireless underground channel. This capacity model takes into account system bandwidth, channel transfer function, and coherence bandwidth of the channel. Underground beamforming approaches for long Distance underground Communications using buried antenna arrays are discussed in Chapter 7. The performance of different modulation schemes in IOUT communications is studied through simulations and experiments in Chapter 8. In Chapter 9, a theoretical model is developed to investigate the the impact of

change of soil moisture on the performance of a dipole antennas buried underground. In Chapter 10, a method has been developed for real-time *in situ* estimation of relative permittivity of soil, and soil moisture, that is determined from the propagation path loss, and velocity of wave propagation of an underground (UG) transmitter and receiver link in wireless underground communications (WUC). Finally, the dissertation is concluded in Chapter 11.

Chapter 2

Related Work

IOUTs have many applications in precision agriculture, border patrol and environment monitoring. IOUT includes communication devices and sensors, partly or completely buried underground for real-time soil sensing and monitoring. In precision agriculture IOUTs are being used for sensing and monitoring of the soil moisture and other physical properties of soil [39], [51], [76], [96], [97], [106], [119], [136], [155], [154], [158], [177], [186], [189]. Border monitoring is another important application area of WUSNs where these networks are being used to enforce border and stop infiltration [40], [181]. Monitoring applications of WUSNs include land slide monitoring, pipeline monitoring [96], [177], [180].

Wireless communication in IOUTs is an emerging field and few models exist to represent the underground communication. Underwater communication [47], [147] has similarities with the wireless underground communication due to the challenged media. However, underwater communication based on electromagnetic waves is not feasible because of high attenuation. Therefore alternative techniques including acoustic [47] are used in underwater communications. Acoustic technique cannot be used in UG channel due to vibration limitation. Acoustic propagation experiences low physical link quality and higher delays due to lower speed of sound. Bandwidth is distance dependent and only extremely low bandwidths are achieved. Moreover, other

limitations, such as size and cost of acoustic equipment, and challenging deployment restrict the use of this approach in the wireless underground sensor networks.

Wireless underground communications using magnetic induction (MI) techniques have been proposed in [136], [125], [130], [178], [179], [183]. Magnetic induction techniques have several limitations. Signal strength decays with inverse cube factor and high data rates are not possible. Moreover, in MI, communication cannot take place if sender receiver coils are perpendicular to each other. Network architecture cannot scale due to very long wavelengths of the magnetic channel. Therefore, due to these limitations and its inability to communicate with above-ground devices, this approach cannot be readily implemented in IOUT.

Channel models for UG communication have been developed in [75], and [200] but empirical validations have not been performed. Proof-of-concept integration of wireless underground wireless sensor networks with precision agriculture cyber-physical systems (CPS) and center-pivot systems has been presented in [76], [166]. In [165], [163], empirical evaluations of underground channel are presented, however, antenna bandwidth was not considered. In [200], we have developed a 2-wave path loss model but lateral wave is not considered. In [52], path loss prediction models have been developed but these do not consider underground communication. A model for underground communication in mines and road tunnels has been developed in [177] but it cannot be applied to IOUT due to wave propagation differences between tunnels and soil. We have also developed a closed-form path loss model using lateral waves in [75] but channel impulse response and statistics cannot be captured through this simplified model. In [158], we have presented a detailed characterization of coherence bandwidth of the underground channel.

Wireless communication in underground channel is an evolving field and extensive discussion of channel capacity does not exist in the literature. Capacity of single-

carrier communication in the UG channel has been investigated in [74] but the analysis does not consider a practical modulation scheme and empirical validations have not be provided. In [155] analyze the capacity of multi-carrier modulation in the UG channel based on empirical measurements of channel transfer function, coherence bandwidth, and antenna return loss under three different soil types and various soil moisture conditions.

Antennas used in IOUT are buried in soil, which is uncommon in traditional communication scenarios. Over the entire span of 20^{th} century, starting from Sommerfeld's seminal work [174] in 1909, electromagnetic wave propagation in subsurface stratified medias has been studied extensively in many work [42], [45], [48], [71], [99], [138], [169], [182], [202], [207], and analysis of effects of the medium on electromagnetic waves has been analyzed. However these studies analyze fields of horizontal infinitesimal dipole of unit electric moment, whereas for practical applications, a finite size antenna with known impedance, field patterns, and current distribution is desirable. Here, we briefly discuss major contributions of this literature. Field calculations and numerical evaluation of the dipole *over* the lossy half space was first presented in [142]. EM Wave propagation *along* the interface has been extensively analyzed in [202]. However, these studies can not be applied to antennas buried underground. A significant effort to analyze the dipole buried *in* the lossy half space was made in [138]. By using two vector potentials, the depth attenuation factor and ground wave attenuation factor of far-field radiation form UG dipole was given. However, reflected current from soil-air interface are not considered in this work. In [45], field components per unit dipole moment are calculated by using the Hertz potential which were used to obtain the EM fields. The work in [138] differs from [45] on the displacement current in lossy half space, where former work does not consider the displacement current. In [182], fields from a Hertzian dipole immersed in an infinite isotropic lossy

medium has been given. King further improved EM fields by taking into account the half-space interface and lateral waves [121, 212]. In King's work complete EM fields, from a horizontal infinitesimal dipole with unit electric moment immersed in lossy half space, are given at all points in both half spaces at different depths. Since buried UG antennas are extended devices, fields generated from these antennas are significantly different from the infinitesimal antennas.

Antennas in matter have been analyzed in [86], [122], where the EM fields of antennas in infinite dissipative medium and half space have been derived theoretically. In these analyses, the dipole antennas are assumed to be perfectly matched and hence the return loss is not considered. In [99], [207], and radiation efficiency and relative gain expressions of underground antennas are developed but simulated and empirical results are not presented. In [108], the impedance of a dipole antenna in solutions are measured. The impacts of the depth of the antenna with respect to the solution surface, the length of the dipole, and the complex permittivity of the solution are discussed. However, this work cannot be directly applied to IOUTs since the permittivity of soil has different characteristics than solutions and the change in the permittivity caused by the variations in soil moisture is not considered. Communications between buried antennas have been discussed in [118], but effects of antennae orientation and impedance analysis has not been analyzed. Performance of four buried antennas has been analyzed [84], where antenna performance in refractory concrete with transmitter buried only at single fixed depth of 1 m without consideration of effects of concrete-air interface is analyzed. In [56], analysis of circularly polarized patch antenna embedded in concrete at 3 cm depth is done without consideration of the interface effects.

In existing IOUT experiments and applications, the permittivity of the soil is generally calculated according to a soil dielectric model [40, 144], which leads to the

actual wavelength at a given frequency. The antenna is then designed corresponding to the calculated wavelength [188]. In [188], an elliptical planar antenna is designed for an IOUT application. The size of the antenna is determined by comparing the wavelength in soil and the wavelength in air for the same frequency. However, this technique does not provide the desired impedance match. In [217], experimental results are shown for Impulse Radio Ultra-Wide Band (IR-UWB) IOUT, however impact of soil-air interface is not considered. In [191], a design of lateral wave antenna is presented where antennas are placed on surface and underground communication scenario is not considered.

The disturbance caused by impedance change in soil is similar to the impedance change of a hand-held device close to a human body [53, 190] or implanted devices in human body [68, 93]. In these applications, simulation and testbed results show that there are impacts from human body that cause performance degradation of the antennas. Though similar, these studies cannot be applied to the underground communication directly. First, the permittivity of the human body is higher than in soil. At 900 MHz, the relative permittivity of the human body is 50 [190] and for soil with a soil moisture of 5%, it is 5 [144]. In addition, the permittivity of soil varies with moisture, but for human body, it is relatively static. Most importantly, in these applications, the human body can be modeled as a block while in underground communications, soil is modeled as a half-space since the size of the field is significantly larger than the antenna.

Beamforming has been studied in [41], [43], [77], [126], [141], [149], [208], for over-the-air (OTA) wireless channels and in [123] for MI power transfer. However, to the best of our knowledge, UG beamforming has not been studied before. In UG communications, lateral component [122] has the potential, via beam-forming techniques, to reach farther UG distances, which otherwise are limited (8 m to 12 m)

because of higher attenuation in soil [158].

Different soil permittivity and moisture estimation approaches have historically been considered in the literature. Following literature review is not all encompassing, rather we emphasize on some of the latest literature on the subject, with the purpose of highlighting similarities and differences with other works. Permittivity estimation and soil water measurement is classified into different approaches. Methods used for quantifying soil water include gravimetric method, TDR, GPR, capacitance probes, remote sensing, hygrometric techniques, electromagnetic induction, tensionmetry, neutron thermalization, nuclear magnetic resonance, gamma ray attenuation, resistive sensors, and optical methods. Some of these methods are reviewed briefly in the following.

First, we discuss laboratory based soil properties estimation approaches. In [104], soil EM parameters are derived as function of soil moisture, soil density, and frequency. This model is restricted to 20 % soil moisture weight, and requires extensive sample preparation. In [65], a probe based laboratory equipment has been developed that requires use of vector network analyzer (VNA), and works in frequency range of 45 MHz to 26.5 MHz. A model based to estimate the dielectric permittivity of soil based on the empirical evaluation has been done in [203]. In [69], a model of dielectric properties of soil has been developed for frequencies higher than 1.4 MHz. In [144], Peplinski modified the model through extensive measurements to characterize the dielectric behavior of the soil in the frequency range of 300 MHz to 1.3 GHz. A comprehensive review of soil permittivity estimation approaches is given in [65]. These methods require the removal of the soil from the site. Moreover, laboratory based measurements of soil samples taken from site are labor-intensive, and are not truly representative of the in-situ soil conditions. Therefore, automated soil moisture monitoring technologies are needed.

Second approach to measure the soil properties, based on TDR, has been proposed in [140], that requires measurement of impedance and refractive index of soil. In [194], a method has been proposed to estimate the EM properties of soils for detection of Dense Non-Aqueous Phase Liquids (DNAPLs) hazardous materials using Cross-Well Radar (CWR). In this method, a wideband pulse waveform is transmitted in the frequency range of 0.5 GHz to 1.5 GHz, and soil permittivity is obtained using reflection and transmission simulations in dry sand. A detailed review of time domain permittivity measurements in soils is given in [198]. TDR based approach requires installation of sensors at each measurement location. However, real-time soil moisture sensing is required for effective decision making in agricultural fields.

Next, antenna based soil properties estimation approaches are discussed. In [171], [172], a method has been developed to measure the electrical properties of the earth using antennas buried in the geological media. However, this approach required adjustment of the length of antenna to achieve zero input reactance. This technique also requires measurement of the input reactance to derive the electrical constitutive parameters of the material. In [173], a GPR measurements based soil permittivity estimation is done in presence of soil antenna interactions by using the Fresnel reflection coefficients. However, only numerical results are presented without empirical validations, and this approach also requires complicated time-domain analysis. In [50], dielectric properties of the soil are measured in the frequency range of 0.1 GHz to 1 GHz using wideband frequency domain method. This method requires use of impedance measurement equipment (LCR meter), and VNA. In [139], [205], a frequency domain method has been proposed to measure complex dielectric proprieties of the soil, that requires removing the soil and pacing it in a probe.

The GPR technique is also utilized to estimate soil permittivity and moisture. A method has been developed in [105] to estimate the permittivity of ground which is

based on the correlation of the cross talk of early-time GPR signal with dielectric properties of ground. However, GPR method works for only shallow depth (0-20 cm), and requires a calibration procedure. Moreover, measurements depth resolution of soil moisture content can not be restrained to a particular burial depth in soil.

Remote sensing of soil moisture is another important measurement approach. Although observation range is much higher with remote sensing [196], it is more sensitive to soil water content [115]. Passive remote sensing soil moisture measurement approaches [44], have very low spatial resolution (in the order of kilometers). Although, high spatial resolution is achieved (in the order of meters) with active sensing, however soil moisture measurement depth is restricted to the few top centimeters of the topsoil layers and vegetation cover effects the accuracy of soil moisture measurement [170].

Overall, this research work has the potential to transform underground communications. The emerging use of IOUT in many areas, including precision agriculture, transportation, environment and infrastructure monitoring, and border patrol, underscores the importance of wireless underground (UG) communications. Yet, existing limitations in terms of communication ranges and data rates prohibit widespread adoption. The goals of this research are to characterize the underground channel; develop environment-adaptive solutions to achieve high data rate, long-range communications. The novel approaches developed in this dissertation have broaden the scope of existing and novel applications, leading to economically viable solutions. Moreover, the results and the insight from this research have the potential to enable a wide array of novel solutions from saving water resources for more food production to saving lives on the roadways.

Chapter 3

Underground Communication Testbeds and Experiments

Internet of underground things (IOUT) is an emerging paradigm which consists of sensors and communication devices, partly or completely buried underground for real-time soil sensing and monitoring. Potential applications of Internet of Underground Things (IOUT) in many emerging fields require theoretical understanding, development of models, and extensive empirical evaluations of the wireless underground channel. In the wireless underground channel, communication is carried out through the soil and is affected by soil properties and moisture. To conduct wireless underground channel experiments in the outdoor and field environment is daunting task due to soil's physical phenomenas and climatic conditions. These challenges of conducting experiments underscores the need to develop indoor testbed for underground channel characterization. An extensive measurement campaign spanning over a period of three years has been carried out. Empirical results of the underground channel transfer functions and underground antenna performance are presented in silty clay loam, sandy and silt loam soils. Experimental results indicates that use of indoor testbed leads to efficient, speedy and improved characterization of underground communications in different soils. It is also shown that performance of underground channel and buried antenna affected by variations in soil moisture. Moreover, soil texture and burial depth also cause fluctuations in underground communications.

Power delay profile analysis of the UG channel indicates that UG communication is carried out by through-the-earth (direct) wave for short distances and through up-over-down (lateral) wave for longer distances. The underground channel experimental results presented in this highlights impacts of different physical phenomena of soil on the UG communications, and help in communication system design and practical implementation of an IOUT system.

The wireless underground channel is being used in many areas including environment and infrastructure monitoring [158], [155], [156], [96], [131], [136], [177], [186], [35], [184], border patrol [40], [181], [180], precision agriculture [76], [33], [166], [216] contaminated soil and dense nonaqueous phase liquids (DNAPLs) detection [82], and in remote sensing, detection of buried objects and ground penetrating radars [173], [143], [105]. Underground communications is an emerging field and lacks well established and empirically validated channel models. Over the air (OTA) channel models cannot be directly applied to underground communications because underground medium is lossy and is affected by soil, air, and moisture. These factors leads to diverse soils dielectric spectra based and time, frequency, and space.

An extensive measurement campaign has been carried out over the period of last three years to investigate the behavior of soil types and moisture on the underground channel for IOUT communications. Antenna return loss, path loss and time domain measurements are reported in Chapter 9, for silt loam, silty clay loam, and sandy soils, under different soil wetness conditions. Underground channel models have been developed in [40], [75], [200] using theoretical electromagnetic fields analysis. However accuracy of these channel models have not been verified through experimentation, therefore, empirical evaluations and validations are necessary characterize the effects of soil moisture, soil texture, burial depth and distance on the underground communications. Furthermore performance of the underground antenna also needs

to be analyzed. Moreover, deeper understanding of the effects of soil-air interface, dielectric properties of the soil, and lateral wave can be realized through extensive experimentation campaign.

In this chapter, we present an indoor testbed, developed in greenhouse settings, for wireless underground channel modeling and wireless underground sensor networks experiments. The developed indoor testbed provides ease of controlling soil moisture, replacement of soil, easy installation and replacement of non-functional equipment, and protection from extreme weather. Potential applications of this testbed include wireless underground channel characterization, antenna performance analysis, testing and calibration soil Volumetric Water Content (VWC) sensors, detection of soil contaminants and buried objects, estimation of dielectric properties of soil, ground-penetrating radar (GPR) and cross-well radar (CWR) experiments and for testing and implementation of different IOUT topologies in different soil types under different soil moisture conditions. We also present empirical results of an extensive measurement campaign for channel transfer function and antenna experiments conduced in sandy and silt loam soils. These testbed design guidelines and results will lead to development of next generation technologies, communication paradigms, and applications of underground communications in wireless communications, biosciences and remote sensing areas. In addition to the testbed design, major contributions are underground channel experiments from near saturation to wilting point at different transmitter and receiver depths and distances with scalable sample size and minimum boundary effects. To the best of our knowledge, this is the first ever work to present path loss, return loss and impulse response measurements in different soils in different soil wetness conditions in an indoor and field testbed.

Rest of the chapter is organized as follows: background is given in Section 3.1. Detailed description of the testbed and field trial sites, measurement techniques with

types of measurement carried out is given in Section 3.2. Path loss, return loss and power delay profile (PDP) results are presented in Section 3.4. Chapter is concluded in Section 3.5.

3.1 Background

Electromagnetic (EM) wave communication in the underground channel consists of three types of links [8], namely underground to aboveground (UG2AG), aboveground to underground (AG2UG) and underground to underground (UG2UG). Soil medium is involved in communication through these three links. Wavelength of an EM wave incident into soil is affected by dielectric properties of the soil. Soil texture and its water holding capacity, bulk density, and salinity affects the propagation of waves. To understand the propagation of waves in soil, it is important to understand the physical processes happening in soil. Soil medium consists of soil particles, pore space, and water content. Soil particles are divided in to silt, sand and clay based on their size. Soils are classified based on these particles sizes. Complex dielectric constant of soil consists of ϵ_s' and ϵ_s''. Dielectric constant of soil that is fully dried is not dependent on frequency can be determined from [195]:

$$\epsilon_s' = [1 + 0.44\rho_b]^2, \tag{3.1}$$

Where ρ_b is the bulk density of soil[1]. Dielectric spectra of the soil becomes more complicated with the increase of moisture content. Water content inside the soil is divided into two bound and free water. Bound water refers to water held by soil particles in the top layers of soil, and depends on particles surface area which is defined by the soil composition. Water content in the soil can be ascertained by

[1]Bulk density is defined as the ratio of dry soil mass to bulk soil volume including pore spaces.

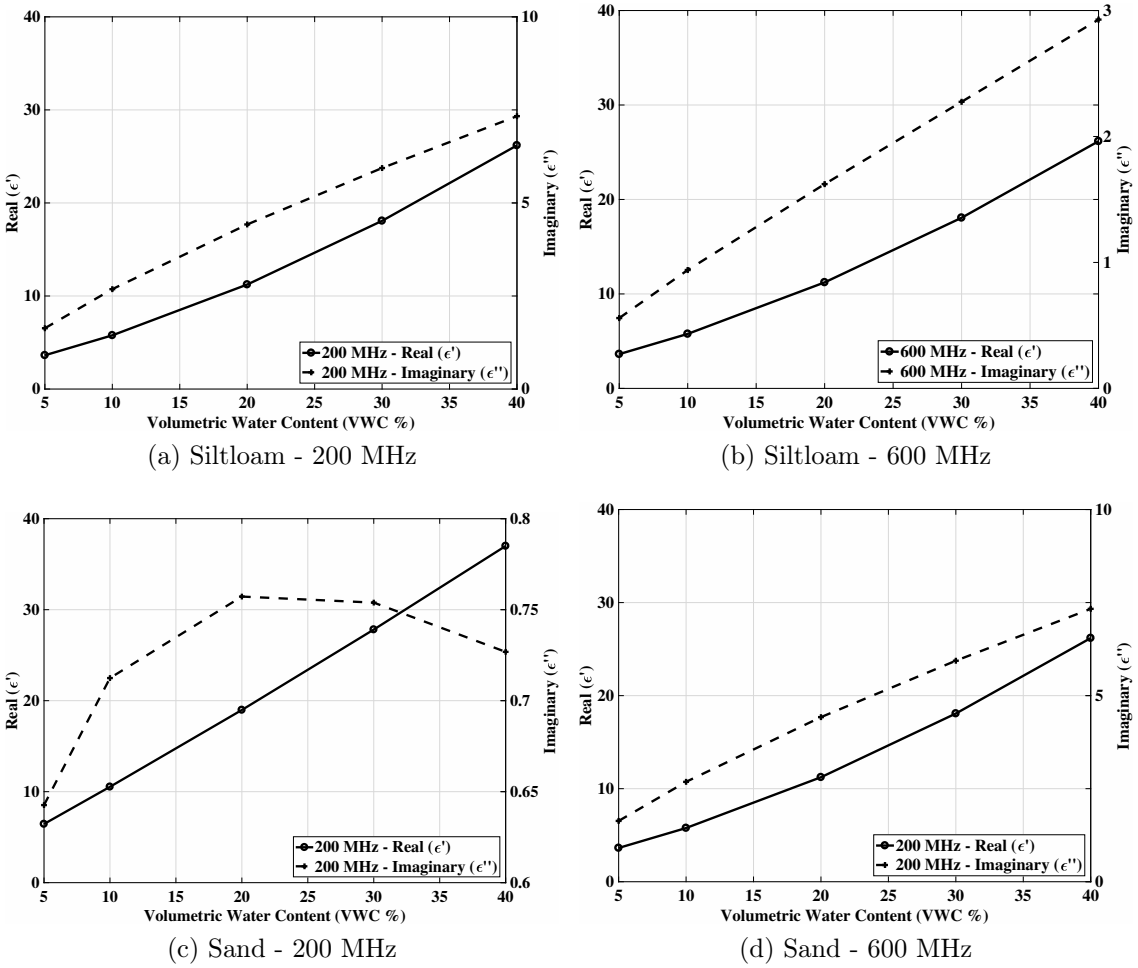

(a) Siltloam - 200 MHz

(b) Siltloam - 600 MHz

(c) Sand - 200 MHz

(d) Sand - 600 MHz

Figure 3.1: Dielectric constant of siltloam and sandy soil at 200 MHz and 600 MHz frequency.

either volumetric or gravimetric bases.

Electromagnetic waves traveling in the soil interacts with soil particles, air, free and bound water. Free and bound water molecules when in interaction electromagnetic wave exhibits different dielectric dispersion and dielectric constant depends on the frequency of EM waves. In addition to the water content and frequency, other factors such as bulk density and soil texture also effects the permittivity of soil.

In [69], a model of dielectric properties of soil has been proposed for frequencies higher than 1.4 MHz. In [144], Peplinski et.al. has modified the model through

extensive measurements to characteristic the dielectric behavior of the soil in the frequency range of 300 MHz to 1.3 GHz. It is given as:

$$\epsilon_s = \epsilon_s' - i\epsilon_s'' \ , \tag{3.2}$$

ϵ_s is the relative complex dielectric constant of the soil-water mixture, and it depends on the soil texture, volumetric water content, bulk density, frequency and particle density.

In Figs. 3.1 dielectric constant in siltloam and sandy soil is shown at different frequency and water content values. It can be observed that ϵ_s' increases linearly when volumetric water content of the soil is increased.

Propagation in the underground channel happens through three different paths. Direct wave and reflected wave paths are through the soil, whereas lateral wave travels through both air and soil. Lateral waves travels along the soil air-interface. A detailed characterization of propagation of these three waves in the underground channel will be given in Chapter 4.

3.2 Experimental Setup

In this section, a complete description of the testbeds used in this dissertation is provided. It is then followed by the techniques and methods employed in the UG channel measurements.

3.2.1 The Indoor Testbed

Conducting WUSN experiments in outdoor settings is a challenging task. These challenges include lack of availability of wide range of soil moisture levels over a

(a) (b) (c) (d) (e)

Figure 3.2: Testbed Development: (a) Testbed box, (c) Packed soil, (b) Layer of gravel at the bottom of the testbed, (d) Antenna placement, (e) Final outlook.

short period of time, difficulty of dynamic control over soil moisture, changing soil types, and installation/replacement of equipment. Furthermore, extreme weather and temperature affects make it hard to conduct experiments in all seasons.

To overcome these challenges faced in outdoor environments, an indoor testbed is developed in a greenhouse settings. It is a 100 in × 36 in × 48 in wooden box (Fig. 3.2(a)) assembled with wooden planks and contains 90 ft^3 of packed soil. A drainage system is installed in the bottom, and sides of the box are covered with water proof tarp to stop water seepage from sides. Before installation of antennas and sensors, 3 in layer of gravel is laid in the bottom of the box for free drainage of water (Fig. 3.2(b)) and then soil is placed in the box (Fig. 3.2(c)).

To monitor the soil moisture level, 8 Watermark sensors are installed on each side of the box at 10 cm, 20 cm, 30 cm and 40 cm depths. These sensors are connected to two Watermark dataloggers. Soil is packed after every 30 cm by using a tamper tool to achieve the bulk density[2] to mimic real-world field conditions. This process is repeated for antenna installation at each depth. Three sets of four dipole antennas are installed (Fig. 3.2(d)) at the depths of 10 cm, 20 cm, 30 cm, and 40 cm. These sets are 50 cm apart from each other. Final outlook of the testbed is shown in Fig. 3.2(e).

We have conducted experiments for two different types of soils in the indoor

[2]Bulk density is defined as the ratio of dry soil mass to bulk soil volume including pore spaces.

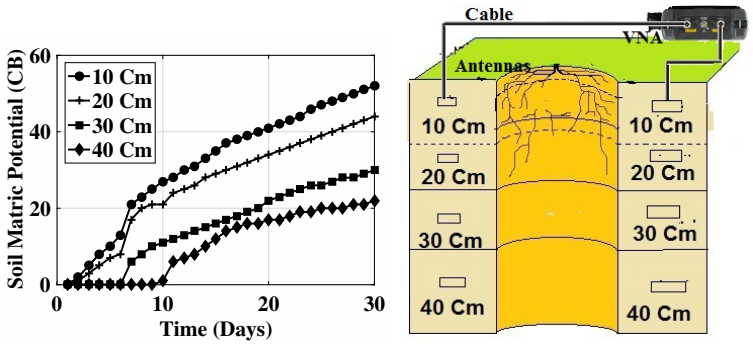

(a) (b)

Figure 3.3: (a) Soil moisture (expressed as soil matric potential; greater matric potential values indicate lower soil moisture and zero matric potential represents near saturation condition) with time in silt loam testbed, (b) Experiment layout.

Table 3.1: Particle Size Distribution and Classification of Testbed Soils.

Textural Class	%Sand	%Silt	%Clay
Sandy Soil	86	11	3
Silt Loam	33	51	16
Silty Clay Loam	13	55	32

testbed: silt loam and sandy soil. Particle size distribution and classification of testbed soils is given in Table 3.1. To investigate the effects of soil texture on underground communication, soils selected for use in the testbed have sand contents ranging from 13 % to 86 % and clay contents ranging from 3 % to 32 %. Before starting the experiments, soil is nearly saturated to attain the highest possible level of volumetric water content (VWC) and then measurements are collected as the water potential first reaches to field capacity[3] and then subsequently to wilting point[4]. The changes in soil moisture level with time are shown in Fig. 3.3(a) for silt loam soil.

[3]Plant available water after the drainage of excess water.

[4]Water content level at which water is no more available to plants.

(a) (b)

Figure 3.4: The field testbed.

3.2.2 The Field Testbed

To compare with the results of indoor testbed experiments and conduct underground-to-aboveground experiments, a testbed of dipole antennas has been prepared in an outdoor field with silty clay loam soil (Fig. 3.4(a)). Dipole antennas are buried in soil at a burial depth of 20 cm with distances from the first antenna as 50 cm-12 m. A pole with adjustable height is used to conduct underground-to-aboveground (UG2AG) experiments with radii of 2 m, 4 m, 5.5 m and 7 m[5] with receiver angles of 0°, 30°, 45°, 60°, 90°. The field testbed is shown in Fig. 3.4.

[5]The maximum distance of 7 m is due to the limitations of the antenna cable length for VNA.

Table 3.2: Underground Channel Measurement Parameters

Parameter	Value
Start Frequency	10 MHz
Stop Frequency	4 GHz
Number of Frequency Points	401
Transmit Power	5 dBm
Vector Network Analyzer	Agilent FieldFox

(a) (b) (c) (d) (e)

Figure 3.5: Field testbed development in the silty loam soil: (a) testbed layout, (b) antenna placement, (c) outlook after antenna installation, (d) antenna cables out of soil at different depths, (e) USRPs and datalogger for soil moisture measurements.

3.2.3 UG Software-Defined Radio (SDR) Testbed

A testbed to conduct UG software-defined radio experiments has been developed in South Central Agricultural Laboratory (SCAL) of University of Nebraska-Lincoln at Clay Center.

The field testbed consists of four sets of buried dipole antennas in silt loam soil. Over-the-air resonant frequency of these dipole antennas is 433 MHz. Each set contains four antennas buried at 50 cm, 2 m, and 4 m distance from the first antenna, respectively. The antenna burial depths are 10 cm, 20 cm, 30 cm, and 40 cm. Testbed development steps are shown in Figs. 3.5, where the testbed layout is shown in Fig. 3.5(a). Antenna placement, and outlook after antenna installation is shown in Fig. 3.5(b)-3.5(c). In Fig. 3.5(d), antenna cables out of soil at different depths are shown. An experiment with USRPs, and datalogger for soil moisture measurements is shown in Fig. 3.5(e)

3.2.4 Soil Moisture Logging

Variations in soil moisture affects the underground communications, therefore it is important to monitor and log the soil moisture with each experiment to accurately characterize channel behavior. In these measurements, Watermark sensors are used to log the soil moisture with time. It is also fast, efficient method with less chances of error. These can overcome the disadvantages of oven drying method of soil water

content determination in which soil has to be removed from the testbed. It has been observed in [164] that presence of a metallic object in the close vicinity of the buried antenna interferes with communication. To avoid any interference, soil moisture sensor are installed at the edges of the testbed.

3.3 Measurement Techniques and Experiments Description

Measurement methods are presented in Section 3.3.1, and measurement campaign is described in Section 3.3.2.

3.3.1 Measurement Methods

Measurements are taken using Keysight Technologies N9923A FieldFox Vector Network Analyzer (VNA). Measurements layout is shown in Fig. 3.3(b). Three types of measurements are conducted in the indoor testbed:

3.3.1.1 Path Loss Measurements

VNA takes the transmission S_{21} measurements for an UG transmitter and receiver (T-R) pair by transmitting a known signal and then loss is measured at the receiver by comparing the received signal with the incident signal. Path loss is the ratio (expressed in decibel (dB)) of the transmitted power P_t to the power received P_r at the receiver. Path loss is determined as follows:

$$PL = P_t - P_r = 10.\log 10(P_t/P_r) \tag{3.3}$$

where PL is the system path loss and includes the effects of transmitting and receiving antenna gains G_t and G_r, respectively. Path loss measurements for the UG channel are taken from 10 MHz to 4 GHz frequency range in 401 discrete frequency point at

different depths and distances. Impact of soil type, soil moisture, distance, and depth on the attenuation of UG channel is analyzed through these measurements.

3.3.1.2 Return Loss Measurements

The return loss of the antenna (in dB) is defined as:

$$RL_{dB} = 20\log_{10}\left|\frac{Z_a - Z_0}{Z_a + Z_0}\right|, \tag{3.4}$$

where Z_a is the antenna impedance and Z_0 is the characteristics impedance of the transmission line.

The reflection coefficient Γ are obtained from the return loss by using the: $|\Gamma| = 10^{\frac{RL}{20}}$. Reflection coefficient are transformed to impedance by using: $Z_a = Z_0\frac{1+\Gamma}{1-\Gamma}$. Standing wave ratio (SWR) is expressed as: $SWR = \frac{1+|\Gamma|}{1-|\Gamma|}$

The resonant frequency f_r is defined as the operation center frequency where the input impedance of the antenna is the pure resistance. At the resonant frequency f_r:

$$Z_a|_{f=f_r} = Z_r = R_a. \tag{3.5}$$

It is the frequency where return loss is maximum such that:

$$f_r = \max(RL_{dB}). \tag{3.6}$$

Return loss measurements are taken to analyze the impacts of soil moisture, soil type, and burial depth on the resonant frequency of the UG antenna.

3.3.1.3 Power Delay Profile (PDP) Measurements

To better investigate the multipath characteristics of the wireless underground channel, we conducted channel sounding experiments. VNA produces sinusoidal waveforms from low to high frequency. Impulse response is measured in one frequency at a time in the frequency domain instead of the time domain. VNA is used to characterize the underground channel with higher accuracy by transmitting a series of sine-waves at the UG transmitter and the receiving signal is measured at the UG transmitter. VNA produces the frequency domain equivalent of the UG channel impulse response in a frequency at one time. Since the measurements are taken in discrete steps, by using the low intermediate frequency bandwidth, very low noise floor of $-100\,\mathrm{dBm}$, and high dynamic range is achieved. A convolution becomes a product operation in the frequency-domain and channel transfer function is obtained as:

$$H = R/T \tag{3.7}$$

where H is the channel transfer function, and R and T received and transmitted signals, respectively. When the channel transfer function, H, is measured, it is converted to time domain to obtain impulse response $h(t)$. Impulse response of the channel is obtained by the inverse Fourier transform (IFFT) of the frequency response data.

3.3.2 Measurement Campaign

Details of these three measurements in each of the soil is explained in the following sections.

3.3.2.1 Sandy Soil Experiments

In sandy soil, all three sets of measurements are conducted at 10 cm, 20 cm, 30 cm and 40 cm depths for transmitter-receiver distance of 50 cm, 1 m in soil moisture range of 0 CB to 255 CB in the indoor testbed.

3.3.2.2 Silty Clay Experiments

In silty clay soil, all three sets of measurements are conducted at 20 cm,depths for transmitter-receiver distance of 50 cm-12 m in two soil wetness conditions of 0 CB and 255 CB in the field testbed.

3.3.2.3 Silt Loam Experiments

In silt loam soil, all three sets of measurements are conducted at 10 cm, 20 cm, 30 cm and 40 cm depths for transmitter-receiver distance of 50 cm, 1 m in soil moisture range of 0 CB to 50 CB in the indoor testbed.

3.3.2.4 Underground-to-aboveground (UG2AG) Channel Experiments

Underground-to-aboveground (UG2AG) channel experiments are conducted in the field testbed in silty clay loam soil. This type of channel is used to transfer monitoring data from underground nodes to above ground nodes for subsequent relays and delivery to sink. The underground transmitter is buried at a depth of 20 cm and the aboveground receiver position is varied at the soil surface at distances of 2 m, 4 m, 5.5 m, and 7 m. Measurements are taken at angles of 0°, 30°, 45°, 60°, and 90° from the transmitter.

3.3.2.5 UG SDR Experiments

Both path loss and return loss experiments are conducted in SCAL testbed. For SDR path loss measurements, a wideband Gaussian signal (2 MHz) RF waveform is transmitted from underground dipole antenna buried at 40 cm depth by using one Universal Software Radio Peripheral (USRP) in the frequency range of 50 MHz-800 MHz. First, signal is received by using USRPs connected to antennas buried at four different depths (10 cm, 20 cm, 30 cm, and 40 cm) with a fixed transmitter receiver distance of 50 cm. then, experiments are repeated for all four depths by varying the distance to 2m and 4m. For each frequency, transmission is done for 3 seconds. Receivers collects IQ data, store it for off-line processing, and acknowledge to the transmitter after finishing. After receiving the acknowledgment, transmitter moves to the next frequency. For each depth and distance three measurements are taken. GNU Radio [89] and USRPs [80] are used to conduct experiments. Post-processing is done in Matlab [137]. For spectral estimation and path loss analysis Welch's method [206] is used. This method is enhanced form of periodogram analysis. By using the computationally efficient Discrete Fourier Transforms, data is divided into fixed blocks to calculate periodograms and modified periodograms. These modified periodogram are averaged to calculate the power spectrum. Our analysis follows details from [206].

3.3.2.6 Planar Antenna Experiments

Planar antenna experiments are conducted in the sandy and silty clay loam soils in the indoor testbed. In sandy soil testbed, two planar antennas are buried at 20 cm depth at a distance of 1 meter and return loss and path loss measurements are taken. To analyze the effects of a planner in the middle of two planners, obstructing the communications, another planner antenna is then buried in the middle at 50cm

distance and same depth (20cm) and path loss and return loss measurements are taken again for 1m distance and 50cm distance.

The planar antennas experiments are also conducted in the silty clay loam soil. To compare the results of this experiment with sandy soil testbed, the same empirical parameters are used. First path loss and return loss measurements are taken for planners buried at 1m distance at 20 cm depth and the another planar is inserted at 50 cm distance and 20 cm depth, then return loss and path loss measurements are taken, again, first for 1 m distance and then 50 cm distance.

3.4 Experimental Results

Three classes of measurement are carried out and detailed of these measurement are explained in next three sections. Antenna measurements are presented in Section 3.4.1. Path loss measurements are reported in Section 3.4.2, and power delay profile measurements are described in Section 3.4.3.

3.4.1 Return Loss Measurements

Burial Depth Effects: Return loss for sandy soil and siltloam at 10 cm, 20 cm, 30 cm depth and 40 cm depth is shown in Fig. 3.6. Effect of burial depth on the return loss of the underground antenna in the siltloam is shown in Fig. 3.6(b). Resonant frequencies are 215 MHz at 10 cm with reflection coefficient of -19.92 dB, 227 MHz at 20 cm depth with reflection coefficient of -15.76 dB, 220 MHz at 30 cm depth with reflection coefficient of -16.04 dB, and 208 MHz at 40 cm depth with reflection coefficient of -19.57 dB, respectively. It can be observed that resonant frequency first increases from 215 MHz to 227 MHz at 20 cm depth and then decreases to 220 MHz at 30 cm and 208 MHz at 40 cm. Antenna bandwidth, with threshold value of -10 dB

at 10 cm depth is 40 MHz. For all our antenna bandwidth analysis, we use - 10 dB. Bandwidth is 32 MHZ at 20 cm depth, 37 MHz at 30 cm depth, and 42 MHz at 40 cm depth.

Antenna return loss measurements in sandy soil at all depths are shown in Fig. 3.6(c). Resonant frequency at 10 cm depth is 278 MHz, with bandwidth of 22 MHz and reflection coefficient of -20.66 dB. At 20 cm depth, resonant frequency is 286 MHz, with antenna bandwidth of 21 MHz, and -14.57 db reflection coefficient. At 30 cm depth, resonant frequency is 275 MHz, bandwidth is 26 MHz with reflection coefficient of -32 db at resonant frequency. Resonant frequency at 40 cm depth is 251 MHz, with reflection coefficient of -16.07 dB and bandwidth of 17 MHz. It can be observed that in sandy soil, similar to return loss of siltloam soil,resonant frequency first increases from 278 MHz to 286 MHz at 20 cm depth and then decreases to 275 MHz at 30 cm and 251 MHz at 40 cm.

Soil Composition Effects: From Fig. 3.6, difference in texture of soil on antenna return loss can also be observed. At 10 cm depth, 63 MHz increase in resonant capacity can be observed in sandy soil as compared to siltloam. Similarly, this difference is 59 MHz at 20 cm depth, 55 MHz at 30 cm depth, 43 MHz at 40 cm depth.

Soil Moisture Effects: In Figs. 3.7, different factors affecting the return loss

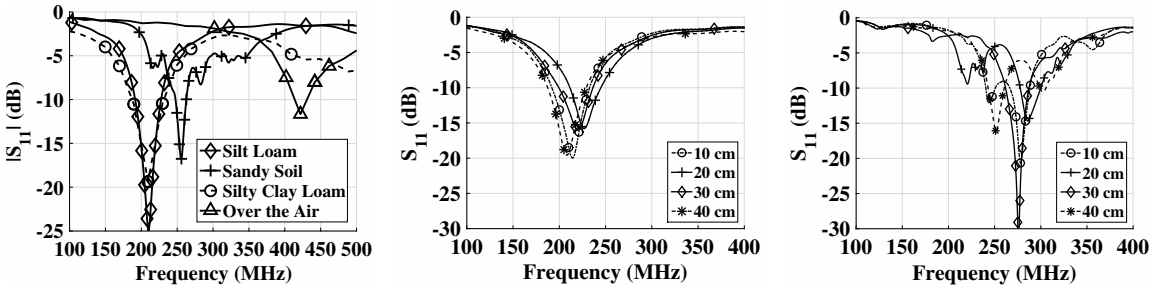

(a) (b) (c)

Figure 3.6: (a) Change in return loss in different soil. Return loss at all four depths in sandy and siltloam soil: (b) Silt loam, (c) Sandy Soil.

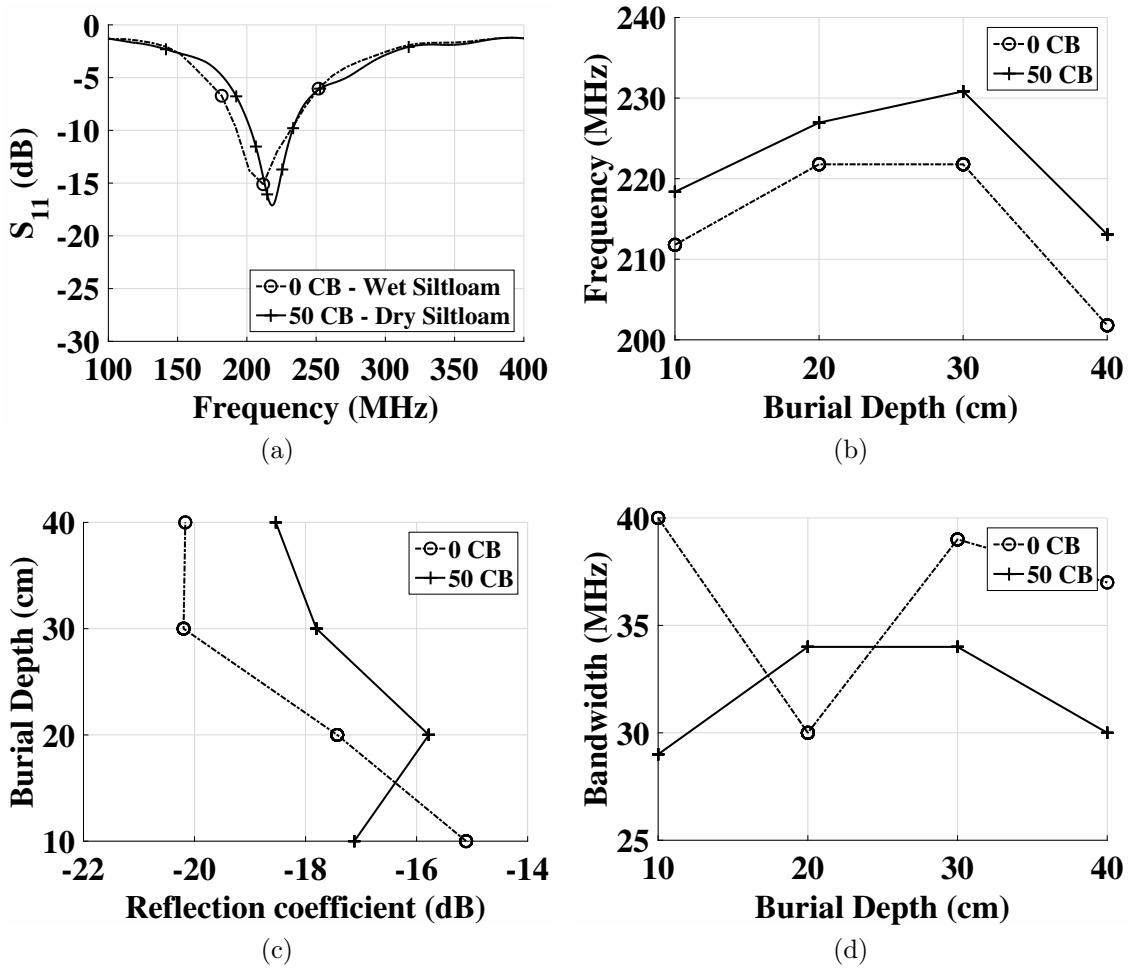

Figure 3.7: Return loss in siltloam soil, : (a) S_{11} at different frequencies, (b) Change in resonant frequency with burial depth, (c) Reflection Coefficient (dB) at different burial depths, (d) Antenna bandwidth at different burial depths.

of antenna in the siltloam soil are shown. In Fig. 3.7(a), return loss in silt loam at 10 cm depth is shown for soil matric potential values of 0 and 50 CB.

It can be observed from Fig. 3.7(b) that when soil moisture decreases (matric potential changes from 0 to 50 CB, resonant frequency has increased from 211 MHz to 219 MHz at 10 cm depth, from 221 MHz to 227 MHz at 20 cm depth, from 221 MHz to 231 MHz at 30 cm depth, and from 201 MHz to 213 MHz at 40 cm depth.

From Fig. 3.7(c), it can be observed that at 10 cm, reflection coefficient has

changed from -15 dB to -17 dB at the shifted frequency. Similarly this change is from -18 dB to -15 dB at 20 cm, -20 dB to -17 dB at 30 cm and -20 dB to -18 dB.

Change in antenna bandwidth with change in soil moisture at different burial depths is shown in Fig. 3.7(d). It can be observed that with decrease in soil moisture bandwidth has decreased from 40 MHz to 29 MHz at 10 cm depth, and increased from 30 MHz to 34 MHz at 20 cm depth. Similarity with decrease in soil moisture at 30 cm depth, bandwidth has decreased from 39 MHz to 34 MHz. At 40 cm , bandwidth decreases from 37 MHz to 30 MHz.

In Fig. 3.8, return loss of antenna with change in soil moisture at different depths in sandy soil is shown. In Fig. 3.8(a), return loss in silt loam at 10 cm depth is shown for soil matric potential values of 0 and 255 CB. When soil moisture decreases (matric potential changes from 0 to 255 CB), resonant frequency has increased from 278 MHz to 305 MHz.

Effects of change in soil moisture on the resonant frequency at different depths are shown in Fig. 3.8(b). At 20 cm, with change in soil moisture from 0 to 255 CB, resonant frequency has increased from 276 MHz to 301 MHz. With the similar change at 30 cm depth, resonant frequency changes from 276 MHz to 301 MHz and at 40 cm depth, it changes 251 MHz to 279 MHz.

In Fig. 3.8(c), change in reflection coefficient is shown with burial depth at 0 CB and 255 CB soil moisture levels. Reflection coefficient changes from -20 dB to -16 dB at 305 MHz at 10 cm depth. Reflection coefficient has decreased from -14 dB to -12 dB at 300 MHz at 20 cm depth. Change in reflection coefficient at 30 cm depth is from -31 dB to -15 dB at 231 MHz. Reflection coefficient has decreased from -16 dB to -15 dB at 40 cm.

From Fig. 3.8(d), change in antenna bandwidth at different burial depths with change in soil moisture can be observed. With decrease in soil moisture bandwidth

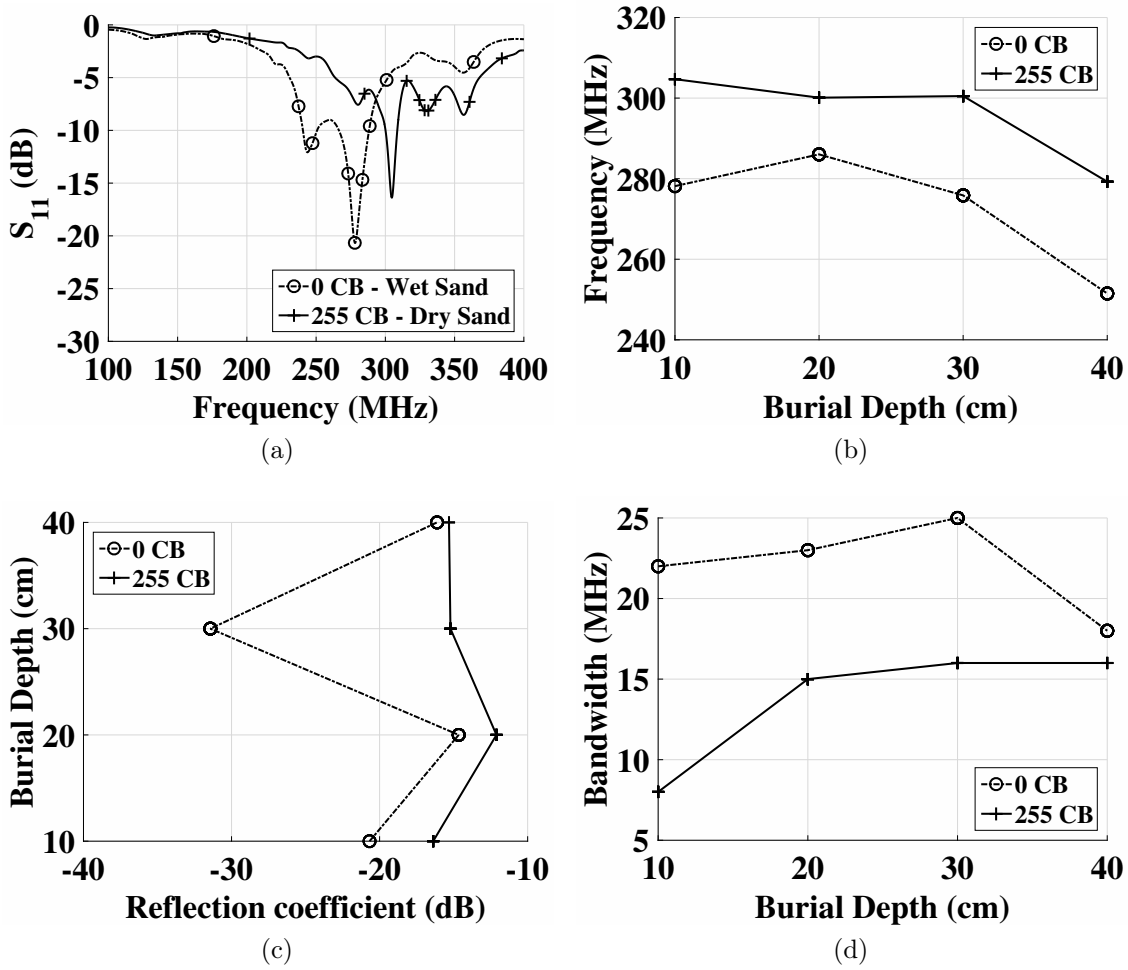

Figure 3.8: Return loss in sandy soil, : (a) S_{11} at different frequencies, (b) Change in resoenet frequency with burial depth, (c) Reflection Cofficient (dB) at different burial depths, (d) Antenna bandwidth at different burial depths.

has decreased from 22 MHz to 8 MHz at 10 cm depth. At 20 cm depth, bandwidth has increased from 23 MHz to 15 MHz at 20 cm with decrease in soil moisture. Similarity, at 30 cm depth, with decrease in soil moisture from 0 CB to 255 CB antenna bandwidth has decreased from 25 MHz to 16 MHz. At 40 cm depth, with decrease in soil moisture bandwidth has decreased from 18 MHz to 16 MHz.

Analysis of the return loss of antenna in silt loam and sandy soils at different burial depths and soil moisture levels shows that the return loss of the antenna changes with

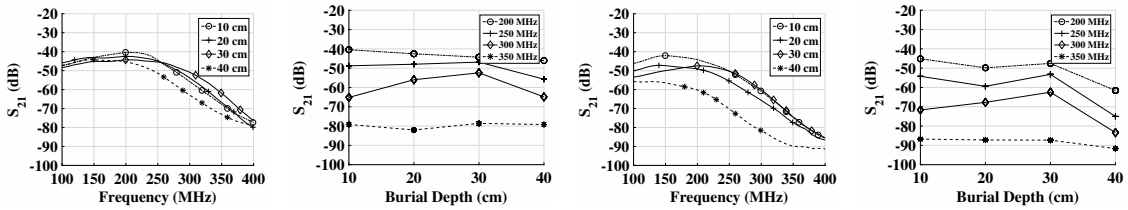

Figure 3.9: Attenuation in siltloam soil at 50 cm distance: (a) with frequency, (b) at different depths, Attenuation in siltloam soil at 1 m distance: (c) with frequency, (d) at different depths.

the soil moisture. Resonant frequency moves to lower frequency ranges when the soil moisture increases. Moreover, unlike over-the-air communications, the optimal frequency where the maximum capacity is achieved is not the same as the resonant frequency of the antenna. In underground communications, the effects of the antenna and the soil need to be considered together to find the optimal frequency.

3.4.2 Channel Transfer Function Measurements

In this section, channel transfer measurement (S_{21}) are shown for different sandy and siltloam soil at different distances, depths and soil moisture levels. Moreover, impacts of soil type, burial depth and soil moisture on channel attenuation are discussed.

Burial Depth Impact on Attenuation: In Figs. 3.9, attenuation at 10 cm, 20 cm, 30 cm, and 40 cm depth in siltloam soil for distance of 50 cm and 1 m distance are shown. In Fig. 3.9(a), attenuation at transmitter-receiver distance of 50 cm is shown. At 200 MHz, path loss is 40.37 dB at 10 cm, 42.44 dB at 20 cm, 44.30 dB at 30 cm, and 45.26 dB at 40 cm. Path loss is 5 dB higher at 40 cm compared to 10 cm depth at 200 MHz. This difference between 10 cm and 40 cm depth increases to 8 dB at 250 MHz. At 40 cm depth, when frequency increases from 200 MHz to 350 MHz, path loss is increased from 45.26 dB to 72.91 dB.

In Fig. 3.9(c), attenuation at transmitter-receiver distance of 1 m is shown. At

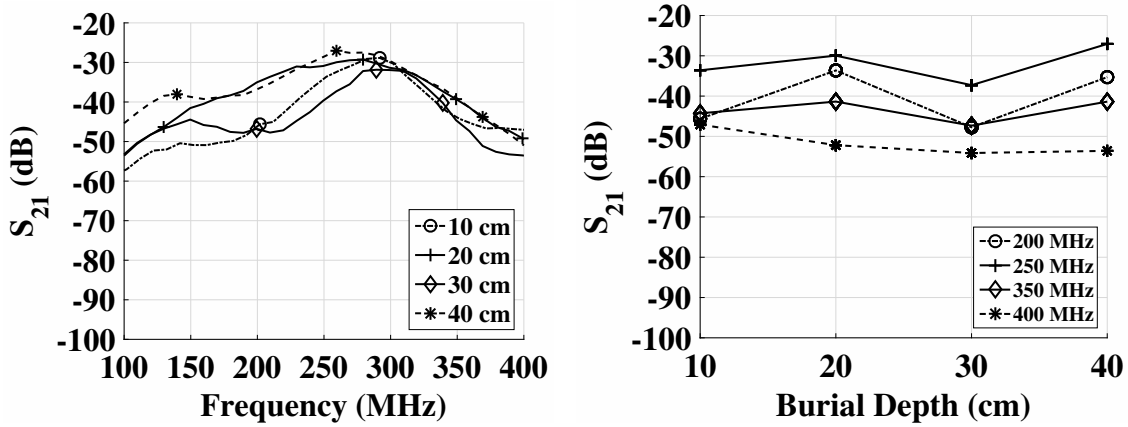

(a) (b)

Figure 3.10: Attenuation in sandy soil at 50 cm distance: (a) with frequency, (b) at different depths.

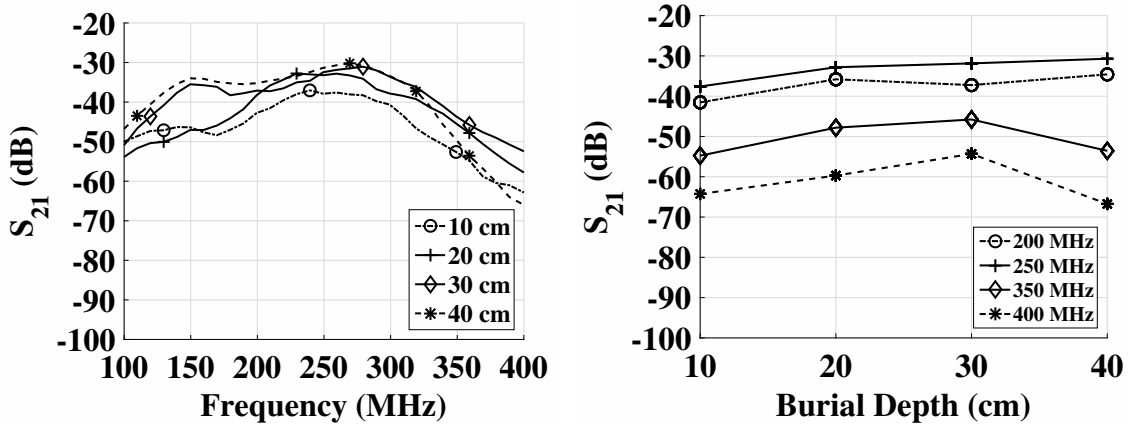

(a) (b)

Figure 3.11: Attenuation in sandy soil at 1 m distance: (a)with frequency, (b) at different depths

200 MHz, path loss is 44.37 dB at 10 cm, 49.03 dB at 20 cm, 47.46 dB at 30 cm, and 60.12 dB at 40 cm. Path loss is 16 dB higher at 40 cm compared to 10 cm depth at 200 MHz. This difference between 10 cm and 40 cm depth increases to 20 dB at 250 MHz. At 40 cm depth, when frequency increases from 200 MHz to 250 MHz, path loss is increased from 44.37 dB to 70.03 dB. The variation of path loss over frequency can be explained by the soil permittivity as it changes with frequency as shown in Fig. 3.1.

In Fig. 3.10(a), attenuation at transmitter-receiver distance of 50 cm in silt loam soil at 10 cm, 20 cm, 30 cm, and 40 cm depth is shown. At 300 MHz, path loss is 29.55 dB at 10 cm, 31.36 dB at 20 cm, 31.93 dB at 30 cm, and 29.66 dB at 40 cm. It can be observed from Fig. 3.10(b), where change in attenuation with change in depth is shown, that the attenuation is highest for 400 MHz frequency at all four depths. In Fig. 3.11(a), attenuation at transmitter-receiver distance of 1 m is shown. At 300 MHz, path loss is 40.63 dB at 10 cm, 37.83 dB at 20 cm, 33.38 dB at 30 cm, and 33.39 dB at 40 cm. It can be observed from Fig. 3.11(b), where change in attenuation with change in depth is shown at 1m T-R distance, that the attenuation is highest for 400 MHz frequency at all four depths. Path loss variations with depth are caused by the multi-path effect. In underground-to-underground communication, there are three dominant paths from the transmitter to the receiver: the direct wave, which is the line-of-sight path, the reflected wave, which is the wave reflected from the soil-air interface and the lateral wave, which is the wave propagating along the soil-air interface. When the burial depth increases, the direct path does not change. However, the reflected wave and the lateral wave change. More specifically, the path losses in the reflected wave and the lateral wave increase. Therefore, the overall path loss increases with the increase of the burial depth.

Transmitter-Receiver (T-R) Distance Effect on Attenuation: It can also be observed from Fig. 3.9(a) and Fig. 3.9(c) that when distance increases from 50 cm to 1 m at the 10 cm depth, at 200 MHz, 5 dB path loss increase can be observed. Similarity, when distance increases from 50 cm to 1 m at the 20 cm depth, at 200 MHz, 7 dB path loss increase can be observed. At 30 cm and 200 MHz, when distance increases from 50 cm to 1 m, path loss increases by 3 dB and at 40 cm and 200 MHz, when distance increases from 50 cm to 1 m, path loss increases by 15 dB.

Effects of increase of transmitter-receiver distance can be observed from Fig. 3.10

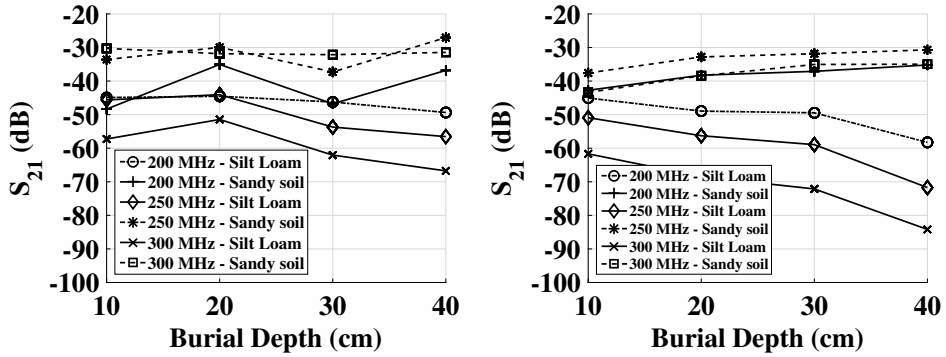

Figure 3.12: (a) Comparison of attenuation in siltloam and sandy soils at 50 cm distance at different frequencies, (b) comparison of attenuation in siltloam and sandy soils at 1 m distance at different frequencies.

and Fig. 3.11. Although the difference due to path loss is not as large as in siltloam because of lower attenuation in sandy soil. When distance increases from 50 cm to 1 m at the 10 cm depth, at 300 MHz, 10 dB path loss increase can be observed. Similarity, when distance increases from 50 cm to 1 m at the 20 cm depth, at 300 MHz, 7 dB path loss increase is observed. At 30 cm and 300 MHz, when distance increases from 50 cm to 1 m, path loss increases by 3 dB and at 40 cm and 300 MHz, when distance increases from 50 cm to 1 m, path loss increases by 4 dB.

(a) Impact of Soil Type on Attenuation: To assess the effect of soil type on the path loss, a comparison of path loss in siltloam and sandy soil is give at 50 cm and 1 m distance at all depths in Figs. 3.12(a) and Figs. 3.12(b).

For transmitter-receiver difference of 50 cm, at 10 cm depth, it can be observed that path loss in sandy soil is 10 dB lower at 250 MHz as compared to siltloam and this difference increases to 30 dB at 450 MHz. At 20 cm depth, at 250 MHz silt loam has 13 dB higher path loss and at 400 MHz path loss has increased to 29 dB. At 30 cm depth, it can be observed that path loss in sandy soil is 18 dB lower at 250 MHz as compared to siltloam and this difference increases to 32 dB at 450 MHz. Similarly,

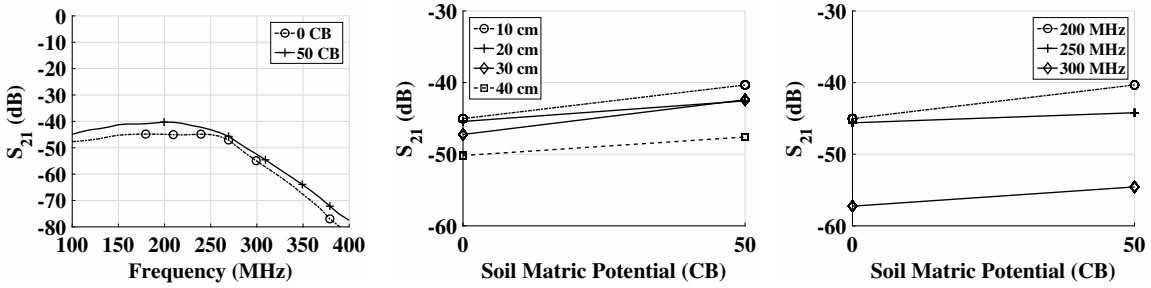

(a) (b) (c)

Figure 3.13: Attenuation with soil moisture in siltloam soil at 50 cm distance, : (a) S_{21}, (b) Effect of change in soil msoiture at different depths at 200 MHz frequency, (c) Effect of change in soil msoiture at different frequencies at 10 cm depth.

At 40 cm depth, at 250 MHz silt loam has 20 dB higher path loss and at 400 MHz path loss has increased to 32 dB.

For transmitter-receiver difference of 100 cm, at 10 cm depth, it can be observed that path loss in sandy soil is 12 dB lower at 250 MHz as compared to siltloam and this difference increases to 24 dB at 450 MHz. At 20 cm depth, at 250 MHz silt loam has 20 dB higher path loss and at 400 MHz path loss has increased to dB. At 30 cm depth, it can be observed that path loss in sandy soil is 18 dB lower at 250 MHz as compared to siltloam and this difference increases to 32 dB at 450 MHz. Similarly, at 40 cm depth, at 250 MHz silt loam has 38 dB higher path loss and at 400 MHz path loss has decreased to 24 dB.

It can be observed that in all depths, path loss in lower in sandy soil than in silt loam. This is because the sandy soil holds less bound water, which is the major component in soil that absorbs electromagnetic waves. Water holding capacity of medium textured soils (silt loam, fine sandy loam, and silty clay loam) is much higher, because of the small pore size, as compared to coarse soils (sand, sandy loam loamy sand) because these soils have lower pore size hence no aggregation and little resistance against gravity [85].

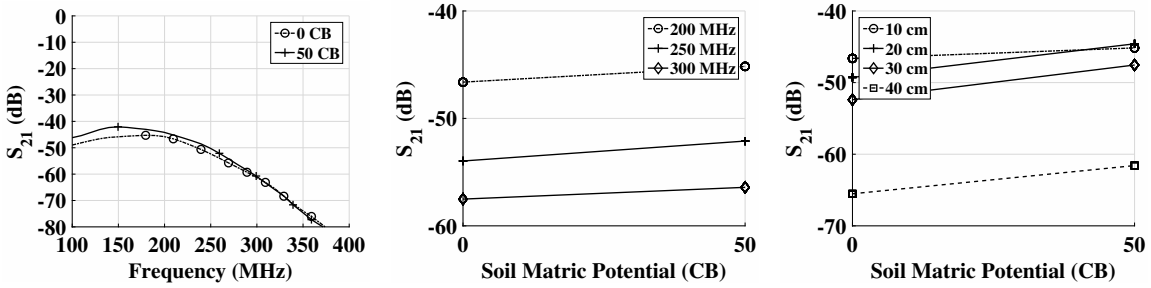

(a) (b) (c)

Figure 3.14: Attenuation with soil moisture in siltloam soil at 1 m distance, : (a) S_{21}, (b) Effect of change in soil msoiture at different frequencies at 10 cm depth, (c) Effect of change in soil msoiture at different depths at 200 MHz frequency.

Impact of Soil Moisture on Attenuation: To assess the effects of soil moisture on path path loss we have conducted experiments in different soils under different soil moisture levels.

Change in path loss due to soil moisture variations in slit loam are shown in Figs. 3.13 and Figs. 3.14 for soil moisture values of 0 and 50 CB. Path loss variations at transmitter-receiver distance of 50 cm are shown in Figs. 3.13. In Fig. 3.13(a), an decrease of 5 dB in path loss, from 100 MHz to 250 MHz, can be observed when soil moisture changes from 0 to 50 CB.

Effect of change in soil moisture at four different depths at 200 MHz frequency is shown in Fig. 3.13(b). At 10 cm depth, path loss is decreased from -45 dB to 40 dB when soil moisture decreases from 0 CB to 50 CB. At 20 cm, a 3 dB decrease is observed when path loss changes from -45 dB to 42 dB. At 30 cm and 40 cm this decrease is 5 db and 3 dB respectively. In Fig. 3.13(c), path loss is shown for 200 MHz, 250 MHz and 300 MHz at 10 cm depth. Path loss decreases by 2 dB and three dB at 250 MHz and 300 MHz, respectively.

Similarly, at 20 cm, an decrease of 2 dB in path loss, from 200 MHz to 250 MHz, is observed. At 250 MHz, there is difference of 4 dB in path loss at two soil moisture

levels at 30 cm depth. At 40 cm depth, path loss is decreased by 4 dB when soil moisture decreases from 0 to 50 CB at 250 MHz.

Path loss variations, in silt loam, at transmitter-receiver distance of 1 m are shown in Figs. 3.14. In Fig. 3.14(a), an decrease of 3 dB in path loss, at 250 MHz, can be observed when soil moisture changes from 0 to 50 CB.

Path loss at different frequencies at 10 cm depth at 1 cm distance in silt loam soil is shown in Fig. 3.13(c). With change in soil moisture, path loss decrease by 2-3 dB in these frequencies. This difference becomes higher with higher frequencies.

In Fig. 3.14(b), path loss versus soil moisture is shown for 200 MHz at four depths. At 10 cm depth, with decrease in soil moisture from 0 to 50 CB, path loss has decreased by 1 dB. At 20cm, change in path loss is 5 dB as it decreases from -49 dB to 44 dB. Similarly, path loss decreases from -52 dB to -47 dB at 30 cm depth (5 dB change). Change in path loss with change in soil moisture at 40 cm depth is 4 dB.

Similarly, at 20 cm, an decrease of 5 dB in path loss, from 200 MHz to 250 MHz, is shown. At 250 MHz, there is difference of 6 dB in path loss at two soil moisture levels at 30 cm depth. At 40 cm depth, path loss is decreased by 2 dB when soil moisture decreases from 0 to 50 CB.

In sandy soil, change in path loss due to soil moisture variations are shown in Figs. 3.15 and Figs. 3.16 for soil moisture values of 0 and 255 CB. Path loss variations at transmitter-receiver distance of 50 cm are shown in Figs. 3.15. In Fig. 3.15(a), an decrease of 10 dB in path loss, at 300 MHz, can be observed when soil moisture changes from 0 to 255 CB. In Fig. 3.15(b), path loss versus soil moisture at 200 MHz, 250 MHz and 300 MHz frequencies at 10 cm depth is shown. It can be observed that path loss has increased by 1 dB at 200 MHz and 250 MHz with change in soil moisture. At 300, when soil moisture changes from 0 to 50 CB, MHz path loss has decreased by 4 dB.

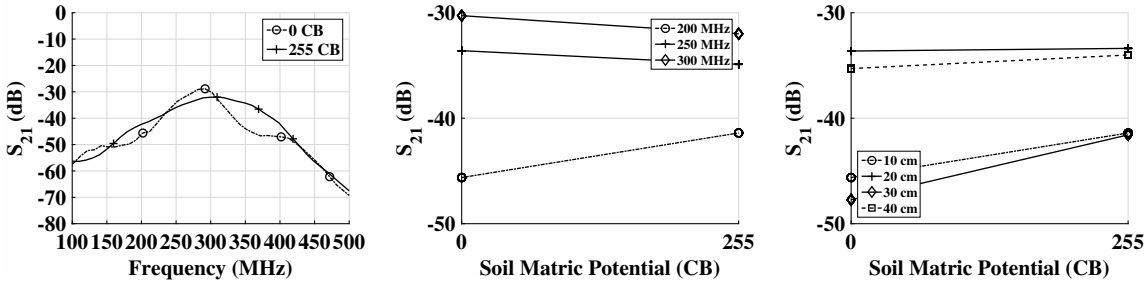

(a) (b) (c)

Figure 3.15: Attenuation with soil moisture in sandy soil at 50 cm distance: (a) S_{21}, (b) Effect of change in soil msoiture at different frequencies at 10 cm depth, (c) Effect of change in soil msoiture at different depths at 200 MHz frequency.

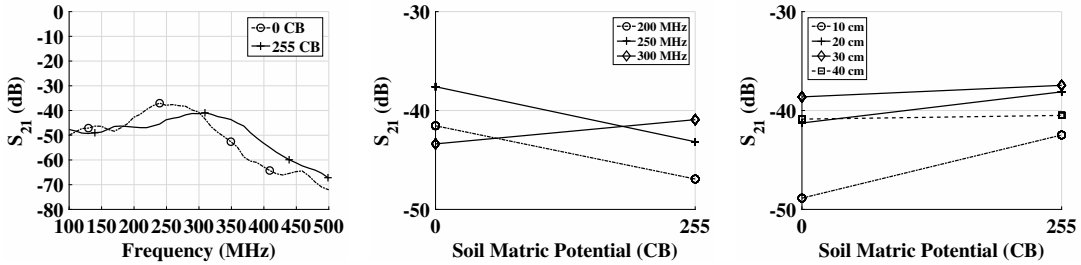

(a) (b) (c)

Figure 3.16: Attenuation with soil moisture in sandy soil at 1 m distance, : (a) S_{21}, (b) Effect of change in soil moisture at different frequencies at 10 cm depth (c) Effect of change in soil moisture at different depths at 330 MHz frequency .

In Fig. 3.15(c), path loss with change in soil moisture at four depths at 200 MHz is shown. At all four depths, path loss has increased slightly with decrease in soil moisture. This can be explained by change in resonant frequency in sandy soil to higher spectrum due to decrease in soil moisture.

Similarly, at 20 cm, an decrease of 9 dB in path loss, at 300 MHz, is shown. At 250 MHz, there is difference of 5 dB in path loss at two soil moisture levels at 30 cm depth. At 40 cm depth, path loss is decreased by 4 dB when soil moisture decreases from 0 to 255 CB at 200 MHz.

Path loss variations at transmitter-receiver distance of 100 cm, in sandy soil, are shown in Figs. 3.16. In Fig. 3.16(a), an decrease of 9 dB in path loss, at 300 MHz,

can be observed when soil moisture changes from 0 to 255 CB.

With decrease in soil moisture path loss has increased at 200 MHz, and 250 MHz, however at 300 MHz it decreases as 300 MHz falls in the antenna bandwidth range.In Fig. 3.16(b), effect of change in soil moisture at different frequencies at 10 cm depth are shown. Path loss with change in soil moisture at four depths at 200 MHz is shown in Fig. 3.16(c). Path loss decrease in all frequencies is observed across all depth.

Similarly, at 20 cm, an decrease of 6 dB in path loss, at 300 MHz, is shown. At 400 MHz, there is difference of 8 dB in path loss at two soil moisture levels at 30 cm depth. At 40 cm depth, path loss is decreased by 6 dB when soil moisture decreases from 0 to 255 CB at 200 MHz.

Our analysis shows that higher soil moisture affects the path loss of underground channel. This is caused by higher permittivity of the soil at higher soil moisture, higher attenuation of waves causes higher path loss. Similarly, we can see that path loss is increased with decrease in soil moisture for both soils. Moreover changes in soil moisture affects the path loss, return loss and bandwidth of antenna therefore capacity achieving frequency spectrum changes as well. Therefore, for design of an underground communication system all these factors should be considered together.

3.4.3 Power Delay Profile Measurements

The resulting power delay profiles are shown in Fig. 3.17. Speed of the wave in soil is given as: $S = c/n$, where n is refractive index and c is speed of light 3x10^8 m/s. Since the permittivity of soil is a complex number, the refractive index of soil is calculated as:

$$n = \sqrt{\frac{\sqrt{\epsilon'^2 + \epsilon''^2} + \epsilon'}{2}}\ , \tag{3.8}$$

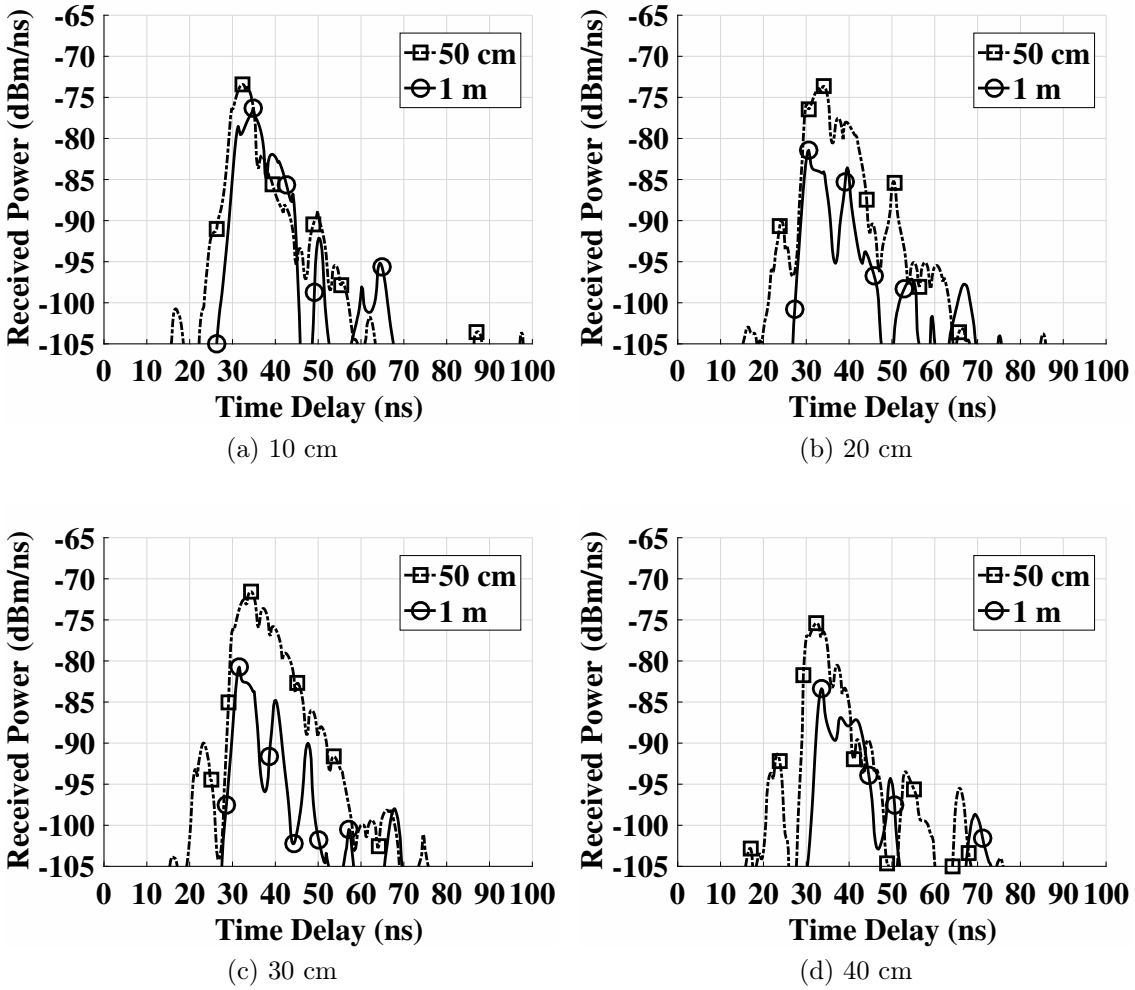

(a) 10 cm

(b) 20 cm

(c) 30 cm

(d) 40 cm

Figure 3.17: Power Delay Profiles (PDP) measured at 50 cm and 1 m distance, at different depths in silt loam soil at near-saturation: (a) 10 Cm, (b) 20 Cm, (c) 30 Cm, (d) 40 Cm.

where ϵ' and ϵ'' are the real and imaginary parts of the relative permittivity of the soil.

We have calculated the speed of wave in silt loam soil by calculating the refractive index based on soil properties given in Table 3.2, which turns out to be 5.6x10^7 m/s and is 19% of speed of light, almost 5 times slower than the speed of light. Based on this result, we see that for 50 cm distance and all burial depths, lateral waves follows the direct wave except for the 10 cm depth where lateral wave reaches the receiver first.

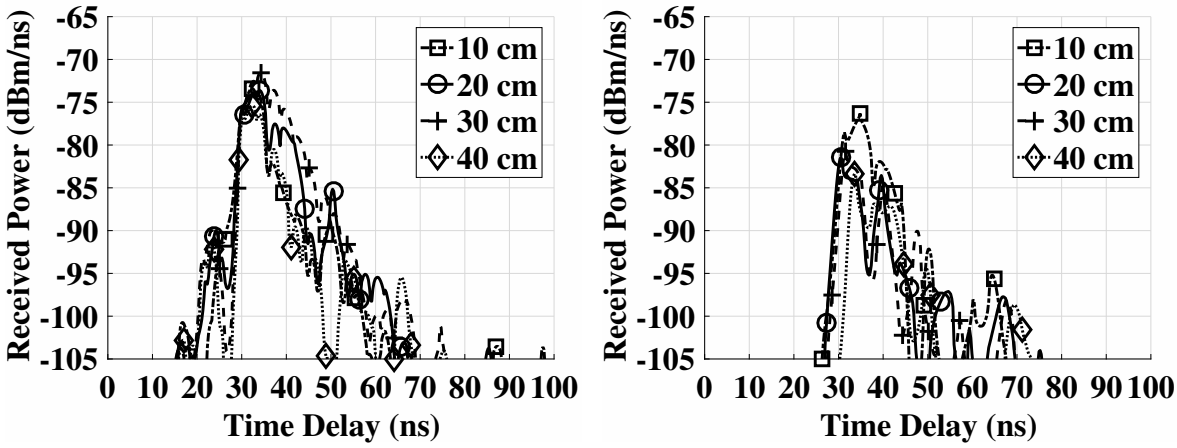

(a) 50 cm (b) 1 m

Figure 3.18: Power Delay Profile in silt loam soil at different depths at: (a) 50 cm T-R distance, (b) 1 m T-R distance.

In Fig. 3.17, PDPs of 50 cm and 1 m distances are compared for all depths. The first multipath component shown in the PDPs is the direct wave component, which is present at $18-28$ ns delay at 50 cm profile and it is not formed at 1 m profile. This is because direct wave suffers less attenuation at 50 cm and more attenuated at 1 m distance. It is observed that the lateral wave component is the strongest in all power delay profiles and is formed at $30-40$ ns delay. The delays of the lateral wave is both 50 cm and 1 m distances are similar because the wave propagates much faster in air. In general, the lateral wave component is 10 dB to 15 dB higher in power than the direct wave component.

In Fig. 3.18, PDPs of the communication channels at four depths are compared. In Fig. 3.18(a), the distance between the transmitter and the receiver is 50 cm, while in Fig. 3.18(b) the distance is 1 m. As shown in figures, at the same distance, with the increase of the depth, the received power of lateral wave decreases. This is more significant in the 1 m case, where the peak power of the lateral wave in the 10 cm depth is -75 dB while it is -83 dB when the depth increases to 40 cm. Also shown in Fig. 3.18(b), with the increase of the depth, the component also delay increases.

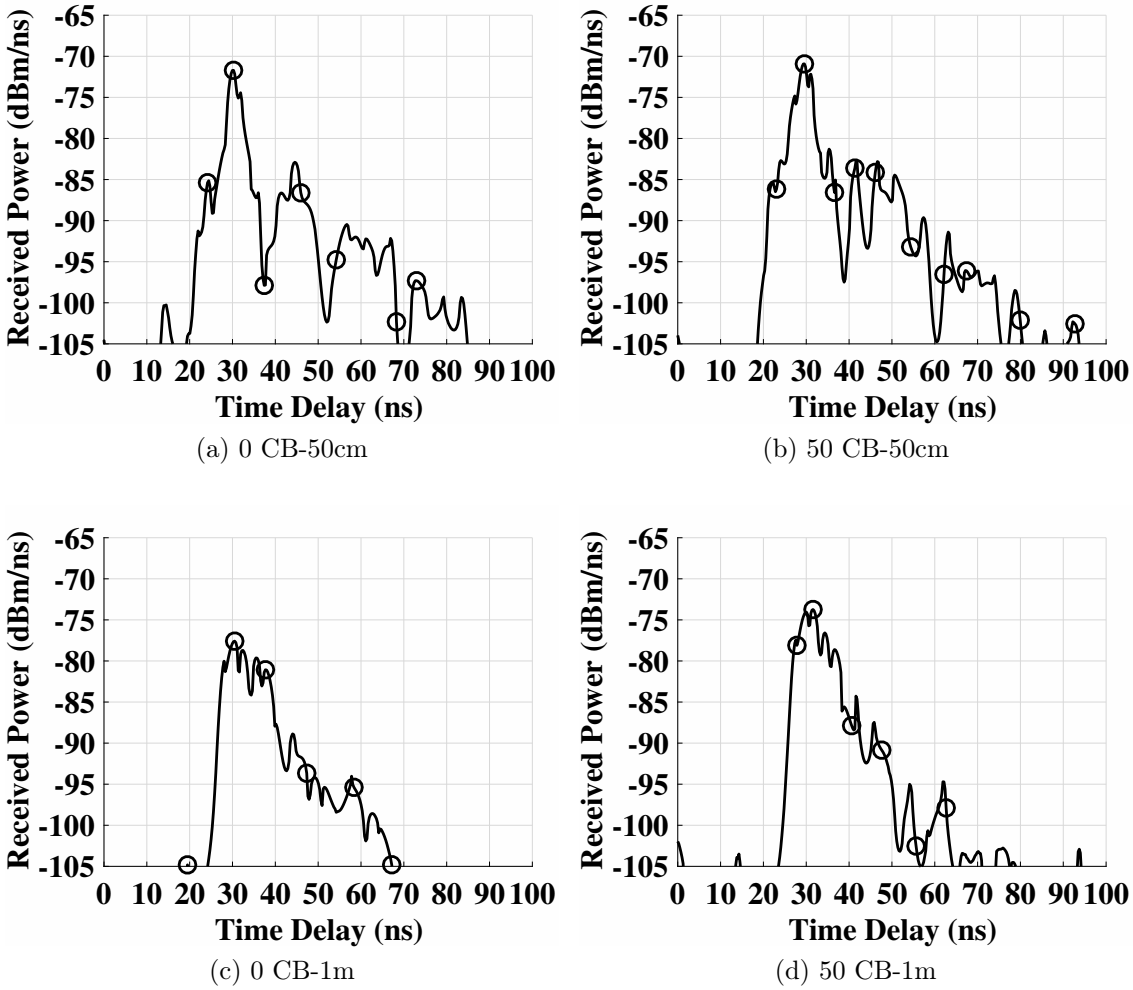

(a) 0 CB-50cm (b) 50 CB-50cm

(c) 0 CB-1m (d) 50 CB-1m

Figure 3.19: Power Delay Profiles (PDP) measured at 50 cm and 1 m distance, at 20 cm depths for different soil moisture levels: (a) 0 CB-50cm, (b) 50 CB-50cm, (c) 0 CB-1m, (d) 50 CB-1m.

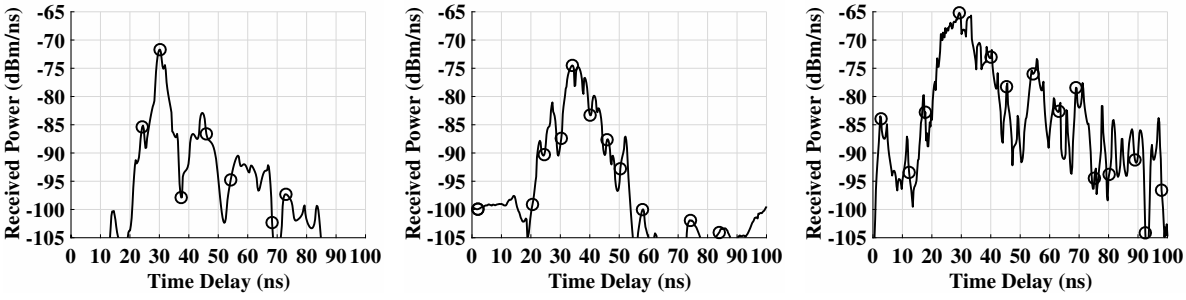

(a) Silt Loam (b) Silty Clay Loam (c) Sandy Soil

Figure 3.20: Power Delay Profiles (PDP) measured in different soils: (a) Silt Loam, (b) Silty Clay Loam, (c) Sandy Soil.

At 10 cm depth, the lateral wave arrives at 29 ns while at 40 cm it arrives at 32 ns. Distance related delay of $10-15$ ns can be also observed in all profiles at 1 meter distance.

In Fig. 3.19, the PDP measured at 50 cm and 1 m distance, at 20 cm depths for different soil moisture levels are shown. It can be observed that at 50 cm distance, with decrease in soil moisture, the received power is increased and also the components at longer delay exhibit more strength. Similar observations are made at 1m distance. It is also important to note that direct component vanishes as distance increase, which is caused by the higher attenuation in the soil.

In Fig. 3.20, measured PDP in different soils is shown. It can be observed that due to the low water holding capacity of the sandy soil, it has higher received power across all three components as compared to the silt loam and silty clay loam soil.

3.4.4 UG2AG Channel Measurements Results

In this section, we present the Underground-to-aboveground (UG2AG) channel experiment results.

In Figs. 3.21(a)-3.21(b), results from UG2AG experiments are shown. This type of channel is used to transfer monitoring data from underground nodes to above ground nodes for subsequent relays and delivery to sink. The underground transmitter is at a depth of 20 cm and the aboveground receiver position is varied at the soil surface at distances of 2 m, 4 m, 5.5 m, and 7 m. Measurements are taken at angles of 0°, 30°, 45°, 60°, and 90° from the transmitter. It is observed that the receiver at the angles of 45°-90° exhibit the lowest attenuation, 90° being the ideal because of no refraction from soil-air interface. Moreover, attenuation does not change for wide range of frequencies and distances.

In Fig. 3.21(c), and Fig. 3.21(d), RMS delay spread, τ_{rms} and coherence bandwidth

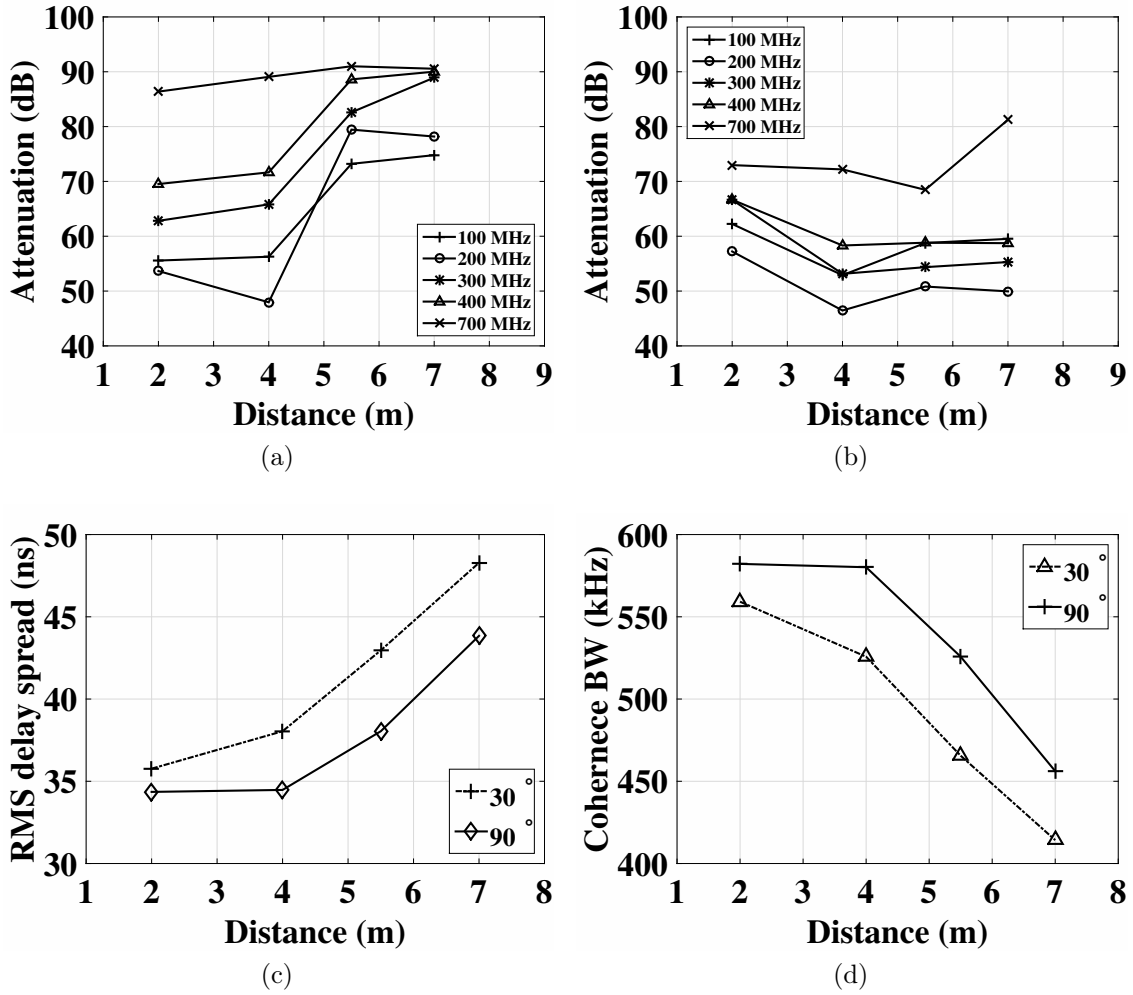

Figure 3.21: Attenuation with distance at different receiver angles (UG2AG) : (a) 0°, (b) 90°, (c) RMS delay spread with distance, (d) Coherence bandwidth with distance.

with distance at receiver angles of 30° and 90° is shown. It can be observed that at the receiver angle of 90°, RMS delay spread increases by 26% from 34 ns to 43 ns, for an in crease in T-R separation from 2 m to 7 m. Our analysis shows that by changing the receiver position from 90° to 30°, by keeping the same radius, RMS delay spread is increased by 11 %. This could be explained by refractions from the soil-air interface. Since at 90°, the wave does not go through refractions, as opposed to the refracted path, to reach the receiver at 30°. Similar to the UG2UG channel, coherence bandwidth for the UG2AG channel is found to be between 457 KHz to

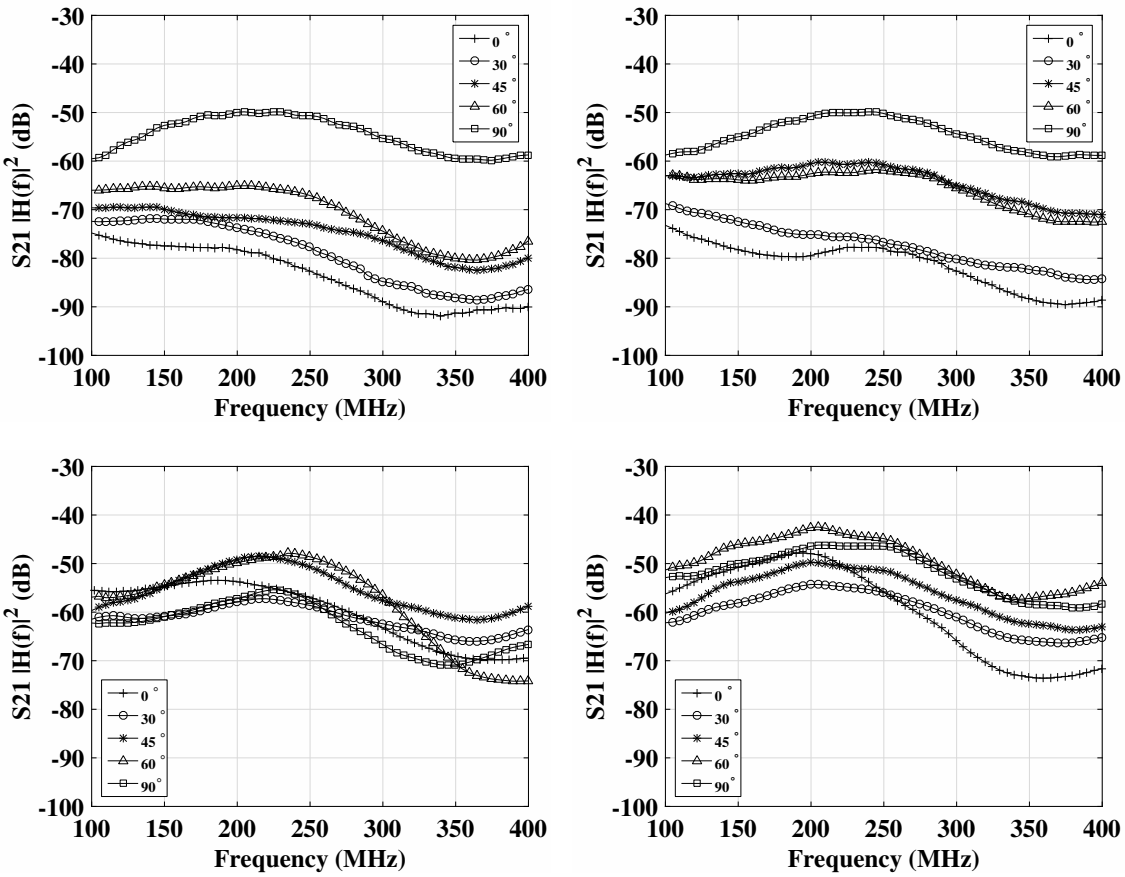

Figure 3.22: Path loss measurements in UG2AG experiments at different distances at different receiver angels: (a) 7m (b) 5m (c) 4m (d) 2m.

579 KHz at 90°, which shows that the soil path is the bottleneck.

In Figs. 3.22(a)-3.22(d), results from UG2AG experiments are shown as function of frequency for different angles at different distances. It can be observed that the receiver at the angles of 90° exhibit the lowest attenuation. Moreover, the pathloss increases with distance, and low frequencies has lower pathloss.

3.5 Conclusion

Characterization of the wireless underground channel models in wireless communications is vital for design of IOUT applications. In this chapter, a design of an indoor

testbed for underground channel modeling is presented and an extensive measurement campaign spanning over a period of a year has been carried out. Empirical results of the underground channel transfer functions and underground antenna performance are presented in silty clay loam, sandy and silt loam soils. Experimental results indicates that use of indoor testbed leads to efficient, speedy and improved characterization of underground communications in different soils. It is also shown that performance of underground channel and buried antenna affected by variations in soil moisture. Moreover, soil texture and burial depth also cause fluctuations in underground communications. These empirical measurements lead to design of next-generation IOUT communications protocols and development of new technologies to improve wireless underground communications.

Chapter 4

Impulse Response Analysis of Wireless Underground Channel

Wireless underground sensor networks (WUSNs) are becoming ubiquitous in many areas and designing robust systems requires extensive understanding of the underground (UG) channel characteristics. In this chapter, UG channel impulse response is modeled and validated via extensive experiments in indoor and field testbed settings. Three distinct types of soils are selected with sand and clay contents ranging from 13% to 86% and 3% to 32%, respectively. Impacts of changes in soil texture and soil moisture are investigated with more than 1,200 measurements in a novel UG testbed that allows flexibility in soil moisture control. Time domain characteristics of channel such as RMS delay spread, coherence bandwidth, and multipath power gain are analyzed. The analysis of the power delay profile validates the three main components of the UG channel: direct, reflected, and lateral waves. It is shown that RMS delay spread follows a log-normal distribution. The coherence bandwidth ranges between 650 kHz and $1.15MHz$ for soil paths of up to 1m and decreases to 418 kHz for distances above 10m. Soil moisture is shown to affect RMS delay spread non-linearly, which provides opportunities for soil moisture-based dynamic adaptation techniques. The model and analysis paves the way for tailored solutions for data harvesting, UG sub-carrier communication, and UG beamforming.

4.1 Motivation

Wireless underground sensor networks (WUSNs) are becoming ubiquitous in many areas including environment and infrastructure monitoring [177], [96], [186], border patrol [40], and precision agriculture [76]. Establishing robust wireless underground communication links between two underground nodes (UG2UG links) or an underground node and a node above the surface (UG2AG links) requires extensive knowledge of the underground (UG) channel characteristics.

In general, performance of a communication system is seriously degraded by multipath fading [101]. Communication in UG channel is affected by multipath fading caused by reflection of electromagnetic (EM) waves in soil and from soil-air interface. Reducing the effects of these disturbances requires characterization of the UG channel. Traditional over-the-air communication channel models cannot be readily used in WUSNs because EM waves in soil suffer higher attenuation than in air due to their incidence in lossy media which consists of soil, water and air, and leads to permittivity variations over time and space with changes in soil moisture [76]. WUSNs are generally deployed at depths which are less than 50 cm [51]. Due to proximity to the Earth surface, a part of the transmitted EM waves propagate from soil to air, then travel along the soil-air interface, and enter the soil again to reach the receiver. These EM waves (*lateral waves* [121]) are a major component of the UG channel.

The analysis of EM wave propagation in underground channel is challenging because of its computation complexity [40]. In [75] and [200], channel models based on the analysis of the EM field and Friis equations have been developed and direct, reflected, and lateral waves are shown to be major contributors of received signal strength. These models provide good approximations when coarse channel measures (e.g., path loss) are concerned but are limited due to the lack of insight into channel

statistics (e.g., delay spread, coherence bandwidth) and empirical validations.

In this chapter, we present an UG channel impulse response model corresponding analysis based on measured data collected from UG channel experiments with a 250 ps delay resolution. Statistical properties of multipath profiles measured in different soil types under different soil moisture levels are investigated. The results presented here describe: Root mean square (RMS) delay spread, distribution of RMS delay spread, mean amplitude across all profiles for a fixed T-R displacement, effects of soil moisture on peak amplitudes of power delay profiles, mean access delay, and coherence bandwidth statistics. The goal of the measurement campaign and the corresponding model is to produce a reliable channel model which can be used for different types of soils under different conditions. Thus, we have considered several possible scenarios with more than $1,200$ measurements taken over a period of 7 months.

The rest of the chapter is organized as follows: The related work is discussed in Section 4.2. Description of UG channel impulse response model is given in Section 4.3. In Section 4.4, measurement sites and procedures are described. Results and analysis of measured impulse responses are presented in Section 4.5. WUSN communication system design is discussed in Section 4.6. Chapter is concluded in Section 4.7.

4.2 Related Work

Wireless communication in WUSNs is an emerging field and few models exist to represent the underground communication. In [200], we have developed a 2-wave model but lateral wave is not considered. In [52], models have been developed but these do not consider underground communication. A model for underground communication in mines and road tunnels has been developed in [177] but it cannot be applied to WUSN due to wave propagation differences between tunnels and soil. We have

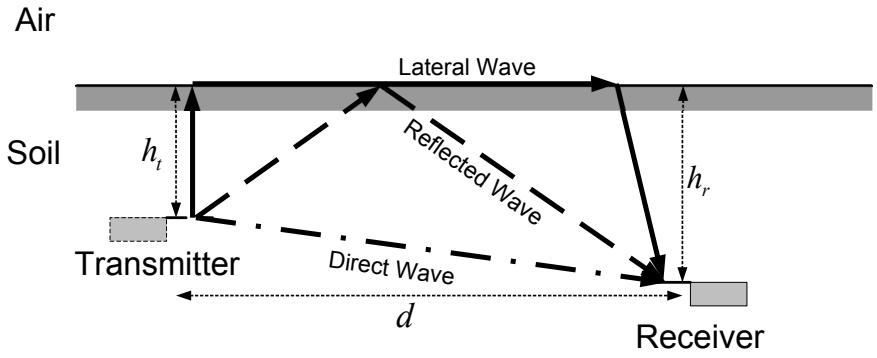

Figure 4.1: The three EM waves in an underground channel [75].

also developed a closed-form path loss model using lateral waves in [75] but channel impulse response and statistics cannot be captured through this simplified model.

Wireless underground communication shares characteristics of underwater communication [47]. However, underwater communication based on electromagnetic waves is not feasible because of high attenuation. Therefore alternative techniques including acoustic [47] are used in underwater communications. Acoustic technique cannot be used in UG channel due to vibration limitation. In magnetic induction (MI), [130],[184], signal strength decays with inverse cube factor and high data rates are not possible. Moreover, communication cannot take place if sender receiver coils are perpendicular to each other. Therefore, MI cannot be readily implemented in WUSNs.

To the best of our knowledge, this is the first measurement campaign conducted to analyze and measure the channel impulse response of UG channel and the first work that proposes guidelines for the development of a novel WUSN testbed to improve the accuracy, to reduce the time required to conduct WUSN experiments, and to allow flexibility in soil moisture control.

4.3 Impulse Response of UG channel

A wireless channel can be completely characterized by its impulse response. Traditionally, a wireless channel is modeled as a linear filter with a complex valued low pass equivalent impulse response which can be expressed as [113]:

$$h(t) = \sum_{l=0}^{L-1} \alpha_l \delta(t - \tau_l) \ , \tag{4.1}$$

where L, α_l, τ_l are the number of, the complex gains of, and the delays associated with multipaths, respectively.

Schematic view of UG channel is shown in Fig. 4.1, where a transmitter and a receiver are located at a distance of d and depths of h_t and h_r, respectively [75]. Communication is mainly conducted through three EM waves. First, the direct wave which travels through the soil in line-of-sight from transmitter to receiver. Second, the reflected wave, also travels through the soil, is reflected from the air-soil interface. Third, the lateral wave propagates out of soil, travels along the surface and enters the soil to reach the receiver.

Based on this analysis, the UG channel process can be expressed as a sum of direct, reflected and lateral waves. Hence (4.1) is rewritten for UG channel as:

$$h_{ug}(t) = \sum_{l=0}^{L-1} \alpha_l \delta(t - \tau_l) + \sum_{d=0}^{D-1} \alpha_d \delta(t - \tau_d) + \sum_{r=0}^{R-1} \alpha_r \delta(t - \tau_r) \ , \tag{4.2}$$

where L, D, and R are number of multipaths; α_l, α_d, and α_r are complex gains; and τ_l, τ_d, and τ_r are delays associated with lateral wave, direct wave, and reflected wave, respectively.

The received power is the area under the profile and is calculated as the sum of powers in all three components in the profile. Accordingly, the received power is given

as:

$$P_r = \sum_{l=0}^{L-1} |\alpha_l|^2 + \sum_{d=0}^{D-1} |\alpha_d|^2 + \sum_{r=0}^{R-1} |\alpha_r|^2 \ . \tag{4.3}$$

The path loss is calculated from the difference of the known transmit power and P_r, and is given as:

$$PL(dBm) = P_t(dBm) + G_t(dBi) + G_r(dBi) - P_r(dBm) \ , \tag{4.4}$$

where P_t is transmit power, P_r is received power, and G_t and G_r are transmitter and receiver antenna gains, respectively. Antenna effects are included, intrinsically, in the impulse response $h_{ug}(t)$ obtained from the channel transfer function. Traditionally, impulse response of wireless indoor channel is also dependent on antenna properties as power radiated and received in a particular direction is defined by directive gains of transmitter and receiver antennas [150]. In our experiments and analysis, we use omni-directional dipole antennas to observe multipath components in all directions.

Next, we review the metrics derived from the channel impulse response, including excess delay and delay spread. Excess delay is the time delay between the first and last arriving components. Last component is defined by a threshold value in dB relative to the strongest component in the power delay profile (PDP). Typically, a threshold value of -30 dB is used [101],[150]. Mean excess delay (τ) is defined as the first moment of power delay profile and is given as [150]:

$$\tau = \sum_k P_k \tau_k \Big/ \sum_k P_k \ , \tag{4.5}$$

where P_k is the absolute instantaneous power at the kth bin, and τ_k is the delay of the kth bin.

Root mean square (RMS) delay spread is the square root of the second central

moment of the power delay profile and is given as [150]:

$$\tau_{rms} = \sqrt{(\tau^2) - (\tau)^2}\ , \tag{4.6}$$

where $(\tau^2) = \sum_k P_k \tau_k^2 / \sum_k P_k$, P_k is the absolute instantaneous power at kth bin, and τ_k is the delay of the kth bin. RMS delay spread is a good indicator of multipath spread and it indicates the potential of inter-symbol interference (ISI).

4.4 Measurement Sites and Procedures

Measurement are conducted in an indoor testbed (Section 3.2.1) and field settings (Section 3.2.2). The measurement procedures are explained in Section 4.4.1.

4.4.1 Measurement Procedure

Accurate measurement of channel impulse response can be obtained from frequency domain measurements due to Fourier transform relationship between transfer function and channel impulse response [107]. Accordingly, we have obtained channel impulse by taking frequency domain measurements and then taking inverse Fourier transform. A diagram of the measurement layout is shown in Fig. 3.3(b). Frequency response of the channel is measured using a Vector Network Analyzer (VNA). VNA-based channel measurements are popular for measuring channel transfer functions in wireless communications and antenna domains [55, 101], [107], [150], [160], [176]. The measurement parameters are given in Table 3.2. The VNA generates a linearly swept frequency signal [146] which is propagated over a frequency range of 10 MHz to 4 GHz. In this range, VNA records 401 complex tones and stores them on external storage for post-processing. The discretized complex channel frequency response H_n

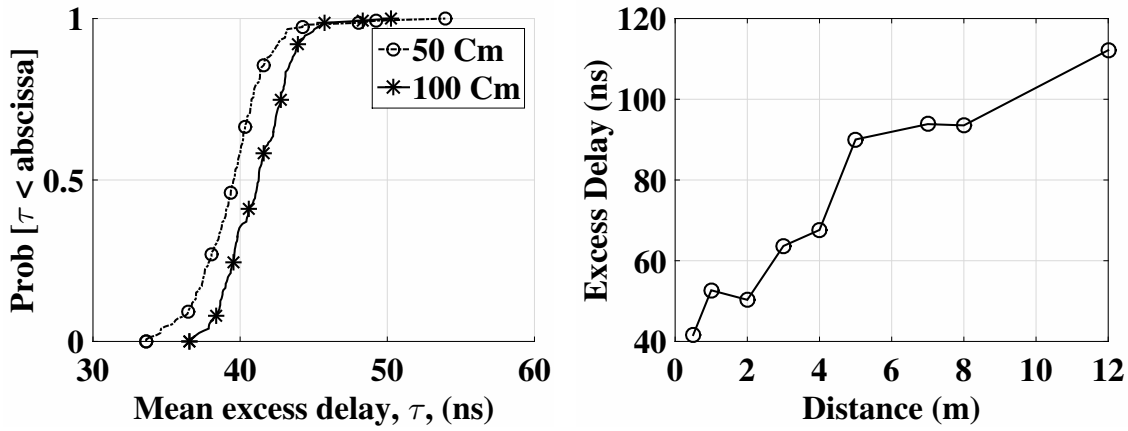

(a) (b)

Figure 4.2: (a) Distribution of mean excess delay τ in indoor testbed (silt loam) experiment, (b) Excess delay with distance at 20 cm depth in field (silty clay loam) experiment.

is given by [176]:

$$H_n = H(f_{start} + nf_{inc}) \ , \tag{4.7}$$

where f_{start} and f_{inc} are the start and increment frequencies of the sweep, respectively. H_n is obtained by measuring the reference (R) and input (A) channels and taking the complex ratio, such that $H_n = A_n/R_n$. This process is repeated over the frequency range F_{sweep} at N discrete points, such that $f_{inc} = F_{sweep}/N$. To obtain channel impulse response, the complex frequency data is inverse Fourier transformed. The resulting N point complex channel impulse response has a delay bin spacing of $1/F_{sweep}$ and an unambiguous FFT range of N/F_{sweep}. The measured H_n are windowed using a minimum three term Blackman-Harris window [176] because of its excellent side lobe suppression and relatively wide main lobe width. Before time domain conversion, windowing of H_n is required to avoid $sinc^2$ side lobes associated with rectangular nature of frequency sweep [176].

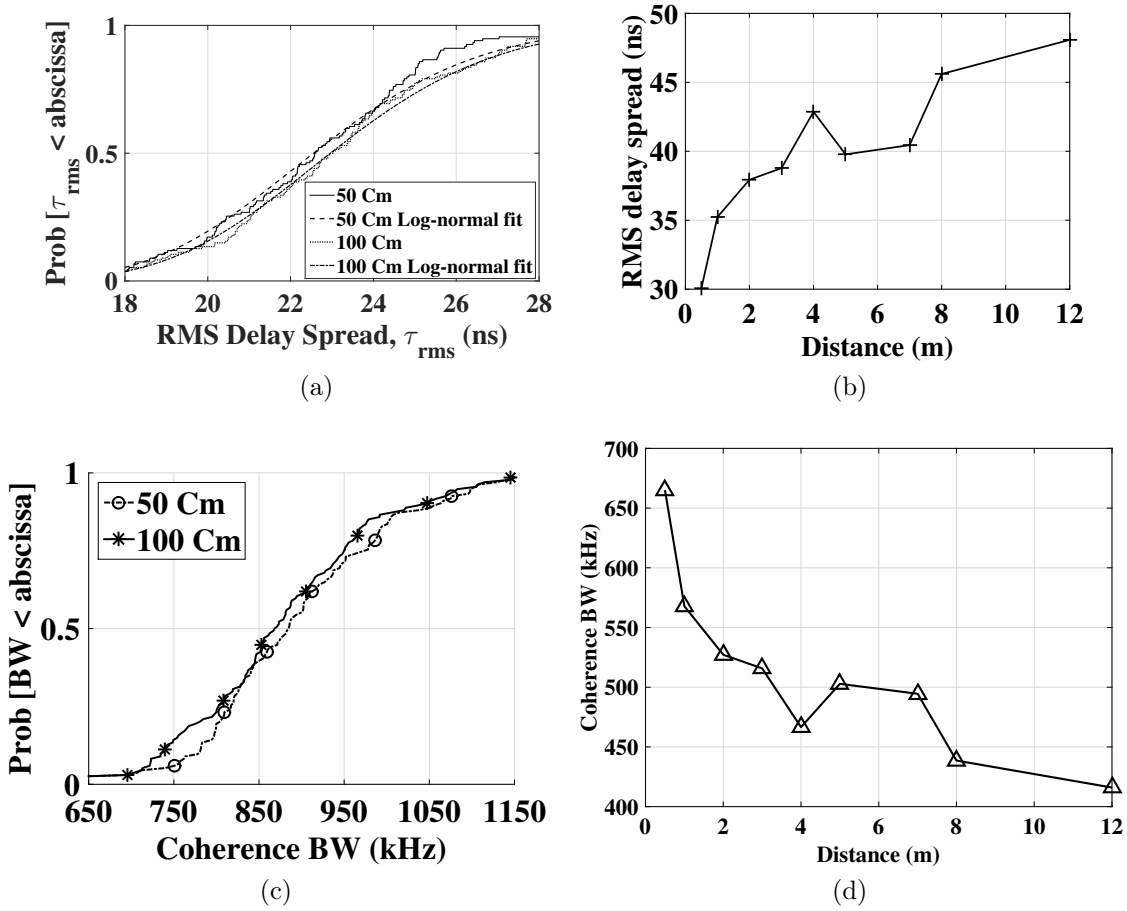

Figure 4.3: (a) Distribution of RMS delay spread, τ_{rms}, for 50 cm and 1 m distance along with log-normal fit over all four depths in indoor testbed (silt loam) experiment, (b) RMS delay spread, τ_{rms}, with distance in field (silty clay loam) experiment, (c) Distribution of coherence bandwidth for 50 cm and 1 m distance in indoor testbed (silt loam) experiment, (d) Coherence bandwidth with distance in field (silty clay loam) experiment.

4.5 Analysis and Results

4.5.1 Characterization of UG Channel Impulse Response

Excess delay, mean access delay (4.5), RMS delay spread (4.6) [160], [150], [55], and coherence bandwidth in relation to RMS delay spread [107] are the parameters used to characterize the channel. For channel characterization, these parameters are used because system performance is not effected by the actual shape of PDP [160]. In the following, we discuss these metrics and the effects of soil moisture, soil types,

distance, and depth on these metrics.

4.5.1.1 Statistics of Mean Excess Delay

Distribution of mean excess delay for 50 cm and 1 m distance over all four depths in indoor testbed (silt loam) experiment is given in Fig. 4.2(a). Higher mean excess delay can be observed with the increase in T-R separation, which corresponds to an increase of 2 −3ns (8 %). In Table 4.1, statistics for mean (μ) and standard deviation (σ) for the mean excess delay for 50 cm and 1 m distances, and the 4 depths are shown. Higher mean excess delays are also observed as transmitter and receiver are buried deeper. In Fig. 4.2(b), excess delay is shown as a function of distance at 20 cm depth in field (silty clay loam) experiment. It can be observed that excess delay is increased from 40 ns up to 116 ns as UG communication distance increases from 50 cm to 12 m.

4.5.1.2 Analysis of RMS Delay Spread

Distribution of RMS delay spreads for T-R separations of 50 cm and 1 m in indoor testbed (silt loam) experiment, are shown in Fig. 4.3(a) with statistical fits. Our analysis shows that empirical distribution of τ_{rms} follows a log-normal distribution and the mean values of 23.94 ns and 24.05 ns and standard deviations of 3.7 ns and 3.4 ns for 50 cm and 1 m distance, respectively. In Table 4.1, statistics for mean (μ) and standard deviation (σ) of the RMS delay spread for 50 m and 1 m distances, and 4 depths are shown. It can be observed from Fig. 4.3(a) and Table 4.1 that RMS delay spread (τ_{rms}) is dependent on T-R separation and burial depth with positive correlation. There is an increase of 2-3 ns (20 %) in RMS delay spread as depth is increased from 10 cm to 40 cm. A 4 ns increase in RMS delay spread can be observed from 10 cm to 20 cm depth at 50 cm distance, which is caused by lateral wave, because at 20 cm lateral wave reaches the receiver after direct wave. At 40 cm, RMS delay

spread decreases to 23 ns because lateral wave attenuates more as the burial depth increases. In Fig. 4.3(b), RMS delay spread is shown as a function of T-R distance at 20 cm depth in field (silty clay loam) experiment. It can be observed that RMS delay spread is increased to 48 ns by increasing distance to 12 m.

The increase in RMS delay spread with depth and distance is contributed by the strong multipaths associated with the lateral and reflected components, since their propagation time differences increase with distance. This increase in RMS delay spread is an important result as it limits the system performance in terms of coherence bandwidth. It has been shown by analysis and simulations that maximum data rate that can be achieved without diversity or equalization is a few percent of the inverse of RMS delay spread [107]. Using this relationship, a coherence bandwidth is established for the RMS delay spread. For our analysis, we have used 90 % signal correlation ($1/50\ \tau_{rms}$) as an approximation of coherence bandwidth, because underground channel experiences higher attenuation in soil as compared to terrestrial WSNs, where typically 50 % and 70 % signal correlation values are used to approximate coherence bandwidth.

In Fig. 4.3(c), distribution of coherence bandwidth for 50 cm and 1 m distance over all depths in indoor testbed (silt loam) experiment is shown. It is observed that

Table 4.1: Mean (μ) and Standard Deviation (σ) in nanoseconds for the mean excess delay and RMS delay spread in indoor testbed (silt loam) experiment.

Depth	Mean Excess Delay τ				RMS Delay Spread τ_{rms}			
	50 cm		**1** m		**5**0 cm		**1**m	
	μ	σ	μ	σ	μ	σ	μ	σ
10 cm	33.53	1.24	36.09	0.80	20.05	2.24	21.94	2.32
20 cm	34.66	1.07	37.12	1.00	24.93	1.64	25.10	1.77
30 cm	35.87	0.72	37.55	0.65	24.84	2.17	25.34	3.41
40 cm	36.43	0.74	40.18	0.94	23.91	2.84	25.62	1.87

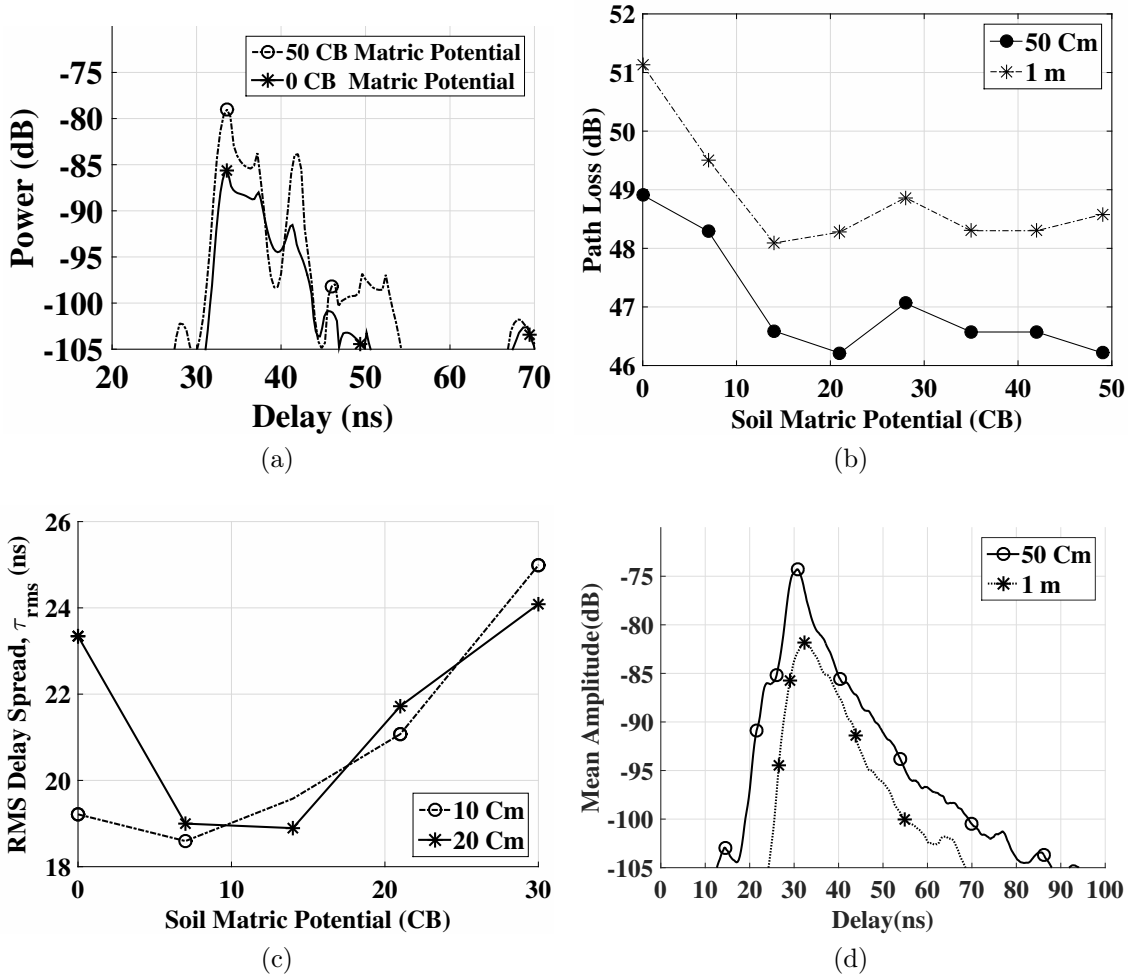

Figure 4.4: Indoor testbed (silt loam) experiment: (a) Power delay profile, (b) Path loss with vs. soil moisture at 10 cm depth, (c) RMS delay spread vs. soil moisture at 50 cm distance, (d) Mean amplitudes of all 50 cm and 1 m profiles across all depths.

the range of coherence bandwidth for UG channel is between 650 kHz to 1.15 MHz for distances up to 1 m. In Fig. 4.3(d), coherence bandwidth as a function of distance in field (silty clay loam) experiment is shown. It can be observed that coherence bandwidth decreases to 418 kHz (63 %) as communication distance is increased to 12 m. The restriction placed on the coherence bandwidth by the increase in RMS delay spread with distance and depth should definitely be considered in system design but a fine design line should not be drawn because of the soil moisture variations, which are discussed next.

4.5.1.3 Soil Moisture Variations

In Fig. 4.4(a), the effect of soil moisture on amplitudes of a delay profiles is shown for 50 cm distance in indoor testbed (silt loam) experiment. Lower amplitudes can be observed for higher soil moisture (lower soil matric potential (CB)) and this increase is consistent over all delay ranges. Amplitude decrease varies between $5-8$ dB across the entire PDP.

Water in soil is classified into bound water and free water. Water contained in the first few particle layers of the soil is called bound water, which is strongly held by soil particles due to the effect of osmotic and matric forces [85]. Below these layers, effects of osmotic and matric forces is reduced, which results in unrestricted water movement. EM waves experience dispersion when interfaced with bound water. Since permittivity of soil varies with time due to the variation in soil moisture, wavelength in soil changes which effects the attenuation that waves experience in soil.

In Fig. 4.4(b), the path loss with change in soil moisture (expressed as soil matric potential[1]) at 50 cm and 1 m distance and 10 cm depth in indoor testbed (silt loam) experiment is shown. Path loss decreases by 3-4 dB (7 %) as soil matric potential changes from 0 to 50 CB (Centibars). In Fig. 4.4(c), change in RMS delay spread with change in soil moisture at 50 cm distance, 10 cm and 20 cm depth in indoor testbed (silt loam) experiment is shown. From near-saturation to 8 CB, RMS delay spread has decreased first and then increases as soil moisture decreases. This is attributed to water repellency of soil particles where infiltration is slowed momentarily at near-saturation levels. For 10 cm depth, RMS delay spread has increased from 19 ns to 25 ns (31 %) as soil moisture decreases. Similar increase in RMS delay spread with decrease in soil moisture can be observed for 20 cm depth. Low water absorption of

[1]Greater matric potential values indicate lower soil moisture and zero matric potential represents near saturation condition.

EM waves with decrease in soil moisture contributes to increase in τ_{rms} as multipath components exhibit less attenuation.

The variations in amplitudes and path loss with the change in soil moisture lead to changes in coherence bandwidth, optimal system capacity and communication coverage range. Specifically, increase in RMS delay spread with soil moisture decreases coherence bandwidth of the channel, and attenuation is also increased when soil moisture increases. Therefore, underground communication devices should have the ability to adjust their operation frequency, modulation scheme, and transmit power to compensate these changes caused by soil moisture variation. Cognitive radio [38] solutions can be used to adopt parameters based on changing channel conditions.

4.5.1.4 Soil Type

Soils are divided into textural classes based on their particle size. To analyze the effects of soil texture, we have measured the channel statistics for silty clay loam, silt loam, and sandy soils. In Table 4.2, statistics of mean (μ) and standard deviation (σ) for the mean excess delay, RMS delay spread and path Loss for 50 cm and 1 m distances, and 4 depths are shown.

RMS delay spread τ_{rms} in sandy soil is 2 ns higher than silty clay loam, which is 1 ns higher than the silt loam on the average. Similarly, path loss is $4-5$dB lower

Table 4.2: Mean (μ) and Standard Deviation (σ) for the Mean Excess Delay, RMS delay spread and Path Loss for 50 cm and 1 m distances, and 20 cm depth for three soils. Values are in nanoseconds.

Soil Type	**M**ean Excess Delay				**R**MS Delay Spread				**P**ath Loss	
	Distance				**D**istance				**D**istance	
	50 cm		1 m		50 cm		1 m		50 cm	1 m
	μ	σ	μ	σ	μ	σ	μ	σ		
Silty Clay Loam	34.77	2.44	38.05	0.74	25.67	3.49	26.89	2.98	49 dB	52 dB
Silt Loam	34.66	1.07	37.12	1.00	24.93	1.64	25.10	1.77	48 dB	51 dB
Sandy Soil	34.13	1.90	37.87	0.80	27.89	2.76	29.54	1.66	40 dB	44 dB

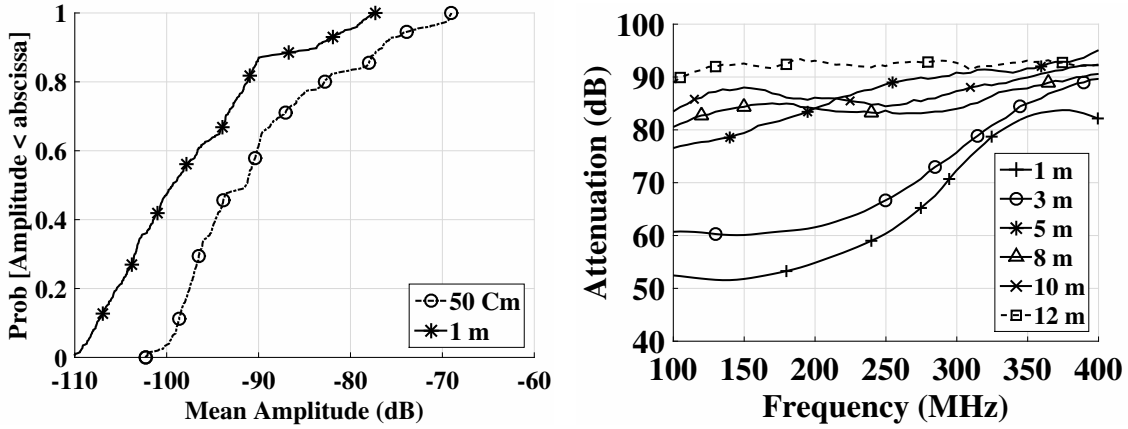

(a) (b)

Figure 4.5: Indoor testbed (silt loam) experiment: (a) Distribution function of mean amplitudes at 40 cm depth. Field (silty clay loam) experiment: (b) Attenuation with frequency.

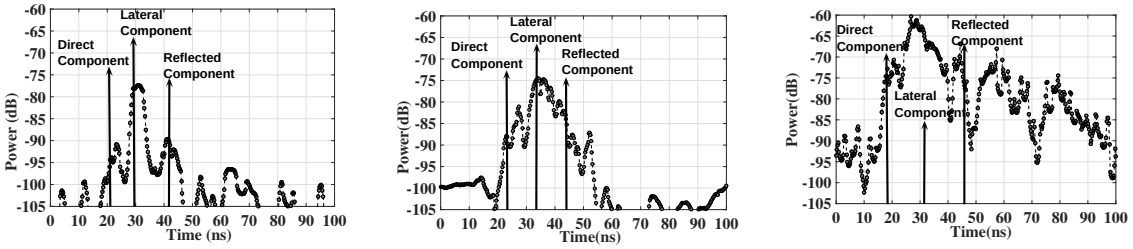

(a) (b) (c)

Figure 4.6: Measured impulse response (dotted lines) and impulse response model (solid lines) in: (a) silt loam, (b) silty clay loam soil, and (c) sandy soil.

in sandy soil as compared to silt loam and silty clay loam. This is due to the lower attenuation in sandy soil. Attenuation of EM waves in soil varies with soil type [69]. Sandy soil holds less bound water, which is the major component in soil that absorbs EM waves. Water holding capacity of fine-textured (silt-loam, silty clay loam) and medium-textured soils (fine sandy loam) is much higher, because of the small pore size (but, greater number of pores), as compared to coarse-textured (sandy, sandy loam, loamy sand) because of larger pore size (but less in number of pores) [85]. Hence the soils containing the highest clay contents suffer more attenuation.

In sandy soil, there is a trade-off between attenuation and RMS delay spread. RMS delay spread τ_{rms} is large due to least attenuated multipath components arriving at the

receiver with large delays. On the other hand, overall attenuation is low as compared to silt loam and silty clay loam. Therefore higher SNR can be achieved with moderate coherence bandwidth. Effects of soil texture must be taken into account during design and deployment of WUSNs and optimal system parameters such as communication range and data rates should be selected based on the physical characteristics of the soil.

4.5.1.5 Distance and Depth

Communication in UG channel is effected by depth and T-R separation. However, these impacts are much more severe then over the air communication. In Fig. 4.4(d), effects of T-R distance are shown in indoor testbed (silt loam) experiment. By increasing the distance from 50 cm to 1 m, the first component in the 1 m PDP is delayed by 10 ns. An 8 dB difference in peak amplitude is observed between profiles at 50 cm and 1 m. Distribution of mean amplitudes of 50 cm and 1 m profiles at 40 cm depth in indoor testbed (silt loam) experiment is shown in Fig. 4.5(a). A $9-10$dB decrease in mean amplitude can be observed when T-R separation is increased from 50 cm to 1 m. Peak amplitude of delay profile is decreased by 5 dB from 10 cm depth to 40 cm depth at 50 cm distance, whereas this decrease in peak amplitude is 20 dB for 1 m distance when depth is changed from 10 cm to 40 cm. Since increase in burial depth increases the path of EM waves in soil, higher attenuation is observed.

Table 4.3: Speed of the wave in all three soils, calculated by refractive indices n based on particle size distribution of soils given in Table 3.2.

Soil Type	Speed in Soil **m/s**	% of c	Refractive Index n
Silt Loam	5.66x10^7	18.89	5.28
Sandy Soil	5.01x10^7	16.71	5.98
Silty Clay Loam	5.67x10^7	18.91	5.29

EM waves in soil are reflected and attenuated by soil-air interface and suffers diffusion attenuation. Additional attenuation is caused by absorption of waves in soil. Higher attenuation is the limiting factor for communication system design. The attenuation is increased with distance and depth because of reflection effects of lateral wave. At soil-air interface phase of lateral wave is randomly changed, which adds constructive-destructive interference at the receiver.

4.5.1.6 Operation Frequency

In Fig. 4.5(b), attenuation with frequency at different distances of up to 12 m are presented. Transmitter and receiver depths are set to 20 cm. At 2 m distance, attenuation increases by 24 dB when frequency increases from 200 MHz to 400 MHz. Similarly, for 200 MHz, attenuation is increased from 51 dB to 92 dB (80 %) when distance increases from 50 cm to 12 m.

Higher frequencies suffer more attenuation because when EM waves propagate in the soil their wavelength shortens due to higher permittivity of soil than the air. Hence, due to less effects of permittivity of soil on lower frequency spectrum, it is more suitable for UG2UG communication as larger communication distances can be achieved. In order to have minimum attenuation, an operation frequency should be selected, for each distance and depth, such that attenuation is minimized. This is important from WUSN topology design perspective because deployment needs to customized to the soil type and frequency range of sensors being used for deployment.

4.5.2 Model Parameters and Experimental Verifications

In this section, arrival of multipath components is validated with a schematic of the three model components and model parameters are given. Moreover, the shape of the PDP is presented and with physical interpretations.

Speed of the wave in soil is given as [64] $S = c/n$, where $c = 3\text{x}10^8$ m/s is the speed of light, n is the refractive index of soil $n = \sqrt{\sqrt{\epsilon'^2 + \epsilon''^2} + \epsilon'/2}$, and ϵ' and ϵ'' are the real and imaginary parts of the relative permittivity of the soil.

Arrival time of each of the three components, in nanoseconds, is calculated as follows:

$$\tau_d = (\delta_s/S) + 2 \times (L_c/S_c) \ , \tag{4.8}$$

$$\tau_r = 2 \times (\delta_s/S) + 2 \times (L_c/S_c) \ , \tag{4.9}$$

$$\tau_l = 2 \times (\delta_s/S) + (\delta_a/c) + 2 \times (L_c/S_c) \ , \tag{4.10}$$

where τ_d, τ_r, and τ_d are arrival times of the direct, reflected and lateral waves, respectively, δ_s is distance traveled by wave in soil, L_c is the length of the coaxial cable attached to antenna, S_c is the speed of wave in coaxial cable calculated with refractive index of 1.2, S is speed of wave in soil, and c is the speed of light $3\text{x}10^8$ m/s.

Based on (4.8), (4.9) and (4.10), the speed of the wave in all three soils is found by calculating the refractive indices n based on particle size distribution and classification of soils given in Table 3.2. The results of these calculations are shown in Table 4.3. In Figs. 4.6, measured PDPs for three soil types at 40 cm depth is compared with a schematic representation of the 3-wave model for T-R separation of 50 cm. Analysis of arrival time of three components reveals that for 50 Cm distance and all burial depths, lateral waves arrive later than the direct wave except for the 10 Cm depth where lateral wave reaches the receiver first. It can be observed that measurement data shows a strong agreement with the model.

In Table 4.4, model parameters for peak amplitude, delays, and number of multipaths statistics for direct, lateral and reflected components for three soil types are shown. From Fig. 4.6 and Table 4.4, it can be observed that lateral component is

the strongest component than the direct and reflected components. This is because direct and reflected components are spherical waves radially outward from the dipole, whereas lateral component is, first, a plane wave that travels upward from the source to the boundary, then travels horizontally as a cylindrical wave, and then travels backward as a plane wave from boundary to point of observation.

4.6 WUSN Communication System Design

The presented impulse response model and experiment results provide insight into the statistics of the UG channel. Moreover, the impacts of distance, depth, soil moisture and soil texture on communication channel can be observed. These analyses provide useful insight to system designers in order to obtain desired performance. These guidelines are discussed in the following.

4.6.1 Underground Beamforming

The dominance of the lateral waves in UG channel as observed in Figs. 4.6 has important implications in wireless underground communication system design. Lateral component has the potential, via beam-forming techniques, to reach at farther underground distances which otherwise are limited (8 m to 12 m) because of higher attenuation in soil. Beam-forming antennas [133] are being used in indoor wireless

Table 4.4: Model parameters: peak amplitude, delays, and number of multipaths statistics for direct, lateral and reflected components for three soils.

	Silty Clay Loam			Silt Loam			Sandy Soil		
	Distance			Distance			Distance		
	1 m			1 m			1 m		
	Peak α dB	τ ns	N	Peak α dB	τ ns	N	Peak α dB	τ ns	N
Direct Component	-90	18-28	3	-103	15-23	2	-87	11-19	4
Lateral Component	-80	30-40	2	-82	26-43	3	-63	22-45	5
Reflected Component	-91	41-47	2	-94	47-59	4	-70	47-61	6

networks to improve capacity. In UG channel, these multiple antenna arrays can be used to focus the maximum signal energy to exploit the lateral wave. Signal footprint can be tailored by limiting energy radiation in direct and reflected components as these are attenuated most. This type of beam-forming in underground channel could be either adaptive based on effects of frequency and soil moisture on channel, or fixed, based on the soil type, depth and distance of system deployment.

4.6.2 Underground OFDM

From an underground communication system design perspective, RMS delay spread and coherence bandwidth findings reported in this chapter, for both UG2UG and UG2AG channel, lead to an important conclusion. To achieve high data rates, single carrier approaches may lead to higher bandwidth requirement and use of all available system bandwidth as a single channel for data transmission would result in inter-symbol interference (ISI). Therefore, to achieve high data rates and to overcome ISI problem, Orthogonal Frequency Division Multiplexing (OFDM) [58] can be used for signal transmission, where signal bandwidth of each sub-carrier is less than the coherence bandwidth of underground channel. Moreover, significant performance improvement can be achieved in underground channel when modulation scheme can be designed and adapted based on measured channel impulse response. Such modular adaptation is supported by discrete multi-tone modulation (DMT), a variant of OFDM, by use of set of non-overlapping narrowband carriers and transmission rate is adopted based on each sub-carrier's individual conditions. To develop an optimum strategy and theory to analyze the effects of such technique on underground channel needs to be investigated further.

4.7 Conclusion

In this chapter, analysis of impulse response of Wireless Underground Sensor Networks (WUSN) channel is presented. A 3-wave based impulse response model of underground channel is developed and validated with measured data. Distribution of mean excess delay and RMS delay spread is determined and it is shown that RMS delay spread is log-normally distributed. Effect of T-R separation on mean amplitudes of power delay profile is showed. We have presented the impact of soil moisture and soil types on RMS delay spread and power gains of delay profiles. It is presented that RMS delay spread increases with increase in soil moisture. It is also showed that coarse-textured soils have larger RMS delay spreads and lower attenuation as compared to fine and medium-textured soils. Coherence bandwidth of UG channel in relation to RMS delay spread is modeled and showed to be less than 1 MHz. Coherence bandwidth findings reveled the use of OFDM for underground channel communication to have ISI free communication and for significant performance improvements. These findings serve as important characterization parameters of UG channel and give guidelines for design of an underground communication system.

Chapter 5

A Statistical Model of Wireless Underground Channel

The Internet of Underground Things (IOUT) has many applications in the area of smart lighting. IOUT enables communications in smart lighting through underground (UG) and aboveground (AG) communication channels. In IOUT communications, an in-depth analysis of the wireless underground channel is important to design smart lighting solutions. In this chapter, based on the empirical and the statistical analysis, a statistical channel model for the UG channel has been developed. The parameters for the statistical tapped-delay-line model are extracted from the measured power delay profiles (PDP). The PDP of the UG channel is represented by the exponential decay of the lateral, direct, and reflected waves. The developed statistical model can be used to generate the channel impulse response, and precisely predicts the UG channel RMS delay spread, coherence bandwidth, and propagation loss characteristics in different conditions. The statistical model also shows good agreement with the empirical data, and is useful for tailored IOUT solutions in the area of smart lighting.

5.1 Motivation

In Internet of Underground Things (IOUT) [155], [157], sensors and communication devices, both buried and over the air (OTA), forms an internet of things for real time

communications and sensing of the environment in which these are deployed. IOUTs have many applications in areas including environment and infrastructure monitoring [36], [39], [95], [132], [177], border patrol [40], and precision agriculture [34], [76], [155], [23], [156], [157], [158], [199].

A potential application of the IOUT is in the area of smart lighting [92], [91], [168], where cables are buried underground for control of intelligent lighting systems. The overview of the smart lighting IOUT system architecture is shown in Fig. 5.1. The IOUT architecture connects underground and aboveground communication devices and sensors using two types of the wireless channel, i.e., underground (UG), and above-ground (AG). The smart lighting IOUT applications include road lighting, lamp posts, airport runway lighting, household driveway and garage illumination, and garden decoration. In these applications, over-the-air (OTA) channel can be eliminated completely, and all communication can be carried out through IOUT UG and AG channels. A smart lighting IOUT architecture has many advantages over the OTA: 1) the need to have a wired underground communication network can be completely eliminated, 2) by bringing the communication devices underground, complexity of cabling to power aboveground devices is reduced, and 3) interference and spectrum congestion issues are avoided. In smart lighting IOUT, through real time sensing of the environment, all illumination needs of the environment can be met effectively with high energy efficiency. This IOUT approach also results in improved smart lighting solutions and cost reduction of the system deployment.

A detailed characteristic of the wireless UG channel is vital for design of such IOUT communication systems. In Chapter 4, we have conducted a detailed empirical characterization of the wireless UG channel in different soils under different soil moisture conditions through both the testbed and field experiments. The goal of the measurement campaign (Chapter 3) and the corresponding model is to produce a re-

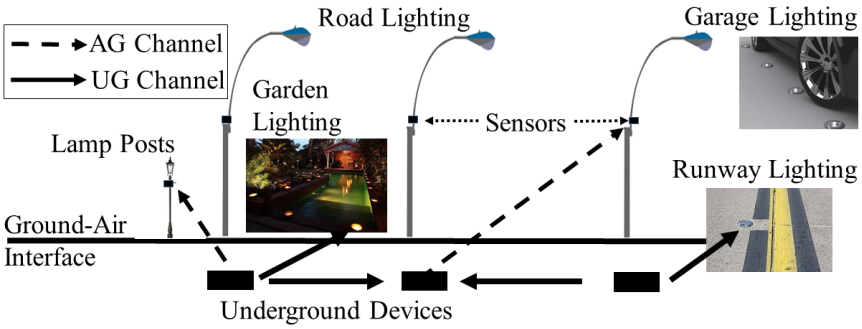

Figure 5.1: Overview of smart lighting IOUT system architecture.

liable channel model which can be used in heterogeneous IOUT deployments. Thus, we have considered several possible scenarios with extensive measurements taken over the period of many years. In Chapter 4, the time domain characteristics of channel such as RMS delay spread, coherence bandwidth, and multipath power gains are analyzed empirically. The analysis of the power delay profile (PDP) validated the three main components of the UG channel, i.e. direct, reflected, and lateral waves. Underground communication challenges are also discussed in Chapter 4.

In this chapter, we develop a statistical model for the wireless UG channel based on the empirical evaluations presented in Chapter 4. The statistical model is based on the analysis of the properties of the power delay profiles measured in different soils under different water content levels in the indoor testbed (Chapter 3) and field settings. To engineer an IOUT communication system for smart lighting, a statistical model of propagation in the wireless underground channel is useful in optimizing system performance, designing tailored modulated/coding schemes, and in end-to-end capacity analysis. Moreover, the developed statistical model can be used to generate the channel impulse response, and precisely predicts the UG channel RMS delay spread, coherence bandwidth, and propagation loss characteristics in different UG conditions. The aim of this chapter is to focus on the statistical analysis and the modeling of the UG channel, rather than on the measurements and experiments, for it we refer the reader to Chapter 3 and Chapter 4. The rest of the chapter is orga-

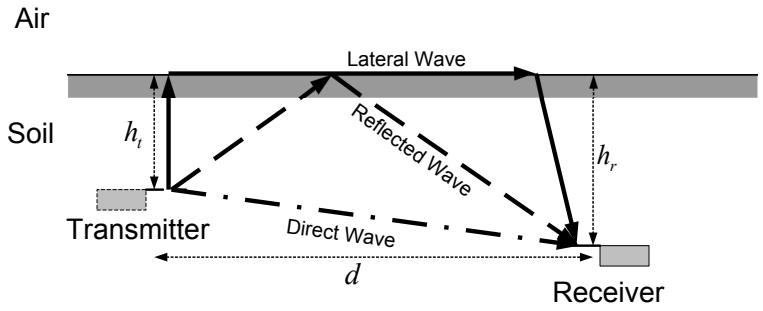

Figure 5.2: L, D, and R-Wave in the UG channel [75].

nized as follows: the related work is discussed in Section 5.2. The statistical channel impulse response model is developed in Section 5.3. In Section 5.4, model evaluations are performed numerically. Empirical validation of the developed statistical impulse response model is done in Section 5.5. Chapter is concluded in Section 5.6.

5.2 Related Work

Smart lighting is an emerging field [91], [92], and there exist only few architectures. Use of the IOUT communications in this field has not been investigated before. Intelligent light control using sensor networks has been proposed in [168], however, it does not use the UG channel. An OTA intelligent lighting control architecture has been proposed in [78].

Smart lighting IOUT UG wireless channels (UG and AG) requires detailed characterization. In [200], we have developed a 2-wave model without consideration of the lateral wave. In [177], a model for underground communication in mines and road tunnels has been developed but it cannot be applied to IOUT due to dissimilarities in wave propagation mechanisms of tunnels and soil. We have also developed a closed-form path loss model using lateral waves in [75] but channel impulse response and statistics cannot be captured through this simplified model. Magnetic induction (MI) [124], [185], is another wave propagation mechanism in the underground communications. In MI, received signal strength decreases rapidly with distance and

high data rates can not be achieved. Moreover, communications cannot be carried out if sender receiver coils are at right angles. Long wavelengths of the MI channel limit the network architecture scalability. To the best of our knowledge, this is the first statistical model for the wireless underground channel based on an empirical campaign conducted to characterize the channel impulse response of UG channel for IOUT communications.

5.3 The Statistical Model

To model the wireless underground channel, our approach follows the standard OTA modeling approaches described in [150], [160], [101], and [209], with modifications due to unique nature of wireless propagation in the underground channel. Based on the measurement analysis, following assumptions are made:

1) Correlation among multipath components at different delays in the lateral, reflected, and direct component is very small and negligible for all practical purposes. However multipaths within each component are affected by the strongest path and hence are correlated. Therefore, the tap-delay-lines are assumed uniformly spaced within each component.

2) At the receiver, phases are completely random with uniform distribution over $[0, 2\pi)$.

To keep model tractable, arrival rate of delays within each component is kept constant, and amplitudes of these multipaths in each component are statistically independent. This helps in modeling the physical characteristics of the UG channel and provide ease of analysis without losing insight into delay statistics. The order of the arrival of the lateral, direct, and reflected component depends upon the burial depth, distance between transmitter-receiver (T-R), because the path traversal through soil

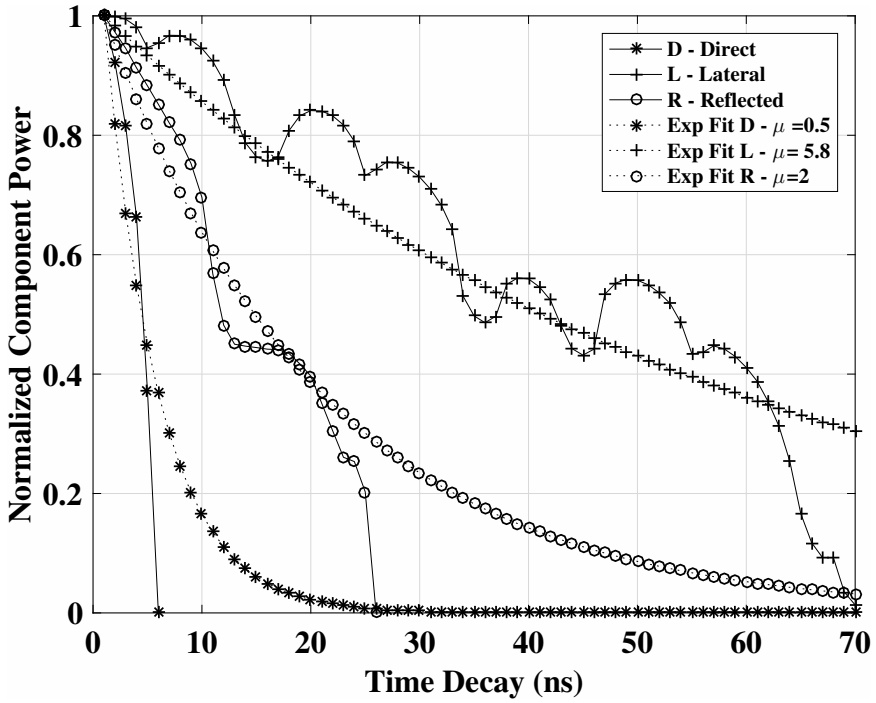

Figure 5.3: Decay of three components with exponential decay fit.

and air exhibits different wave propagation speeds depending on the soil characteristics, and soil moisture level. Only for the T-R distances less than 50 cm, direct component arrives first, and as the distances increases, the lateral component reaches at the receiver first due to higher propagation speed in the air medium. Due to significant differences in speed of the three components in soil and air mediums, no component overlap is observed, and power of multipaths (gain) within each components decays before the arrival of the next component. Moreover, in our measurements, there were not any significant detectable components observed beyond the 100 ns time delay.

Next, statistics of amplitudes α_{li}, α_{dj}, α_{rk} at delays τ_{li}, τ_{di}, τ_{ri} for lateral, direct, and reflected waves, respectively, are derived. In Fig. 5.3, mean amplitudes of a profile have been shown at 50 cm distance with exponential decay fit. Analysis of the measurement data shows that gains of multipaths within each component follow the exponential decay. Therefore, the path amplitudes of the three components are

modeled as decaying exponentials within each component. The multipath amplitudes calculated from the arrival time τ_L, decay rate γ_L, and amplitude α_L of the lateral component. It is given as [160]:

$$\alpha_{li} = \alpha_{l0} e^{-(i-\tau_L)/\gamma_L} \ \forall \ i > \tau_l \ and \ i < \tau_l + L. \tag{5.1}$$

The α_{dj} for the direct component is obtained from the arrival time τ_D, decay rate γ_D, and amplitude α_D of the direct component. It is expressed as:

$$\alpha_{dj} = \alpha_{d0} e^{-(j-\tau_D)/\gamma_D} \ \forall \ j > \tau_d \ and \ j < \tau_d + D. \tag{5.2}$$

Similarly, for the reflected component, α_{rk} is given as:

$$\alpha_{rk} = \alpha_{r0} e^{-(k-\tau_R)/\gamma_R} \ \forall \ k > \tau_r \ and \ k < \tau_d + R. \tag{5.3}$$

Gain of first multipath is denoted as α_{d0}, α_{l0}, and α_{r0}. These multipaths within each components are calculated as follows [75]:

$$\begin{aligned}
\alpha_{d0} &= P_t + 20\log_{10}\lambda_s - 20\log_{10} r_1 - 8.69\alpha_s r_1 \\
&\quad -22 + 10\log_{10} D_{rl} \ , \\
\alpha_{r0} &= P_t + 20\log_{10}\lambda_s - 20\log_{10} r_2 - 8.69\alpha_s r_2 \\
&\quad +20\log_{10}\Gamma - 22 + 10\log_{10} D_{rl} \ , \\
\alpha_{l0} &= P_t + 20\log_{10}\lambda_s - 40\log_{10} d - 8.69\alpha_s (h_t + h_r) \\
&\quad +20\log_{10} T - 22 + 10\log_{10} D_{rl} \ ,
\end{aligned} \tag{5.4}$$

where P_t is the transmitted power, Γ and T are reflection and transmission coefficients

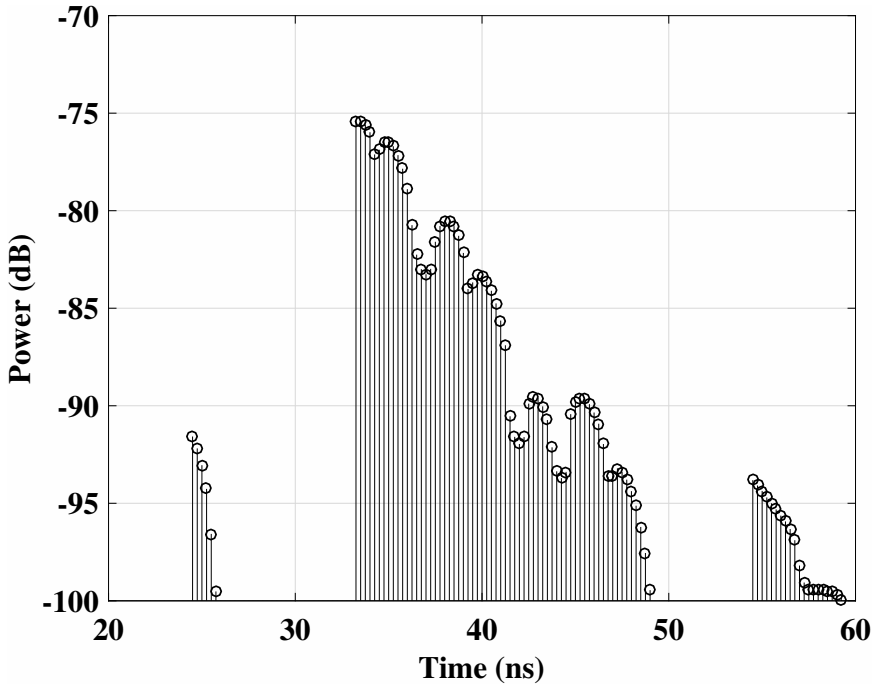

Figure 5.4: A realization of wireless underground channel impulse response

[75], respectively, r_2 is the length of the reflection path, $r_1 = \sqrt{(h_t - h_r)^2 + d^2}$, $r_2 = \sqrt{(h_t + h_r)^2 + d^2}$, where h_t and h_r are transmitter and receiver burial depth, and λ_s is the wavelength in soil [23].

In the statistical model, exponential decay is justified because the time delay depends on the travel paths, and the path gains are affected by the soil. Therefore gains of the successive multipaths depends on the delay of those multipaths. It is also important to note that, in addition to the soil moisture, the multipath gains α_{li}, α_{dj}, α_{rk} are also impacted by soil type. For example, in sandy soils path gains are much higher due to lower attenuation as compared to the silt loam and silty clay loam soils due to the less water absorption of EM waves in sandy. This is attributed to the low water holding capacity of sandy soils. However, soil type impact on multipaths gains α_{li}, α_{dj}, α_{rk} does not require separate modeling in (5.1) - (5.3), therefore, it is captured in the main lateral, direct, and reflected components α_{l0}, α_{d0}, α_{r0} and is propagated to α_{li}, α_{dj}, α_{rk} in (5.1) - (5.3) due to their dependence on α_{l0}, α_{d0}, α_{r0}.

Table 5.1: The impulse response model parameters.

Parameter	Description	Model	Values
S	Speed of wave in soil [158]	C/η	$C = 3 \times 10^8$
η	Refraction Index [158]	$\eta = \sqrt{\sqrt{\epsilon'^2 + \epsilon''^2} + \epsilon'/2}$	ϵ', ϵ''
ϵ'	Real part of relative permittivity of the soil [144]	$\epsilon'_s = \begin{cases} 1.15\Big[1 + \rho_b/\rho_s\left(\epsilon_s^{\delta} - 1\right) + (m_v)^{\nu'}(\epsilon'_{fw})^{\delta} - \\ \quad m_v\Big]^{1/\delta} - 0.68 \qquad 0.3\,\text{GHz} \le f \le 1.4\,\text{GHz}\ , \\ \Big[1 + \rho_b/\rho_s\left(\epsilon_s^{\delta} - 1\right) + (m_v)^{\nu'}(\epsilon'_{fw})^{\delta} - m_v\Big]^{1/\delta} \\ \qquad 1.4\,\text{GHz} \le f \le 18\,\text{GHz}\ , \end{cases}$	S = Sand in %, C= Clay in %, $\delta = 0.65$, $\nu' = 1.2748 - 0.519S - 0.152C$, $\nu'' = 1.33797 - 0.603S - 0.166C$ ϵ'_{fw}, ϵ''_{fw}
ϵ''	Imaginary part of relative permittivity of the soil [144]	$\epsilon''_s = \left[(m_v)^{\nu''}(\epsilon''_{fw})^{\delta},\right]^{1/\delta}$	
ϵ'_{fw}	Real part of relative permittivity of the free water [144]	$\epsilon'_{fw} = e_{w\infty} + \frac{\epsilon_{w0} - \epsilon_{w\infty}}{1 + (2\pi f \tau_w)^2}$	$\epsilon_{w\infty} = 4.9$ is the limit of ϵ'_{fw} when $f \to \infty$, ϵ_{w0} is the static dielectric constant for water, τ_w is the relaxation time for water, and ϵ_0 is the permittivity of free space. At room temperature,$2\pi\tau_w = 0.58 \times 10^{-10}s$ and $\epsilon_{w0} = 80.1$, effective conductivity, δ_{off}
ϵ''_{fw}	Imaginary part of relative permittivity of the free water [144]	$\epsilon''_{fw} = \frac{2\pi f \tau_w(\epsilon_{w0} - \epsilon_{w\infty})}{1 + (2\pi f \tau_w)^2} + \frac{\delta_{eff}}{,2\pi\epsilon_0 f}\frac{(\rho_s - \rho_b)}{\rho_s m_v}$	
δ_{eff}	Effective conductivity of soil [144]	$\delta_{eff} = \begin{cases} 0.0467 + 0.2204\rho_b - 0.4111S + 0.6614C \\ \qquad 0.3\,\text{GHz} \le f \le 1.4\,\text{GHz}\ . \\ -1.645 + 1.939\rho_b - 2.25622S + 1.594C \\ \qquad 1.4\,\text{GHz} \le f \le 18\,\text{GHz} \end{cases}$	ρ_b is bulk density
τ_d	Arrival time of direct component	$\tau_d = (\delta_s/S)$	S is speed of wave in soil
τ_r	Arrival time of reflected component	$\tau_r = 2 \times (\delta_s/S)$	S is speed of wave in soil
τ_l	Arrival time of reflected component	$\tau_l = 2 \times (\delta_s/S) + (\delta_a/c)$	S is speed of wave in soil C is speed of wave in air
α_{d0}, α_{r0}, α_{l0},	Gains of the three main components	$\alpha_{d0} = P_t + 20\log_{10}\lambda_s - 20\log_{10} r_1 - 8.69\alpha_s r_1$ $-22 + 10\log_{10} D_{rl}$ $\alpha_{r0} = P_t + 20\log_{10}\lambda_s - 20\log_{10} r_2 - 8.69\alpha_s r_2$ $+20\log_{10}\Gamma - 22 + 10\log_{10} D_{rl}$ $\alpha_{l0} = P_t + 20\log_{10}\lambda_s - 40\log_{10} d - 8.69\alpha_s(h_t + h_r)$ $+20\log_{10} T - 22 + 10\log_{10} D_{rl}$, See also analysis from Table VI.	μ and σ
α_{di}, α_{rj}, α_{lk}	Path amplitudes of the three components	$\alpha_{li} = \alpha_{l0}e^{-(i-\tau_L)/\gamma_L}\ \forall,\ i > \tau_l$ *and* $i < \tau_l + L$ $\alpha_{dj} = \alpha_{d0}e^{-(j-\tau_D)/\gamma_D}\ \forall,\ j > \tau_d$ *and* $j < \tau_d + D$ $\alpha_{rk} = \alpha_{r0}e^{-(k-\tau_R)/\gamma_R}\ \forall,\ k > \tau_r$ *and* $k < \tau_d + R$	

Next, number of significant paths are determined. Number of multipaths L, D, and R in each of the components are determined by setting a gain threshold (paths within 30 dB from peak). Multipath generation in a particular component is stopped once the path amplitude in that bin falls below the threshold value. This results in larger number for the sandy soils, and lower number of multipaths for silt loam, and silty clay loam soils which is also in good agreement with empirical observations. Moreover, this number being an indicator of the channel spread, also depends on the soil moisture. Higher soil moisture leads to lower spread, and on the other hand lower soil moisture decrease attenuation, which leads to emergence of higher number of multipaths falling above the threshold value and higher number of multipaths. A realization of underground channel impulse response model is shown in Fig. 5.4. Model parameters are shown in Table 5.1.

Up to this point, α_l, α_d, α_r are calculated based on the delays within lateral, re-

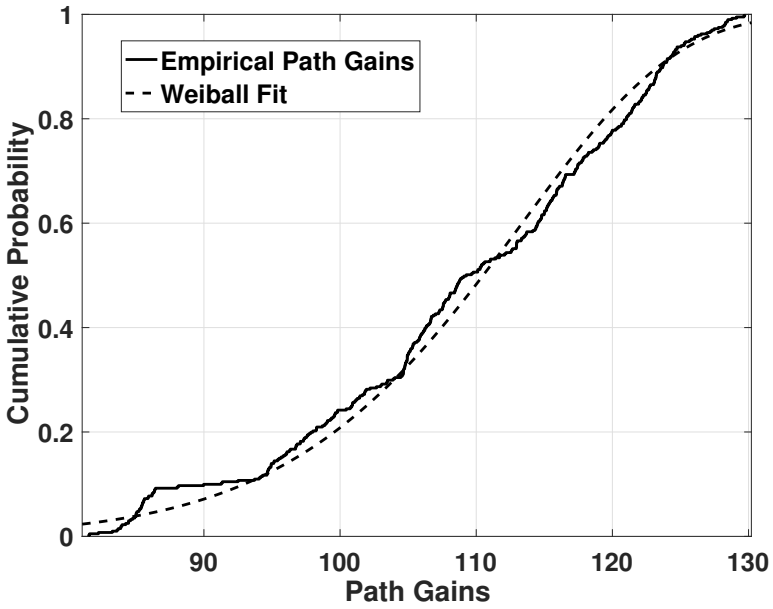

Figure 5.5: Amplitude gains with Weibull distribution fit.

flected, and direct components which depends on the exponential decay of multipath with respect to the main path gain in each component. This is a good realization of physical measurements. However, if we normalize the path gains with each components by average of these gains such that $\alpha_{li}/\bar{\alpha_{li}}$, $\alpha_{dj}/\bar{\alpha_{dj}}$, and $\alpha_{rk}/\bar{\alpha_{rk}}$, then, these amplitudes become independent of the delays to which these are associated [160]. Accordingly, a commutative distribution of path gains normalized through this process

Algorithm 1 UG Channel Impulse Response Simulation

Initialization :
Input soil parameters
Obtain the soil moisture level
BEGIN
Generate decay exponents for the lateral, direct, and reflected components
Determine the arrival time
Calculate the first multipath gain of each of the three components
Generate multipaths and impulse response
END

is shown in Fig. 5.5, which follows the Weibull probability distribution.

5.4 Model Evaluation

Model parameters required to evaluate the statistical model are summarized in the Table 5.1. In the numerical evaluation, first, we need to find the the α_{li}, α_{dj}, α_{rk} and their associated delays τ_{li}, τ_{di}, τ_{ri}. After generating the delays and amplitudes of these three components, other impulse response parameters are found and compared with the measurement data. An algorithm to generate UG channel impulse response is shown in Algorithm 1.

Simulation algorithm takes soils parameters such as soil type, and soil moisture as input and calculates the arrival times of the direct, reflected, and lateral components, τ_d, τ_r and τ_d by using the (4.8) to (4.10). Based on the soil type, peak power gains τ_{d0}, τ_{r0}, τ_{l0}, are determined from the [158, Table VI]. Model parameters for peak amplitude, delays, and number of multipaths statistics for direct, lateral and reflected components for three soil types are given in [158, Table VI].

Different statistical parameters computed from the measurement data, and the channel model numerical evaluations are compared in Table 5.2. UG channel is evaluated numerically using the the statistical model. The RMS delay spread and the coherence bandwidth parameters are derived and compared with the parameters obtained through experimental data. Model prediction error for RMS delay spread is 14.67%, and for the the coherence bandwidth, it is 14.08%. It can be observed that the difference in predicted and measured values, which is due to model uncertainty and observational error, is less than 15%. Overall, the developed statistical model shows a good agreement with the empirical data, and statistics of the coherence bandwidth and RMS delay spread prove the validity of the statistical model.

Table 5.2: Validation of impulse response model parameters.

Impulse Response Parameter	**Measured**	**Modeled**
RMS Delay Spread (τ_{rms})	45.52 ns	38.84 ns
Coherence Bandwidth	439 kHz	514 kHz

5.5 Empirical Validation

A good statistical model should be able to simulate the empirical measurements with higher accuracy. Moreover, simulated response must have the same characteristics as of the measurements results. In this section, arrival of multipath components is validated with experiments conducted in the indoor testbed (Chapter 3). Moreover, the shape of the PDP is presented and physical interpretations are discussed.

Based on (4.8), (4.9) and (4.10), the speed of the wave in all three soils is found by calculating the refractive indices n based on particle size distribution and classification of soils given in (Chapter 3). The results of these calculations are shown in Chapter 4. In Fig. 5.6, a measured PDP for a silt loam at 40 cm depth is compared with a schematic representation of the 3-wave model for T-R separation of 50 cm. Analysis of arrival time of three components reveals that for 50 cm distance and all burial depths, lateral waves arrive later than the direct wave except for the 10 cm depth where lateral wave reaches the receiver first. It can be observed that measurement data shows a strong agreement with the model.

From Fig. 5.6, it can also be observed that lateral component is the strongest component than the direct and reflected components. This is because direct and reflected components are spherical waves, propagating radially outward from the antenna, whereas, the lateral component is, initially, a plane wave that travels upward from the source to the boundary, then horizontally as a cylindrical wave, and subsequently travels backward as a plane wave from boundary to the point of observation.

The proposed model is applicable to heterogeneous smart lighting scenarios. However, in order to improve the model, it is important to further understand the spe-

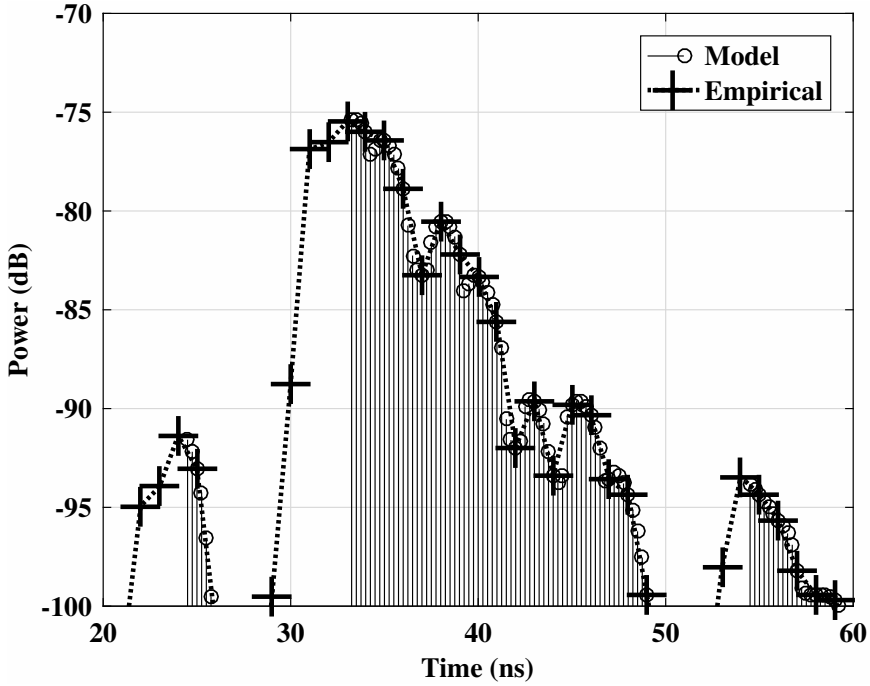

Figure 5.6: Comparison of model and empirical impulse response in silt loam.

cialized smart lighting requirements for a particular environment IOUT deployment. Accordingly, tailored sensing, control, and communication strategies can be exploited.

5.6 Conclusion

In this chapter, we presented an application of the IOUT to the smart lighting. We analyzed the UG channel data, collected through extensive measurements in the indoor and a field testbed. Accordingly, a statistical impulse response model of underground channel in IOUT communications is developed and validated through empirical evaluations. Power delay profile data from the measured delay profiles is analyzed and model statistics are developed. The model is capable of generating the wireless underground channel impulse response for different soils under different soil moisture conditions. It also accurately captured the delay spread and coherence bandwidth statistics. This statistical model serves as an important characterization tool for the

UG channel, and gives practical insight for design of a smart lighting IOUT communications system.

Chapter 6

Impacts of Soil Type and Moisture on the Capacity of Multi-Carrier Modulation in Internet of Underground Things

Unique interactions between soil and communication components in wireless underground communications necessitate revisiting fundamental communication concepts from a different perspective. In this chapter, capacity profile of wireless underground (UG) channel for multi-carrier transmission techniques is analyzed based on empirical antenna return loss and channel frequency response models in different soil types and moisture values. It is shown that data rates in excess of 124 Mbps are possible for distances up to 12 m. For shorter distances and lower soil moisture conditions, data rates of 362 Mbps can be achieved. It is also shown that due to soil moisture variations, UG channel experiences significant variations in antenna bandwidth and coherence bandwidth, which demands dynamic subcarrier operation. Theoretical analysis based on this empirical data show that by adaption to soil moisture variations, 180% improvement in channel capacity is possible when soil moisture decreases. It is shown that compared to a fixed bandwidth system; soil-based, system and sub-carrier bandwidth adaptation leads to capacity gains of 56%-136%. The analysis is based on indoor and outdoor experiments with more than $1,500$ measurements taken over a period of 10 months. These semi-empirical capacity results provide further evidence on the

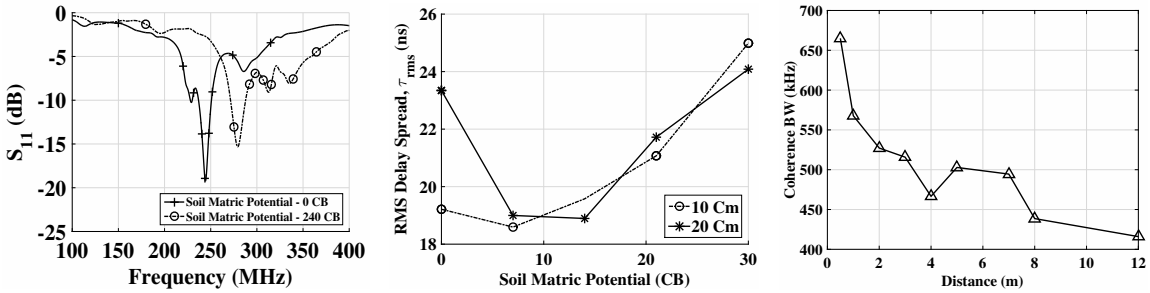

(a) (b) (c)

Figure 6.1: (a) Antenna return loss with change in soil moisture at 40 cm depth in sandy soil, (b)RMS delay spread vs. soil moisture at 50 cm distance in silty clay loam soil (greater matric potential values indicate lower soil moisture and zero matric potential represents near saturation condition), (c) Coherence bandwidth as a function of distance at transmitter receiver depth of 20 cm in silty clay loam soil.

potential of underground channel as a viable media for high data rate communication and highlight potential improvements in this area.

Internet of underground things (I-OUT) are types of networks, where communication is carried out through the underground sensors buried in the soil. I-OUTs are emerging from the recent prevalence and widespread use of wireless underground sensor networks (WUSNs) and has applications in many areas including environment and infrastructure monitoring [39], [96], [136], [177], [186], border patrol [40], and precision agriculture [76], [166]. These developments underscore the need of high data rates and makes it vital to determine the capacity limits of the wireless underground channel.

6.1 Motivation

The ultimate potential of IOUTs for high data rate communication depends on the underground channel characteristics, which are not well modeled. Therefore, experimentation is required to characterize its nature. Furthermore, interactions between soil and communication components, including antenna and wireless underground

channel, result in unique performance characteristics in I-OUTs. Three components i.e., direct, reflected and lateral waves are observed as major propagation components of the underground channel. Based on the depth and distance between transmitter and receiver, these components are received with different delays. These delays in different components result in fading envelope of the received signal being decorrelated or partially decorrelated. In addition, variations in amplitude and phase of the received signal are observed. We provide three distinct examples in this chapter, based on empirical measurements, on the effects of soil on antenna bandwidth and coherence bandwidth of the underground channel and discuss challenges faced in the design of an underground communication system.

Soil type, soil moisture, burial distance, and depth effect the communication performance [200], leading to dynamic changes in antenna return loss, channel impulse response, and root mean square (RMS) delay spread. In Fig. 6.1(a), empirical antenna return loss with change in soil moisture has been shown at a 40 cm depth in sandy soil. It can be observed that resonant frequency of antenna changes from 244 MHz to 289 MHz when soil matric potential (inversely proportional to soil moisture) changes from 0 CB to 240 CB. This significant change of 45 MHz necessitates a dynamic change in operation frequency with soil moisture to achieve maximum system bandwidth [74]. Similarly, with a decrease in soil moisture, antenna bandwidth, defined as the frequency range where the return loss is less than -10 dB, has increased from 14 MHz to 20 MHz. Accordingly, soil moisture also impacts available system bandwidth.

Variations in RMS delay spread with soil moisture is another impairment in the underground communication system. In Fig. 6.1(b) the change in RMS delay spread with soil moisture is shown at a 50 cm distance, and 10 cm and 20 cm depths in silt loam [158]. It can be observed that RMS delay spread decreases first as soil moisture

is decreased from near-saturation (0 CB) to 8 CB. Then, a consistent increase in delay spread is observed. The delay spread prohibits higher data rate communication in the underground channel which is in contrast to over the air wireless communication systems where higher data rates can be achieved by increasing the bandwidth and by employing higher order modulation schemes. Symbol rate of the channel depends on delay spread of the underground channel leading to keep the rate less than or equal to the inverse of the delay spread in order to avoid inter symbol interference. These variations, which may occur within a short span of time due to external impacts such as rain or irrigation, causes the wireless underground channel to be frequency-selective. Due to these variations in channel impulse response, frequency response, and coherence bandwidth, underground communications exhibits inter-symbol interference (ISI). In general, to overcome ISI, multi-carrier modulation has generally been considered as favorable approach for signal transmission. Accordingly, signal bandwidth of each sub-channel can be kept below the coherence bandwidth of the channel. Hence considerable performance improvements and throughput gains can be made in an underground communication system.

Moreover, the coherence bandwidth of the underground channel also needs to be considered for system design. The coherence bandwidth statistics (for 90% signal correlation based on root mean square delay spread) are shown as a function of distance in Fig. 6.1(c). It can be observed that the coherence bandwidth ranges from 411 kHz to 678 kHz for distances up to 12 m. More details on the impulse response and coherence bandwidth statistics of the wireless underground channel can be found in Chapter 4. The resulting small coherence bandwidth prohibits high data rate communication in underground channel using single carrier techniques. The dynamic and significant changes in coherent bandwidth, however, suggests that fixed-bandwidth operation, even with multi-carrier techniques may not be the best approach.

Given these spatio-temporal variations in soil moisture, RMS delay spread, and coherence bandwidth statistics at different burial depths and distances, it is desirable to find a design of underground communication system which have the potential and flexibility of adjustments in response to these soil dynamics. Above mentioned impairments could be overcome by designing a communication system which uses sub-channel based multi-carrier data communication approach in the underground channel. In this design, available system bandwidth is divided into sub-carriers and a small bandwidth of system is occupied by each sub-carrier. The subcarrier bandwidth depends on the delay spread of the underground channel and needs to be in proportion to the delay spread of the channel in order to solve the issues caused by the delay spread impairments. However, an underground multi-carrier communication system designed on a fixed sub-carrier bandwidth may experience inter carrier interference (ICI) [66]. ICI is caused by time-varying coherence bandwidth channel statistics due to soil moisture variations. To mitigate ICI resulting from time-varying coherence and fixed subcarrier bandwidths, transmission parameters should be adjusted by setting bandwidth of subcarriers to the coherence bandwidth.

By using multi-carrier modulation, we have investigated the impacts of soil moisture and soil type on wireless underground channel by adapting coherence bandwidth changes intrinsic to soil moisture variations and hence adapting the system and subcarrier bandwidth accordingly. These factors have significant impact on the performance of data communications in the underground channel and should be considered for design of an efficient underground communication system.

To the best of our knowledge, this is the first work on the capacity of UG channel based on multi-carrier modulation and empirical channel parameters. These parameters include return loss, channel transfer function, and coherence bandwidth in different soil types. Results of capacity limits of UG channel highlight the potential

of high data rate communication in UG channel and support the use of soil-based adaptation in the underground channel.

The rest of the chapter is organized as follows: the related work is discussed in Section 6.2. Measurement setup and experiment details are presented in Section 6.3. UG capacity model by using multi-carrier modulation is given in Section 6.4. Results and factors affecting the UG channel capacity are discussed in Section 6.5. Performance comparison of the proposed approach is given Section 6.6. We conclude in Section 6.7.

6.2 Related Work

Wireless communication in underground channel is an evolving field and extensive discussion of channel capacity does not exist in the literature. Capacity of underground channel using magnetic induction (MI) techniques has been discussed in [125], [130], [136], [178], [179]. Magnetic induction techniques have several limitations. Signal strength decays with inverse cube factor and high data rates are not possible. Moreover, in MI, communication cannot take place if sender receiver coils are perpendicular to each other. Network architecture cannot scale due to very long wavelengths of the magnetic channel. Therefore, due to these limitations and its inability to communicate with above-ground devices, this approach cannot be readily implemented in I-OUTs.

Underwater communication [47], [147] has similarities with the wireless underground communication due to the challenged media. However, acoustic communication techniques are primarily used under water. This technique is impractical in underground due to vibration limitations. Acoustic propagation experiences low physical link quality and higher delays due to lower speed of sound. Bandwidth is distance

dependent and only extremely low bandwidths are achieved. Moreover, other limitations, such as size and cost of acoustic equipment, and challenging deployment restrict the use of this approach in the wireless underground sensor networks.

Channel models for UG communication have been developed in [75], and [200] but empirical validations have not been performed. Proof-of-concept integration of wireless underground wireless sensor networks with precision agriculture cyber-physical systems (CPS) and center-pivot systems has been presented in [76], [166]. In [165], [163], empirical evaluations of underground channel are presented, however, antenna bandwidth was not considered. Capacity of single-carrier communication in the UG channel has been investigated in [74] but the analysis does not consider a practical modulation scheme and empirical validations have not be provided.

In Chapter 4, we have presented a detailed characterization of coherence bandwidth of the underground channel. The development in this chapter builds upon the analysis in Chapter 4 to design an underground multicarrier communication system. To the best of our knowledge, this is the first work to analyze the capacity of multicarrier modulation in the UG channel based on empirical measurements of channel transfer function, coherence bandwidth, and antenna return loss under three different soil types and various soil moisture conditions.

6.3 Experiment Methodology

Capacity of UG channel is affected by soil texture, soil moisture, distance, and depth variations [74]. We present a detailed analysis of the impact of these factors on channel capacity by taking extensive measurements in the indoor testbed (Section 3.2.1) and a field testbed (Section 3.2.2) with three distinct types of soils (silty clay loam, sandy soil, and silt loam) and under different soil moisture conditions. Thus, we have

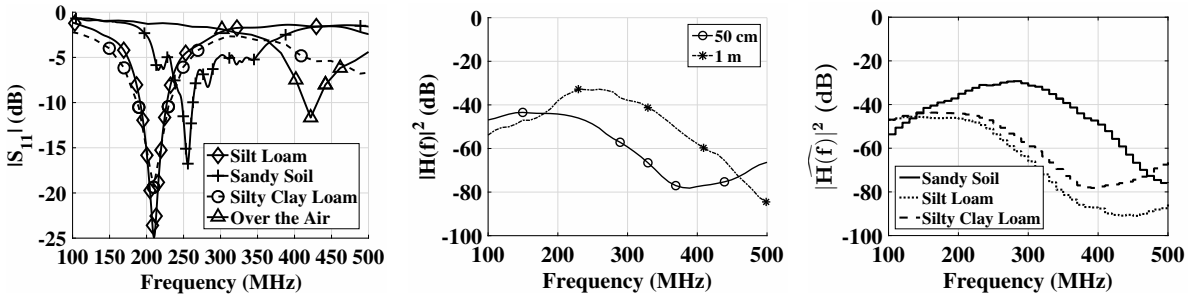

(a) (b) (c)

Figure 6.2: (a) Return loss of the antenna at 0 CB soil matric potential, (b) Channel transfer function in sandy soil, (c) An approximation of channel transfer function through staircase function at transmitter receiver depth of 20 cm and distance of 50 cm.

considered several possible scenarios with more than $1,500$ measurements taken over a period of 10 months.

Experiments: Sensors in I-OUT applications are usually buried in topsoil and subsoil layers[1] [129], [164]. Therefore, for underground channel experiments, we have taken measurements for depths of 10 cm to 40 cm with transmitter-receiver (T-R) distances of 50 cm to 12 m. Near-field effects of underground antenna for frequency range used in these experiments are within the 30 cm region.

Frequency response and return loss of the channel are measured using a Agilent FieldFox N9923A Vector Network Analyzer (VNA). Use of VNA for channel measurements have been studied extensively in [55, 101], [107], [150], [160], [176].

The first set of experiments is conducted in the indoor testbed in silt loam soil. Return loss, channel transfer function, and impulse response measurements are recorded at T-R distances of 50 cm and 1 m, and for depths of 10 cm, 20 cm, 30 cm and 40 cm. The soil moisture range for these experiment is recorded in terms of matric potential values in the range of 0-50 CB, where greater matric potential values indicate lower soil moisture and zero matric potential represents near saturation condition.

[1]Topsoil layer (root growth region) consists of top 1 Feet of soil and $2-4$ Feet layer below the topsoil is subsoil.

The second set of experiments is also conducted in the indoor testbed in sandy soil. Soil moisture range for these experiment is 0-250 CB. Return loss, channel transfer function, and impulse response measurements are taken at the same T-R distances and depths as the first set of experiments. The third set of experiments is conducted in the field testbed in silty clay loam soil. Return loss, channel transfer function, and impulse response measurements are taken at T-R distances of 50 cm to 12 m, and at a depth of 20 cm.

6.4 Capacity Model

To evaluate the capacity of underground channel, we consider the bandwidth of sender-receiver antenna pair along with channel transfer function of UG channel, because channel capacity changes with bandwidth [148]. Bandwidth is determined from the return loss of antenna, which is a measure of the efficacy of power delivery from the transmission system to the antenna. Impedance mismatch gives rise to the return loss which is defined as [49]:

$$RL_{dB} = 20 \log_{10} \left| \frac{Z_s + Z_a}{Z_s - Z_a} \right| , \tag{6.1}$$

where Z_s and Z_a are the transmission line and antenna impedance, respectively.

The return loss of an antenna in three different soils at zero soil matric potential (saturated conditions) is shown in Fig. 6.2(a). The bandwidth of an antenna is traditionally calculated based on its return loss values below a threshold, δ, value. In the literature, -10 dB is generally used as the threshold value [49]. For the bandwidth analysis, we assume that the sender and receiver have the same return loss[2]. It is

[2]Because of short distances and spatial homogeneity in soil, probability of major differences between sender and receiver return loss, and in resonant frequencies is very low.

also assumed that the system is operating at the antenna resonant frequency, which maximizes the bandwidth [74]. Accordingly, the bandwidth of an underground system operating at the underground antenna resonant frequency is defined as [74]:

$$B_s = \begin{cases} 0 & \text{if -}R(f) > \delta, \\ 2(f - f_m) & \text{if -}R(f) \leq \delta \text{ and } f < f_r, \\ 2(f_M - f) & \text{if -}R(f) \leq \delta \text{ and } f \geq f_r, \end{cases} \tag{6.2}$$

where f_r is the resonant frequency, f_m and f_M are the lowest and highest frequency at which $R(f) \leq \delta$.

For multi-carrier modulation, the number of subcarriers can be calculated as the minimum number of subcarriers needed to avoid inter-symbol interference (ISI) based on the system bandwidth, B_s. Let B_{cb} denote the coherence bandwidth of underground channel[3]. Then, the number of subcarriers is given as:

$$N_c = \left\lceil \frac{B_s}{B_{cb}} \right\rceil. \tag{6.3}$$

To express the UG channel capacity, we assume m-ary quadrature amplitude modulation (MQAM) for each carrier of multi-carrier transmission system because of its higher spectral efficiency [134].

Given a total number of subcarriers, N_c, and bandwidth of each subcarrier B_{cb}, the overall underground channel bit rate is given as:

$$R_{ug} = \sum_{i=1}^{N_c} r_i B_{cb}, \tag{6.4}$$

[3]In our analysis of underground channel capacity we have used empirical coherence bandwidth values obtained from time domain impulse response measurements taken in field and testbed settings.

where r_i is the number of bits per symbol in each carrier.

At high SNR , the symbol-error probability, P_{sc_i}, for the ith carrier is given as [117]:

$$P_{sc_i} = K_{r_i} Q\left(\sqrt{\frac{3En}{(M_i - 1)N_0}}\right), \tag{6.5}$$

where the value of the constant K_{r_i} depends on the number of bits in each symbol and can take values in the range of $2 \leq K_{r_i} < 4$.

$$\sum_{i=1}^{N_c} \gamma_i \cdot P = P, \quad \gamma_i > 0. \tag{6.6}$$

The bit rate of the underground channel, R_{ug}, can be maximized by optimizing power allocation between all subcarriers based on a target probability of symbol error of each subcarrier, $P_{sc}^* > P_{sc_i}$, $\forall i$, and a fixed power constraint, P.

In Fig. 6.2(b), empirical channel transfer functions at 50 cm and 1 m distances in sandy soil are shown. For multi-carrier transmission, the channel transfer function is approximated by a step (staircase) function $\widehat{|H(f)|^2}$, because for smaller B_{cb}, staircase function gives close approximation of channel transfer function $|H(f)|^2$. An approximation of channel transfer function through staircase function in sandy soil at transmitter receiver depth of 20 cm and distance of 50 cm is shown in Fig. 6.2(c). Then the overall bit rate is obtained by summing over all subcarriers [117]:

$$R_{ug} = \sum_{i=1}^{N_c} B_{cb}\ log_2 \left\{ 1 + \frac{\frac{3\gamma_i P}{(N_0 B_{cb})|H_i(f)|^2}}{\left[Q^{-1}\left\{\frac{P_{sc}^*}{K_{r_i}}\right\}\right]^2} \right\}, \tag{6.7}$$

where N_c is the number of subcarriers from (6.3), P is transmit power constraint, and

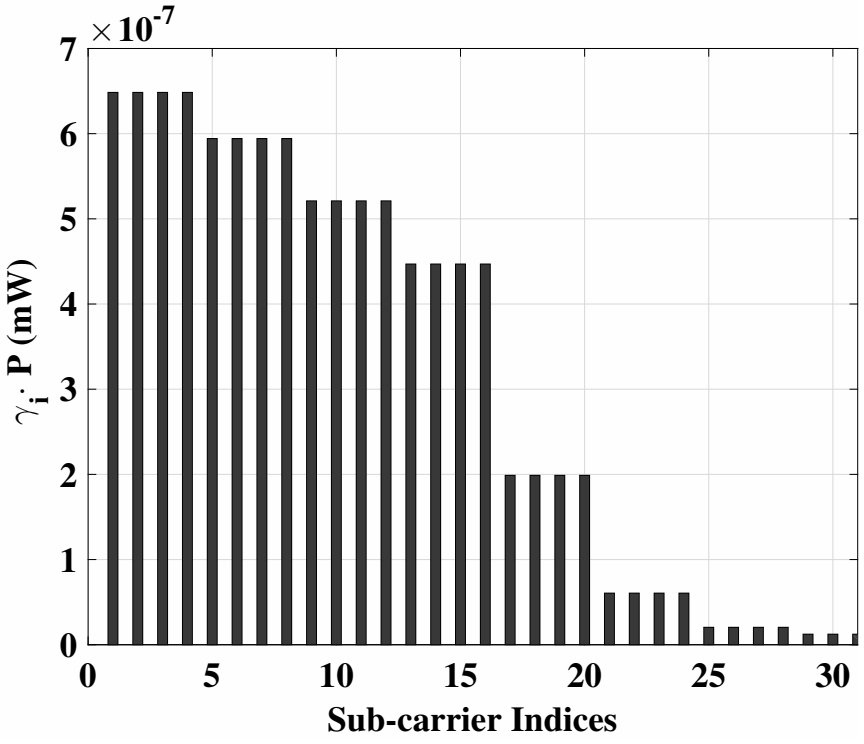

(a)

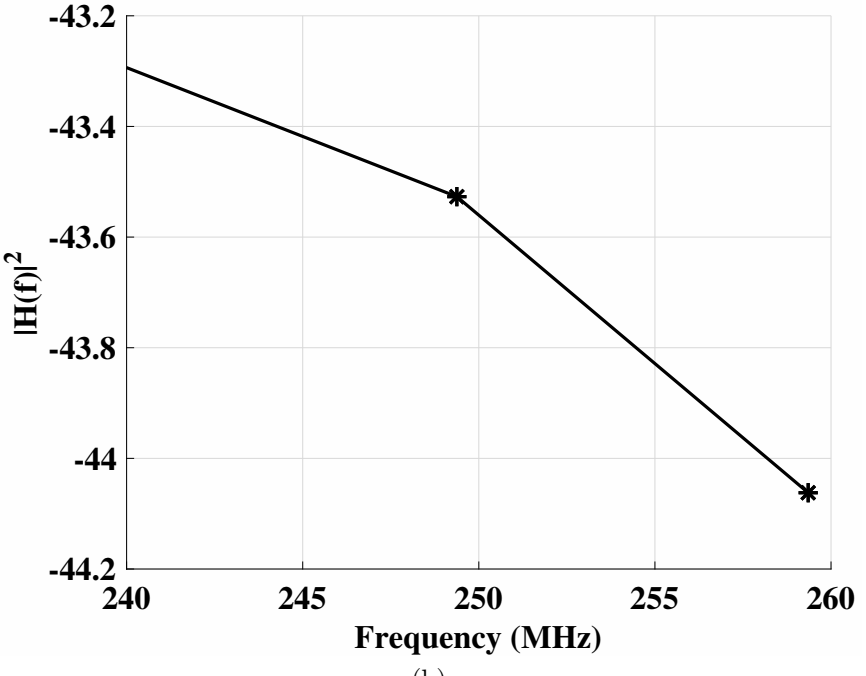

(b)

Figure 6.3: (a) γ_i's for channel frequency response in silt loam soil for T-R distance of 50 cm at 20 cm depth, (b) Corresponding channel tranfer function.

γ_i's are given such that:

$$\sum_{i=1}^{N_c} \gamma_i = 1, \quad \gamma_i > 0. \tag{6.8}$$

The UG channel bit rate, R_{ug}, is maximized by optimizing the power distribution over all subcarriers. The solution to this optimization problem [151], [213] is similar to water filling of [63, chap. 9], [59]. Accordingly, the optimum power allocation, γ_i^*, is obtained by using a Lagrangian multiplier, λ, which leads to water-filling allocation [63]:

$$\gamma_i^* = \begin{cases} \lambda - \frac{1}{K_0 |H(f)_i|^2} & \text{if } \gamma_i > 0, \\ 0 & \text{otherwise,} \end{cases} \tag{6.9}$$

where $\sum_{i=1}^{N_c} \gamma_i^* = 1$, and $K_0 = 3P/(N_0[Q^{-1}[.]^2)$. By jointly solving (6.8) and (6.9) the maximum bit rate is obtained as [117]:

$$R_{ug}^{\max} = \sum_{i=1}^{N_c} B_{cb} \ \cdot \ log_2 \left\{ \lambda K_0 |H_i(f)|^2 \right\}, \tag{6.10}$$

where the maximization applies to the high-SNR cases. Thus, we denote this rate as *high-SNR optimal*.

A sub-optimal solution, of allocating equal power to subcarriers, has been shown to achieve capacity close to the optimal solution [60], [151]. To compare with (6.10), the underground bit rate of equal power allocation is given as:

$$R_{ug}^{eq} = \sum_{i=1}^{N_c} B_{cb} \ log_2 \left\{ 1 + \frac{\frac{3P/N_c}{(N_0 B_{cb}) |H_i(f)|^2}}{\left[Q^{-1} \left\{ \frac{P_{sc}^*}{K_{r_i}} \right\} \right]^2} \right\}, \tag{6.11}$$

which we denote as *equal power* in the following. In the next section, the results and impacts of different factors on the underground channel are discussed.

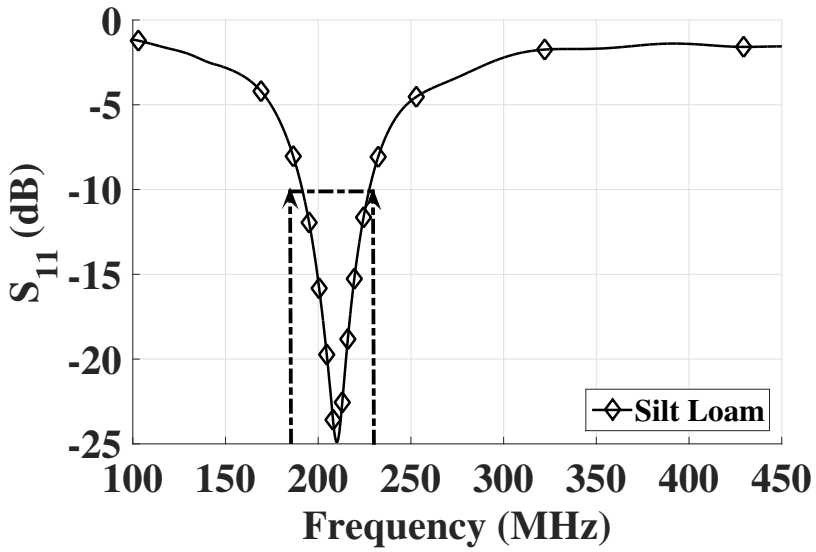

Figure 6.4: The bandwidth of the antenna in silt loam.

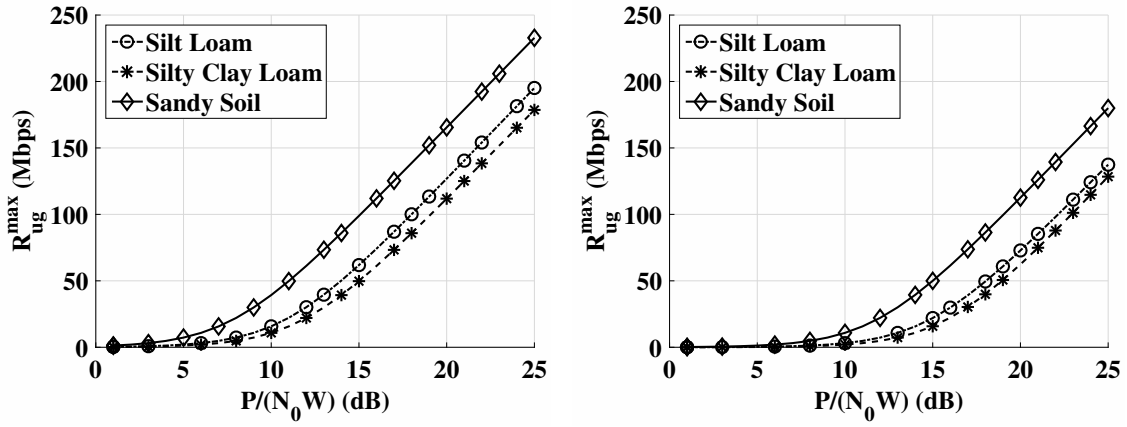

(a) 50 cm (b) 1 m

Figure 6.5: Capacity in three different soils. Bandwidth is 20 MHz. Transmitter receiver depth of 20 cm and distance of: (a) 50 cm, where the number of subcarriers in the sandy, silty clay loam, and silt loam soils are 25, 25, and 24, respectively, (b) 1 m, where these are 27, 21, and 25, respectively.

6.5 Results and Discussions

The performance of a communication system is generally evaluated under the probability of bit error rate constraints for a specified data rate and SNR values. However, transmission power is limited in underground nodes due to energy constraints to achieve longer operation periods [192]. Therefore, in wireless underground channel,

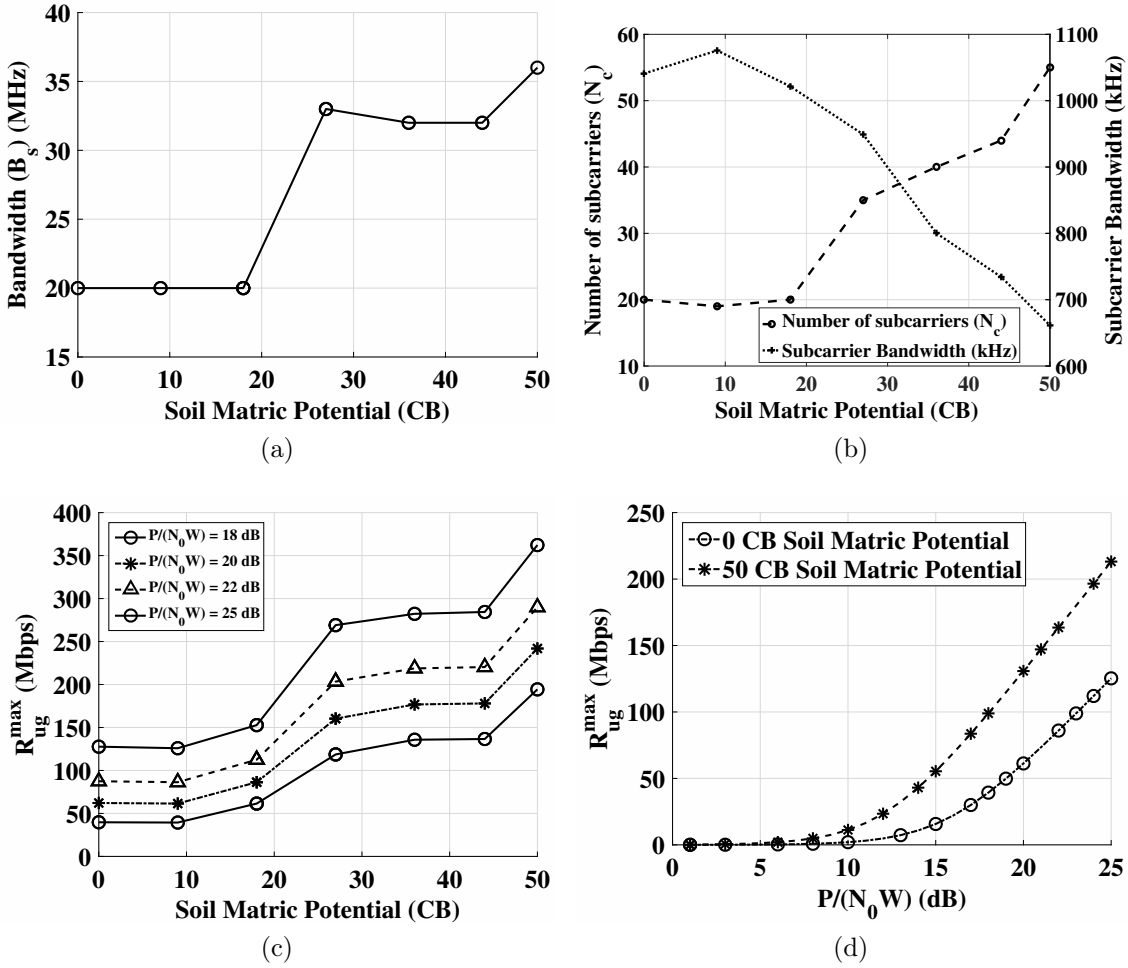

Figure 6.6: Effects of change in soil moisture in silt loam soil: (a) System bandwidth with soil moisture, (b) Number of subcarriers with soil moisture, (c) Rate with soil moisture, (d) Capacity in sandy soil at transmitter receiver depth of 20 cm and distance of 50 cm.

it is useful to determine achievable data rate for a fixed BER and under low power transmission power requirements. By using (6.3), we have determined the minimum number of subcarriers required to avoid ISI based on coherence bandwidth analysis.

In Fig. 6.3(a), high-SNR optimal $\gamma_i \cdot P$ values are shown for a channel frequency response in sandy soil (Fig. 6.3(b)) for transmitter receiver distance of 50 cm at 20 cm depth. It can be observed that optimized power distribution closely follows the channel transfer function curve. To maximize the rate, we have set K_{r_i} to 2 and P_{sc}^* to 10^{-5}, with $P/(N_0W)$ given. $P/(N_0W)$ represents the signal-to-noise ratio (SNR).

In Fig. 6.4, an example of the bandwidth calculation of an antenna operating at resonant frequency in silt loam soil is shown for $\delta = -10\,\text{dB}$, where S_{11} is shown as a function of frequency. The minimum frequency, f_{min} is 191.2 MHz and the maximum frequency, f_{max} is 227.91 MHz, results in a bandwidth of 36.71 MHz.

In Section 6.5.1, we present the effects of soil texture on the capacity of underground channel with measurements recorded in three different soil types. Impacts of soil moisture on UG channel capacity are discussed in Section 6.5.2 and the effects of underground T-R distance on the channel capacity are analyzed in Section 6.5.3.

6.5.1 Soil Texture and Channel Capacity

In Figs. 6.5, multi-carrier capacity of UG channel in three different soil types is compared at distances of 50 cm and 1 m. At 50 cm, sandy soil has 30 % higher capacity compared to silt loam and silty clay loam soil. The system bandwidth in all three soils is measured as 20 MHz. Capacity in sandy soil is 233 Mbps. In silt loam, 195 Mbps capacity is achieved, and in silty clay loam data rates up to 178 Mbps are possible. When the distance increases from 50 cm to 1 m, capacity in sandy soil decreases from 233 Mbps to 180 Mbps (22% decrease). Similarly in silt loam soil capacity has decreased from 195 Mbps to 137 Mbps (29% decrease) and in silty clay loam soil it has decreased from 178 to 129 Mbps (27% decrease).

In soil, electromagnetic waves experience attenuation, which varies with soil texture and bulk density [69]. Attenuation of EM waves in soil depends on the water holding capacity, because water absorbs electromagnetic waves incident in the soil. Water holding capacity of fine-textured (silt-loam, silty clay loam) and medium-textured soils (fine sandy loam) is much higher, because of the small pore size (but, greater number of pores), as compared to coarse-textured (sandy, sandy loam, loamy sand) because of larger pore size (but less in number of pores) [85]. Therefore, the soils

containing the highest clay contents exhibit higher attenuation. It can be observed from Fig. 6.5 that silty clay loam soil, which has the highest clay content as compared to sandy and silty clay loam soils, has the lowest capacity. Decrease in capacity at 1 m as compared to 50 cm can be attributed to increase in attenuation with distance. At 1 m, the number of required subcarriers is larger because of decrease in the coherence bandwidth with distance (Fig. 6.1(c)). Waves traveling in underground channel reach the receiver through different paths in soil and air with different permittivity and conductivity. These properties affect the speed of wave propagation in soil and air. Therefore, as the distance increases, the delay spread increases which leads to decrease in the coherence bandwidth.

6.5.2 Soil Moisture and Channel Capacity

Traditionally, parameters in a multi-carrier modulated system are optimized under a fixed system bandwidth constraint [61], [151], [211], [215]. However, fixing the system bandwidth to the worst-case scenario in UG communication (e.g., 20 MHz) can lead to significant performance loss as soil moisture decreases. On the other hand, when soil moisture increases, decreasing the system bandwidth under fixed transmit power constraint may lead to improvement in SNR which would compensate the increase in attenuation due to higher soil moisture.

In Figs. 6.6(a)-6.6(b), antenna (system) bandwidth, coherence (subcarrier) bandwidth, and the number of subcarriers are shown as a function of soil moisture (expressed as soil matric potential[4]) in silt loam soil. It can be observed that with decrease in soil moisture, antenna bandwidth increases from 20 MHz to 36 MHz (80% increase).

[4]Greater matric potential values indicate lower soil moisture and zero matric potential represents near saturation conditions.

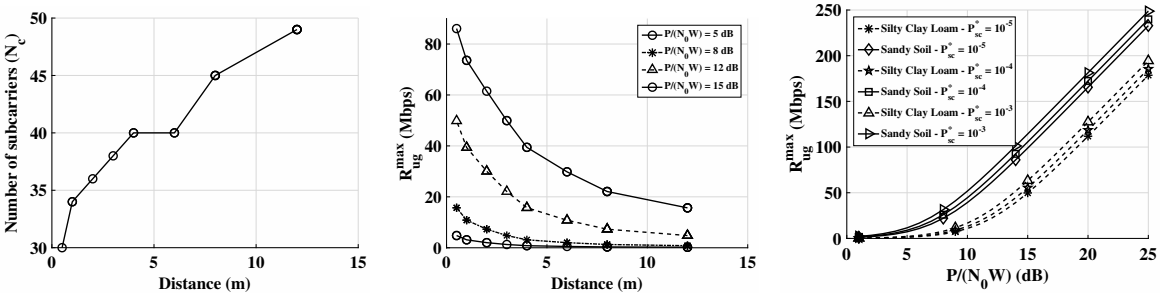

(a) (b) (c)

Figure 6.7: Effects of distance on underground channel capacity in silty clay loam soil: (b) Change in number of subcarriers (N_c) with distance for antenna bandwidth of 20 MHz and coherence bandwidth values shown in Fig. 6.1(c), (b) Rate with distance, (c) Capacity with different P^*_{sc} values in two different soils. Bandwidth is 20 MHz. Transmitter receiver depth of 20 cm and distance of 50 cm.

It can also be observed from Fig. 6.6(b) that coherence bandwidth decreases with decreasing soil moisture. By adjusting the sub-carrier bandwidth according to the coherence bandwidth of the channel, impacts of soil moisture on each carrier can be mitigated.

The number of subcarriers has increased from 20 to 55 when soil moisture changes from 0 CB to 50 CB.

From an implementation point of view, number of sub-carriers has to be 2^n. Moreover, hardware implementation of programmable FFT [88] can be used to adjust the bandwidth of each subcarrier under coherence bandwidth constraints. Accordingly, the number of subcarriers can be adjusted.

In Fig. 6.6(c), maximum rate in (6.10) is shown for silt loam soil as a function of soil moisture. It can be observed that for a $P/(N_0W)$ value of 18 dB, rate increases from 39 Mbps to 194 Mbps, when soil moisture decreases from 10 CB to 50 CB. For a similar change in soil moisture at $P/(N_0W) = 25$ dB, rate increases from 127 Mbps to 362 Mbps (185% increase). Similar results are observed for sandy soil as shown in Fig. 6.6(d), where for a decrease in soil moisture from 0 CB to 50 CB, capacity increases from 126 Mbps to 213 Mbps (69% increase). The significant gains highlight

the potential of adaptive communication approaches where soil moisture is tightly integrated into communication parameters.

Absorption of electromagnetic waves by soil water content protrude additional attenuation along with diffusion attenuation. This phenomena results because effective permittivity of soil is a complex number. Water held by soil in its pore space can be classified into bound water and free water. Bound water is strongly contained because of the effects of osmotic and matric forces [85] acting on it and is held in top few particle layers. Effect of osmotic and matric forces is diminished in lower soil layers causing unrestrained movement of water. Bound water causes more absorption of electromagnetic waves because of its low infiltration as compared to unrestrained water which can infiltrate and drain easily. Variations in soil moisture leads to variations in permittivity of soil due to which wavelength in soil fluctuates causing more attenuation of waves. It is evident from Fig. 6.6(c) and Fig. 6.6(d), that low water absorption of EM waves with decrease in soil moisture has contributed to the increase in capacity in both sandy and silt loam soils.

6.5.3 Distance and Channel Capacity

To analyze the effects of distance on channel capacity, we have conducted experiments in the field testbed in silty clay loam soil for antennas buried at 20 cm depth. In Fig. 6.7(a), change in the number of subcarriers (N_c) as a function of distance is shown. For the empirical 20 MHz antenna bandwidth, when distance increases from 50 cm to 12 m, the coherence bandwidth decreases from 678 kHz to 411 kHz. Hence, number of subcarriers for a fixed system bandwidth increases from 30 to 49. The decrease in coherence bandwidth with distance can be explained by RMS delay spread variations with distance.

Effects of increasing T-R distance on channel capacity are shown in Fig. 6.7(b).

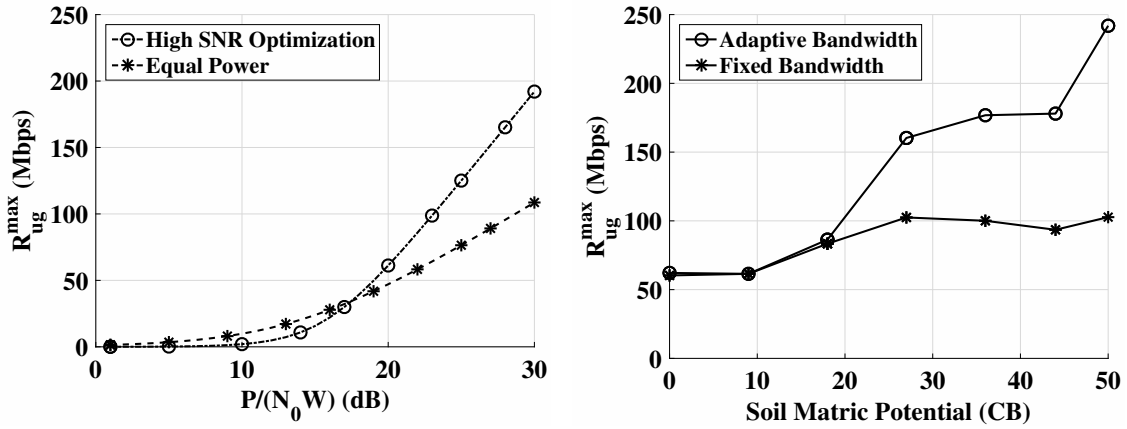

(a) (b)

Figure 6.8: (a) Comparison of higher SNR optimization with fixed power allocation in the silty clay loam soil. Transmitter receiver depth of 20 cm and distance of 1 m, (b) Comparison of fixed vs. adaptive system, and subcarrier bandwidth approaches with change in soil moisture in silt loam soil.

In Fig. 6.7(b), it can be observed that rates up to 80 Mbps can be achieved up to distance of 12 m. Capacity increases further up to 124 MHz for $P/(N_0W)$ value of 25 dB. For higher values of $P/(N_0W)$, it can be observed that capacity can be as high as 200 Mbps.

Communication in the underground channel is mainly carried out by three electromagnetic waves [75]. First, the line-of-sight wave (direct wave), from transmitter to receiver, which goes through the soil. Second, the wave which is reflected from soil-air interface (reflected wave) and its path is also through the soil. Third, a wave which goes along the soil surface (lateral wave) and reaches the receiver. When distance is increased, the effects of the direct and reflected wave diminish and only the lateral wave contributes significantly to the received signal power at the receiver. With further increase in distance, the lateral wave attenuates, decreasing the maximum rate.

6.6 Performance Comparisons

In Fig. 6.7(c), capacity under three different P_{sc}^{*} constraints in two soils (sandy soil and silty clay loam) is shown. P_{sc}^{*} values are changed from 10^{-5} to 10^{-3}. In sandy soil, when P_{sc}^{*} is increased to 10^{-3}, rate increases from 233 Mbps to 248 Mbps (6 % increase). Similarly, in silty clay loam, rate has increased from 178 Mbps to 194 Mbps (9 % increase).

In Fig. 6.8(a), the high-SNR optimal rate in (6.10) is compared with equal power rate in (6.11) in the silty clay loam soil. It can be observed that for low $P/(N_0W)$ values (i.e., less than 17 dB), equal power solution leads to slightly higher rates. However, for high $P/(N_0W)$ values, as expected [151], [61], high-SNR optimal solution performs better. For a $P/(N_0W)$ value of 25 dB, rate has increased from 76 Mpbs to 125 Mbps (64% increase).

It is also of interest to compare the adaptive system and subcarrier bandwidth approach with fixed system and subcarrier bandwidth technique. This comparison with fixed system bandwidth (20 MHz), and fixed subcarrier bandwidth (411 kHz) is shown in Fig. 6.8(b). It can be observed that at 27 CB soil moisture, fixed bandwidth approach has capacity of 102 Mpbs, whereas adaptive technique results in 56 % higher capacity (161 Mpbs). Similarly, this difference in capacity of both schemes is further increased at 50 CB soil moisture level where capacity of adaptive approach is 241 Mpbs, and hence leads to 136 % improvement in capacity.

6.7 Conclusions

In this chapter, we provide an analysis of the multi-carrier modulation capacity in underground channel in different soils through extensive empirical channel transfer function, and antenna return loss measurements. Impacts of different soil types on

channel capacity are investigated by conducting experiments in silt loam, sandy, and silty clay loam soils under different soil moisture conditions. Results reveal that soil type, moisture, and T-R distances have an impact on the capacity of multi-carrier modulation in the underground channel. Accordingly, system performance can be enhanced by adjusting transmission parameters such as subcarrier bandwidth based on these changing environmental phenomena. Significant performance improvements can be made by using adaptive channel width [57], [60] and adaptive subcarrier bandwidth (ASB) [66], [167] techniques. Based on our findings and analysis in this chapter, we can argue that an underground communication system using adaptive subcarrier bandwidth (ASB) approach is expected to enhance capacity of underground channel. This paves the way for adaptive communication approaches in the underground channel, where soil dynamics are tightly integrated with communication parameter selection.

Chapter 7

Smart Underground Antenna Arrays: A Soil Moisture Adaptive Beamforming Approach

Current wireless underground (UG) communication techniques are limited by their achievable distance. In this chapter, a novel framework for underground beamforming using adaptive antenna arrays is presented to extend communication distances for practical applications. Based on the analysis of propagation in wireless underground channel, a theoretical model is developed which uses soil moisture information to improve wireless underground communications performance. Array element in soil is analyzed empirically and impacts of soil type and soil moisture on return loss (RL) and resonant frequency are investigated. Accordingly, beam patterns are analyzed to communicate with underground and above ground devices. Depending on the incident angle, refraction from soil-air interface has adverse effects in the UG communications. It is shown that beam steering improves UG communications by providing a high-gain lateral wave. To this end, the angle, which enhances lateral wave, is shown to be a function of dielectric properties of the soil, soil moisture, and soil texture. Evaluations show that this critical angle varies from 0° to 16° and decreases with soil moisture. Accordingly, a soil moisture adaptive beamforming (SMABF) algorithm is developed for planar array structures and evaluated with different optimization approaches to

improve UG communication performance.

7.1 Motivation

Despite the recent developments in wireless underground (UG) communications [39], the communication ranges are still limited for many potential applications. Therefore, advanced techniques, which are designed based on the unique characteristics of the wireless UG channel, are required to extend the communication ranges. Soil properties and soil moisture significantly impact the UG communications (Chapter 4). This necessitates the adaption of parameters of the UG communication system based on the changing environment. Such adaption requires tight integration of soil sensing technologies with the communication devices to improve UG communication performance. For an UG antenna, change in soil moisture requires changing operation frequency and bandwidth to maintain high throughput and gain [74]. Similarly, to enhance UG communications ranges, maximum energy should be focused at a particular angle which should be determined dynamically according to ambient soil properties (Chapter 4). Due to these phenomena, the use of a high-gain fixed-directional antennas [187], which lack the capability to adjust their beam direction dynamically, may not result in ideal system performance. To this end, a soil moisture adaptive beamforming (SMABF) approach, based on antenna arrays, is developed in this chapter. SMBAF adjusts its parameters and beams the maximum energy at the desired angle based on ambient environmental conditions.

Many factors impact beamforming from UG antenna arrays. The distance that waves travel from each antenna element to reach the soil-air interface is different based on the array geometry. Change in index of refraction causes delay in the speed of beams. Soil moisture variations lead to change in the resonant frequency of antenna

elements. Bandwidth, return loss (RL), and reflection coefficients at the resonant frequency also change with soil moisture. Moreover, a reliable beamforming architecture requires deep understanding of the propagation in the wireless communication channel to exploit the nature of spatial properties of multipath components for an effective beamforming solution.

In addition to physical constraints, from a networking perspective, communication from an UG node to another UG node (UG2UG) and an aboveground node (UG2AG) require different beam shapes. In UG2UG communications, lateral wave is the most dominant component and travels along the soil-air interface [158, 200]. The lateral component has the potential, due to its lower attenuation, to reach higher distances. This lateral wave is formed and carries the most energy when antenna orientation is at a specific angle. This angle varies with variations in soil moisture and also depends on soil properties such as soil texture, and bulk density. On the contrary, for UG2AG communication, energy needs to be focused in the broadside to avoid refraction losses at the soil-air interface. Differences in wave propagation in these two links require different angles at which waves should be incident at soil-air interface. Due to these factors, adjustment of the phase at the UG antenna elements need phase alignment to add up coherently to avoid errors in beam steering.

To the best of our knowledge, this is the first work to propose soil moisture adaptive beamforming (SMABF) for UG communications. Antenna array structures buried underground are considered which communicate through soil and air. We analyze the UG channel impulse response model from a UG beamforming perspective. Challenges in UG beamforming are highlighted and use of soil adaptive beamforming approach is motivated. We present the effects of different soil properties on single antenna array element. The proposed mechanism estimates the best beam steering angle based on the soil moisture sensing. Next, based on the optimal angle, a steer-

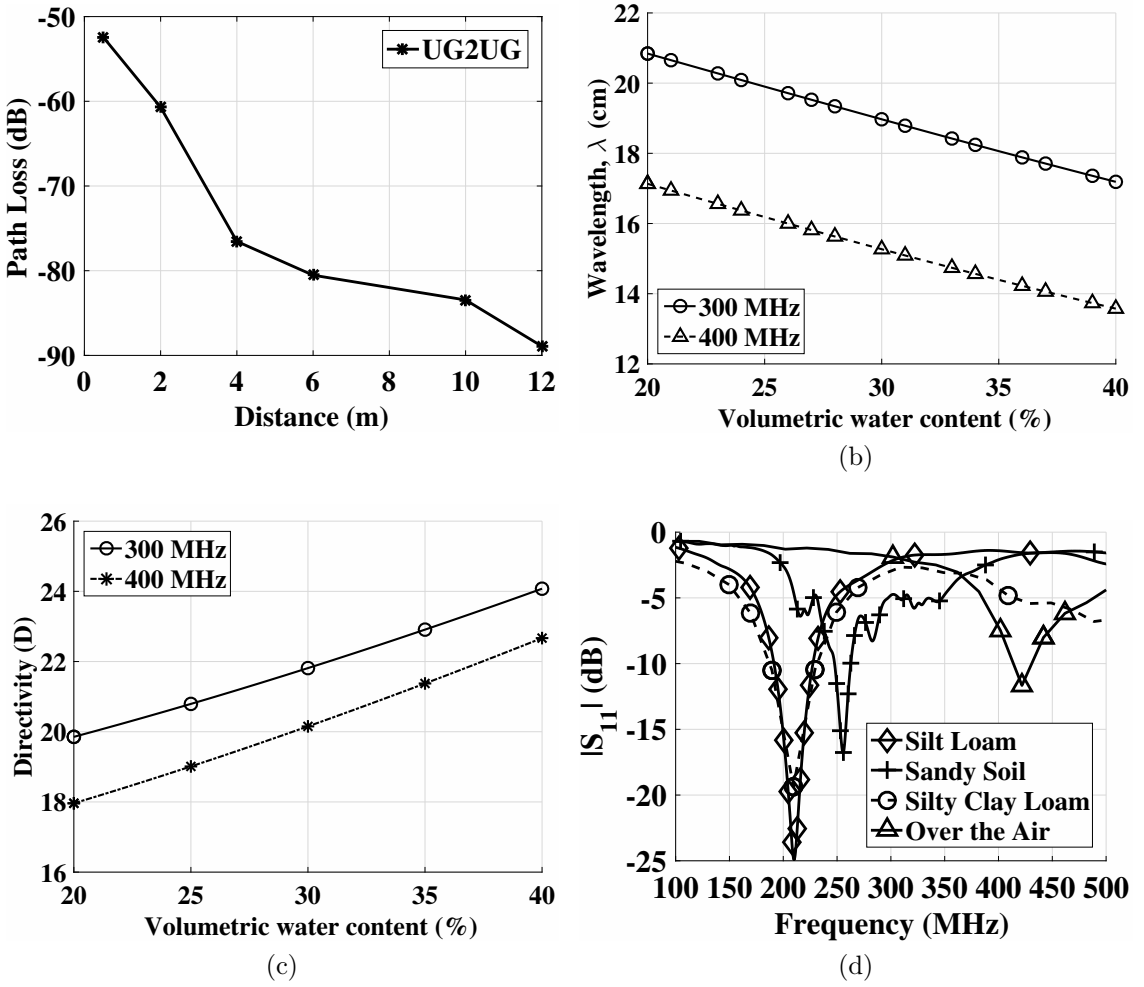

Figure 7.1: (a) Pathloss in UG2UG channel, (b) Change in wavelength with change in soil moisture (c) Array directivity with change in soil moisture (d) Reflection coefficients of a dipole array element.

ing algorithm is developed for beamforming. This method works on array element weighting based on the UG2UG and UG2AG communications. Array element positions, inter-element distance are analyzed for best performance. Then an optimization algorithm is developed which is based on soil moisture sensing information. Sidelobe reduction is accomplished by using element thinning, and element positions optimization. Performance analysis based on testbed experiments and simulation results of SMABF communications are presented.

The rest of the chapter is organized as follows: the related work is discussed in

Section 7.2. The channel model is discussed in Section 7.3. Challenges to UG beamforming are presented in Section 7.4. An antenna array element in soil is analyzed in Section 7.5. Design of SMABF array and steering algorithm is given in Section 7.6. Results are presented in Section 7.7. We conclude in Section 7.9.

7.2 Related Work

Wireless UG channel is the medium of communication in Internet of Underground Things (IOUT) [155], [157], [159], which are being used in the area of precision agriculture [39], [51], [72], [76], [96], [155], [187], border monitoring [40], land slide monitoring, and pipeline monitoring [96], [180]. IOUT communications are based on both EM-wave propagation [200] and magnetic induction (MI) communications [184]. IOUT include MI, use EM communication devices and sensors, partly or completely buried underground for real-time soil sensing and monitoring.

Beamforming antennas [133] are used in wireless networks to reduce interference and improve capacity. Beamforming has been studied in [126] for over-the-air (OTA) wireless channels and in [123], for MI power transfer. However, MI beamforming cannot be readily applied to IOUT because the spatial multipath modularity does not exist in MI, and sender-receiver coils have to be parallel to each other in MI-communications, which is a restriction which can be avoided in UG communications. In UG communications, lateral component [122] has the potential, via beam-forming techniques, to reach farther UG distances, which otherwise are limited (8 m to 12 m) because of higher attenuation in soil. To the best of our knowledge, adaptive UG beamforming has not been studied before in literature, and this is the first work to develop soil moisture adaptive UG beamforming for the wireless UG channel.

7.3 Channel Model for SMABF

Estimation of propagation characteristics through the soil is crucial to design a UG communication systems. The UG channel impulse response can be expressed as a sum of direct, reflected and lateral waves (Chapter 4):

$$h_{ug}(t) = \sum_{l=0}^{L-1} \alpha_l \delta(t - \tau_l) + \sum_{s=0}^{S-1} \alpha_s \delta(t - \tau_s) + \sum_{r=0}^{R-1} \alpha_r \delta(t - \tau_r) \ , \tag{7.1}$$

where L, S, and R are the number of multipaths; α_l, α_s, and α_r are complex gains; and τ_l, τ_s, and τ_r are delays associated with lateral wave, direct wave, and reflected wave, respectively. We highlight in Chapter 4 that based on the power delay profile (PDP) of wireless UG channel, lateral wave is the strongest component because it suffers from lower attenuation as it propagates through the air along the soil-air interface. Reflected and direct waves undergo higher attenuation due to the higher losses in soil medium. This unique phenomenon allows the design of buried antenna arrays with reasonable sizes. Furthermore, because of the unique three-wave structure of the PDP by focusing the transmitted energy to lateral waves, the delay spread can be further decreased, leading to higher data rates and long-range communications. It is worth noting that the interactions between soil, antennas, and the UG channel create unique opportunities that are not possible in other media. Moreover, due to higher permittivity of soil as compared to air, wavelength at a particular frequency is lower than that of air. This allows the use of lower frequency waves, which attenuate less in soil, with smaller-size antennas.

In Fig. 7.1(a), attenuation with distance is shown. Channel transfer functions are measured for dipole antennas buried at 20 cm depth up to the distance of 12 m. A 30 dB path loss is observed when UG distance increases from 2 m to 12 m. Due to these

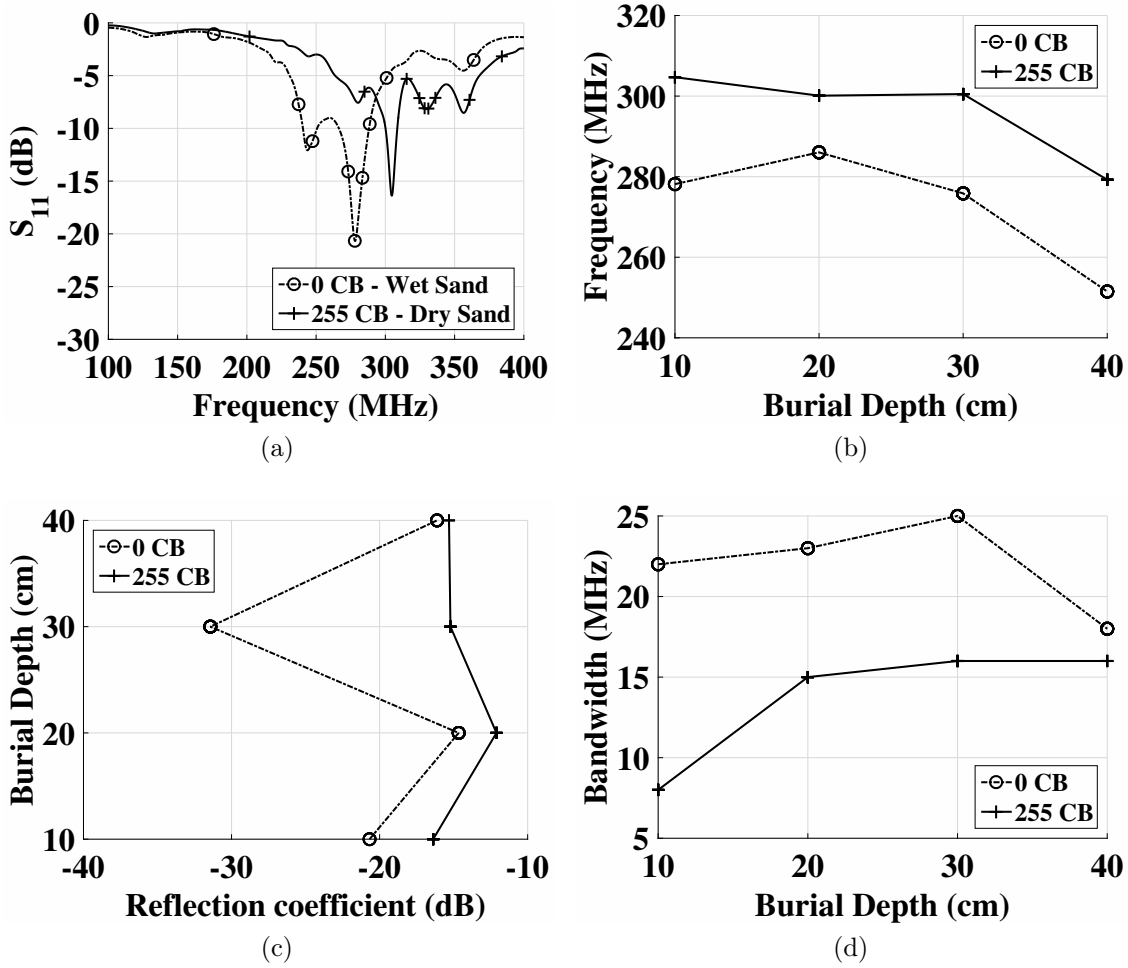

Figure 7.2: Return loss in sandy soil, : (a) S_{11} at different frequencies, (b) Change in resonant frequency with burial depth, (c) Reflection coefficient (dB) at different burial depths, (d) Antenna bandwidth at different burial depths for near-saturation and dry sandy soil.

factors, an impedance-matched antenna for OTA communication is not matched in soil and new designs are necessary [76]. High attenuation in soil is one of the limiting factors for long range communications.

Due to their buried deployment and the dominance of the lateral wave in the wireless UG channel, sending signals in an isotropic direction (i.e., partly towards the Earth) would be waste of the resources. Thus, SMABF aims to communicate with UG and AG devices by forming a focused narrow width beam in the desired direction, hence, extending the communication ranges.

7.4 Challenges in Underground Beamforming

In this section, we first analyze a *fixed-beam system* based on impacts of soil moisture on wavelength and directivity. Accordingly, we review UG beamforming challenges.

Impact of Soil Moisture on Wavelength: Wavelength in soil is calculated as $\lambda_s = (2\pi)/k_s$, where k_s is the wave number in soil ([23, Appendix B]). In Fig. 7.1(b), change in wavelength is shown as a function of volumetric water content (VWC). It can be observed that when VWC increases from 20% to 40%, wavelength at 300 MHz decreases from 21 cm to 17 cm. Similarly at 400 MHz wavelength decreases from 17 cm to 14 cm. Accordingly, for an antenna array, the distance between succeeding elements needs to be selected in a way to accommodate wavelength changes due to soil moisture variations without affecting the directivity and beam patterns.

Impact of Soil Moisture on Directivity: Directivity of an one-dimensional UG antenna array can be expressed as $D_a \approx 2\frac{Nd}{\lambda_s}$ [100], where N is the number of elements, d is the distance between elements, and λ_s is the wavelength in soil. In Fig. 7.1(c), directivity pattern is shown with change in soil moisture for antenna elements that are half wavelength $\lambda_0/2$ (in the air) apart. It can be observed that soil moisture leads to linear changes in directivity, which needs to be mitigated for SMABF. Moreover, since the UG communication devices are buried to the close proximity of soil-air interface in homogeneous soil [76], therefore, soil moisture changes are not abrupt. Analysis of the layered soil effects on UG communications is left for future investigation. Phased arrays are used to steer the main beam of the antenna without physically moving the antenna [83], [94], [103]. Due to the requirement of accurate phase control with wavelength change, smart antennas with phase shifters are suitable in UG communications. In the following, we analyze the effects of soil on UG beamforming, and design a UG SMABF solution which is robust and adaptive to these variations.

7.5 Analysis of Single Array Element in Soil

We first analyze the behavior of a single array element in soil medium. To this end, first, an antenna element in soil is compared with an OTA antenna element through empirical evaluations in an indoor testbed (Chapter 3). The indoor testbed provides flexible control over the soil moisture, and holds dipole antennas at 10 cm, 20 cm, 30 cm, and 40 cm depths for transmitter-receiver distances of 50 cm, and 1 m. Then, the array element impedance and soil-air interface effects are analyzed by taking RL measurements.

7.5.1 Comparison of In-Soil and OTA Array Element

Return Loss in Soil: In Fig. 7.1(d), the performance of single array element (dipole) buried in soil is compared with that of a free space element. Return loss measurements of a 433 MHz OTA antenna element in three different soils are shown for a frequency range of 100 MHz to 500 MHz. It can be observed that the resonant frequency of the antenna shifts to lower frequency values when buried underground. Resonant frequency in silt loam soil is 202 MHz, in silty clay loam (SCL) it is 209 MHz, and in sandy soil resonant frequency is 278 MHz. Resonant frequency in sandy soil is 76 MHz higher than the silt loam soil. This is because the relative permittivity of a particular soil depends on its net water content [144] and silt loam has a higher water holding capacity than sandy soil. Therefore, due to silt loam's higher relative permittivity, lower resonant frequency is observed. Next, we analyze the effects of soil moisture variations on the RL, and resonant frequency of the array element.

Impact of Soil Moisture on Element RL: In Fig. 7.2(a), RL of element in silt loam at 10 cm depth is shown for soil matric potential values of 0 and 255 CB. When soil moisture decreases (matric potential changes from 0 to 255 CB), resonant

frequency has increased from 278 MHz to 305 MHz. Effects of change in soil moisture on the resonant frequency at different depths are shown in Fig. 7.2(b). At 20 cm, with change in soil moisture from 0 to 255 CB, resonant frequency increases from 276 MHz to 301 MHz. With the similar change at 30 cm depth, resonant frequency changes from 276 MHz to 301 MHz, and at 40 cm depth, it changes from 251 to 279 MHz. Analysis of the RL of antenna (Fig. 7.2(a)-7.2(d)) in sandy soil at different burial depths and soil moisture levels shows that the RL of the antenna changes with the soil moisture. Resonant frequency moves to lower frequency ranges when the soil moisture increases. Moreover, unlike OTA communications, the optimal frequency where the maximum capacity is achieved is not the same as the resonant frequency of the antenna [74].

7.5.2 Element Impedance in Soil

The knowledge of impedance of an array element in soil is important to match the array to a transmission line. For efficient wireless communication, the impedance of an antenna element, Z_a, should be matched to the output impedance of the transceiver, Z_s, such that the radiated power is maximized and the returned power to the transmitter is minimized. Due to soil-air interface effects, soil cannot be considered as an infinite medium, as is typically considered in OTA antenna models. Consequently, antenna RL is not merely a shift in spectrum space when the antenna is moved from air to soil, but the shape of the RL curve also changes.

Soil-Air Interface Impacts on Element Impedance: When a buried antenna is excited, a current distribution of $I_0(\zeta)$ is generated along the antenna. The generated wave propagates towards the soil-air interface, where it is reflected and refracted. The reflected electric field, E_r, that reaches the antenna induces an additional current, I_r, on the antenna, affecting its impedance [199]. The induced current

further impacts the generated wave and higher order reflection effects exist. However, due to the high attenuation in soil, these higher order effects are negligible and only the first order effects are considered. The induced current on the dipole, I_r, as well as the resulting impedance, Z_r, can be modeled as the result of a field generated by an imaginary dipole placed in a homogeneous soil environment. Accordingly, Z_r is modeled based on a modified mutual impedance model between two dipole antennas [135] and the reflection coefficient at the soil-air interface. The mutual impedance, Z_r, is then added to the self impedance, Z_a, to obtain the total impedance of the buried antenna in half space [199]. With insights gained from the analysis of individual antenna element, we design multi-element SMABF array next.

7.6 Design of SMABF Array

In this section, we investigate array configuration and element positioning of phased array antenna for UG communications (Section 7.6.1). In Section 7.6.2, beam patterns for UG2AG communications are developed. UG2UG beam patterns are analyzed in Section 7.6.3. In this development, we emphasize the beamforming aspects related to the UG2UG and UG2AG communications without going into details of beamforming basics. For a comprehensive treatment of the subject, we refer the reader to [90].

Table 7.1: UG2UG and UG2AG steering angles.

Communication Link		$\boldsymbol{\theta}$	$\boldsymbol{\phi}$
UG2AG	**No Steering**	$0°$	$0°$
	Beam Steering	$0° - 60°$	$0°$
UG2UG	**Lateral Wave**	VWC Dependent (Sect. 7.6.3)	$0°$
	Direct Wave - X Orientation	$90°$	$0°$
	Direct Wave - Y Orientation	$90°$	$90°$

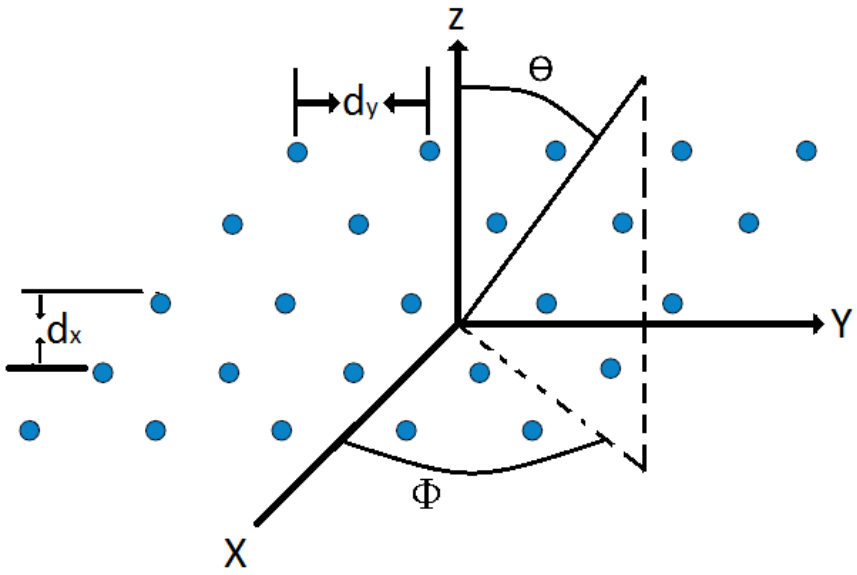

Figure 7.3: Arrangement of array elements in a planar grid.

7.6.1 Array Layout and Element Positioning

First, we investigate the desired size and number of antenna elements in the SMABF array which can form beams to communicate with UG and AG devices. The AG nodes can be fixed sinks or mobile nodes mounted on movable infrastructures. Then, we analyze SMABF inter-element spacing.

Following features are desirable in the design an SMABF antenna array: 1) Due to wavelength changes in soil, inter-element spacing should be such that the directivity and desired beam shape are not lost significantly with changes in soil conditions, 2) Array is to be designed to work in a wide range of frequencies, 3) Elements are half-wave length with support for multiple inter-element spacing, 4) The array is to have number of elements which are not prohibitive for UG deployment and maintains higher directivity, 5) Both UG2UG and UG2AG array patterns are desirable with support of steering angles, 6) It should be able to adjust its parameters when the soil moisture changes.

7.6.2 UG2AG Communication Beam Pattern

Since UG2AG link is different than the UG2UG link, energy radiated in the vertical direction from the buried SMABF array needs to be determined at different receiver angles. Experiments conducted for a UG sender buried at a depth of 20 cm to an AG node at different distances and angles in (Chapter 3) show that for the receiver at the angle of 0°, highest attenuation occurs, whereas the lowest attenuation is observed at 90°. At 90°, the wave does not experience high refraction compared to the 0° case. Therefore, in UG2AG communications, the wave energy directed closer to the normal of the soil surface leads to higher gains and throughput. In the following, we discuss two scenarios of UG2AG communications.

Case 1: Beam Steering. We consider an $M \times N$ planar array where the array elements are arranged in a two-dimensional rectangular grid, with inter-element spacing d_x, and d_y in the x and y directions, respectively (Fig. 7.3). For the reminder of the chapter, we assume that $d_x = d_y$. If the precise location of the AG node (θ_{AG}, ϕ_{AG}) is known (i.e. through GPS), then beam is steered accordingly by adding the phase shifts δ_{ij} at the ij^{th} element. Accordingly, the array factor for UG2AG pattern can be expressed as [103]:

$$AF_{bs}(\theta,\phi) = \sum_{i=1}^{M}\sum_{j=1}^{N} w_{ij}\, exp\Big(- \big[jk_s(x_{ij}\sin\theta\cos\phi + y_{ij}\sin\theta\sin\phi)\big] + \delta_{ij}\Big), \tag{7.2}$$

where k_s is the wave number in soil ([23, Appendix B]), and for the ij^{th} antenna element, w_{ij} is the weight, x_{ij} and y_{ij} are the coordinates, and δ_{ij} is the phase shift.

For the intended direction (θ_{AG}, ϕ_{AG}), the phase shift is [83]:

$$\delta_{ij} = -k_s(x_{ij} \sin\theta_{AG} \cos\phi_{AG} + y_{ij} \sin\theta_{AG} \sin\phi_{AG}) \forall i, j. \tag{7.3}$$

It can be observed from (7.2-7.3) that both the array factor and the antenna element phase shifts are a functions of wave number in soil, k_s, which is a function of soil moisture. Therefore, compared to OTA beamforming, for UG beam steering, the antenna element phase shifts need to be dynamically adjusted to maintain beams formed at a particular direction when soil moisture changes.

Case 2: Refraction Adjustment. When UG2AG beam is steered at angles other than normal to the soil-air interface, RF waves experience refraction. The refraction process not only degrades the performance of the SMABF but also changes the angle-of-arrival at the AG nodes. Moreover, an optimal angle of incidence exists with respect to burial depth of the SMABF antenna array, at which refraction is more dominant. Hence, less reflection of incidence wave occurs. Moreover, these phenomena result in different propagation speeds because of different refraction indices of soil and air, leading to spreading, and decay of focused beam. Due to these factors, adjustment of the phase at the UG antenna elements does not align the phase to add up coherently and leads to errors in beam steering and beam pointing direction. Depending on the incident angle, this has adverse effects in the UG communications. The error caused by refraction from soil-air interface is called beam squint [103] and results in time dispersion of the signal.

To address this issue, we use time-delay beam steering [103] in SMABF to align signal envelopes and achieve the desired performance to mitigate soil-air interface effects. Time delay units are used to adjust the beam pointing direction by using the refraction angle. Given the position of the AG node, (θ_{AG}, ϕ_{AG}), time delay to correct

this effect, τ_{ij}, is expressed as [102]:

$$\tau_{ij} = \sin\theta_r \times h[i \times d_x \cos\phi_r + j \times d_y \sin\phi_r]/S, \quad \forall i, j, \tag{7.4}$$

where S is the speed of the wave in soil ([23, Appendix C]), d_x and d_y are the element spacing in the x and y direction respectively, h is the burial depth, and θ_r is the refraction angle, which is calculated by Snell's law as:

$$\theta_r = \arcsin\left(\frac{\eta_a}{\eta_s}\sin\theta_{AG}\right), \tag{7.5}$$

where η_a, and η_s are the refractive indices of air, and soil, respectively.

In (7.4), τ_{ij} is a function of burial depth from soil-air interface, and soil moisture. Higher refraction index (slow speed of wave in soil) leads to higher delay. Once τ and δ_i are determined, the array factor is expressed as [103]:

$$\begin{aligned} AF_{ra}(\theta,\phi) = \sum_{i=1}^{M}\sum_{j=1}^{N} w_{ij} exp(-\big[jk_s(x_{ij}\sin\theta\cos\phi \\ + y_{ij}\sin\theta\sin\phi) + 2\pi f\tau_{ij} + \delta_{ij}\big], \end{aligned} \tag{7.6}$$

Next, we analyze the UG2UG communication beam pattern.

7.6.3 UG2UG Communication Beam Pattern

In this section, two scenarios for UG2UG communications are discussed. First, we investigate the optimal angle for soil moisture-based beam steering using lateral waves. Then, the case for direct wave communication is discussed.

Case - 1: Estimation of Soil Moisture-Based Optimum Steering Angle: It has been shown in [75], [158], that in UG communications lateral wave travels along the soil-air interface to reach the receiver. This lateral wave is maximized if

the energy from the UG antenna is radiated in an optimum angle θ^*_{UG}. This angle depends on the dielectric properties of the soil and is given by [175]:

$$\theta^*_{UG} = \frac{1}{2}\tan^{-1}\left(\frac{2Re(\eta_s^2-1)^{1/2}}{|\eta_s^2-1|-1}\right)rad, \tag{7.7}$$

where θ^*_{UG} is used to indicate optimum value, and η_s is the refractive index of the soil. The derivation of optimal angle, θ^*_{UG}, is given in ([23, Appendix A]).

Case - 2: Direct Wave. For short UG2UG communication distances, when direct wave is more dominant than the lateral wave, communication is enhanced by forming a direct UG beam towards the receiver UG node through the soil. Steering angles for lateral and direct wave beams are given in Table. 7.1. In both cases, (7.2) is used based on the desired beam pattern.

7.6.4 SMABF Directivity Maximization

Consequently, directivity of a SMABF array is defined as [83]:

$$D = \frac{4\pi|AF_{max}|^2}{\int_0^{2\pi}\int_0^{\pi}|AF|^2\sin\theta d\theta d\phi}, \tag{7.8}$$

where AF_{max} is the main beam peak (maximum of the array factor).

In the UG channel, wavelength changes with soil moisture, hence, fixed inter-element spacing results in deterioration of array factor, and decreased directivity. This is unique to the UG channel, since in OTA channel wavelength remains fixed, hence, inter-element spacing does not change and directivity does not vary. Therefore, with soil moisture changes, the goal is to optimize the inter-element spacing which maximize directivity and avoids grating lobes. This optimization problem is

formulated as [83]:

$$\wp: \quad maxD \qquad\qquad s.t. \quad \frac{d_x}{\lambda_s} < \frac{1}{1+\sin\theta_{UG}}, \tag{7.9}$$

where D is directivity (7.8), θ_{UG} is the steering angle for UG2UG and UG2AG communications from the broadside, d_x is the inter-element spacing in the x and y direction, respectively, and λ_s is the wavelength in soil.

7.6.5 SMABF Element Thinning Through Virtual Arrays

To maintain a optimum inter-element spacing, implementation of d_x^* is not feasible from practical design point, therefore, SMABF uses array thinning (virtual arrays) [103], to adapt to wavelength changes due to soil moisture variations. In UG array thinning, a subset of the elements from the full planar structure is selected to avoid grating lobes. Through element thinning, virtual arrays of elements are formed, where the physical antenna elements are turned on and off. By using this approach, optimum configuration of elements is determined from the wavelength at the current soil moisture level. Virtual array inter-element spacing is denoted by d_x^v. Element weights w_{ij} are turned on and off as following [103]:

$$w_{ij} = \begin{cases} 1 & \text{if } i \text{ is multiple of } \frac{\lfloor d_x^* \rfloor}{d_x^v} \ \forall i,j \in K \\ 0 & \text{otherwise.} \end{cases} \tag{7.10}$$

where d_x^* is the optimal inter-element spacing, $i = j$, and K is the total number of elements such that $K > M$. Virtual array inter-element spacing d_x^v is chosen such that with change in wavelength due to soil moisture variations, higher directivity is maintained.

7.6.6 Feedback Control

In addition to soil moisture adaptive weights which are based on soil moisture sensing, feedback signals are used to adjust the weights by using the array gain feedback loops. This problem is formulated as maximize the array gain by using the pilot signals. In this method, SMABF array at the transmitter receives the pilot signal in receive mode and then accordingly adjusts its parameters for the transmit mode. In receive mode at the transmitter, scan angles are varied to to get the estimate of channel state. The best SNR statistics are used and with change in soil moisture, parameters are adjusted accordingly. In Fig. 7.4, SMABF control with feedback is shown. Received power at a UG receiver is derived next.

The SMABF effective isotropic radiated power (EIRP) can be expressed as product of the transmitted power and antenna gain:

$$P_{rad} = G_t P_t, \tag{7.11}$$

where P_t is the transmitted power and G_t is the array gain.

The far-field power density P_{av} can is expressed as [75]:

$$P_{av} = P_{av}^{D} + P_{av}^{R} + P_{av}^{L} \ . \tag{7.12}$$

where D, R, L denotes the power densities of the direct, reflected and lateral component. The received power is calculated as the product of far-field power density P_{av}

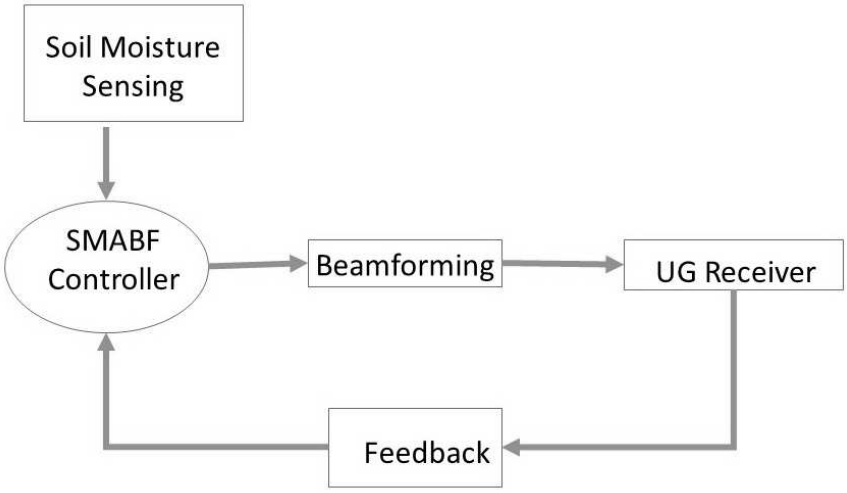

Figure 7.4: SMABF with feedback.

and antenna aperture ($\lambda_s^2/4\pi$). The received power is given as [75]:

$$\begin{aligned} P_r^d &= P_t + 20\log_{10}\lambda_s - 20\log_{10} r_1 - 8.69\alpha_s r_1 \\ &\quad -22 + 10\log_{10} D_{rl} \ , \\ P_r^r &= P_t + 20\log_{10}\lambda_s - 20\log_{10} r_2 - 8.69\alpha_s r_2 \\ &\quad +20\log_{10}\Gamma - 22 + 10\log_{10} D_{rl} \ , \\ P_r^L &= P_t + 20\log_{10}\lambda_s - 40\log_{10} d - 8.69\alpha_s(h_t + h_r) \\ &\quad +20\log_{10} T - 22 + 10\log_{10} D_{rl} \ , \end{aligned} \tag{7.13}$$

where Γ and T are reflection and transmission coefficients [75], and λ_s is the wavelength in soil. The received power, for an isotropic antenna, is expressed as [75]:

$$P_r = 10\log_{10}(10^{\frac{P_r^d}{10}} + 10^{\frac{P_r^r}{10}} + 10^{\frac{P_r^L}{10}}) \ . \tag{7.14}$$

7.6.7 Adaptive SMABF Element Weighting

Signals of array elements of beamforming antennas can be controlled to produce the desired beam by phase and amplitude weighting [208]. In SMABF, current environment and the soil moisture information is used to weight the elements which leads to improvements in received SNR. Adaptive weight adjustment is done to keep the desired UG2UG and UG2AG characteristics based on the soil moisture variations.

Soil moisture adaptive weights are expressed as:

$$\boldsymbol{w} = \{w_0, w_1, w_2 ... w_{n-1}\}^T \tag{7.15}$$

Permittivity of the soil changes with the change in soil moisture and hence the wavelength. Weight factor γ_s is defined as:

$$\gamma_s = \frac{1}{\lambda_s} \times d \times \pi \times sin\theta_0 \tag{7.16}$$

where d is the inter-element distance. Accordingly, with this weight factor, i^{th} soil moisture adaptive weight w_{sm}^i becomes:

$$w_{sm}^i = \alpha_i exp(-j\gamma_s(2i - n - 1)) \tag{7.17}$$

where α_i is the element coefficient. These element coefficients are optimized to obtain desired sidelobe levels and beam patterns through element thinning and positioning approach. Once the beamforming vector is populated with the adaptive weights, then the desired beam pattern is produced as following:

$$F = \boldsymbol{X} w_{sm}^i \tag{7.18}$$

where $\boldsymbol{X}$ is the intended signal. To repeat this process with soil moisture change, gradient method is used. In this method, soil moisture adaptive weights are adjusted for next $(l+1)$ iteration as following [208]:

$$w^i_{sm,l+1} = w^i_{sm,l} + s(-\nabla_l) \tag{7.19}$$

where s ensures stability and convergence and ∇_l is the gradient estimate vector. It is well known that performance of an adaptive antenna array system degrades with faster adaption [208]. Since soil moisture is a slowly varying process, this simple-to-implement approach exhibits minimum noise and high tolerance to performance degradation caused by faster adoption due to limited sampling.

A beam steering algorithm is given in Algorithm 2 to produce different beam patterns required for UG2UG and UG2AG communications. This algorithm addresses the communication requirement on these two separate links.

7.7 Results

In this section, first, SMABF simulation results are presented, then the developed model is validated through empirical and numerical evaluations. Then, comparisons of SMABF performance improvements with a nonadaptive system are presented.

SMABF Simulations: SMABF array design is evaluated through simulations in CST Microwave Studio (MWS), a simulation program which is used to simulate full wave 3D EM problems. A SMABF phased array antenna consisting of 5×5 dipole element has been simulated in sandy soil. Array is capable of operating in 0.2 - 0.6 GHz in soil, and supports beam steering for communication links and angles given in Table 7.1 to maintain connectivity with UG and AG nodes.

First, a dipole antenna element is simulated in the sandy soil and different pa-

rameters are analyzed. Element is modeled using PEC cylinder material. Excitation is done using port placed in a gap in the middle of the element. OTA resonant frequency at one half-wavelength is 433 MHz. Higher mesh (40 per wavelength) is used for higher accuracy and time-domain solver is employed using unit cell approach. 50-ohms feed impedance is specified. S-parameters of the simulated element are compared with measurements to validate the simulated element design. Simulated and empirical results (Fig. 7.5(a)) show a very good agreement.

Algorithm 2 SMABF Beam Steering

Let A and U be the set of AG and UG nodes respectively
Let RN be the receiver node
Sense the moisture level and determine wavelength in soil
Select the array layout based on wavelength
Activate desired elements based on soil moisture
Produce the initial weights and calculate the excitation and current distribution (root matching, pole-residue)
BEGIN
if RN $\in$ A **then**
    if θ_{AG} is known **then**
$AF_{bs}(\theta,\phi) = \sum_{i=1}^{M}\sum_{j=1}^{N} w_{ij} exp(-\left[jk_s(x_{ij}\sin\theta\cos\phi + y_{ij}\sin\theta\sin\phi)\right] + \delta_{ij})$
ELSIF
        Normal to the surface beam using
$AF(\theta,\phi) = \sum_{i=1}^{M}\sum_{j=1}^{N} w_{ij} exp(-\left[jk_s r_i(x_{ij}\sin\theta\cos\phi + y_{ij}\sin\theta\sin\phi)\right]),$
    end if
else if R $\in$ U **then**
    BEGIN
    Sense soil moisture and determine optimal angle using
$\theta^*_{UG} = \frac{1}{2}\tan^{-1}\left(\frac{2Re(\eta_s^2-1)^{1/2}}{|\eta_s^2-1|-1}\right)$
    Output UG2UG Beam
    END
end if
Optimize to get low side-lobes when wavelength changes
Optimize element positions and activate virtual arrays
Adjust weights and excitation, and repeat this process to adjust these parameters when soil moisture changes
END

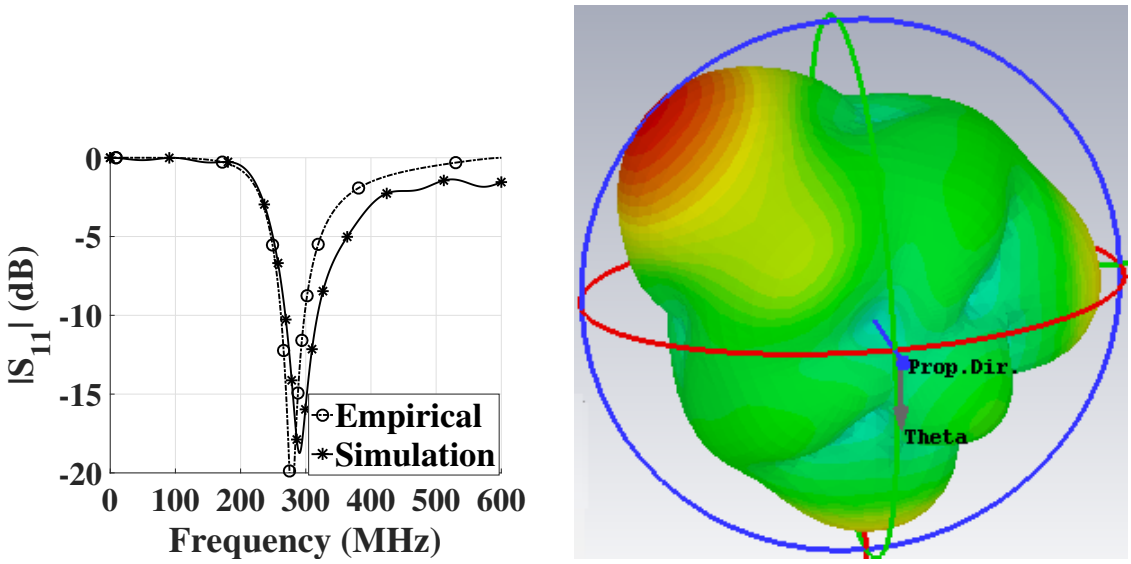

(a) (b)

Figure 7.5: (a) Comparison of measured and simulated reflection coefficients, (b) 3D view of UG2AG beam.

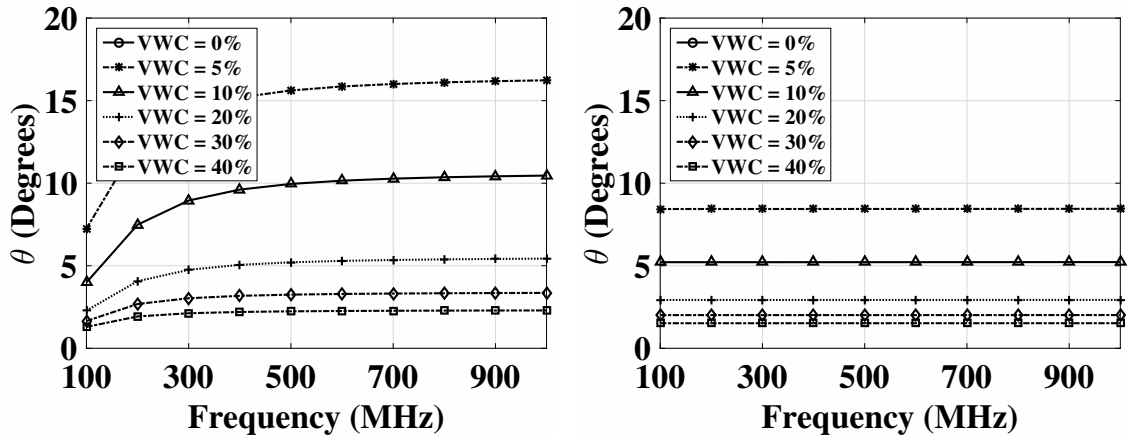

(a) (b)

Figure 7.6: Optimal angle with frequency in different soils: (a) Silty Clay Loam, (b) Sandy Soil.

Once the individual SMABF element is simulated and validated, then a full array simulation configuration is created to incorporate element into the array design [6]. In CST MWS, once the UG2UG and UG2AG beam patterns are specified, a distribution matrix is calculated. This distribution matrix is used for element excitation to generate the desired beam pattern. With change in soil moisture, a new distribution

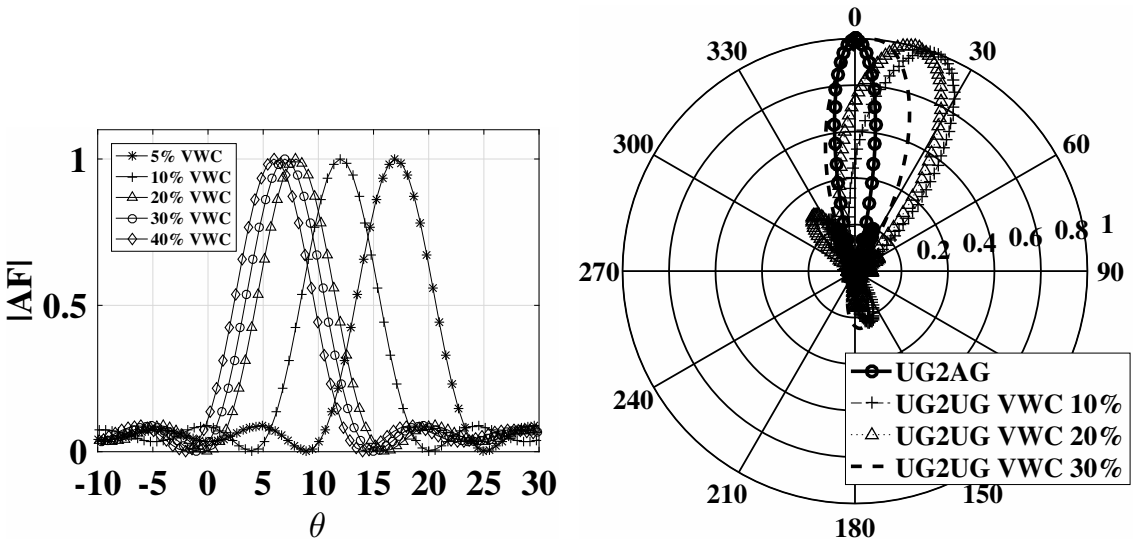

(a) (b)

Figure 7.7: (a) Array factor for UG2UG communications for different soil moisture levels, (b) UG2AG communications.

matrix is produced to adjust the beam steering angle. A 3D view of UG2AG beam is shown in Fig. 7.5(b).

Optimum UG Angle: The optimum angle to maximize UG2UG lateral wave communication is obtained as a function of the properties of soil medium by using (7.7). We analyze the lateral wave angle for silty clay loam (SCL) and sandy soils for volumetric water content range of 0% to 40% in the frequency range of 100 to 1,000 MHz. Particle distributions of these two soils are shown in Table 3.1.

In Fig. 7.6, optimal angle, θ_{UG}, for different soils are shown as a function of frequency for soil moisture (VWC) range of 0% to 40%. It can be observed that optimal angle is higher in the SCL soil as compared to sandy soils. In SCL soil it goes up to 16°, whereas in sandy soil it is 9°. This is explained by the higher dielectric constant of the silty clay soil than that of the sandy soil. It can also be observed that optimal angle decreases with increase in soil moisture and it becomes close to zero when soil moisture (VWC) reaches to 40%. This is attributed to increase in permittivity of soil due to increase in soil moisture. Summary of steering angles for

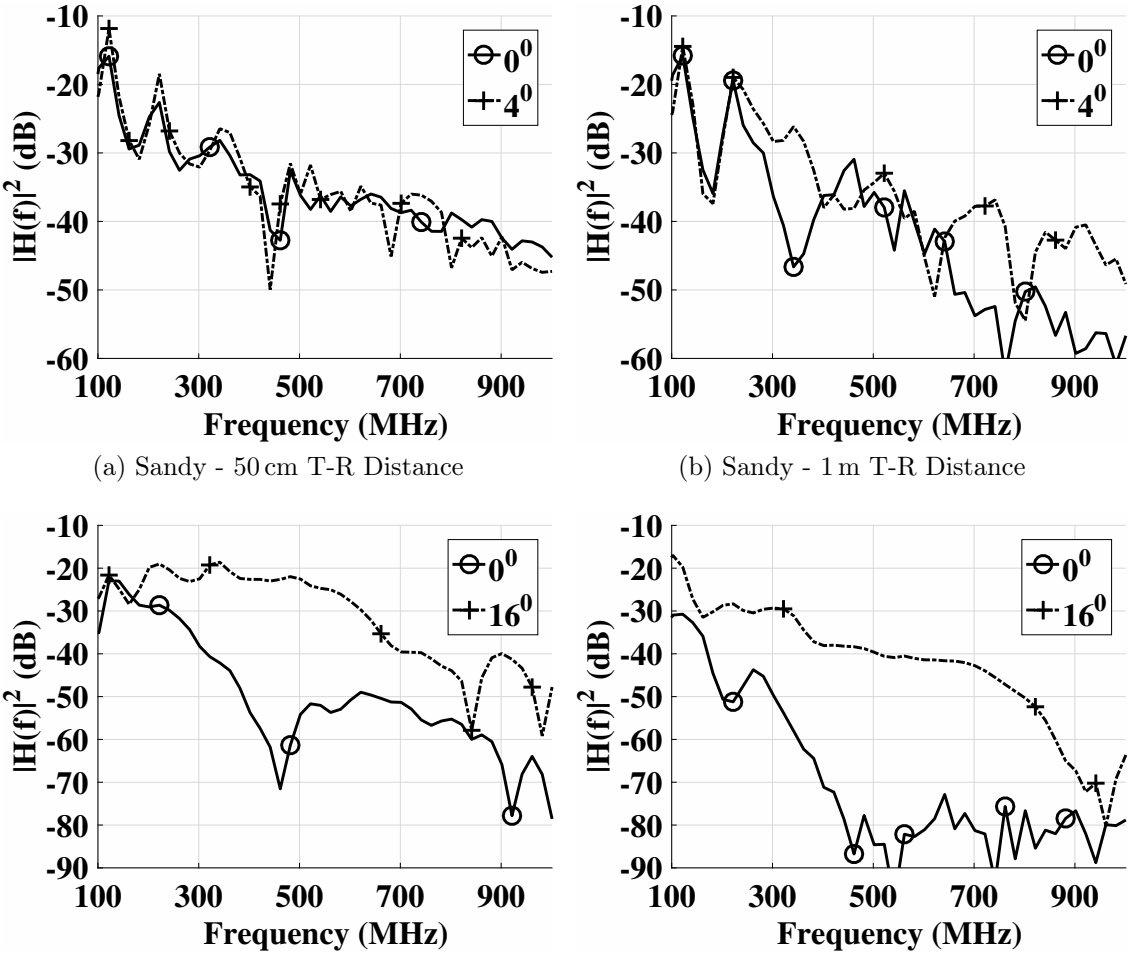

(a) Sandy - 50 cm T-R Distance

(b) Sandy - 1 m T-R Distance

(c) SCL - 50 cm T-R Distance

(d) SCL - 1 m T-R Distance

Figure 7.8: Comparison of optimum angle UG communications with fixed orientation.

UG2UG and UG2AG communications is given in Table 7.1. UG beam patterns for different soil moisture levels are shown in Fig. 7.7(a)-7.7(b). In Fig. 7.7(a), linear plot of UG2UG array factor for different VWC values is shown. Polar plot with broadside UG2AG beam is shown in Fig.7.7(b). Next, enhancement in UG2UG communications are validated through empirical evaluations in SCL and sandy soil.

Empirical Evaluation of Lateral Wave Enhancement Through Optimum UG Angle: To evaluate the lateral wave enhancement, experiments are conducted in an indoor testbed in sandy soil, and in an outdoor testbed in silty clay soil (Chapter 3). By using a directional antenna buried at the 20 cm depth, measurements

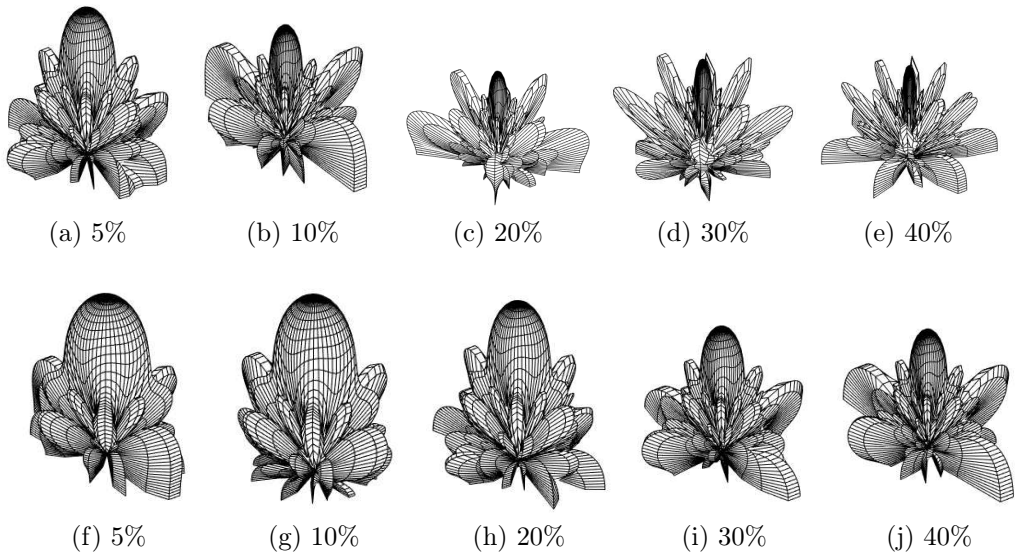

(a) 5% (b) 10% (c) 20% (d) 30% (e) 40%

(f) 5% (g) 10% (h) 20% (i) 30% (j) 40%

Figure 7.9: Deterioration of array factor with change in soil moisture for a nonadaptive beamforming system. (a-e) SCL soil, (f-j) sandy soil.

are conducted using a Keysight Fieldfox Vector Network Analyzer (VNA) N9923A. Chanel transfer functions are recorded and channel gain is determined, first, without the orientation change. Then, experiments are repeated by determining the optimum lateral wave angle and accordingly changing orientation in both soils. VWC values for sandy and SCL soil are 37% and 0%, respectively, which lead to the optimum angle of 4° in sandy soil and 16° in SCL soil.

In Figs. 7.8, channel gain results of experiments conducted in SCL and sandy soils are shown for 50 cm and 1 m transmitter receiver (T-R) distance. It can be observed that, at 50 cm T-R distance, when energy is directed at 4° in sandy soil, a gain of 4 dB is realized at 500 MHz as compared to no steering case (Fig. 7.8(a)). It can also be observed that by focusing energy in UG optimum angle, the channel gain is higher at higher frequencies, because path of the wave through soil is more affected by permittivity of the soil. In Fig. 7.8(b), channel gain in sandy soil for 1 m T-R distance is shown. It can be observed that at 1 m, a 8 dB higher gain is achieved as compared to 50 cm because of the lower contribution by the direct wave at 0° at

1 m. Therefore, lateral wave communication is enhanced through optimum steering angle. An improvement of 32 dB and 37 dB channel gain is observed in SCL soil at 50 cm and 1 m distances, respectively, (Fig. 7.8(c) - Fig. 7.8(d)) as compared to fixed orientation. SCL soil has higher losses due to high permittivity of soil, which leads to high channel gains through UG lateral wave enhancement.

In the following sections, we first analyze the performance of a 5×5 SMABF planar array with an *OTA fixed* and a *soil fixed* system through numerical evaluations in MATLAB. These two fixed systems do not adapt their parameters to soil moisture variations. In OTA fixed system, in both soils, inter-element spacing, d_x, is fixed at 433 MHz OTA frequency half-wavelength, which is 34.64 cm. In soil fixed scenario, the array deployment in both soils is customized for one particular soil moisture level (30%). Accordingly, inter-element spacing for both soils is determined, and a fixed

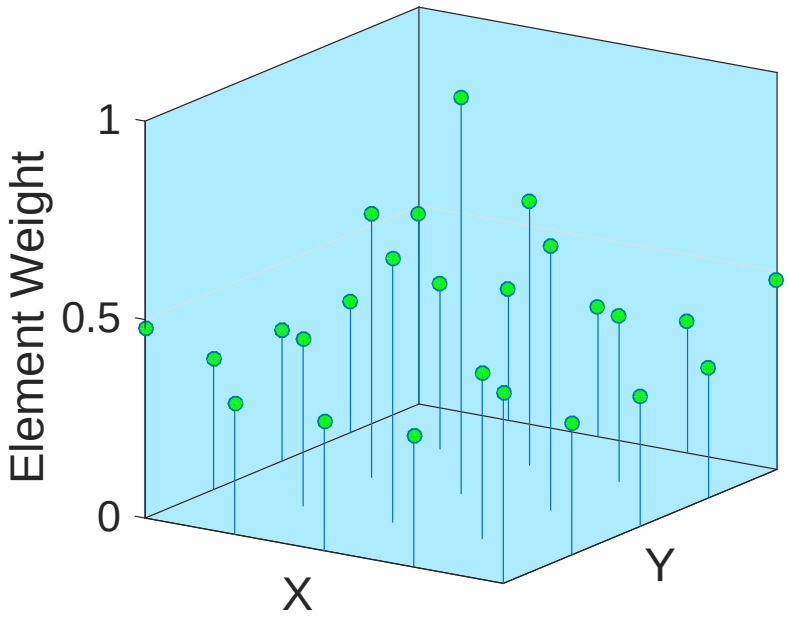

Figure 7.10: Element weights for a 5×5 planar array in soil for broadside UG2AG pattern, for 40% soil moisture level, at 433 MHz.

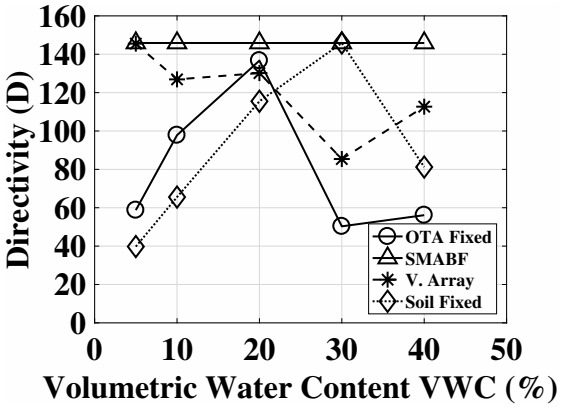

(a) SCL

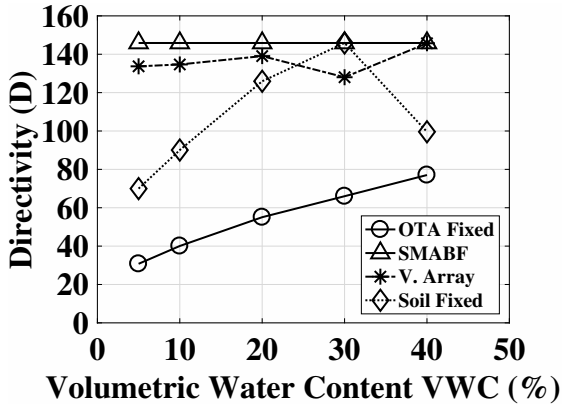

(b) Sand

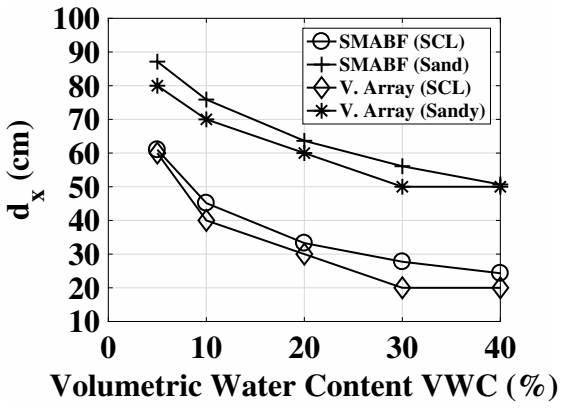

(c)

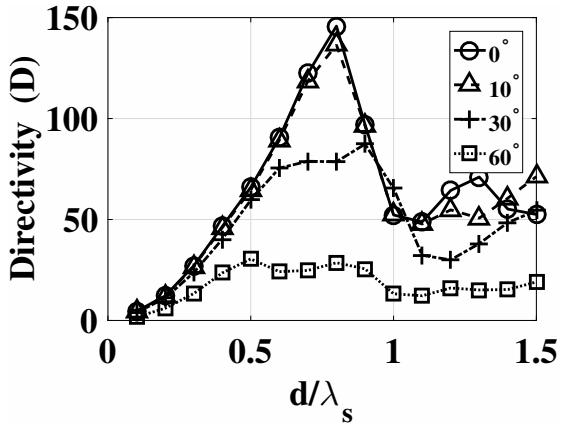

(d)

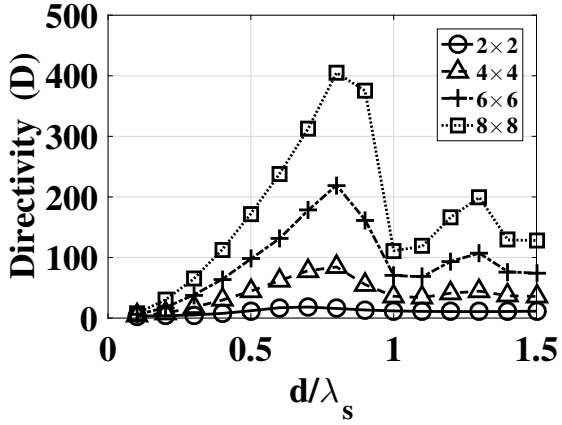

(e)

Figure 7.11: (a) Change in directivity in change in soil moisture: (a) silty clay loam soil, (and) sandy soil, (c) inter-element spacing, d_x, to maximize directivity, (d) change in directivity with element spacing at different steering angles in sandy soil, (d) directivity with different array size in SCL soil.

array design is deployed in soil without the support of the virtual arrays. For sandy soil, at 30% soil moisture level, $d_x = 56$ cm, and in silty clay loam soil at 30% soil moisture level, $d_x = 27$ cm. The half-wavelength inter-element spacing d_x values, at 433 MHz, with 10% to 40% change in volumetric water content (VWC) are shown in Table 7.2. Then, the performance of virtual arrays is analyzed. Virtual array inter-element spacing, d_x^v is 10 cm.

SMABF vs. Nonadaptive Beamforming: In this section, impacts of soil moisture variations on array factor and directivity are investigated. In Fig. 7.9, the deterioration of array factor with change in soil moisture for the OTA fixed beamforming system is shown in sandy and SCL soil, for the soil moisture (VWC) ranges from 5% to 40%. In both soils, higher side lobes are observed when soil moisture increases from 5% to 40%. However, in sandy soil, these effects of the change in soil moisture are less severe as compared to the silty clay soil. This is caused by larger wavelength changes due to soil moisture variations induced by higher permittivity in SCL soil. Element weights in soil for broadside UG2AG pattern, for 40% soil moisture level, at 433 MHz are shown in Fig. 7.10.

Virtual Arrays: In virtual arrays, adaptive thinning is done based on wavelength changes due to soil moisture changes. Virtual SMABF array helps to maintain side-lobe levels and fixed directivity. It also avoids high side-lobe distortions as observed in nonadaptive beamforming case.

Table 7.2: SMABF half wavelength inter-element spacing with change in soil moisture. All values are in cm.

	Volumetric Water Content (VWC)			
Soil Type	**10%**	**20%**	**30%**	**40%**
Silt Loam	30.79	23.72	20.25	18.03
Sandy	46.83	39.28	34.62	31.28
Silty Clay Loam	27.86	20.53	17.12	15.01

In Figs. 7.11(a)-7.11(b), directivity of SMABF and virtual array is compared with nonadaptive OTA fixed beamforming system for different soil moisture levels in sandy and SCL soils. Moreover, the change in directivity with change in soil moisture is also shown for the soil fixed deployment optimized at 30% soil moisture level in both sandy and silt loam soil. It can be observed that the SMABF and virtual array system is able to adapt to soil moisture variations to maintain its directivity whereas drastic changes are observed in nonadaptive fixed OTA beamforming system in both soils. In sandy soil, at 5% soil moisture level, directivity is 115.09 less than the SMABF, and 75.67 less than the virtual array. When soil moisture increases to 40%, directivity of nonadaptive system in sandy soil remains 68.81 less than the SMABF. Similarly, in SCL soil, for 10% and 30% soil moisture level, it is 48.05 and 95.57 below the optimum case. At 20% soil moisture level in fixed OTA SCL soil, directivity approaches close to the optimum case, which is caused by the resulting wavelength at 20% soil moisture becoming closer to d_x/λ_s, which leads to higher directivity.

It can also be observed from Figs. 7.11(a)-7.11(b), that in soil fixed nonadaptive system, for smaller changes in soil moisture (30% to 20%), directivity decrease is smaller (13% decrease in sandy soil, and 21% decreases in SCL, when soil moisture decreases to 20%). However, at 5% soil moisture level, a 51%, and 72% decrease is observed in sandy soil, and silty clay loam soil, respectively. Hence, in soils where soil moisture variations are not large (such as in growing crop soils), the deployment can be tailored to a recurrent soil moisture level to decrease complexity. Directivity in SMABF is maximized by optimizing the inter-element spacing for a current soil moisture level. SMABF directivity maximization results are presented next.

SMABF Directivity Maximization Results: SMABF and virtual array's inter-element spacing which maximizes directivity in sandy and SCL soil at different soil moisture levels are shown in Fig. 7.11(c). Sandy soil has larger spacing due to low

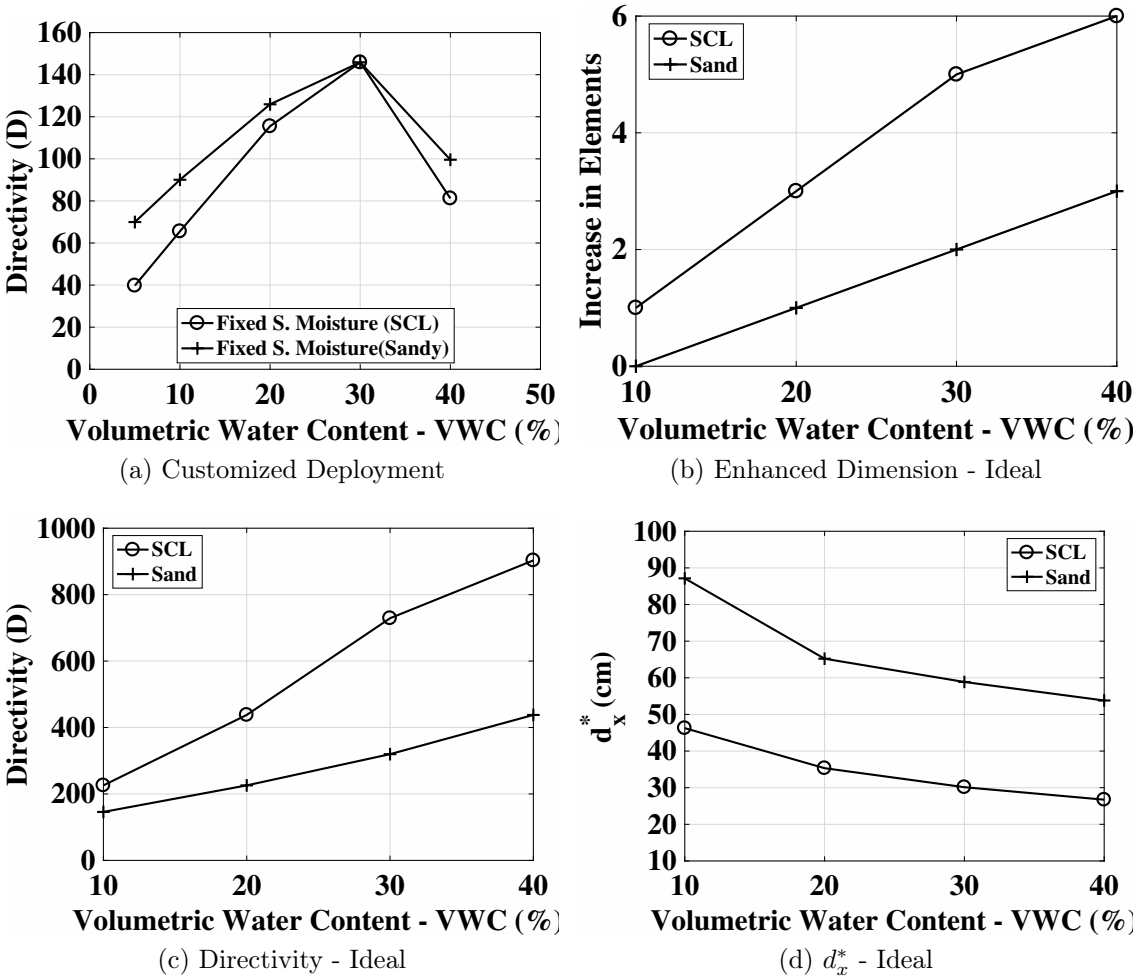

(a) Customized Deployment

(b) Enhanced Dimension - Ideal

(c) Directivity - Ideal

(d) d_x^* - Ideal

Figure 7.12: Change in directivity for a deployment optimized at 30% soil moisture level in both sandy and silt loam soil. Enhancement of array dimension: (b) Number of elements, (c) Directivity, (d) d_x^*.

losses whereas SCL soil requires shorter inter-element spacing because of higher permittivity. It can also be observed that inter-element spacing decreases with increase in soil moisture in both soils.

In Fig. 7.11(d), directivity of a SMABF array for inter-element spacing as a function of wavelength is shown for different steering angles in sandy soil. It can be observed that, for d_x/λ_s values of 0.5 to 1, higher directivity is achieved at 0° and 10° and it starts to fall at 30° and decreases at 60°. Moreover, for inter-element spacing of less than $\lambda_s/2$, the directivity variations between angles are low and overall direc-

tivity is lower as well. This decrease in directivity is caused by grating lobes which start to appear when d_x/λ_s is greater than 1 or less than 0.5.

In Fig. 7.11(e), effects of increase of SMABF array size on directivity are shown in SCL soil at 0° steering angle. It can be observed that larger arrays have higher directivity and this effect is more pronounced for $\lambda_s/2 < d_x < \lambda_s$. It can be also observed that at when $d_x/\lambda_s = 0.75$, by increasing the array size from 4×4 to 8×8, a 4 times increase in directivity is observed. For the $d_x/\lambda_s = 1.25$, directivity of 8×8 array is significantly higher than the smaller size arrays. Hence, for a fixed inter-element spacing system, larger arrays can be used to maximize the directivity. However, when array size is increased, beamwidth of main lobe and grating lobes become narrower, therefore a small change in steering angle leads to higher variations in directivity.

Fixed Soil Moisture Based Deployment: In this scenario, the array deployment in both soils is customized for one particular soil moisture level. Accordingly, inter-element spacing for both soils is determined, and a fixed array design is deployed in soil without the support of the virtual arrays. For sandy soil, at 30% soil moisture level, $d_x = 56$ cm, and in silty clay loam soil at 30% soil moisture level, $d_x = 27$ cm. In Fig. 7.12(a), change in directivity with change in soil moisture is shown for a deployment optimized at 30% soil moisture level in both sandy and silt loam soil. It can be observed that for smaller changes in soil moisture (30% to 20%), directivity decrease is smaller (13% decrease in sandy soil, and 21% decreases in SCL, when soil moisture decreases to 20%). However, at 5% soil moisture level, a 51%, and 72% decrease is observed in sandy soil, and silty clay loam soil, respectively. Hence, in soils where soil moisture variations are not large (such as in growing crop soils), deployment can be tailored to a recurrent soil moisture level.

Beyond Optimality: Enhancing Array Dimensions for Higher Soil Mois-

ture Levels: It can be observed that for low soil moisture levels, the larger inter-element spacing is required, hence, overall array dimension is large, as well. With decrease in soil moisture, in virtual array scenario, for fixed (such as 5×5) configuration, array size dimensions are also reduced, in spite of the fact that optimum directivity is maintained. Nevertheless, keeping a fixed 5×5 configuration by leaving elements over the fixed 5×5 unused, will be wastage of resources at high soil moisture levels. Performance of the SMABF can be enhanced by activating the more elements at high soil moisture levels, and therefore, beyond optimum directivity can be achieved. First, the ideal case is considered. In this case, a 5×5 array is designed on the optimum inter-element spacing, d_x^*, at 5% moisture level for both soils. This initial design yields the maximum possible physical dimensions of the array. Then, for each increasing soil moisture level, the number of elements are determined, which are incorporated within these maximum physical dimensions without placing any constraint on practical achievable the inter-element spacing, d_x. The enhanced configuration of the array (number of elements within the maximum dimensions) are also determined based on the d_x^* of the current soil moisture level. Then, in the second case, by using practical constraints on the d_x, we study performance of the enhanced system.

In Fig. 7.12(b), with increase in soil moisture, enhancement of a 5% soil moisture level 5×5 array is depicted by showing the additional number of elements in both soils for different soil moisture levels. It can be observed that in SCL soil, with addition of 1, 3, 5, and 6 elements for 10%, 20%, 30%, and 40% soil moisture levels, the array configuration is enhanced to 6×6, 8×8, 10×10, and 11×11, respectively. Whereas in sandy soil, for these soil moisture level, for 10% soil moisture level, there is no enhancement, however, for 20%, 30%, and 40% soil moisture levels, an enhancement of 6×6, 7×7, and 8×8, is observed, respectively.

The directivity of the enhanced configuration is shown in Fig. 7.12(c). Although both soils exhibit higher directivity, a substantial increase in directivity is observed with enhanced configuration in SCL soil at higher soil moisture levels. This happens because due to larger decrease in wavelength from low to high soil moisture change, and also because of smaller d_x^* inter-element spacing in SCL soil (Fig. 7.12(d)), the enhanced array is able to incorporate higher number of elements into the array dimensions which results in higher directivity in SCL soil. Therefore, soils with higher clay contents in high soil moisture environment can benefit from enhanced array deployment.

7.8 SMABF Implementation

In this section, we discuss software and hardware implementation aspects of the SMABF.

Software Defined Implementation: Recent advancements in SDR technology and digital equipment allows efficient implementation of SMABF. Through software defined control of individual array elements, steering solutions can be used for communications with static and mobile AG devices. Moreover, complex algorithm processing capabilities can be implemented easily. SDR implementation [149] of UG beamforming is challenging due to many reasons. The major challenge is the phase shift between antenna elements. To get a desired beam pattern, the phase shifts between antenna elements needs to be equal in the desired direction. This requires calibration of phase shifters and dynamic on-the-fly synchronization and phase correction to achieve the desired beam.

Digital beamforming based on soil moisture conditions to form dynamic beam patterns can be used. This design consists of a planar array with its own phase shifter

with pre-defined parameters for communication with UG and AG arrays. Furthermore beams can be stitched such that a number of beam patterns can be determined and designed based on the analyses of UG and AG devices and can be stored in configuration database for on-demand usage.

Another SDR approach is based on phase shifting done in the software. This approach is based on processing in the software defined radio to adapt to wavelength changes due to soil moisture conditions. The advantage of using this approach is that dynamic changes in the wavelength and phase variations due to UG channel dynamism are compensated without changing physical array arrangements. Moreover, less energy is required in comparison to traditional mechanical phase shifters [83].

Hardware Components: For SMABF hardware array elements can use dipole and printed circuit antennas. Other microwave components such as phase shifters, amplifiers, dividers, and hybrids can also be implemented as printed circuits through inexpensive equipment [83]. Beamforming network can consist of stripline configuration. Good wideband characteristics can be achieved within limited underground volume by using large diameter, closely spaced, conducting tubular SMABF elements. EM simulations can be used for design of prototype system. Use of resistive (dummy) elements at the edges of the array can be used to avoid performance degradation at the edge of the array due to abrupt changes. Once the simulated design meets the desired specifications, then an initial array layout configuration can be selected and optimized by observing the performance using a vector network analyzer. A vector network analyzer is used to measure the return loss (antenna reflection coefficients).

Obviously, any implementation of SMABF is a complicated and expensive as compared to existing solutions. Moreover, practical implementation of SMABF integrated with soil moisture sensing, and optimization is a challenging task. Decreasing cost and complexity of hardware, and importance of long range, high data rate UG com-

munications, compared to conventional solutions, makes SMABF a viable candidate for next generation wireless UG communication systems.

7.9 Conclusions

In this chapter, a soil moisture adaptive UG beamforming technique has been developed. It has been shown that when lateral wave in UG communication is exploited using SMABF, it results in improved performance of the UG communications. Soil moisture variations, change in wavelength and directivity have been identified as main challenges in UG beamforming communications. A method has been developed to find the optimal angle to focus energy in the desired direction based on soil moisture changes. SMABF is validated through simulations and empirical evaluations. Directivity analysis of the array has been presented in different soils for different soil moisture levels. SMABF outperformed both OTA fixed and soil fixed nonadaptive beamforming systems under different soil moisture levels in different soils.

Chapter 8

Wireless Underground Channel Diversity Reception with Multiple Antennas for Internet of Underground Things

Internet of underground things (IOUT) is an emerging paradigm which consists of sensors and communication devices, partly or completely buried underground for real-time soil sensing and monitoring. In this chapter, the performance of different modulation schemes in IOUT communications is studied through simulations and experiments. The spatial modularity of direct, lateral, and reflected components of the UG channel is exploited by using multiple antennas. First, it has been shown that bit error rates of 10^{-3} can be achieved with normalized delay spreads (τ_d) lower than 0.05. Evaluations are conducted through the first software-defined radio-based field experiments for UG channel. Moreover, equalization has a significant impact on the performance improvement of an IOUT system. An 8-Tap DFE (decision-feedback equalizer) adaptive equalizer achieves better performance. It is also found that DBPSK, and DPSK are more suitable for digital communications in the UG channel without adaptive equalization. Then, two novel UG receiver designs, namely, 3W-Rake and Lateral-Direct-Reflected (LDR) are developed and analyzed for performance improvement. It has been shown that with a three antenna LDR design, BER of lower than 10^{-5} can be achieved. The BER of these two approaches are compared

and the LDR has been shown to perform better.

8.1 Motivation

The realization of the high data rate, and long-range wireless underground (UG) communications is one of the major enabling factors of the Internet of Underground Things (IOUT) [155]. The delay spread of the UG channel causes performance degradation and leads to frequency selective fading (Chapter 4). This effect restricts the data rates in the UG channel and results in irreducible bit error rates (BER). The impact of the delay spread, soil moisture, soil type, and frequency selective fading due to the delay spread is an important issue in the UG communications channel [155, 158]. The UG communications system should have the ability to adjust to soil dynamics such as soil moisture variations, and also support high data rate communications with low BER [74]. Due to these factors, characterization and performance analysis of the UG channel is a challenging task.

In [74], we have employed the channel capacity as a tool for IOUT system performance analysis. However, to date, a study to analyze the performance of digital modulation schemes in an IOUT system employing the wireless UG channel as a communication medium is unavailable. These effects are investigated in this work by using the detailed impulse response data of the wireless underground communications channel (Chapter 4).

In this chapter, we develop a model to generate the channel impulse response from measured data and use it to simulate a fully functional IOUT communications system using conventional modulation schemes, i.e., pulse-amplitude modulation (PAM), differential phase shift keying (DPSK), quadrature phase shift keying (QPSK), m-ary quadrature amplitude modulation (MQAM), and Gaussian minimum-shift keying

(GMSK). The purpose of this work is to analyze the impact of the normalized RMS delay spread on the digital modulation in the UG channel by using measured UG channel responses, and to optimize the IOUT communications system design parameters such as modulation scheme and bit error rates. Adaptive equalization of the UG frequency selective fading channel has also been considered in this work and it has been shown that the use of adaptive equalization in the UG channel leads to performance improvements.

Moreover, in this chapter, issue of design of a UG receiver based on lateral, direct and reflected components of the wireless UG channel is addressed. We develop two novel techniques, 1) a single antenna 3W-Rake receiver to combat multipaths effects, 2) a spatial diversity multi-antenna Lateral-Direct-Reflected (LDR) receiver, which exploits the spatial modularity and angular diversity found in the propagation environment of the wireless UG channel. We describe the 3W-Rake and LDR system models, and analyze their performance in different soil types, depths, distances, and soil moisture levels. The results reported in this work are useful for design and optimization of a wireless IOUT communications system.

The rest of the chapter is organized as follows: The related work is discussed in Section 8.2. The description of wireless UG channel model is given in Section 8.3. System models are described in Section 8.4. Performance evaluations are performed in Section 8.5. We conclude in Section 8.6.

8.2 Related Work

Underground communications in IOUT has many applications in precision agriculture [39], [51], [76], [159], [23], [156], [189], [199], border monitoring [40], [181], land slide monitoring, and pipeline monitoring [180], [200]. A detailed characterization of the

wireless UG channel has been provided in [158]. Impacts of soil type and moisture on the capacity of multi-carrier modulations are discussed in [155]. However, to the best of our knowledge, no performance analysis of digital modulation schemes has been carried out in the electromagnetic (EM) based UG wireless communication channel. Capacity analysis [125], has been done for magneto-inductive (MI) based UG communications [35], [184], but it cannot be readily applied to IOUT because the spatial multipath modularity does not exist in MI, and sender-receiver coils have to be parallel to each other in MI-communications.

To the best of our knowledge, this is the first work to analyze the performance of digital wireless UG channel receivers in IOUT and to analyze the impact of normalized delay spread, and different modulation schemes on the bit error rate of wireless UG channel.

8.3 Background

Despite the recent developments in wireless UG communications, the communication ranges are still limited for many potential applications. Therefore, advanced communication techniques, designed based on the unique characteristics of the wireless UG channel, are required. A robust IOUT communication system can be designed through physical insight into the propagation characteristics of the wireless UG channel. A channel model for UG communications has been developed in [158] and has been validated empirically. Direct, lateral, and reflected components have been identified at the UG receiver. Direct wave (D-wave) propagates through the soil in the line-of-sight (LOS). Reflected wave (R-wave) is reflected from the soil air interface and reaches at the receiver. The lateral wave (L-wave) propagates along the soil-air interface and continuously diffuses inward to reach at the receiver. L-wave is the

strongest component as it suffers low attenuation when passes through the air along the soil-air interface as compared to the reflected and direct wave which undergoes higher attenuation due to the high losses in soil medium.

The UG channel impulse response is expressed as a sum of direct, reflected and lateral waves [158]:

$$h_{ug}(t) = \sum_{l=0}^{L-1} \alpha_l \delta(t - \tau_l) + \sum_{d=0}^{D-1} \alpha_d \delta(t - \tau_d) + \sum_{r=0}^{R-1} \alpha_r \delta(t - \tau_r) \ , \tag{8.1}$$

where L, D, and R are number of multipaths; α_l, α_d, and α_r are complex gains; and τ_l, τ_d, and τ_r are delays associated with lateral wave, direct wave, and reflected wave, respectively.

The measurements have been taken both in indoor testbed and field settings. The indoor testbed and experiment layout has been shown in Fig. 3.2(e). In the indoor testbed, three sets of four dipole antennas are buried at a distances of 50 cm, at the depths of 10 cm, 20 cm, 30 cm, and 40 cm. Silt loam and sandy soils are used in the indoor testbed. In the outdoor testbed, antennas are buried at 20 cm depth up to 12 m distance. Agilent FieldFox N9923A Vector Network Analyzer (VNA) is used to measure channel transfer functions. More details about the testbed development, measurement procedures, experiments, and results can be found in Chapter 3 and Chapter 4.

8.4 System Models

Let $u(t)$ be the baseband input to the UG channel, the convolution of the h_{ug} with $u(t)$ gives the received signal output waveform.

$$z(t) = u(t) * h_{ug} \ , \tag{8.2}$$

which can be expressed as:

$$z(t) = \sum_{l=0}^{L-1} \alpha_l u(t - \tau_l) + \sum_{d=0}^{D-1} \alpha_d u(t - \tau_d) + \sum_{r=0}^{R-1} \alpha_r u(t - \tau_r) \ . \tag{8.3}$$

In this analysis, we normalize UG channel delay spread τ_d based on the sample period T and RMS delay spread (τ_{rms}), where τ_d is given as:

$$\tau_d = \frac{\tau_{rms}}{T}. \tag{8.4}$$

Bandwidth can be expressed as $BW = 1/T$. For the modulation schemes considered, signaling waveform $u(t)$ is convolved with h_{ug}. Both rectangular, and raised cosine pulses are used for signaling. Raised cosine filter helps to minimize ISI and is realized through raised cosine spectrum with roll-off factor β. At the receiver, we compute the BER performance.

The UG channel impulse responses, h_{ug}, used in this analysis are sampled from measured power delay profiles (PDP) in different soils under different soil moisture conditions at different depths and distances. In this work, we do not use coding schemes, and results reported in this work are without employing coding. A detailed analysis of the error correcting coding schemes in the UG channel is given in [73]. Use of coding improves the performance of the system at the cost of increased complexity

and energy consumption of the UG receiver. Performance analysis using conventional receiver approach results in high error rates (Section 8.5). A 3W-Rake receiver design is developed next to mitigate the effects of multipath fading and to improve system performance.

8.4.1 UG 3W-Rake Receiver

In this section, a UG receiver design without spatial diversity is presented. Since three components, namely, direct, lateral, and reflected wave are resolvable, this approach is based on the use of RAKE [148] to resolve three independently faded components by exploiting the high diversity in the three components. UG 3W-Rake consists of three branches, one for each of the lateral, direct, and reflected components. In the UG 3W-Rake receiver, each branch correlates the received signal with its specified component to separate the three components.

Due to the UG multi-path fading phenomena, the received instantaneous signal-to-noise ratio (SNR) is a random process. Therefore, we average the Additive White Gaussian Noise (AWGN) error probability over the probability density function (pdf) of the SNR γ_b. The average BER probability, $P_b(\bar{\gamma}_b)$, of the UG 3W-Rake is calculated as [148]:

$$P_b(\bar{\gamma}) = \int_0^\infty P_{e|\gamma_b} p(\gamma_b)\ d\gamma_b, \tag{8.5}$$

where $\bar{\gamma}_b$ denotes the average SNR per bit, $P_{e|\gamma_b}$ is the conditional AWGN error probability, and $p(\gamma_b)$ is the pdf of SNR. Since, no close form solution of the pdf of the γ_b is available for the UG channel, we determine $p(\gamma_b)$ from experimental UG channel impulse response measurements [158] by averaging $P_{e|\gamma_b}$ over the instantaneous SNR for each measured response. Since UG 3W-Rake can process multipaths in all the

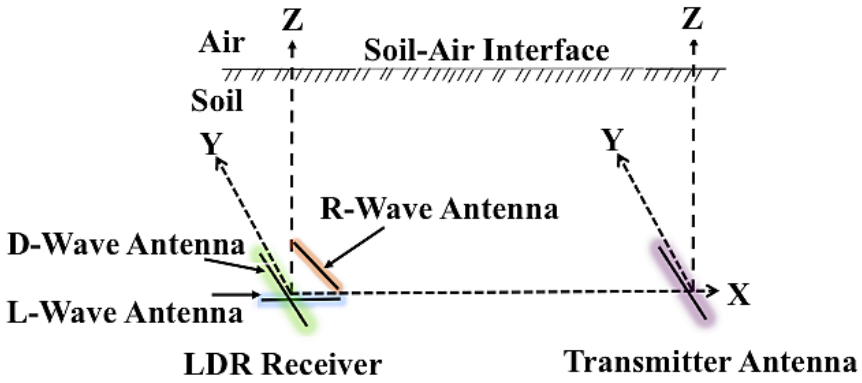

Figure 8.1: LDR antenna orientation.

three components, received per bit SNR γ_b is expresses as:

$$\gamma_b = \sum_{l=0}^{L-1} \gamma_l + \sum_{d=0}^{D-1} \gamma_d + \sum_{r=0}^{R-1} \gamma_r \ , \tag{8.6}$$

where L, D, and R are number of multipaths; γ_l, γ_d, and γ_r are gains associated with lateral wave, direct wave, and reflected wave, respectively. (8.6) can be rewritten as:

$$\gamma_b = \frac{E_b}{N_0} \left[\ \sum_{l=0}^{L-1} |\gamma_l|^2 + \sum_{d=0}^{D-1} |\gamma_d|^2 + \sum_{r=0}^{R-1} |\gamma_r|^2 \ \right], \tag{8.7}$$

where energy per bit to noise PSD (power spectral density ratio), $\frac{E_b}{N_0}$, is given as:

$$\frac{E_b}{N_0} = \frac{P_t T}{N_0 PL}, \tag{8.8}$$

where P_t is the transmitted power, T is the sample period, N_0 is noise density, and PL is the path loss.

Through this procedure, a discrete $p(\gamma)$ is approximated. Once $p(\gamma)$ is determined for 3W-Rake, the average bit error probability, $P_b(\bar{\gamma})$, is calculated by using (8.5). In the next section, we extend the idea of 3W-Rake to the Lateral-Direct-Reflected (LDR) case to exploit spatial modularity of the UG channel.

8.4.2 LDR Receiver Design

In this section, a novel LDR diversity reception technique is developed. LDR is based on the knowledge of the angular arrival, delay spreads, and travel paths of three EM wave components in the UG channel. This approach offers considerable performance improvement over the conventional matched filter based UG receiver and 3W-Rake. Three antennas are used to combine direct, lateral, and reflected wave multipath components, which eliminate multipath fading of the wireless UG channel. Delay spreads of the wireless UG channel presented in [158], provide a detailed insight into the propagation characteristics of the wireless UG channel. As discussed in Section 8.3, there exists a natural spatial modulation (SM) in the UG channel in the form of direct, lateral, and reflected waves. However these three waves cause inter-symbol-interference and lead to performance deterioration of an IOUT system. By the LDR receiver design, these issues are addressed and performance is improved by eliminating interference between these three components.

LDR Antenna Orientation: We consider an IOUT system where both transmitter and receiver are buried underground. Transmitter has a single antenna, whereas, receiver has three antennas, each for one of the three components. For UG channel diversity reception, the following antennas are configured: the antenna designated to receive the D-wave is at 90° from the x-axis; the R-wave antenna is at a line connecting x-z axis, with center at 45° from x-axis; whereas, L-wave antenna is placed at 0° from the x-axis. For this orientation, to avoid any variations in receiver's axis, transmitter and receiver are assumed to be on the same depth on a straight line along the x-axis. LDR antenna orientation is shown in Fig. 8.1.

LDR System Model: Based on the LDR antenna orientation of one transmitter

antenna and three L, D, and R-wave antennas, the received signal is expressed as:

$$\boldsymbol{z} = \boldsymbol{h_{ug}} u + \boldsymbol{n} \tag{8.9}$$

where u is the transmitter's data symbol, $\boldsymbol{z}$ is a 3×1 received output vector, $\boldsymbol{h_{ug}}$ is the channel vector representing the L, D, and R-wave channel response, and $\boldsymbol{n}$ is the 3×1 noise vector. For each component antenna, the channel response is separable and is denoted as h_d, h_l, and h_r, for the direct, lateral and reflected components, respectively. At the each receive component, the instantaneous SNR is defined as:

$$\gamma_i = \frac{E_b |h_i|^2}{N_0}, \tag{8.10}$$

where i represents the L, D, and R components.

Optimum Maximum Ratio Combining (MRC-LDR): By using maximum ratio combining (MRC) [148], LDR can achieve three times SNR enhancement as compared to the SNR of a single antenna matched filter UG receiver:

$$\gamma = \sum_{i=1}^{3} w_i \frac{E_b |h_i|^2}{N_0}, \tag{8.11}$$

where w_i is the combining weight. MRC-LDR achieves the maximum gain, however the interference from the reflected components is still present. Therefore, to suppresses undesired interference adaptive switching and selection is presented next.

Adaptive Combining (AC-LDR): Based on the proximity of the LDR receiver, either the D-wave or L-Wave component is dominant at the receiver. AC-LDR exploits this by adaptively switching and selecting the strongest L, or D-Wave (R-Wave is not considered because it is the weakest component and results in performance degradation), such that:

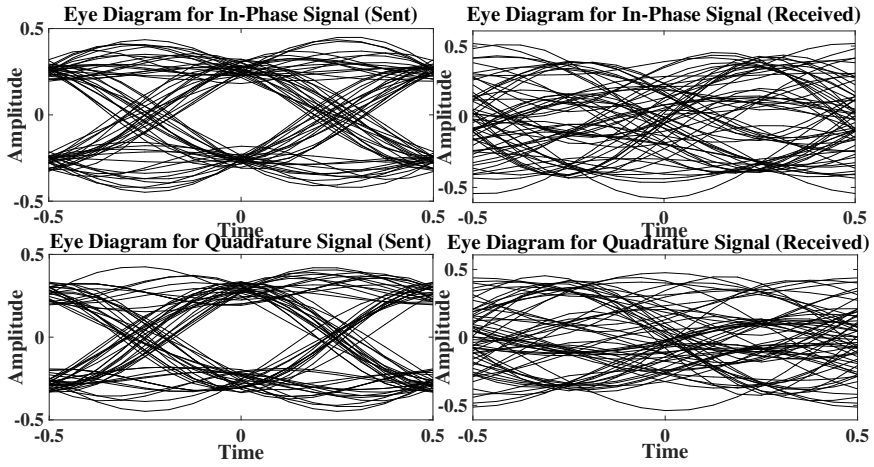

Figure 8.2: QPSK eye patterns of transmitted and received signals.

$$\gamma = \begin{cases} \frac{E_b|h_L|^2}{N_0}, & \text{if } |h_L|^2 > |h_D|^2, \\ \frac{E_b|h_D|^2}{N_0}, & \text{otherwise.} \end{cases} \tag{8.12}$$

The main difference between MRC-LDR and AC-LDR is that AC-LDR removes all the interference at the cost of channel gain. The average BER probability, $P_b(\bar{\gamma}_b)$, of the both LDR approaches is calculated as [148]:

$$P_b(\bar{\gamma}) = \int_0^\infty P_{e|\gamma_b} p(\gamma_b)\ d\gamma_b, \tag{8.13}$$

8.5 Performance Analysis

Since UG channel multipath power delay profile depends mainly on the soil type and moisture, depth, and distance of the UG transmitter and receiver, in this study, we simulate the UG channel with τ_d range of 0.4-0.002. In Section 8.5.1, we analyze the performance of the coherent modulation schemes. Empirical evaluation results are presented in Section 8.5.2. Differential detection schemes in UG channel are evaluated in Section 8.5.4. Performance analyses of 3W-Rake and LDR are presented

in Section 8.5.5, and 8.5.6, respectively. Finally, implementation issues are discussed in Section 8.5.7.

8.5.1 Coherent Detection

Four digital modulation schemes, namely, PSK, QAM, PAM, and MSK are evaluated in this section. Performance of these four modulation schemes has been compared for an UG channel in silty clay loam soil. The soil moisture level is 0 CB[1] and τ_{rms} is 25 ns. The transmitter and receiver distance is 50 cm and these are buried at 20 cm depth. Our analysis reveals high error rates of higher than 10^{-1} for all four modulation schemes. In the UG channel propagation environment is highly degraded due to the multipath fading which is the main cause of the worst performance of the coherent modulation in the UG channel. Moreover, coherent modulation requires exact knowledge of the channel state. Due to higher delay spreads in the UG channel, reference symbol tracking is difficult to implement. It is also interesting to note that for τ_d range 0.002-0.4, error rate does not change, which indicates that error floor is irreducible and does not depend on the sample time. This suggests that the performance of the digital modulations in the UG channel is severely effected by the multipath fading, and increasing the transmit power of the UG the transmitter will not result in reduction of error rate.

To further investigate the cause of high error rates, we plot the constellation and eye diagrams. In Fig. 8.2 and 8.3(a), the constellation and eye diagrams are shown for QPSK modulation in the UG channel. It can be observed from Fig. 8.2 that eye suffers from severe performance deterioration (both horizontal and vertical closure) due to inter symbol interference and large delay spreads between the three

[1]Soil moisture expressed as soil matric potential (CB); greater matric potential values indicate lower soil moisture and zero matric potential represents near saturation condition

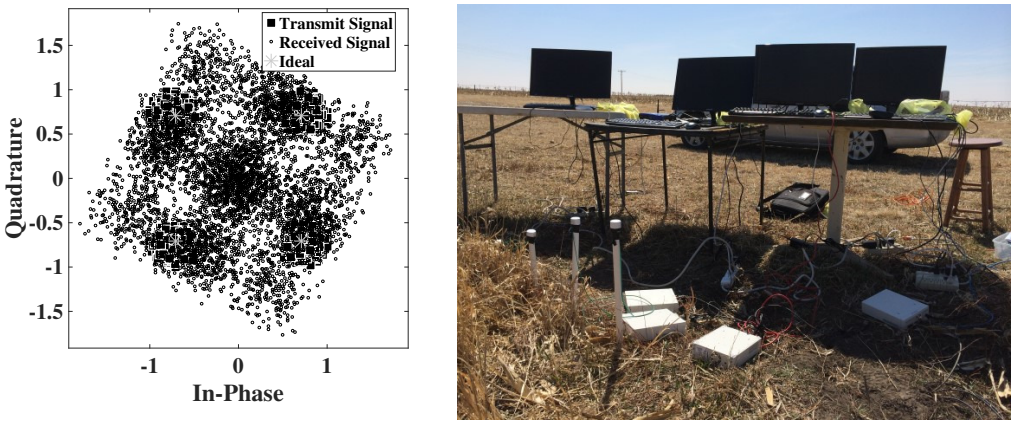

(a) (b)

Figure 8.3: a) Constellation diagram of QPSK, b) BER experiment layout in the silty clay loam soil.

components. Complete eye closure due to these phenomena has led to high error rates. These simulations results are validated with empirical evaluations. Empirical results are shown in the next section.

8.5.2 Experimental Evaluation

In this section, first, we describe the experimental setup and validation, and then results are shown.

8.5.2.1 Setup

To analyze the BER performance of the UG channel, we conducted experiments using GNU Radio [89] and Ettus N210 USRPs [80]. Dipole antennas in these experiments are buried at 20 cm depth at a distance of 50 cm in silty clay loam soil. Soil moisture level is 50 CB and $\tau_{rms} = 25.67$ ns [158]. Transmitter-Receiver (TR) are synchronized by using a MIMO cable. Transmit power is 10 dBm. The operation frequency range is from 100 MHz to 300 MHz. Normalized delay spread τ_d range is 0.005-0.43. A series of sequences of 1000 bits are sent from transmitter using amplitude-shift keying (ASK) modulation. At the receiver side, error statistics of the channel are obtained

by comparing the output with input. For each τ_d, we calculate the bit error rate by adding the bits in error of each correct symbol and then dividing this sum by total number of bits in all symbols at receiver. Experimental setup is shown in Fig. 8.3(b).

8.5.2.2 Empirical Results

Evaluations are conducted through the first software-defined-radio (SDR) based field experiments for UG channel. BER results of empirical ASK are evaluated for τ_d range of 0.005-0.43. Empirical results also exhibit very high error rate (higher than 10^{-1}) and show vulnerability of UG communications to the multipath fading of the UG channel. Since, transmitter and receiver are synchronized, and reference signal is available at the receiver, which confirms that, in UG channel, in addition to the timing and phase recovery issues which effect the performance of the coherent modulation schemes, an additional factor of delay distortion of three major multipath components significantly impacts the performance of coherent modulation techniques in the IOUT environment. In over-the-air (OTA) channels, use of adaptive equalization [148] is very effective against this type of performance deterioration (ISI and multipath fading). Therefore, we investigate the use of adaptive equalization to overcome these effects in the UG channel. In the next section, we analyze the performance of equalization in the UG channel.

8.5.3 Performance of Equalization in the UG Channel

In this section, we analyze of the performance of PSK modulation in the UG communication channel. PSK is used because adaptive equalization works best for constant modulus modulation [148] as compared to ASK. Three equalization scenarios are considered. All three uses training sequences for equalization. These three cases are explained below:

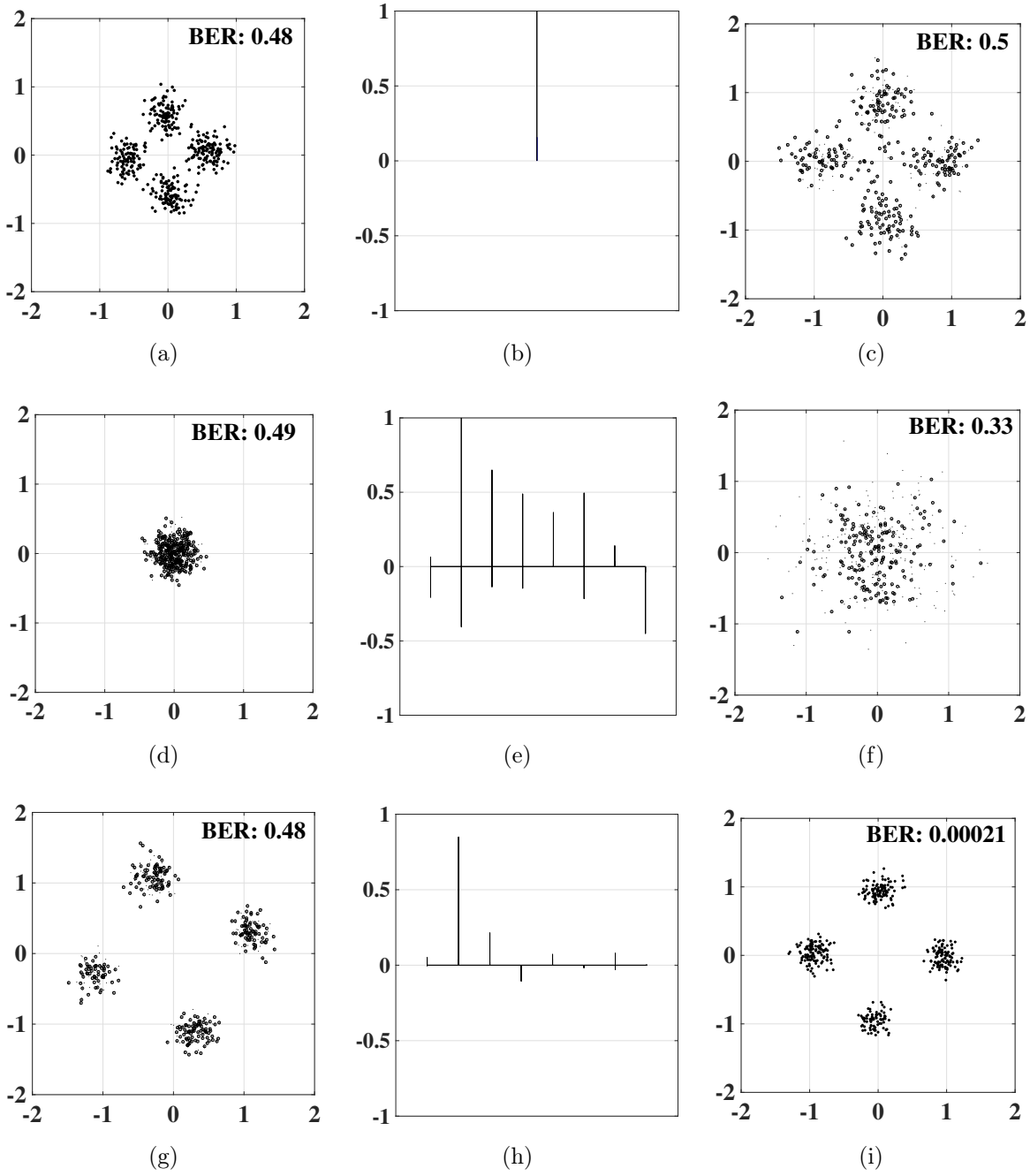

Figure 8.4: Single tap linear equalizer: a) Received constellations b) Equalizer weights, c) Equalized constellations. Eights tap linear equalizer: d) Received constellations. e) Equalizer weights f) Equalized constellations. DFE (decision-feedback equalizer) with two tap feedback weights and a six tap feedforward filters: g) Received constellations, h) Equalizer weights, i) Equalized constellations.

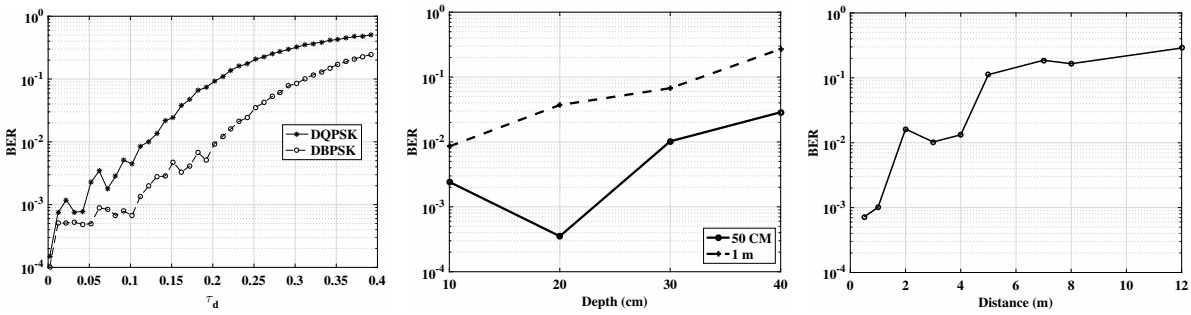

(a) (b) (c)

Figure 8.5: Average BER performance comparison: (a) Differential BPSK and QPSK at τ_{rms} 25 ns, (b) With burial depth at 50 cm and 1 m distance in silt loam soil, (c) With distance at 20 cm depth for distances up to 12 m in silty clay loam soil.

Case 1 - Single Tap Linear Equalizer: Single tap least-mean square (LMS) equalizer is used with phase and gain control. Modulation scheme is QPSK, and 50 blocks are transmitted in each simulation run. *Case 2 - Eight Tap Linear Equalizer:* In this case, simulations are performed by using eight tap linear recursive least square (RLS) equalizer with QPSK modulation and 50 blocks are transmitted. *Case 3 - Adaptive Equalization:* In this case, adaptive equalization is performed in the receiver using a decision-feedback equalizer (DFE) with two tap feedback weights and a six tap feedforward filters. The DFE uses an eight-tap linear recursive least squares (RLS) equalizer with symbol spaced taps.

In Figs. 8.4(a)-8.4(c), results of the single tap linear equalizer are shown. Received constellation with equalization is shown in the Fig. 8.4(a) with BER of 0.48. Equalizer weights are shown in Fig. 8.4(b). It can be observed from Fig. 8.4(c) that use of single tap equalizer does not improve the receiver performance and BER remains unchanged (0.5). In Figs. 8.4(d)-8.4(f), performance of the eight tap linear equalizer is shown. In Fig. 8.4(d), the received constellation with BER of 0.49 is shown. It can be observed that increase in number of taps (Fig. 8.4(e)) has made some improvements, but received constellation was severely corrupted therefore it only results in minor gain and BER has reduced from 0.49 to 0.33 (Fig. 8.4(f)).

Adaptive equalization performance is shown in the In Figs. 8.4(g)- 8.4(i). Received constellation (Fig. 8.4(g)) has the BER of 0.48, and it can be observed that use of 8-tap adaptive equalizer (Fig. 8.4(h)) has removed most channel distortions and results in BER less than 10^{-3}. Improvements in the equalized constellations are clearly visible in Fig. 8.4(i). From these results, it can be observed that performance of an unequalized UG communication system is limited due to the UG channel propagation characteristics and inter symbol interference (ISI). Therefore, increase in the transmit power does not lead to substantial performance improvements. Hence, use of equalizer is required in UG communications for a reliable communication system design. By equalization, ISI is removed which leads to performance improvement. Our analysis shows that minimum size of DFE equalizer should be 8-tap with two tap feedback weights and a six tap feedforward filters. In the next section, we evaluate the performance of the differential detection schemes in the UG channel.

8.5.4 Differential Detection

In this section, performance of the UG channel communications is evaluated by using differential binary phase shift keying (DBPSK), and differential quadrature phase shift keying (DQPSK). In Fig. 8.5(a), BER performance comparison of DBPSK, and DQPSK for τ_{rms} 25 ns is shown. Since soil moisture is a slowly changing phenomena, variations in the UG channel response are slow. The channel estimation (carrier accusation and tracking) is not required in the differential detection at the UG receiver. Instead, symbols received in the previous symbol period are used as phase reference in the current symbol period, therefore differential technique works better in the UG channel as compared to coherently detected modulation schemes. It can be observed that for normalized delay spread τ_d values of less than 0.1 error rate has decreased to 10^{-3} as compared to the 10^{-1} error rate of the coherent modulation schemes. It can

also be observed that performance of the UG channel starts to degrade with higher τ_d. For τ_d greater than 0.2, error rate is higher than the 10^{-2} for both DBPSK and DQPSK. However, differential schemes still perform better than the 10^{-1} BER of coherent modulation.

8.5.5 3W-Rake Performance in UG Channel

In this section, we evaluate the performance of UG 3W-Rake receiver. In the UG channel, SNR required for the target BER threshold is analyzed for different modulation schemes. Different factors such as soil type and soil moisture affects the UG communications. Therefore, we consider different representative scenarios of the UG communications in silt loam, sandy, and silty clay loam soils; for soil moisture level of 0-50 CB, at depths of 10 cm, 20 cm, 30 cm, and 40 cm; and distances up to 12 m. As discussed in Section 8.5.5, we need to determine the $p(\gamma_b)$ to compute the average BER, $P_b(\bar{\gamma})$, in the UG channel. We get the SNR from empirical impulse responses [155], [158] and evaluate performance for τ_d of 0.01, and measured noise density of $1E-15$, in PAM modulation.

In Fig. 8.5(b), average BER with burial depth at 50 cm and 1 m distance in silt loam soil is shown. BER for 40 cm depth are highest as compared to shallow depths. It can be observed that at 50 cm distance, BER first decreases from 10 cm to 20 cm depth, and then increases at 30 cm and 40 cm depth. This happens because at shallow 10 cm depth, reflections from surroundings affect the received signal. With increase in burial depth at 1 m distance, BER increases, which is caused by the additional attenuation of the EM waves at higher depths. Error rates further increase with increase in transmitter-receiver (TR) distance from 50 cm to 1 m. BER in silty clay loam soil at 20 cm depth for distances up to 12 m is shown in Fig. 8.5(c). BER of 10^{-3} are observed for distances less than 1 m, and BER of 10^{-2} can be achieved

for distances up to 4 m. For distances higher than 5 m, error rates are higher than 10^{-1}. Increase in propagation loss of the all three components with distance causes higher attenuation and lead to higher BER. Degradation in system performance can be improved by utilizing the error correcting codes [73] for larger distances in the UG channel.

In Fig. 8.6(a), change in average BER with soil moisture at 50 cm and 1 m distance in silt loam soil is shown. It can be observed that decrease in soil moisture from 10 CB to 50 CB leads to variations in BER for both 50 cm and 1 m distance. At 50 cm depth, from 10 CB to 50 CB change in soil moisture, BER decreased first and then increases as soil moisture decreases. This is caused by water repellency of soil texture where water infiltration is slowed momentarily at high soil moisture levels. Moreover, change in soil moisture impacts the attenuation through which UG channel undergoes due to the absorption of the EM waves by the water contained in the different horizons of the soil. In the next section, we evaluate the performance of the LDR technique.

8.5.6 LDR Performance Analysis

Let us now consider performance improvement with LDR. We use normalized delay spread, $\tau_d < 0.1$. Results of the comparison of 3W-Rake with MRC-LDR and AC-LDR are shown in Fig. 8.6(b). It can be observed that both LDR outperform the 3W-Rake and substantial BER performance improvement is realized for SNRs greater than 13 dB. BER of 10^{-3} is achieved with E_b/N_0 of 15 dB in MRC-LDR, which is 18 dB smaller as compared to E_b/N_0 required for 3W-Rake, which is 33 dB. This is attributed to the LDR diversity, because, in the LDR three main components are sampled through the use of separate antennas for each direct, lateral, and reflected component, whereas for 3W-Rake performance suffers because of the bottlenecks in correlation of the three components.

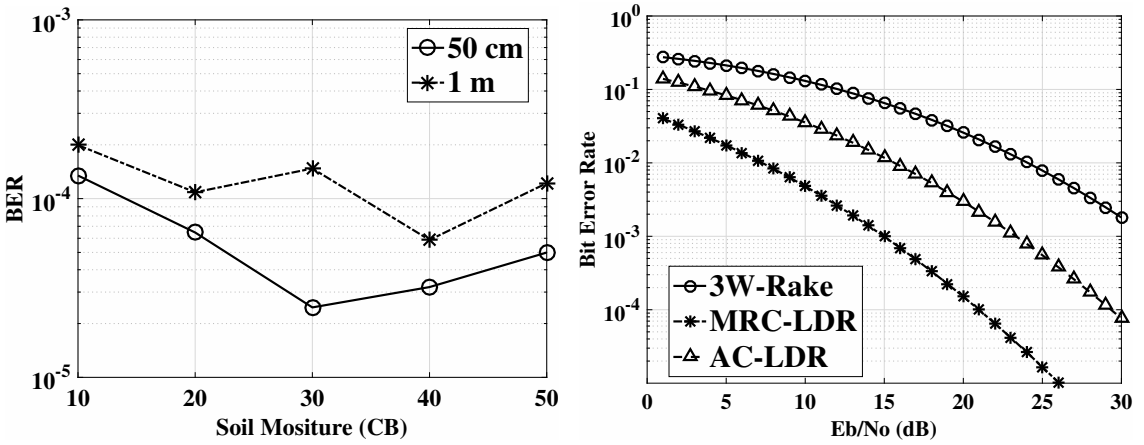

Figure 8.6: a) Variations in average BER with change in soil moisture at 50 cm and 1 m distance in silt loam soil, b) Comparison of 3W-Rake, MRC-LDR, and AC-LDR.

8.5.7 LDR Implementation

Although, the implementation of the LDR is much more complex as compared to conventional matched filter, adaptive switched selection combining is easy to implement, especially with dominant a L-wave or D-wave. AC-LDR can be implemented through zero-forcing (ZF) precoding, which inverts the channel matrix to remove the undesired components. Moreover, optimum MRC combining requires extra hardware due to co-phasing and weighing requirement and is practical through digital signal processing (DSP) hardware. Therefore, optimum MRC combining can be used as benchmark for theoretical performance analysis of the wireless UG channel, as it allows to analyze the performance improvements by using the LDR diversity approach in IOUT. However, keeping in view the importance of high data rate and long distance communications in wireless UG channel, LDR lends itself into consideration for the next generation IOUT system architecture.

8.6 Conclusions

This chapter has reported the performance analysis of different modulation schemes of the UG wireless communication channel in an IOUT system. Adaptive equalization has been shown to be effective against the high delay spread and multipath fading in the UG channel. Novel UG receiver designs for the IOUT have been developed and performance analysis has been done by presenting the BER curves under different soil moisture levels for different depths and distances. Various physical phenomena of soil medium have been shown to impact the BER performance of the UG channel. With change in soil moisture, communications distance, and depth, the IOUT system performance can be determined from our results. The analysis show promising performance improvements with UG 3W-Rake and LDR receivers in IOUT.

Chapter 9

Underground Dipole Antennas for Communications in Internet of Underground Things

The realization of Internet of Underground Things (IOUT) relies on the establishment of reliable communication links, where the antenna becomes a major design component due to the significant impacts of soil. In this chapter, a theoretical model is developed to capture the impacts of change of soil moisture on the return loss, resonant frequency, and bandwidth of a buried dipole antenna. Experiments are conducted in silty clay loam, sandy, and silt loam soil, to characterize the effects of soil, in an indoor testbed and field testbeds. It is shown that at subsurface burial depths (0.1-0.4m), change in soil moisture impacts communication by resulting in a shift in the resonant frequency of the antenna. Simulations are done to validate the theoretical and measured results. This model allows system engineers to predict the underground antenna resonance, and also helps to design an efficient communication system in IOUT. Accordingly, a wideband planar antenna is designed for an agricultural IOUT application. Empirical evaluations show that an antenna designed considering both the dispersion of soil *and* the reflection from the soil-air interface can improve communication distances by up to five times compared to antennas that are designed based on *only* the wavelength change in soil.

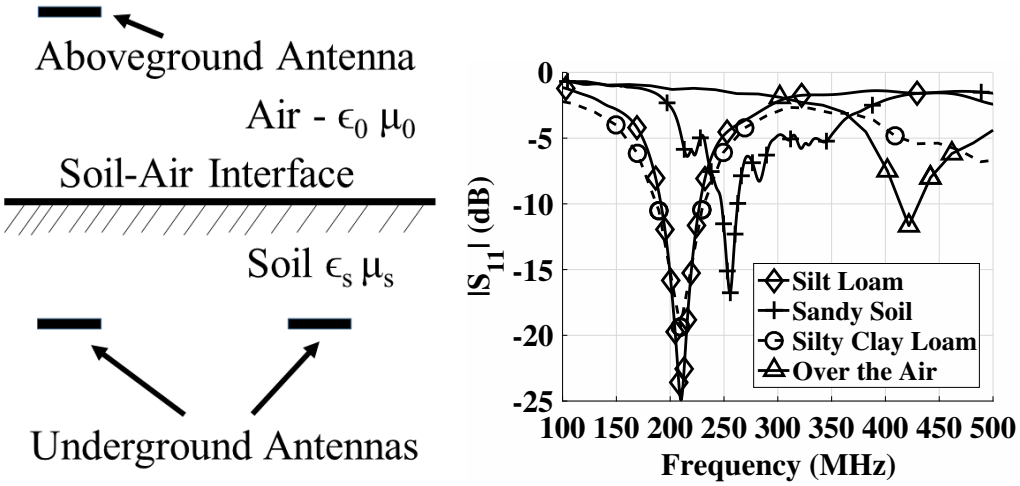

(a) Buried antennas

(b) Return loss of a UG antenna

Figure 9.1: Underground Communications Scenario.

9.1 Motivation

Internet of underground things (IOUT) are a natural extension of Internet of Things (IoT) to underground settings. IOUTs include sensor motes that are buried in soil and provide applications in precision agriculture [70], [158], [156], [157], [166], border patrol, pipeline monitoring, environment monitoring [35], [152, 159, 189, 188], and virtual fencing [39]. The main challenge towards the realization of IOUT is the establishment of reliable wireless communication links. In this aspect, several challenges exist for the design of an antenna that is suitable for underground (UG) communication. Particularly, input impedance of the UG antenna is a function of soil properties, soil moisture, operation frequency, and burial depth [217].

In this chapter, we consider three major factors that impact the performance of a buried antenna. First, due to higher permittivity and frequency dispersion of soil compared to that of air, the wavelength of the electromagnetic wave propagating in soil is significantly different than that in air. Second, soil moisture changes over time with the natural precipitation or irrigation, which dynamically impacts the permittivity of soil. This causes variations in the antenna wavelength. Third, a unique

challenge is posed by the difference in electromagnetic wave propagation mechanism in underground and aboveground communications links (Figs. 9.1). In underground to underground link, lateral wave [121] is the most dominant contributor of the received signal strength at the receiver [54], [158], [155]. Lateral wave travels along the surface and continuously makes ingress to the soil to reach the receiver. It suffers lowest attenuation as compared to other direct and reflected components which have their total path through the soil. Due to these factors, an impedance matched antenna for over-the-air (OTA) communication will not be matched in soil (Fig 9.1(b)) and separate antenna designs are required for optimal underground and aboveground communication links. Our experiments show that these changes in wavelength is an important factor to consider in the design of an underground antenna. In Fig. 9.1(b), when a 433 MHz dipole antenna is buried underground, a 47 % (229 MHz) shift in resonant frequency can be observed in silt loam soil in comparison to OTA case. Therefore, an underground communication system should be designed to account for this shift due to soil medium. Moreover, the variations in wavelength over different soil moisture values dictate that an underground antenna should accommodate a wide range of wavelengths.

In this chapter, we first develop an UG antenna impedance model to capture these effects on buried dipole antennas. The model is then compared with simulations and experimental results. Experiments are conducted using antennas buried in silt loam, sandy, and silty clay loam to verify the impact of soil moisture and burial depth on the performance of dipole antenna in three different types of soil. Based on the insight gathered from the experiments, it is highlighted that for the design of an underground antenna, it is desirable to have the ability to adjust its operation parameters such as radiation pattern, and operation frequency based on dynamic changes in soil moisture.

To the best of our knowledge, no return loss measurements are available to show

the impact of soil-air interface, soil properties, and soil moisture on the return loss of underground dipole antenna and this is the first work to present this analysis. The rest of the chapter is organized as follows: In Section 9.2, related work on communication in medium and the impact of the medium on antenna impedance is introduced. The impedance and the return loss of dipole antenna buried in soil are analyzed theoretically in Section 9.3, where an antenna impedance model is developed. Underground antenna simulations and experiments setup is presented in Section 9.4. Validation of theoretical, simulated and measured results are shown in Section 9.5. Antenna considerations in design of an Internet of underground communication systems are discussed in Section 9.6. The chapter is concluded in Section 9.7.

9.2 Related Work

Antennas used in IOUT are buried in soil, which is uncommon in traditional communication scenarios. Over the entire span of 20^{th} century, starting from Sommerfeld's seminal work [174] in 1909, electromagnetic wave propagation in subsurface stratified medias has been studied extensively [42], [45], [48], [71], [99], [138], [169], [182], [202], [207], and effects of the medium on electromagnetic waves has been analyzed. However these studies analyze fields of horizontal infinitesimal dipole of unit electric moment, whereas for practical applications, a finite size antenna with known impedance, field patterns, and current distribution is desirable. Here, we briefly discuss major contributions of this literature. Field calculations and numerical evaluation of the dipole *over* the lossy half space are first presented in [142]. EM Wave propagation *along* the interface has been extensively analyzed in [202]. However, these studies can not be applied to antennas buried underground. Analysis of a dipole buried *in* a lossy half space is presented in [138]. By using two vector potentials, the depth attenua-

tion factor and ground wave attenuation factor of far-field radiation form UG dipole was given. However, reflected current from soil-air interface is not considered in this work. In [45], field components per unit dipole moment are calculated by using the Hertz potential which were used to obtain the EM fields. The work in [138] differs from [45] on the displacement current in lossy half space, where former work does not consider the displacement current. In [182], fields from a Hertzian dipole immersed in an infinite isotropic lossy medium has been given. King further improved EM fields by taking into account the half-space interface and lateral waves [121, 212]. In King's work, complete EM fields, from a horizontal infinitesimal dipole with unit electric moment immersed in lossy half space, are given at all points in both half spaces at different depths. Since buried UG antennas are extended devices, fields generated from these antennas are significantly different from the infinitesimal antennas.

Antennas in matter have been analyzed in [86], [86], [122], where the EM fields of antennas in infinite dissipative medium and half space have been derived theoretically. In these analyses, dipole antennas are assumed to be perfectly matched and hence the return loss is not considered. In [99], [207] radiation efficiency and relative gain expressions of underground antennas are developed but simulated and empirical results are not presented. In [108], the impedance of a dipole antenna in solutions are measured. The impacts of the depth of the antenna with respect to the solution surface, the length of the dipole, and the complex permittivity of the solution are discussed. However, this work cannot be directly applied to IOUTs since the permittivity of soil has different characteristics than solutions and the change in the permittivity caused by the variations in soil moisture is not considered. Communications between buried antennas have been discussed in [118], but effects of antennae orientation and impedance analysis has not been analyzed. Performance of four buried antennas has been analyzed [84], where antenna performance in refractory concrete

with transmitter buried only at single fixed depth of 1 m without consideration of effects of concrete-air interface is analyzed. In [56], analysis of circularly polarized patch antenna embedded in concrete at 3 cm depth is done without consideration of the interface effects.

In existing IOUT experiments and applications, the permittivity of the soil is generally calculated according to a soil dielectric model [40, 144], which leads to the actual wavelength at a given frequency. The antenna is then designed corresponding to the calculated wavelength [188]. In [188], an elliptical planar antenna is designed for an IOUT application. The size of the antenna is determined by comparing the wavelength in soil and the wavelength in air for the same frequency. However, this technique does not provide the desired impedance match. In [217], experimental results are shown for Impulse Radio Ultra-Wide Band (IR-UWB) IOUT, however impact of soil-air interface is not considered. In [191], a design of lateral wave antenna is presented where antennas are placed on surface but underground communication scenario is not considered. Closed form expressions to predict the resonance frequency of the microstrip, and patch antennas have been proposed in [37], [219], that only take into account the antenna substrate properties and dimensions, but dispersion of the surrounding medium and boundary effects are not considered.

In [98], the current distribution and impedance properties of dipole elements in a large subsurface antenna array are derived and compared with experimental data. However, this analysis assumes a homogeneous conducting medium with a large loss tangent with array immersed in a tank containing salt solution, which is not the case in soil. The disturbance caused by impedance change in soil is similar to the impedance change of a hand-held device close to a human body [53, 190] or implanted devices in human body [68, 93]. In these applications, simulation and testbed results show that there are impacts from human body that cause performance degradation

of the antennas. Though similar, these studies cannot be applied to the underground communication directly. First, the permittivity of the human body is higher than in soil. At 900 MHz, the relative permittivity of the human body is 50 [190] and for soil with a soil moisture of 5%, it is 5 [144]. In addition, the permittivity of soil varies with moisture, but for human body, it is relatively static. Most importantly, in these applications, the human body can be modeled as a block while in underground communications, soil is modeled as a half-space since the size of the field is significantly larger than the antenna.

To the best of the our knowledge, no existing work takes into account the soil type and soil moisture variations on the underground antenna characteristics, *and* soil-air interface effects on antenna input impedance. Major contribution of this work is the development and validation of a resonant frequency model to predict resonance under different soil moisture levels in different soil types at different depths. This knowledge of shift of resonant frequency of UG antenna for different soil moisture levels is also useful to determine the transmission loss due to antenna mismatch in IOUT communications

Since, main emphasis of this chapter is on the finding resonance for different soil types, depths, soil moisture levels and choosing the right wavelength for IOUT communications, therefore, impedance matching problem is not considered in this work. As depth and soil moisture variations affect the wide range of frequencies, it is challenging to achieve broadband matching over this wide spectrum and leads to performance degradation [68]. Moreover, the model and analysis in this work applies only to antennas buried up to 1 m depth, because of the considered application, such as in precision agriculture devices are buried in this depth range. In this depth, due to close proximity to surface, soil-air interface plays an important role.

9.3 System Model

In this section, first, input impedance of a UG antenna is modeled as a function of soil properties and soil moisture by defining the wavenumber in soil, and then, other important parameters of the UG antenna such as resonant frequency, and bandwidth are derived.

9.3.1 Terminal Impedance of Underground Dipole Antenna as a Function of Soil Properties

Antenna impedance, Z_a, is the ratio of voltage and current at the same point on driving point of the antenna. Complex power radiated by antenna can be calculated by integrating Poynting's vector $\mathbf{S} = \mathbf{E}\ X\ \mathbf{H}$, that gives the energy flow intensity at some point in field, over the enclosing surface of antenna. It is given as [86]:

$$Z_a = \frac{1}{I^2} \int \int \mathbf{E}\ X\ \mathbf{H}\ .\ \mathbf{da}\ , \tag{9.1}$$

where I is antenna current, **da** is perpendicular in the direction of surface of antenna. For a perfectly conducting antenna, it can be assumed that other than antenna feeding region $\mathbf{E}(x, y, z) \equiv 0$. Then impedance is ascertained by integration of surface current density and tangential electric field over antenna enclosing surface. Then, (9.1) becomes [86]:

$$Z_a = \frac{1}{I^2} \int \int \mathbf{E}\ X\ \mathbf{J_{se}}\ .\ da\ , \tag{9.2}$$

where $\mathbf{J_{se}}$ is surface current density. By using the induced EMF method [79], (9.2) can be rewritten as:

$$Z_a = -\frac{1}{I(0)^2} \int_{-l}^{l} \mathbf{E_z}\ \mathbf{I}(\zeta)\ d\zeta\ , \tag{9.3}$$

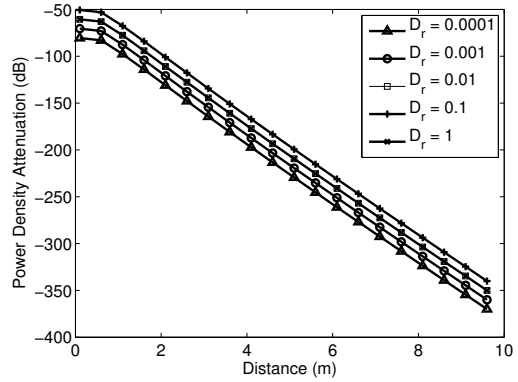

(a) Buried antenna in the half-space

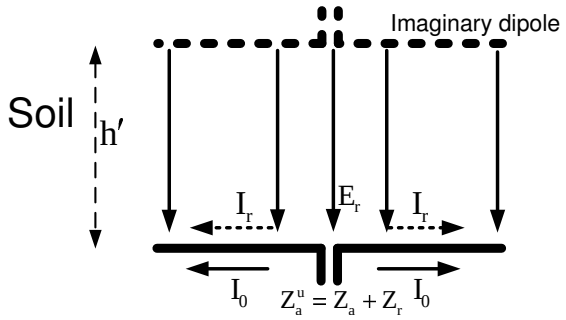

(b) The mutual impedance model

Figure 9.2: The analysis of the impedance of a buried dipole antenna.

By using (9.3), the self-impedance of the underground dipole antenna is determined by calculating the electric field $\mathbf{E_z}$ produced by an assumed current distribution $\mathbf{I(0)}$. Accordingly, current and electric field is integrated over the antenna surface.

To model the impedance and return loss of a buried antenna, we consider the antenna in a homogeneous soil. In this setting, the impacts of the soil properties on the impedance are captured. First, however, it is important to consider the wavenumber. The dispersion[1] in soil is given in Appendix A.4.

Current distribution on antenna is a function of radiation and absorption in soil, which in turn depends on the dielectric properties of the soil. In stratified media, it is difficult to measure current distribution with high accuracy [86]. In [122], mea-

[1]Another approximation of the complex wavenumber is given in [120], which involves Fourier transform of the Bessel function kernel $K(z)$. A similar wavenumber has also been presented in [202].

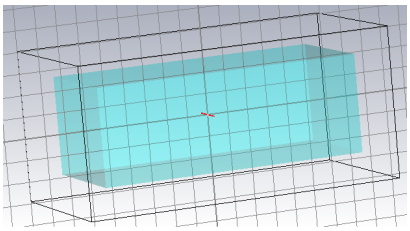

(a)

Figure 9.3: (a) CST MWS design of antenna buried in soil,

surement data is shown to match well with sinusoidal current distribution. When the dipole antenna is buried underground, the current has the simple sinusoidal form with complex wave number of the soil k_s:

$$I_0(\zeta) = I_m \sin[k_s(l - |\zeta|)] \ , \tag{9.4}$$

where I_m is the amplitude of the current, l is the half length of the antenna, and $k_s = \beta_s + i\alpha_s = \omega\sqrt{\mu_0\hat{\epsilon}_s}$ is the wave number in soil. $\mathbf{E_z}$ is given as:

$$\mathbf{E_z} = -\int_{-l}^{l} \frac{1}{4\pi j\omega\epsilon_s} \frac{e^{-jk_s r}}{R} \left(\frac{\partial^2}{\partial\zeta^2} + k_s^2\right) I(\zeta) d\zeta, \tag{9.5}$$

By substituting the $\mathbf{E_z}$ in (9.5) and $\mathbf{I(0)}$ from (9.4) in (9.2) we get [114, Ch. 4]:

$$Z_a \approx f_1(\beta l) - i\left(120\left(\ln\frac{2l}{d} - 1\right)\cot(\beta l) - f_2(\beta l)\right) \ , \tag{9.6}$$

where

$$f_1(\beta_s l) = -0.4787 + 7.3246\beta_s l + 0.3963(\beta_s l)^2 + 15.6131(\beta_s l)^3 \tag{9.7}$$

$$f_2(\beta_s l) = -0.4456 + 17.0082\beta_s l - 8.6793(\beta_s l)^2 + 9.6031(\beta_s l)^3 \tag{9.8}$$

β_s is the real part of the wave number k_s, d is the diameter of the dipole, and l is half

of the length of the dipole. βl is expressed as

$$\beta_s l = \frac{2\pi l}{\lambda_0} \mathrm{Re}\left\{\sqrt{\epsilon_s}\right\} \ , \tag{9.9}$$

where ϵ_s is the relative permittivity of soil and λ_0 is the wavelength in air. Since the permittivity of soil, ϵ_s, is frequency dependent, βl is not a linear function of l/λ_0. Thus, when the antenna is moved from air to soil, not only its resonant frequency changes, but its impedance value at the resonant frequency also varies with the soil properties.

In a real deployment for IOUTs, sensor motes are buried at subsurface depths (0.3 m–1 m) [75]. At these depths, the environment cannot be modeled as homogeneous soil due to the impacts of soil-air interface. Next, we model the environment as a half-space consisting of air and soil to capture the impacts of the reflected waves from the soil-air interface on the impedance and return loss of the antenna.

We formulate the expression for mutual impedance of the underground dipole antenna by considering the effects of soil-air interface and burial depth of antenna. When a buried antenna is excited, a current distribution of $I_0(\zeta)$ is generated along the antenna (Fig. 9.2(a)). The generated wave propagates towards the soil-air interface, where it is reflected and refracted. The reflected electric field that reaches the antenna is denoted as E_r, which induces a current, I_r, on the antenna. The induced current further impacts the generated wave and higher order reflection effects exist. Due to the high attenuation in soil, these higher order effects are negligible and we consider only the first order effects in the following.

The induced current on the dipole, I_r, as well as the resulting impedance, Z_r, can be modeled as the result of a field generated by an *imaginary dipole* placed in a homogeneous soil environment. The distance of the two dipoles, h, is chosen such

that E_r is the same at the real dipole. Based on this current distribution (9.4), the reflected E_r field from the soil-air interface at the antenna is [79, Ch. 7]:

$$E_r = -i30I_m \left(\frac{e^{-ik_s r_1}}{r_1} + \frac{e^{-ik_s r_2}}{r_2} - 2\cos k_s l \frac{e^{-ik_s r}}{r} \right) \times \Gamma \ , \tag{9.10}$$

where

$$r = [(2h)^2 + \zeta^2]^{1/2} \ , \tag{9.11}$$

$$r_1 = [(2h)^2 + (\zeta - l)^2]^{1/2} \ , \tag{9.12}$$

$$r_2 = [(2h)^2 + (\zeta + l)^2]^{1/2} \ , \tag{9.13}$$

h is the burial depth of the antenna, and Γ is the reflection coefficient at the soil-air interface, which is given by:

$$\Gamma = \frac{2}{1 + k_0/k_s} - 1 = \frac{2}{1 + \sqrt{\frac{1}{\epsilon_s}}} - 1 \ , \tag{9.14}$$

and k_0 is the wave number in air.

The expression for induced current on the UG dipole is given in Appendix A.5. Once I_r is determined, the antenna impedance is calculated as: $Z_a^u = Z_a . \frac{I_0}{I_r^2}$ and accordingly, the return loss of the antenna (in dB) is given by:

$$RL_{dB} = 20 \log_{10} \left| \frac{Z_s + Z_a^u}{Z_s - Z_a^u} \right| . \tag{9.15}$$

The reflection coefficient Γ is given as: $|\Gamma| = 10^{\frac{RL}{20}}$. Reflection coefficient is transformed to impedance by using: $Z_a^u = Z_s \frac{1+\Gamma}{1-\Gamma}$. Standing wave ratio (SWR) is expressed as: $SWR = \frac{1+|\Gamma|}{1-|\Gamma|}$

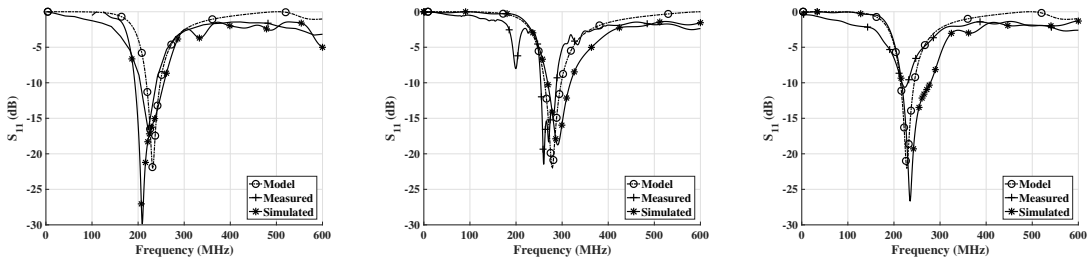

(a) Silt Loam (b) Sandy Soil (c) Silty Clay Loam

Figure 9.4: Comparison of measured, simulated and theoretical return loss at 20 cm depth in a) Silt Loam b) Sandy soil c) Silty clay loam soil.

9.3.2 Resonant Frequency of UG Dipole Antenna

The resonant frequency, f_r, is defined as the operation frequency where the input impedance of the antenna is the pure resistance, i.e.:

$$Z_a^u|_{f=f_r} = Z_r = R_a. \tag{9.16}$$

and where return loss is maximum such that:

$$f_r = \max(RL_{dB}). \tag{9.17}$$

We also compare the performance of this analytical model by using the resonant frequency of an antenna designed based only on the permittivity by using: $f_r = f_0/\sqrt{\epsilon_s}$, where f_0 is the OTA resonant frequency, and ϵ_s is the permittivity of the soil.

9.3.3 UG Antenna Bandwidth

To find a closed-form formula for the bandwidth of the UG antenna is a challenging task since many factors such as soil moisture, soil type, permittivity, and burial depth are taken into account. However, based on the resonant frequency, we define the

bandwidth expression. Over the resonant frequency, the bandwidth of the antenna is defined as the range of frequencies for which antenna impedance is within a specified threshold. Accordingly, bandwidth (BW) is defined as [74]:

$$BW = \begin{cases} 0 & \text{if -}RL_{dB}(f) > \delta, \\ 2(f - f_m) & \text{if -}RL_{dB}(f) \leq \delta \text{ and } f < f_r, \\ 2(f_M - f) & \text{if -}RL_{dB}(f) \leq \delta \text{ and } f \geq f_r, \end{cases} \tag{9.18}$$

where f_r is the resonant frequency, f_m and f_M are the lowest and highest frequency at which $RL_{dB}(f) \leq \delta$. There is no fixed value of δ, and it depends on a particular application. In literature, value of 10 dB is generally used [49].

9.4 Underground Dipole Antenna Simulations and Experiment Setup

To simulate an underground dipole antenna, CST Microwave Studio Suite (MWS) [5] is used. For controlled experiments, an indoor testbed has been shown in Chapter 3. Same antenna and soil parameters are simulated which are used in the testbed measurements. In Fig. 9.3(a), underground antenna simulation workspace has been shown. It can be observed that the simulation contains antenna inside the soil. Particle size distribution and classification of simulated soils is shown in Table 3.1. Return loss measurement are conducted in an indoor testbed Chapter 3 and field settings under different volumetric water content (VWC). The indoor testbed is shown in Fig. 3.2(e).

To compare with the results of indoor testbed experiments and conduct underground-to-aboveground communications experiments, a testbed of dipole antennas has been

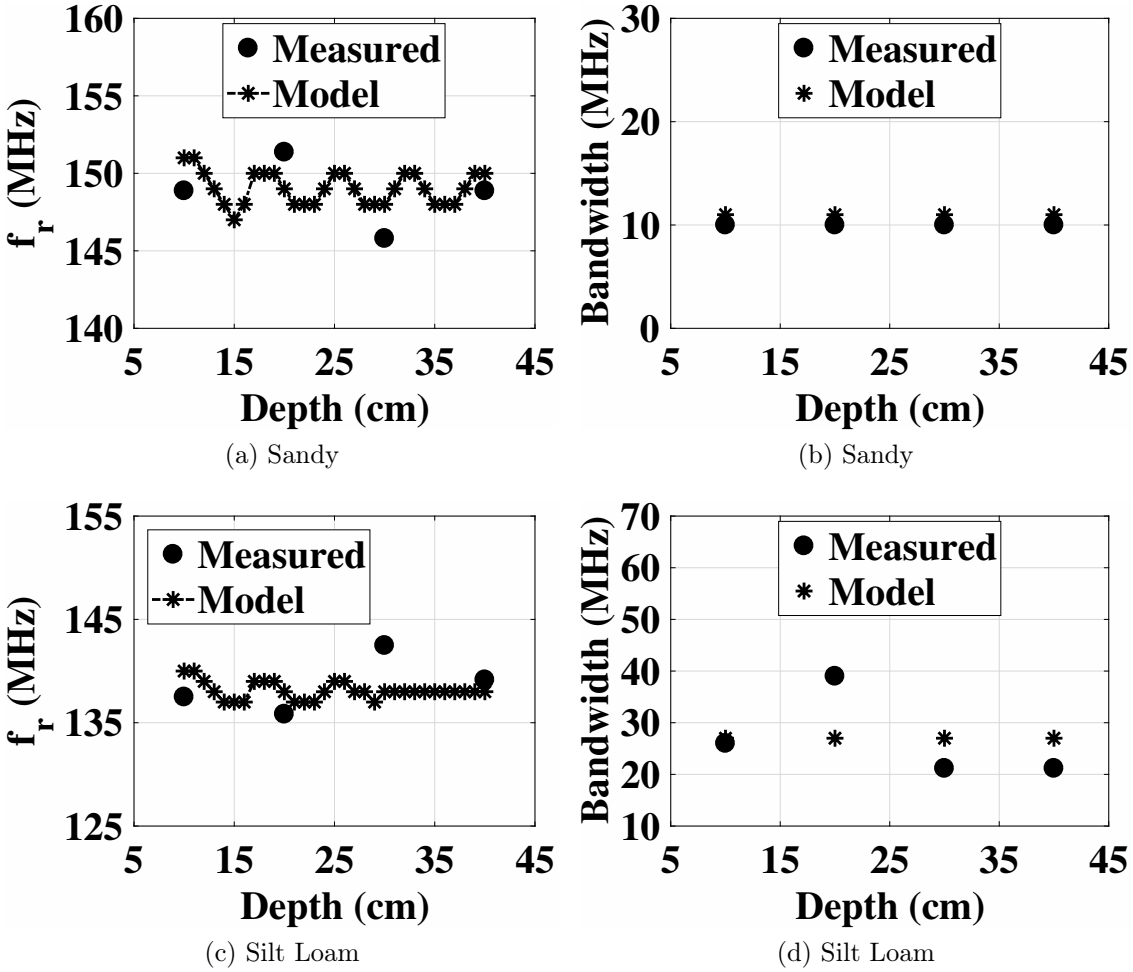

(a) Sandy (b) Sandy

(c) Silt Loam (d) Silt Loam

Figure 9.5: Comparison of measured and theoretical resonant frequency and bandwidth at different depths (40% VWC). a) Resonant frequency in sandy soil, b) Bandwidth in sandy soil, c) Resonant frequency in silt loam soil, c) Bandwidth in silt loam soil.

prepared in an outdoor field with silty clay loam soil (Fig. 3.4(a)). Dipole antennas are buried in soil at a burial depth of 20 cm with distances from the first antenna as 50 cm-12 m. Antenna S_{11} and frequency responses of the channel are measured using a Vector Network Analyzer (VNA). A diagram of the measurement layout is shown in Fig. 3.3(b). Further details about experiment setup and methodology used can be found in Chapter 3.

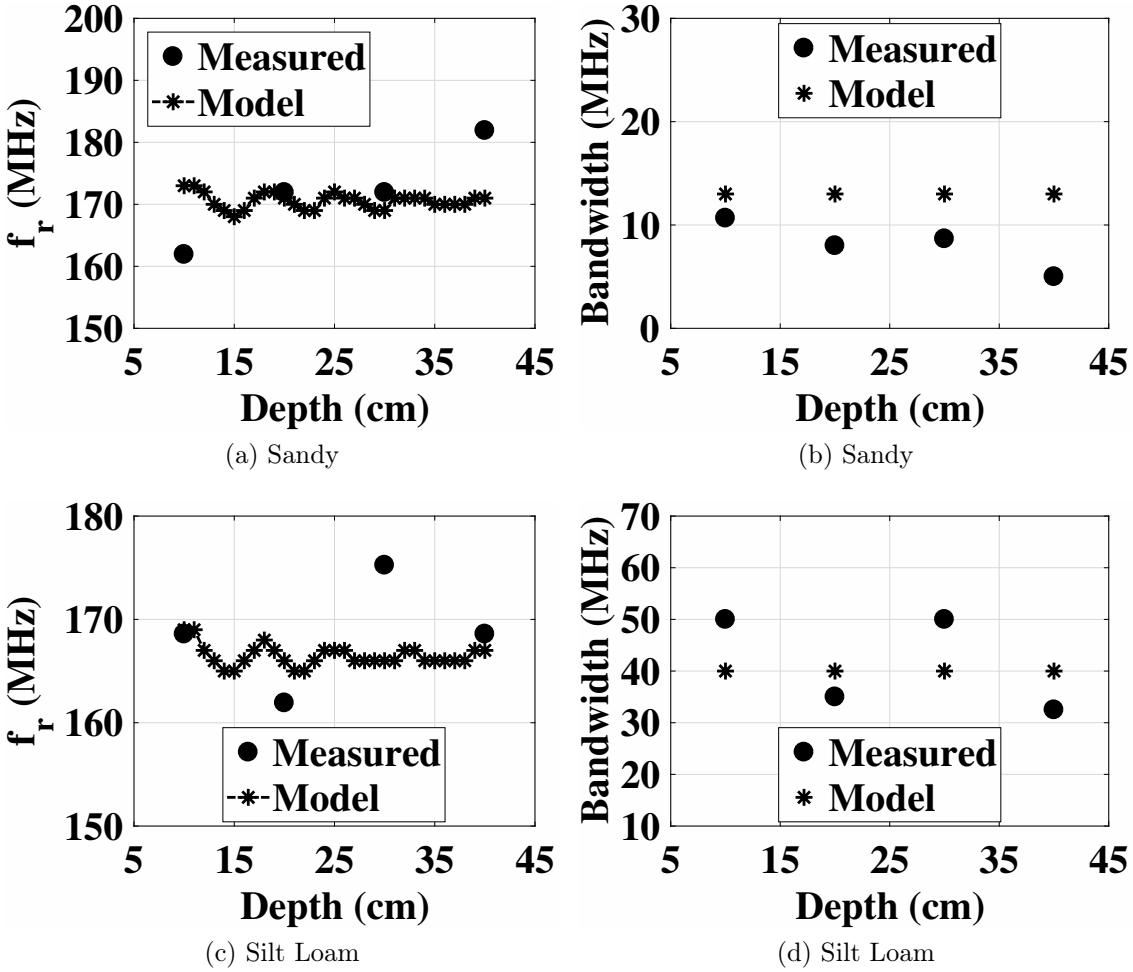

(a) Sandy (b) Sandy

(c) Silt Loam (d) Silt Loam

Figure 9.6: Comparison of measured and theoretical resonant frequency and bandwidth at different depths (30% VWC). a) Resonant frequency in sandy soil, b) Bandwidth in sandy soil, c) Resonant frequency in silt loam soil, c) Bandwidth in silt loam soil.

9.5 Model Validation

9.5.1 Comparison of Theoretical, Simulated, and Measurement Results

In this section, we present the comparison of theoretical model, simulations, and measurements of dipole antenna for silt loam, silty clay loam, and sandy soil. Resonant frequency, bandwidth, and return loss at the resonant frequency are compared. To validate the theoretical analysis, we have conducted experiments in silty clay loam, sandy, and silt loam soil, by using the setup described in Section 9.4.

In Fig. 9.4(a), theoretical model and simulated results are compared with the measured return loss of antenna buried in silty clay soil at 20 cm depth. Measured return loss results agrees well with the model. Measured resonant frequency is 221 MHz and model value is 228 MHz. On the other hand, simulation results shows the resonant frequency at 210 MHz which is 11 MHz less than the measured return loss. Moreover, simulated return loss is also 7% lower at the resonant frequency as compared to measured and and model return loss values at the resonance. This is caused by simulation uncertainties due to soil simulation in the simulator.

Return loss measurements at 20 cm depth in sandy soil are compared with theoretical and simulated results in Fig. 9.4(b). Measured, theoretical, and simulated resonant frequencies are within 1% difference range with measured resonant frequency at 283 MHz, model at 280 MHz and simulated at 286 MHz, respectively. Moreover, in sandy soil, only 1 % variations in return loss values at resonant frequency are observed as compared to the silt loam soil (7 %).

In Fig. 9.4(c), theoretical model, measured results, and simulations of antenna return loss are compared for the antenna buried in silty clay loam soil at 20 cm depth. Resonant frequency for both simulations and measurements is at 227 MHz and theoretical model value of resonant frequency is at 231 MHz, which is in agreement of all three results in the silty clay loam soil. These 1%-7% differences are mainly because of simulation effects in the software, as simulation setup can not realize the actual soil testbed scenario with maximum accuracy. Moreover, uncertainty in application of boundary conditions to the soil configurations in the software also lead to variations between measured and simulated results of the underground antenna in soil.

In Figs. 9.5-9.8, measured and theoretical resonant frequency and bandwidth at different depths in sandy and silt loam soil is compared for 10%-40% VWC range. At

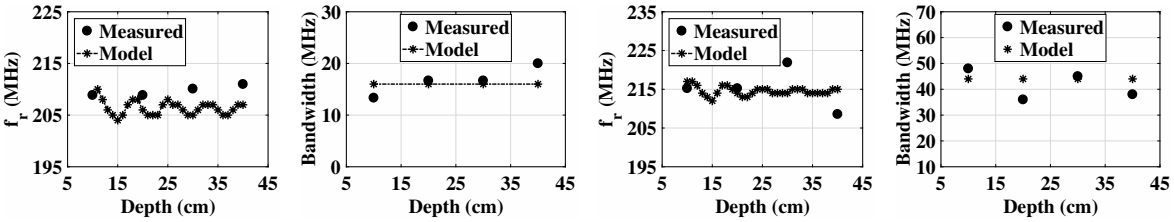

(a) Sandy (b) Sandy (c) Silt Loam (d) Silt Loam

Figure 9.7: Comparison of measured and theoretical resonant frequency and bandwidth at different depths (20% VWC). a) Resonant frequency in sandy soil, b) Bandwidth in sandy soil, c) Resonant frequency in silt loam soil, c) Bandwidth in silt loam soil.

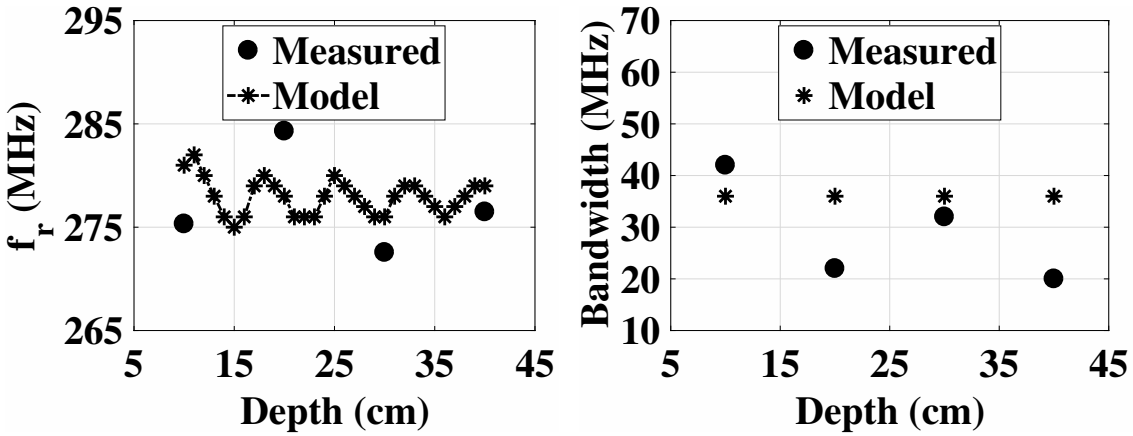

(a) Sandy (b) Sandy

Figure 9.8: Comparison of measured and theoretical resonant frequency and bandwidth at different depths (10% VWC). a) Resonant frequency in sandy soil, b) Bandwidth in sandy soil.

40% VWC, in sandy soil (Fig. 9.5(a)), the measured resonant frequency value show a very good agreement with the model, where the resonant frequency is only 1.39 %, 1.61 %, 1.48 %, 0.73 %, different from the measured value of 148.9 MHz, 151.4 MHz, 145.8 MHz, 148.9 MHz, at 10 cm to 40 cm depths, respectively. The measured bandwidth in sandy soil (Fig. 9.5(b)) is also in very good agreement with the model value with only 1 MHz difference at all depths.

Similarly, at 40% VWC, in silt loam soil (Fig. 9.5(c)), the measured resonant frequency is only 1.78 %, 1.59 %, 4.01 %, 0.08 %, different from the measured value of 137.5 MHz, 135.8 MHz, 142.5 MHz, 139.2 MHz, at 10 cm to 40 cm depths, respec-

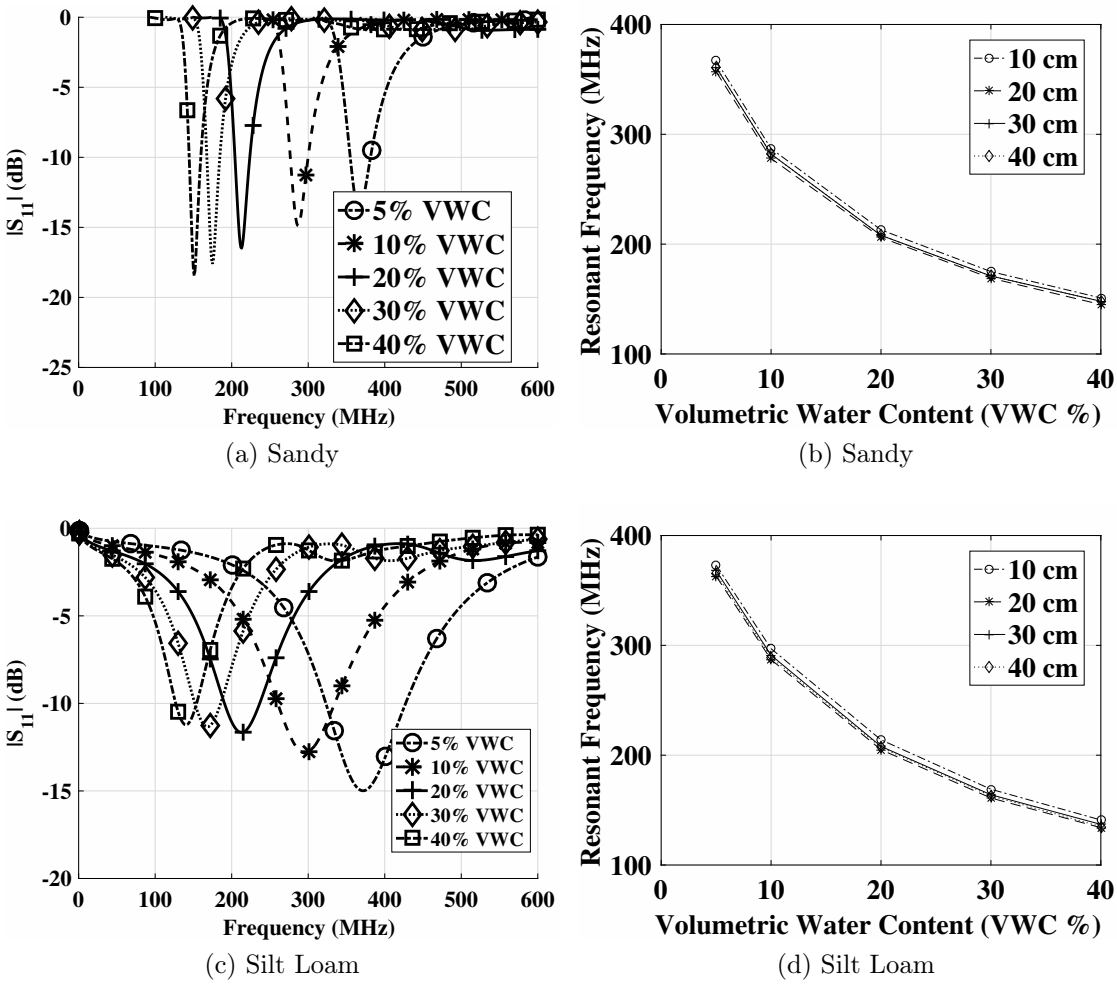

(a) Sandy (b) Sandy

(c) Silt Loam (d) Silt Loam

Figure 9.9: Theoretical return loss and resonant frequency in sandy, and silty clay loam soil at different burial depths.

tively. The measured bandwidth in silt loam (Fig. 9.5(d)) is 1 MHz, 7 MHz, 5.83 MHz, 5.83 MHz different from the model value at 10 cm-40 cm depths, respectively.

The comparison of measured and model resonant frequency and bandwidth at different depths in sandy soil at 30% VWC is given in Fig. 9.6(a)-9.6(b). The difference of measured and model resonant frequencies is 6.41 %, 0.58 %, 1.71 %, and 6.02 %, at 10 cm, 20 cm, 30 cm, and 40 cm depths, respectively. Similarly, the difference of measured and model bandwidth is 2.33 MHz, 5 MHz, 4.34 MHz, and 8 MHz, at 10 cm, 20 cm, 30 cm, and 40 cm depths, respectively.

In Fig. 9.6(c)-9.6(d), the comparison of measured and theoretical resonant fre-

quency and bandwidth at different depths in silt loam soil at 30% VWC is given. The difference of measured and model resonant frequencies is 0.02 %, 2.46 %, 5.45 %, and 0.09 %, at 10 cm - 40 cm depths, respectively. The measured bandwidth in silt loam (Fig. 9.7(d)) is 10 MHz, 5 MHz, 10 MHz, and 7.5 MHz different from the model value at 10 cm-40 cm depths, respectively.

At 20% VWC, in sandy soil (Fig. 9.7(a)), the measured resonant frequency value show a very good agreement with the model, where the resonant frequency is only 0.01 %, 1.40 %, 2.48 %, and 1.93 %, different from the measured value of 208.9 MHz, 208.9 MHz, 210.1 MHz, and 211 MHz, at 10 cm to 40 cm depths, respectively. The measured bandwidth in sandy soil (Fig. 9.7(b)) is also in very good agreement with the model value with only 2.77 MHz, 0.67 MHz, 0.67 MHz, and 4 MHz difference at at 10 cm-40 cm depths, respectively.

Similarly, at 20% VWC, in silt loam soil (Fig. 9.7(c)), the measured resonant frequency is only 1.01 %, 0.47 %, 3.69 %, and 3.53 %, different from the measured value of 215.2 MHz, 215.2 MHz, 221.9 MHz, and 208.6 MHz, at 10 cm to 40 cm depths, respectively. Similarly, the difference of measured and modeled bandwidth is 4 MHz, 8 MHz, 1 MHz, and 6 MHz, at 10 cm - 40 cm depths, respectively.

In sandy soil at 10% VWC (Fig. 9.8(a)), the measured resonant frequency value show a very good agreement with the model, where the resonant frequency is only 2.24 %, 1.89 %, 1.66 %, and 1.25 %, different from the measured value of 275.3 MHz, 284.3 MHz, 272.6 MHz, and 276.5 MHz, at 10 cm to 40 cm depths, respectively. The measured bandwidth in sandy soil (Fig. 9.8(b)) is also in good agreement with the model value with only 6 MHz, 14 MHz, 2 MHz, and 16 MHz difference at at 10 cm-40 cm depths, respectively.

These variations in resonant frequency (up to 6.41 % in sandy soil and up to 5.45 % in silt loam) do not adversely impact the UG communications as bandwidth of the

UG antenna (generally more than 20 MHz) [155] is higher than these variations in resonant frequency. Moreover, in this analysis, antenna bandwidth is calculated from the antenna return loss based on a threshold value (10 dB). Therefore, it is relative to the resonant frequency of the antenna. These differences in measured and model antenna bandwidth are caused by the variations in return loss shape and resonant frequency at a particular depth. Higher return loss and resonant frequency variations in soil lead to higher differences in antenna bandwidth.

It should be noted that since the theoretical resonant frequency model does not capture EM fields inside the coaxial cable connected to the antenna, the differences in resonant frequency between theory and experiment at different depths suggests that these variations are not caused by the soil medium but are primarily due to the coaxial cable effects. In theory, a perfect lossless transmission line is assumed, however, in practice, there are dielectric and conduction loss in a coaxial cable used in measurements. Due to fact that antennas are buried in the soil, it is not possible to take direct impedance measurements at antenna connectors and use of cables is inevitable. Therefore, the empirical resonant frequency clearly depends on the properties of the soil medium, depth, soil moisture but also on the coaxial cable used in these measurements. Moreover, difficulty in achieving the fine depth in soil due to moisture and compaction effects over time, also lead to deviations that occur at different depths. This is also consistent with the fact that effects of the soil-air interface impacts the resonant frequency of the underground antenna in soil and is ascribed to changes in the reflect field with depth. The soil-air interface effects are minimal when the transition in resonant frequency is smooth from one depth to another depth and accordingly the effects of coupling are decreased as the depth changes (Fig. 9.6(a)). However, these effects can be more complicated to capture when phase change occurs in a smaller depth variation (Fig. 9.7(a)). Therefore, at

these 10 cm, 20 cm, 30 cm, and 40 cm depths measured data provides a meaningful comparison with the theoretical results. In summary, change in the wave number, EM fields in coaxial cable and abrupt changes in phase and impedance with depth and soil interface effects are main factors of these differences in model and experimental data. Overall, the bandwidth and resonant frequency results show a very good agreement with the model. Additionally, the good fit with experimental results show that the model also captures the interface effects on the return loss of the antenna. Measured return loss values show the impacts of soil properties and soil moisture in the near vicinity of the antenna. Comparison of measurements with theoretical values makes the model a powerful analysis tool for the underground antenna.

9.5.2 Analysis of Impact of Operation Frequency

From an IOUT communication system design perspective, it is useful to analyze the performance of a dipole antenna return loss and resonant frequency in different soil types to get an insight for communication system design. In this section, first, the change in resonant frequency in different soils, under different soil moisture levels, for different operation frequencies, is analyzed through model evaluations. The connection of resonant frequency with the OTA frequency is also discussed. Then, we compare the model performance with the antenna designed based on the permittivity only, without consideration of the burial depth effects.

In Figs. 9.9(c)-9.9(d), return loss, and resonant frequency, in silt loam soil, is shown for soil moisture level of 5 %-40 %. Resonant frequency decreases from 369 MHz to 137 MHz (62% decrease), when soil moisture increases from 5 % to 40 %. Similarly, from Figs. 9.9(c)-9.9(d), where return loss, and resonant frequency is shown in sandy soil, it can be observed that with soil moisture increase from 5 % to 40 %, resonant frequency decreases from 357 MHz to 146 MHz (59% decrease).

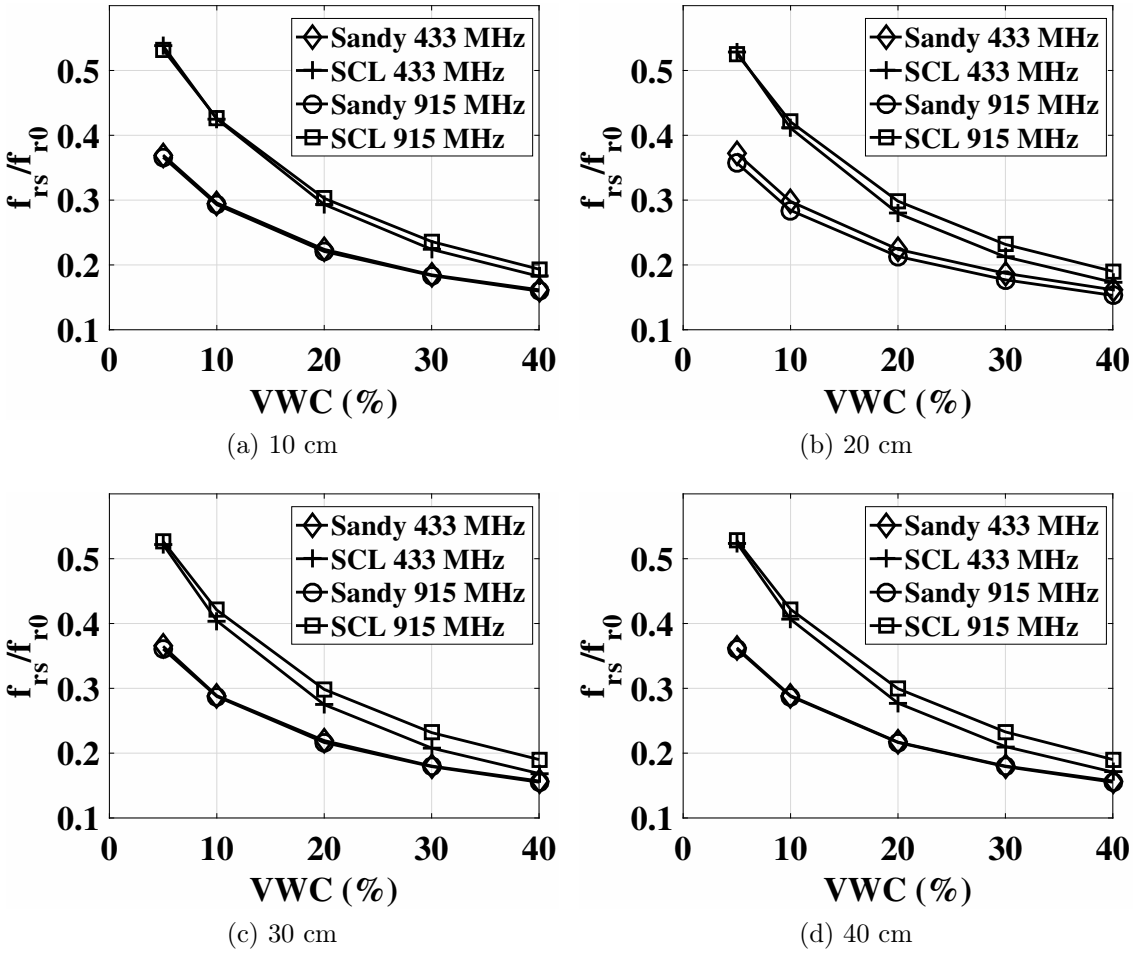

(a) 10 cm (b) 20 cm

(c) 30 cm (d) 40 cm

Figure 9.10: Ratio of resonant frequency in soil to the OTA resonant frequency of the antenna in sandy and silty loam soil is at 433 MHz and 915 MHz.

Ratio of resonant frequency of dipole antenna, $\frac{f_{rs}}{f_{ro}}$, in sandy, and silty clay loam soil to the OTA resonant frequency of the dipole antenna at 433 MHz and 915 MHz is shown in Fig. 9.10(a)-9.10(d), at different depths. f_{rs} and f_{ro} represents the resonant frequency in soil, and OTA, respectively. It can also be observed that with increase in soil moisture, $\frac{f_{rs}}{f_{ro}}$ becomes smaller (because resonant frequency decreases). Moreover, the It can be observed that $\frac{f_{rs}}{f_{ro}}$ ratio at 915 MHz, as compared to the 433 MHz, is not the same at different burial depths in both soils.

Soils are generally classified based on the percentage of clay, sand, and silt particles

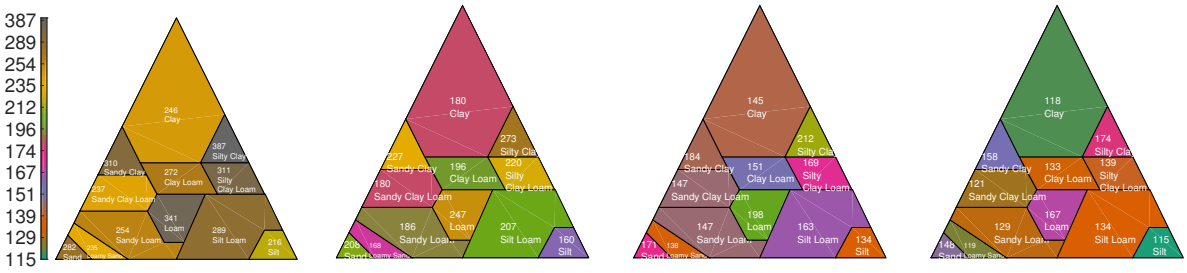

(a) 10% VWC (b) 20% VWC (c) 30% VWC (d) 40% VWC

Figure 9.11: Resonant frequency (MHz) of different soils in textural triangle at different soil moisture levels for a 433 MHz OTA antenna

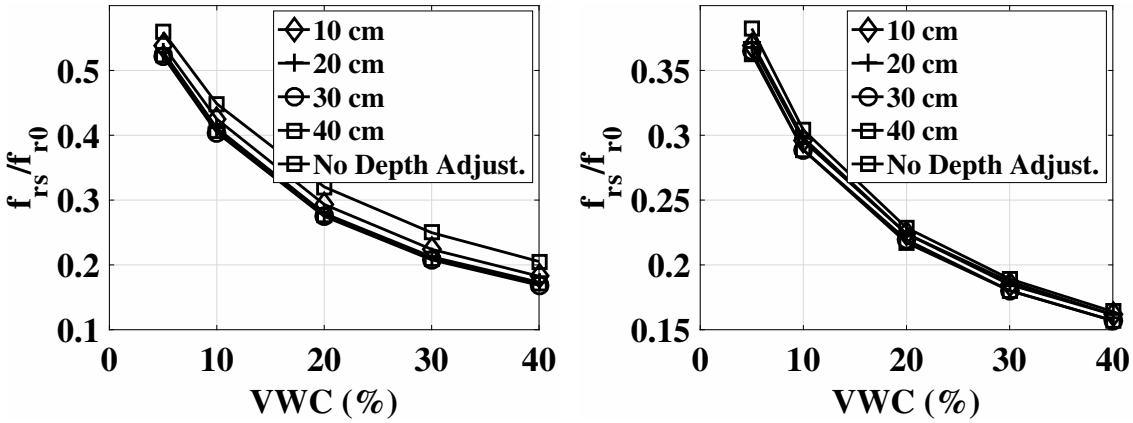

(a) SCL-433MHz (b) Sandy-433MHZ

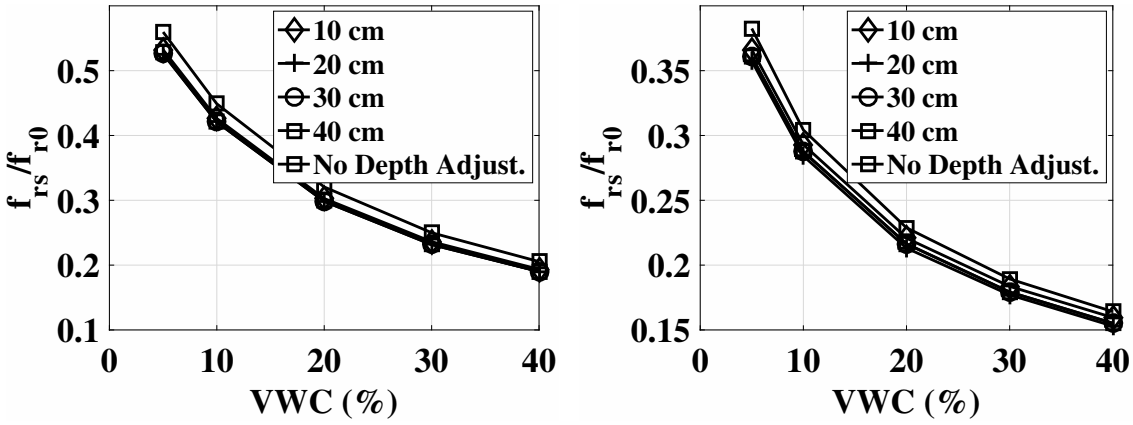

(c) SCL-915MHz (d) Sandy-915MHz

Figure 9.12: Comparison of ratio of resonant frequency in soil to the OTA resonant frequency of the antenna in sandy and silty clay loam soil is at 433 MHz and 915 MHz at different depths with permittivity antenna.

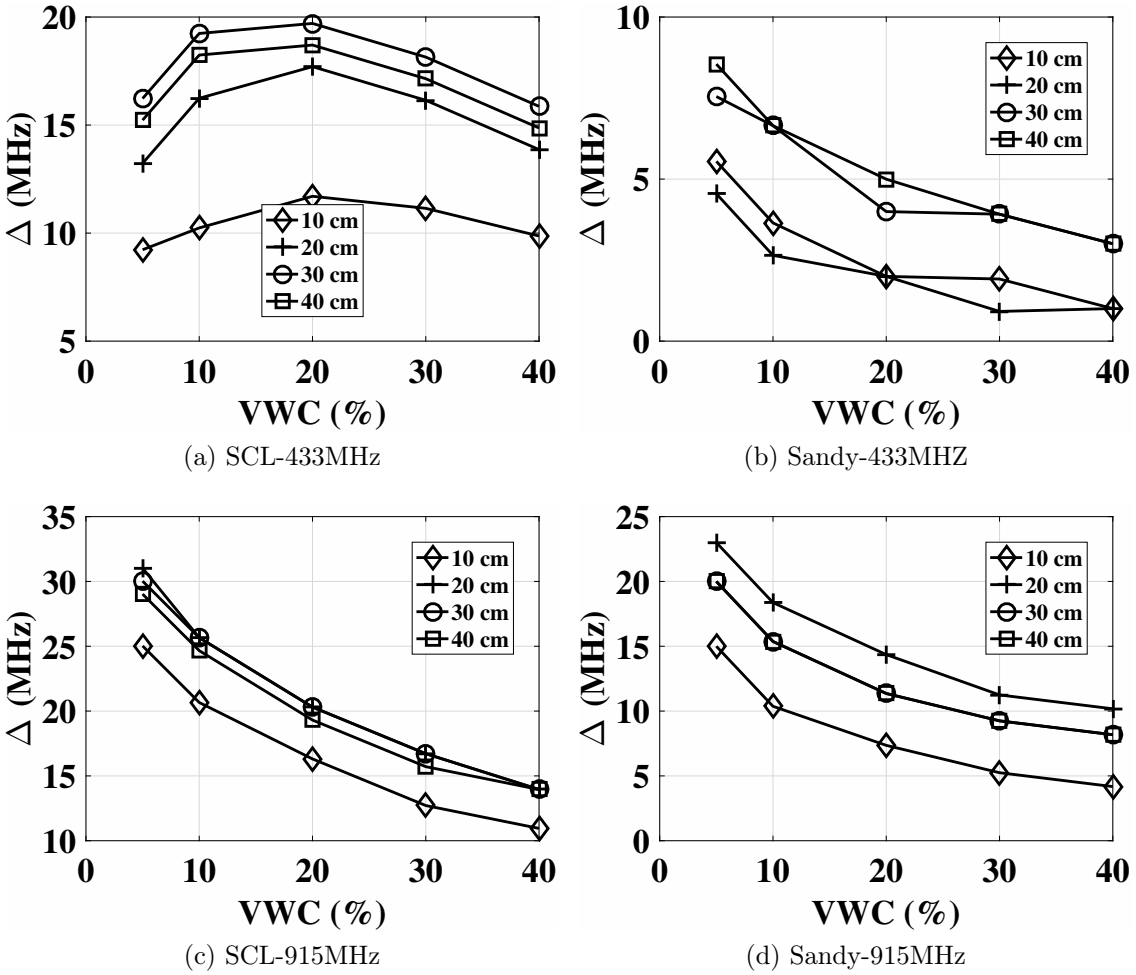

(a) SCL-433MHz (b) Sandy-433MHZ

(c) SCL-915MHz (d) Sandy-915MHz

Figure 9.13: Difference of the resonant frequency of the analytical model, Δ, as compared soil permittivity based antenna design.

in soil using a soil textural triangle. Resonant frequency of soils in textural triangle are analyzed for volumetric water content range of 5% to 40% for a 433 MHz OTA antenna. Resonant frequency of different soils in textural triangle at different soil moisture levels are shown in Fig. 9.11. This antenna resonant frequency triangle can be used to predict the resonant frequency of an underground dipole antenna in different soils when soil type (sand, clay, silt particles) and soil water content is given.

Comparison of *permittivity antenna* (Section 9.3.2) and ratio of resonant frequency of a dipole antenna in soil to the OTA resonant frequency of the antenna in sandy,

and silty clay loam soil is at 433 MHz and 915 MHz at different depths permittivity antenna is shown in Fig. 9.12(a)-9.12(d). Difference of change in resonant frequency is different at different depths, and this ratio also changes in comparison to the OTA. A more clear picture can be seen from the Fig. 9.13(a)-9.13(d), where difference in resonant frequency, Δ, of the resonant frequency of the theoretical model as compared to an antenna which is designed based on the soil permittivity only, is shown at different depths, at different soil moisture levels, in silty clay loam, and sandy soils, and at 433 MHz and 915 MHz frequencies. It can be observed that Δ is low at high soil moisture levels, and as soil moisture level decreases, Δ increases. Similarly, at 433 MHz, Δ is low, and increases by 10 MHz-15 MHz at 915 MHz frequency. Hence, an IOUT system designed based on the permittivity *only* will lead to performance degradation. Operation frequency is more probable to fall outside of the antenna bandwidth region, leading to minimal power transfer from antenna to the soil medium. It also underscores the effects of soil-air interface. Therefore, for an efficient power transfer, the antenna burial depth consideration is important in IOUT communications.

9.6 Underground Wideband Antenna Design

In IOUT communications, two approaches can be used to mitigate the shift in resonant frequency of the underground dipole antenna. First approach is based on the software defined radio (SDR) operation, such that the operation frequency of the UG transceivers is adapted to soil moisture variations. Details of the cognitive wireless underground communications can be found in [74]. Second approach is based on the wideband operation, which we follow in this work. With insights gained from the analysis in shift of the underground dipole antenna, a wideband antenna has been designed. In this section, we design a wideband antenna for 433 MHz frequency, and

results show that it has good performance in different soils. Different sizes of the wideband antenna based on the same design are designed and fabricated for testing. After experiments, the final design is chosen with a wideband plane of diameter 100 mm. The substrate of the antenna is a FR-4 material and its thickness is 1.6 mm. The feed line of the antenna is a coplanar waveguide structure. Further details about the antenna design can be found at [199]. The layout of the antenna is shown in Fig. 9.14(a).

9.6.1 Radiation Pattern for Underground Communications

In addition to the wide bandwidth of the wideband planar antenna, another advantage of using this antenna is its radiation pattern. For underground communications at this range of depth, there exist three paths [121]: direct wave, reflected wave and lateral wave as shown in Fig. 9.14(b). Of the three paths, lateral wave is dominant in the far field [75], [175], because the attenuation in air is much smaller than the attenuation in soil. Therefore, the radiation pattern of the antenna buried in soil should have a radiation pattern such that the lateral wave is maximized. It is shown in [121], [175], that lateral wave occurs only when the incident wave is at the critical angle θ_c, which is the angle above

The critical angle, θ_c, is a function of soil permittivity, which is a function of soil moisture. Hence, θ_c varies with the change in soil moisture. On the other hand, due to the fact that the relative permittivity of soil is ten to hundred times higher than air, θ_c is less than 15° in all soil moisture settings.

Based on this analysis, the desired radiation pattern of the underground antenna is unidirectional towards the soil-air interface. The beamwidth of the antenna should cover all the critical angles in different soil moisture values, which are in the range of 5° to 15°. Thus, the planar antennas have desirable radiation patterns when they are

placed parallel to the soil-air interface.

9.6.2 The Return Loss

The performance of the antenna is tested in the same manner as in Section 9.4. Three antennas are buried at different depths: 0.13 m, 0.3 m, and 0.4 m. During natural precipitation, return loss results for three soil moisture values, 10%, 30% and 40% are recorded. The return loss results of the designed antenna are shown in Fig. 9.15, where the return loss values at three different depths are depicted in Fig. 9.15(b) and the return loss values for the three soil moisture values are shown in Fig 9.15(c). The bandwidth analysis is also shown in Fig. 9.16. As shown in these figures, even though the resonant frequency varies in different situations, the return loss at 433 MHz is always below 10 dB for all the burial depth and soil moisture values.

9.6.3 Communication Results

The designed circular planar antenna is employed in our test bed to measure the communication quality of the underground-aboveground communications. For comparison, the 25 mm wideband antenna and the elliptical antenna are also employed.

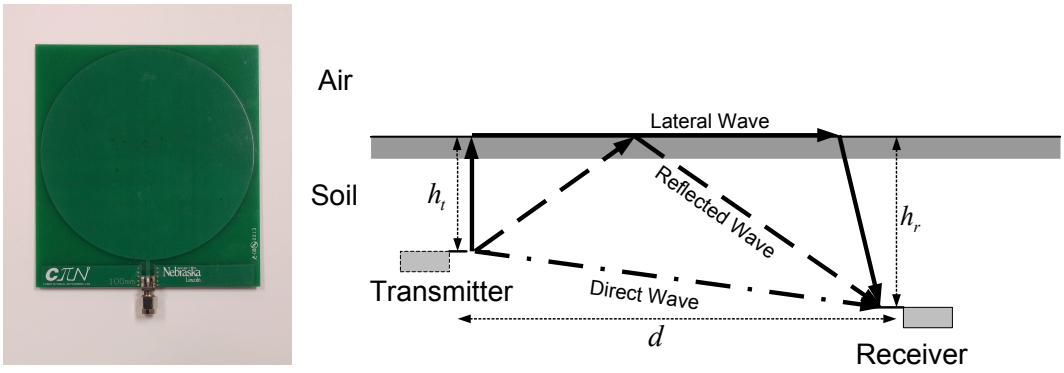

(a) (b)

Figure 9.14: (a) UG wideband planar antenna, (b) The three paths of subsurface underground communication [75], [175].

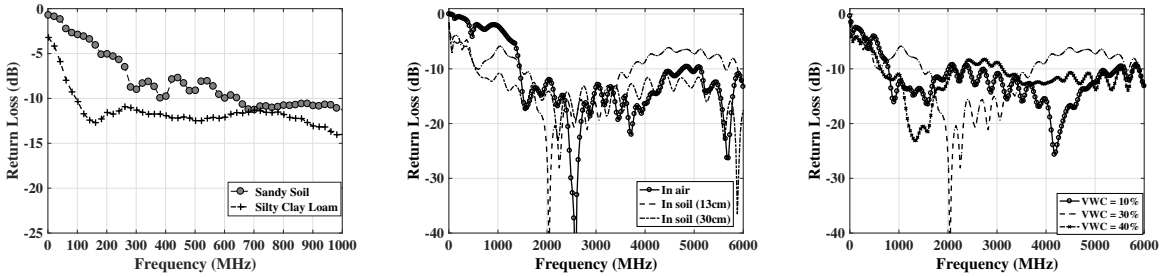

(a) (b) (c)

Figure 9.15: The return loss results of the 100 mm wideband planar antenna: (a) in silty clay loam and sandy soil, (b) at different depths, (c) under different volumetric water content.

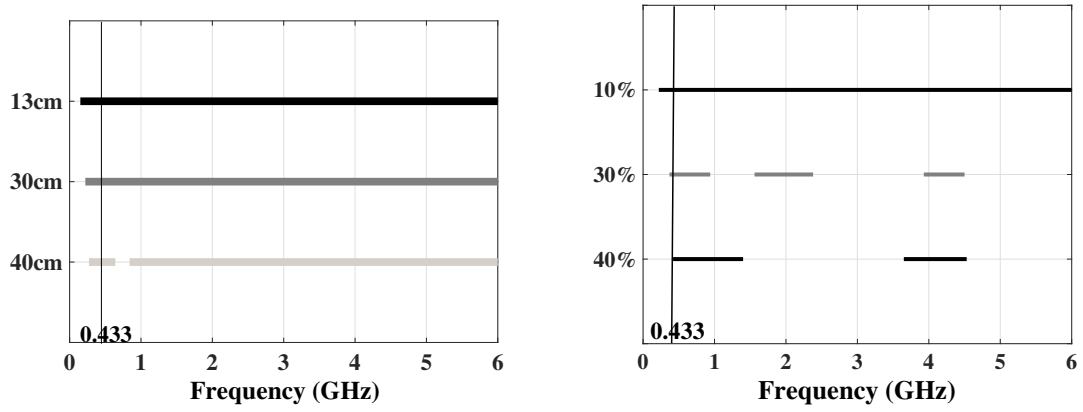

(a) (b)

Figure 9.16: The bandwidth analysis of the 100 mm planar antenna at (a) three depths and (b) two soil moisture levels.

In these experiments, a mote with the planar antenna is buried at 40 cm depth and an aboveground mote with a directional Yagi antenna is employed to communicate with the underground mote for both the underground to aboveground channel (UG2AG) and aboveground to underground channel (AG2UG). The three antennas are attached to the same mote and buried at the same location for fair comparison. The received signal strength (RSS) values at different distance are recorded and depicted in Fig. 9.17. It can be observed that practical underground link distances are still limited to allow for practical multi-hop connectivity. Yet, communication ranges of up to 200 m is possible for aboveground communications.

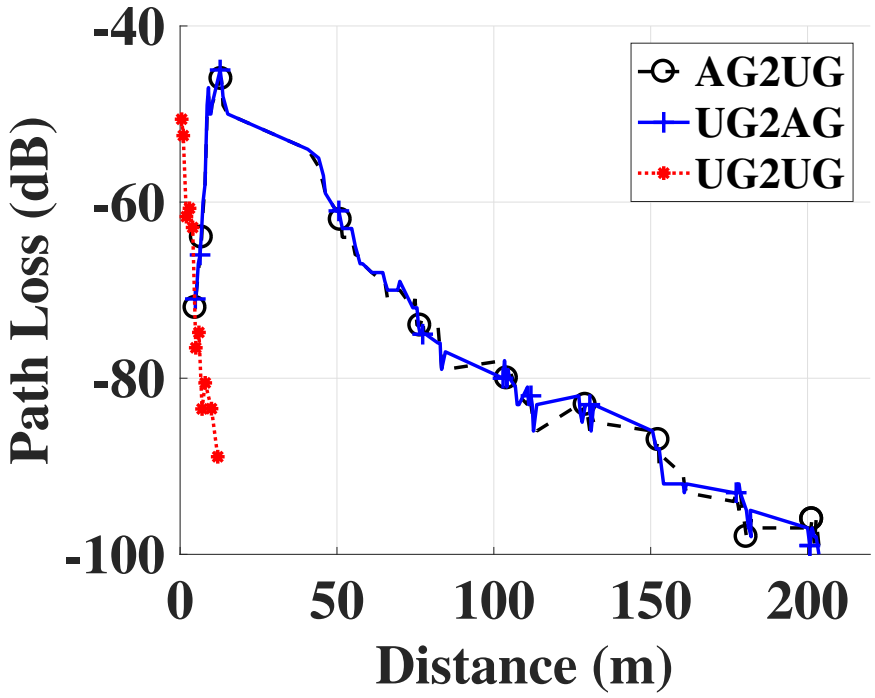

Figure 9.17: The received signal strength at different difference for the underground to aboveground communication and aboveground to underground communication.

It is shown that the 100 mm wideband antenna improves the communication range for both channels compared with the 25 mm circular and the elliptical antennas. For the UG2AG channel, the communication distance increases from 8 m (elliptical) and 17 m (25 mm circular) to 55 m. In other words, the designed antenna provides a 587.5% increase in communication range compared to the elliptical antenna and a 223.5% increase compared to the 25 mm circular antenna. For the AG2UG channel, the distance increases from 8 m (elliptical) and 15 m (25 mm circular) to 55 m, a 587.5% and a 266.7% increase, respectively. The results show that designing an antenna that is well matched in the soil environment is critical for the applications of IOUTs and can significantly increase the communication quality.

9.7 Conclusions

In this chapter, we investigated the effects of soil on antennas in underground communications. A model is developed to predict the resonant frequency of the UG antenna in different soils, at different depths, under water content variations. Theoretical analysis, simulations, and experimental validations are done to show that the high permittivity of the soil, and the effects of soil moisture variations mainly impact the performance of the antenna. The testbed and field experiments are conducted to further analyze these effects. The results show a very good agreement with the model. Moreover, the good fit with experimental results show that the model also captures the interface effects on the return loss of the antenna. Measured return loss values show the impacts of soil properties and soil moisture in the near vicinity of the antenna. Comparison of measurements with theoretical values makes the model a powerful analysis tool for the underground antenna design.

Chapter 10

Di-Sense: *In Situ* Real-Time Permittivity Estimation and Soil Moisture Sensing using Wireless Underground Communications

Internet of Underground Things (IOUT) communications have the potential for soil properties estimation and soil moisture monitoring. In this chapter, a method has been developed for real-time *in situ* estimation of relative permittivity of soil, and soil moisture, that is determined from the propagation path loss, and velocity of wave propagation of an underground (UG) transmitter and receiver link in wireless underground communications (WUC). The permittivity and soil moisture estimation processes (*Di-Sense*, where *Di-* prefix means *two*) are modeled and validated through an outdoor UG software-defined radio (SDR) testbed, and indoor greenhouse testbed. SDR experiments are conducted in the frequency range of 100 MHz to 500 MHz, using antennas buried at 10 cm, 20 cm, 30 cm, and 40 cm depths in different soils under different soil moisture levels, by using dipole antennas with over the air (OTA) resonant frequency of 433 MHz. Experiments are conducted in silt loam, silty clay loam, and sandy soils. By using Di-Sense approach, soil moisture and permittivity can be measured with high accuracy in 1 m to 15 m distance range in plant root zone up to depth of 40 cm. The estimated soil parameters have less than 8 % estimation error

from the ground truth measurements and semi-empirical dielectric mixing models.

10.1 Motivation

Internet of Underground Things (IOUT) have many applications in precision agriculture [35], [39], [51], [76], [96], [136], [189]. Border monitoring is another important application area of IOUT, where these networks are being used to enforce border and stop infiltration [40], [181]. Monitoring applications of IOUT include land slide monitoring, and pipeline monitoring [96], [177], [180]. IOUT provides seamless access of information collected from agricultural fields through the Internet. IOUT include in situ soil sensing capabilities (e.g., soil moisture, temperature, salinity), but also provide the ability to communicate through plants and soil, and real-time information about the environment (e.g., wind, rain, solar). When interconnected with existing machinery on the field (seeders, irrigation systems, combines), IOUT enable complete autonomy on the field, and pave the way for more efficient food production solutions. At agricultural farm level, IOUTs are being used to provide valuable information to the farmers.

Continuous sensing of soil moisture is essential for smart agriculture variable rate irrigation (VRI), real-time agricultural decision making, and water conservation [109]. Therefore, development of simple techniques to measure the in situ properties of soil is of vital importance. Moreover, permittivity estimation has applications in electromagnetic (EM) wave propagation analysis in the soil medium, depth analysis, subsurface imaging, and UG localization. Different methods for soil permittivity and moisture estimation are time-domain reflectometry (TDR) [140], [162], [194], ground-penetrating radar (GPR) measurements [62], [105], [145], and remote sensing [115], [170], [195], [196]. Moreover, one major bottleneck in the current laboratory-

based permittivity estimation techniques is off-line measurement of the collected soil samples. Remote sensing approaches are limited to shallow depths of 20 cm.

In situ measurements and inversion approach can be used to measure the soil properties at higher depths with greater accuracy. In this chapter, we have developed Di-Sense, an in situ, real-time soil moisture and permittivity estimation approach based on the wireless underground communications (WUC) in IOUT. For a transmitting antenna in the soil, the generated electromagnetic (EM) waves propagates through the soil, and are not only effected by the depth, distance, frequency and soil moisture [158], but also depend on the properties of the soil [65]. Path loss of these attenuated waves received at the UG receiver can be used to deduce the proprieties of soil, and can also be used to estimate the soil moisture. Our approach to derive the soil moisture and relative permittivity is based on the path loss of the UG communications channel in IOUT. Path loss of transmitter-receiver (T-R) pair in WUC depends on distance, depth, and soil moisture. In Di-Sense, a transmitter antenna buried at a certain depth in soil transmits a wideband signal in frequency range of 100 MHz to 500 MHz, which propagates through the UG channel. The received signal is measured at the receiver to determine the path loss. Di-sense enables an IOUT system to communicate simultaneously besides real-time permittivity estimation and soil moisture sensing. A model has been developed to estimate the soil moisture and permittivity based on path loss using Di-Sense. The model has been validated through experiments in a software-defined radio (SDR) testbed and in an indoor testbed in different soils at different depths under different soil moisture levels. Relative permittivity results show a very good agreement with less than 8 % estimation error from ground truth measurements, semi-empirical Peplinski dielectric mixing model [144], and Topp model [193].

The rest of the chapter is organized as follows: The related work is discussed in

Section 10.2. Di-Sense permittivity estimation and soil moisture sensing is modeled in Section 10.3. Model validation approaches are presented in Section 10.4. The description of empirical setup and measurements procedures is given in Section 10.5. Model validations and performance evaluations are performed in Section 10.6. Potential applications of the Di-Sense estimation approach are discussed in Section 10.7. Chapter is concluded in Section 10.8.

10.2 Related Work

Different soil permittivity and moisture estimation approaches have historically been considered in the literature. Following literature review is not all encompassing, rather we emphasize on some of the latest literature on the subject, with the purpose of highlighting similarities and differences with other works. Permittivity estimation and soil water measurement is classified into different approaches. Methods used for quantifying soil water include gravimetric method, TDR, GPR, capacitance probes, remote sensing, hygrometric techniques, electromagnetic induction, tensionmetry, neutron thermalization, nuclear magnetic resonance, gamma ray attenuation, resistive sensors, and optical methods. Some of these methods are reviewed briefly in the following.

First, we discuss laboratory based soil properties estimation approaches. In [104], soil EM parameters are derived as function of soil moisture, soil density, and frequency. This model is restricted to 20 % soil moisture weight, and requires extensive sample preparation. In [65], a probe based laboratory equipment has been developed that requires use of vector network analyzer (VNA), and works in frequency range of 45 MHz to 26.5 MHz. A model based to estimate the dielectric permittivity of soil based on the empirical evaluation has been done in [203]. In [69], a model of dielec-

tric properties of soil has been developed for frequencies higher than 1.4 MHz. In [144], Peplinski modified the model through extensive measurements to characterize the dielectric behavior of the soil in the frequency range of 300 MHz to 1.3 GHz. A comprehensive review of soil permittivity estimation approaches is given in [65]. These methods require the removal of the soil from the site. Moreover, laboratory based measurements of soil samples taken from site are labor-intensive, and are not truly representative of the in-situ soil conditions. Therefore, automated soil moisture monitoring technologies are needed.

Second approach to measure the soil properties, based on TDR, has been proposed in [140], that requires measurement of impedance and refractive index of soil. In [194], a method has been proposed to estimate the EM properties of soils for detection of Dense Non-Aqueous Phase Liquids (DNAPLs) hazardous materials using Cross-Well Radar (CWR). In this method, a wideband pulse waveform is transmitted in the frequency range of 0.5 GHz to 1.5 GHz, and soil permittivity is obtained using reflection and transmission simulations in dry sand. A detailed review of time domain permittivity measurements in soils is given in [198]. TDR based approach requires installation of sensors at each measurement location. However, real-time soil moisture sensing is required for effective decision making in agricultural fields.

Next, antenna based soil properties estimation approaches are discussed. In [171], [172], a method has been developed to measure the electrical properties of the earth using antennas buried in the geological media. However, this approach required adjustment of the length of antenna to achieve zero input reactance. This technique also requires measurement of the input reactance to derive the electrical constitutive parameters of the material. In [173], a GPR measurements based soil permittivity estimation is done in presence of soil antenna interactions by using the Fresnel reflection coefficients. However, only numerical results are presented without empirical

validations, and this approach also requires complicated time-domain analysis. In [50], dielectric properties of the soil are measured in the frequency range of 0.1 GHz to 1 GHz using wideband frequency domain method. This method requires use of impedance measurement equipment (LCR meter), and VNA. In [139], [205], a frequency domain method has been proposed to measure complex dielectric proprieties of the soil, that requires removing the soil and placing it in a probe.

The GPR technique is also utilized to estimate soil permittivity and moisture. A method has been developed in [105] to estimate the permittivity of ground which is based on the correlation of the cross talk of early-time GPR signal with dielectric properties of ground. However, GPR method works for only shallow depth (0-20 cm), and requires a calibration procedure. Moreover, measurements depth resolution of soil moisture content can not be restrained to a particular burial depth in soil.

Remote sensing of soil moisture is another important measurement approach. Although observation range is much higher with remote sensing [196], it is more sensitive to soil water content [115]. Passive remote sensing soil moisture measurement approaches [44], have very low spatial resolution (in the order of kilometers). Although, high spatial resolution is achieved (in the order of meters) with active sensing, however soil moisture measurement depth is restricted to the few top centimeters of the topsoil layers and vegetation cover effects the accuracy of soil moisture measurement [170].

From the review of soil moisture and permittivity measurement methods, it can be observed that there is a gap between the point based measurements, and large scale measurements. WUC have the potential to fill this gap for intermediate range (in the order of meters) spatial resolutions. The main focus of this chapter is on the use of WUC in permittivity estimation and soil moisture sensing. EM-wave communication in soil is impacted by soil properties and soil moisture [155], [158].

The presence and movement of even small amount of water results in significant changes in characteristics of the wireless UG channel between the sender and receiver nodes of an IOUT communication system. Therefore, these changes can be identified by analysis of the path loss at the receiver. Main advantage of this approach is that field IOUT infrastructure can be utilized for this purpose simultaneously by eliminating the need of specific soil moisture sensors. Hence, WUC are effectively used for soil sensing purpose. Over the last decade, a significant progress in UG communications, UG channel modeling, and characterization of impact of soil type and moisture has been witnessed [35], [51], [76], [96], [136], [156], [158], [184], [189], [199]. A detailed characterization of the wireless UG channel has been provided in [158]. Impacts of soil type and moisture on the capacity of multi-carrier modulations are discussed in [155]. In this work, WUC are utilized by developing an approach to use the propagation path loss in IOUT as soil sensing method, and is also validated through empirical measurements. To the best of our knowledge, there exists no other technique for real-time in situ estimation of these properties based on WUC, and this is the first work that utilizes wireless UG channel path loss, and velocity of EM wave propagation in the UG channel to estimate soil moisture and permittivity.

Table 10.1: Empirical VWC range, depth, and particle size distribution and classification of testbed soils.

Textural Class	%Sand	%Silt	%Clay	**V**WC (%) Range	**D**epth
Silty Clay Loam - Greenhouse (SCL-G)	13	55	32	32 - 38	20 cm
Silt Loam - Field (SL-F)	17	55	28	22 - 38	10, 20, 30, and 40 cm
Sandy Soil - Indoor Testbed (S-I)	86	11	3	15 - 38	10, 20, 30, and 40 cm
Silt Loam - Indoor Testbed (SL-I)	33	51	16	30 - 37	10, 20, 30, and 40 cm

10.3 System Models

To estimate the soil permittivity and moisture at a distance range of 1 m to 15 m, expressions are derived that connect these quantities to the measurable parameters

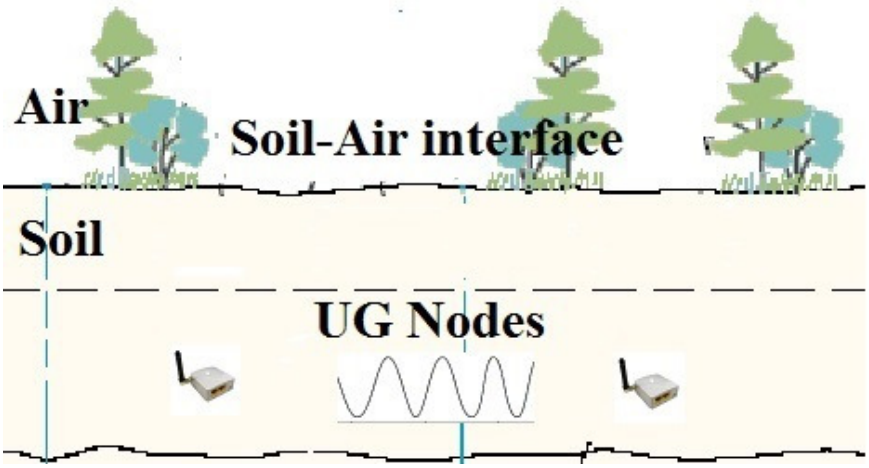

Figure 10.1: Estimation of soil properties using WUC.

of the WUC. For the permittivity estimation, these quantities are propagation path loss and velocity of wave propagation in soil. Problem to be investigated is framed as follows: given the path loss of communication link in the soil medium, derive a function that estimates the permittivity, and soil moisture of understudy soil medium. A schematic of WUC for soil relative permittivity estimation and soil moisture sensing is shown in Fig. 10.1. It is also important to note that the effective permittivity is equivalent to complex permittivity under low electrical loss. Moreover, in this chapter, permittivity refers to the relative permittivity. First, Di-Sense permittivity estimation using propagation path loss, and velocity of EM-wave propagation in soil is developed in Section 10.3.1, and then the soil moisture model is presented in Section 10.3.2.

10.3.1 Di-Sense Permittivity Estimation

Propagation Path Loss Approach: When EM wave communication is carried through the soil in IOUT, the propagation loss due to the water molecules held in the soil medium, is function of the real effective permittivity (dielectric constant) of soil. Therefore, propagation path loss of the soil direct path (between the transmitter-

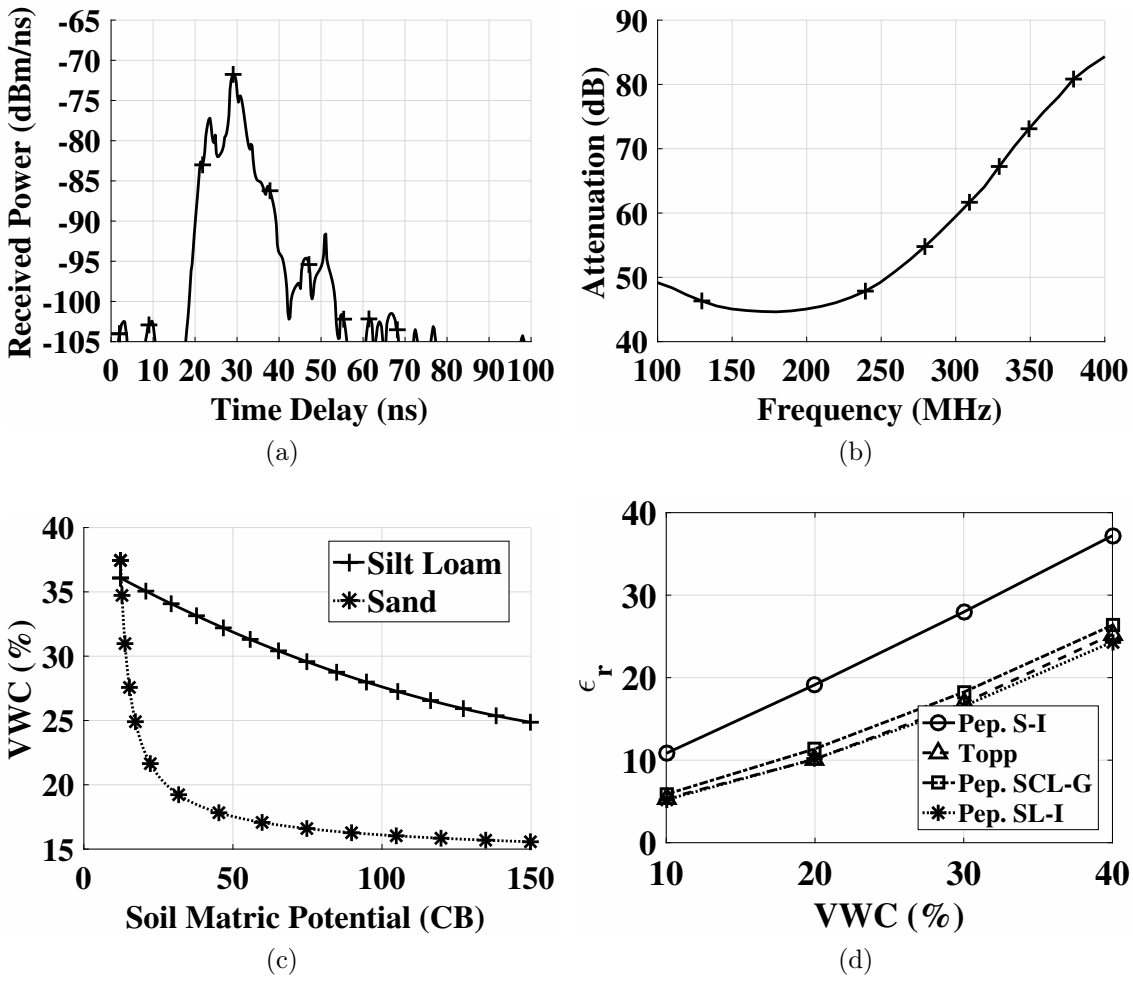

Figure 10.2: (a) An example power delay profile (PDP) in the silt loam soil in the indoor testbed, (b) attenuation in soil as a function of operation frequency, (c) water-retention curve of the sandy soil, and silt loam soil, to convert soil matric potential (SMP) to volumetric water content (VWC) [110, 111], (d) the VWC-permittivity relationship by the Topp (soil independent) and Peplinski model (for three different soils).

receiver (T-R) pair) can be used to estimate the relative permittivity and soil moisture within 100 MHz-500 MHz range. To model soil permittivity, lowest path loss (LPL) across the all frequency range is found by transmitting a known signal. The propagation path loss is determined by measuring the received signal. The transmitter transmits one signal using the narrow bandwidth at a time and frequency is increased sequentially in predefined step, Δf. Path loss is the ratio (expressed in decibel (dB))

of the transmitted power P_t to the power received P_r at the receiver. Path loss is determined as

$$PL = P_t - P_r = 10.\log 10(P_t/P_r) \ , \tag{10.1}$$

where PL is the system path loss, and includes the effects of transmitting and receiving antenna gains G_t, and G_r, respectively. Once the path loss is measured, the frequency of the lowest path loss is determined by

$$f_{min} = F(\min(PL(f))) \ , \tag{10.2}$$

where f_{min} is the frequency of the minimum pathloss. The f_{min} is not affected by distance between transmitter and receiver antennas, because of the antennas gains. Therefore, system path loss PL is inclusive of the antenna gains. Since PL measurements are done in narrowband, noise effects are minimal. Next the soil factor, ϕ, is calculated as:

$$\phi_s = f_{min}/f_0 \ , \tag{10.3}$$

where f_0 is the resonant frequency of the antenna in the free space. Once the soil factor, ϕ_s, has been determined, the wavelength of at the f_0 frequency is found

$$\lambda_0 = c/f_0 \ , \tag{10.4}$$

where c is the speed of light. Accordingly, relative permittivity of the soil is determined as:

$$\epsilon_r = \frac{1}{(\phi_s \times \lambda_0)^2} \ . \tag{10.5}$$

Permittivity Estimation through Velocity of Wave Propagation in Soil: Due to the inhomogeneity of the soil medium, permittivity of the soil varies along

the communication link from point to point. This leads to variations in wavelength and phase velocity, as the wave propagates in soil. Therefore, permittivity of the soil can be measured from the velocity of wave propagation soil. Power delay profile (PDP) are measured to get velocity of the wave propagation, that is determined from the known geometry layout of the testbed, by calculating the time that wave takes to reach at the receiver from transmitter. Once the velocity of the wave in soil, C_s, is determined relative permittivity in soil is calculated from the difference of transmission and arrival time of the direct component in the soil. Path of the direct component is completely through the soil. Accordingly, ϵ_r is determined as:

$$\epsilon_r = \left[C_s \times \frac{(\tau_{dr} - \tau_{dt})}{l}) \right] , \tag{10.6}$$

where l is the distance between transmitter and receiver antennas, $\tau_{dr} - \tau_{dt}$ is travel time of the direct component in the soil, and C_s is the wave propagation velocity in soil. Due to different prorogation velocities of the air and soil, direct wave is separate from the lateral wave which travels through the air along the soil-air interface, and has less attenuation as compared to the lateral wave (Chapter 4). In Fig. 10.2, an example power delay profile in the silt loam soil in the indoor testbed, and attenuation in soil as a function of operation frequency are shown.

10.3.2 Di-Sense Soil Moisture Sensing

The relationship of the soil moisture and permittivity is independent of the soil texture, bulk density, and frequency [193]. Since, soil permittivity depends on the soil moisture only, soil water content can be determined from soil permittivity [116], [193][1]. Since dry soil has relative permittivity of 3, and relative permittivity of the

[1]Although, there is some error in soil moisture-permittivity relationship, and its dependence is also weak for mineral soils, it has been shown to work well in fine, and coarse textured soils [128].

water is 80. Soil permittivity is calculated using (10.5) and (10.6), and accordingly, soil moisture is determined as [116], [193]:

$$VWC(\%) = \frac{\epsilon_r - 3}{.77} + 14.97 \ . \tag{10.7}$$

10.4 Model Validation Techniques

To validate the model, ground truth measurements of soil water content are taken using the soil moisture sensors. Water content in soil is represented by two methods - soil matric potential (SMP), and volumetric water content (VWC). Soil matric potential (SMP) is measured using the Watermark sensors buried at different depths. SMP is measured in centibars (CB)/kilopascals (kPa)[2]. By using the soil-water retention curve [110], soil matric potential is converted to soil volumetric water content. Water-retention curves of the sandy soil, and silt loam soil are shown in Fig. 10.2(c). It can be observed that, in sandy soil, as compared to the silt loam soil, a small increase in SMP leads to significant decrease in VWC. This is caused by the large pore size in sandy soil [112]. Hence, it is important to develop soil specific water-retention curves, due to textural and water holding capacity differences within different soil types [111].

In addition to the ground truth measurements in testbed soils, model validation is also done with Topp, and Peplinski's dielectric mixing models to validate the Di-Sense model for different soil types under varying soil water content. Topp model [193] is not dependent on soil type, and it relates the soil permittivity to soil water content.

[2]Greater matric potential values indicate lower soil moisture and zero matric potential represents near saturation condition, and 1 CB = 1 kPa.

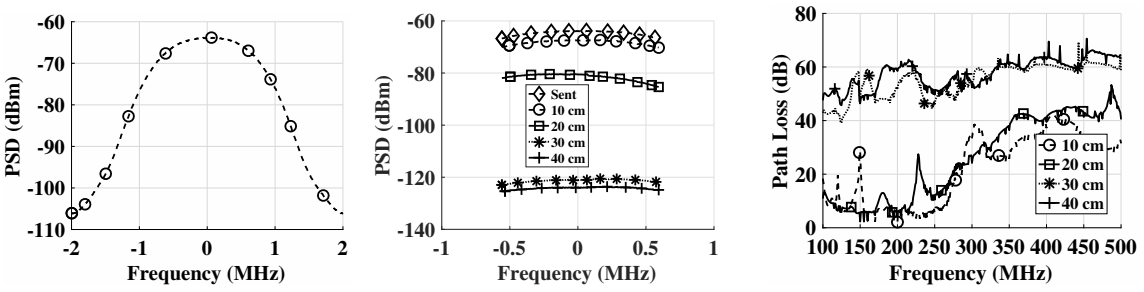

(b) (c)

Figure 10.3: (a) Power spectral density of the sent signal, (b) PSD of received signal at 50 cm,distance at 225 MHz, (c) path loss vs. frequency at different burial depths.

Topp model is given as [193]:

$$\theta = 4.3 \times 10^{-6}\epsilon^3 - 5.5 \times 10^{-4}\epsilon^2 + 2.92 \times 10^{-2}\epsilon - 5.3 \times 10^{-2} \tag{10.8}$$

where θ is the soil water content, and ϵ is the dielectric constant of the soil.

The Peplinski model [144] is used to determine the dielectric constant of soil, which is expressed as $\gamma = \alpha + j\beta$ where

$$\alpha = \omega\sqrt{\frac{\mu\epsilon'}{2}\left[\sqrt{1+(\frac{\epsilon''}{\epsilon'})^2}-1\right]}, \tag{10.9}$$

$$\beta = \omega\sqrt{\frac{\mu\epsilon'}{2}\left[\sqrt{1+(\frac{\epsilon''}{\epsilon'})^2}+1\right]}, \tag{10.10}$$

where $\omega = 2\pi f$ is the angular frequency, μ is the magnetic permeability, and ϵ' and ϵ'' are the real and imaginary parts of the dielectric constant as given in Appendix A.5. The VWC-permittivity relationship by the Topp (soil independent) and Peplanski model (for three different soils) is shown in Fig. 10.2(d).

10.5 Empirical Setup

In this section, we describe the measurement setup and experiment methodology for model validation experiments. Development of outdoor software-defined radio (SDR) testbed, and measurements details are given in Section 3.2.3. Power delay profile (PDP) measurements are explained in Section 10.5.2. Empirical VWC range, burial depths, and particle size distribution and classification of testbed soils is given in Table 10.1. Soil name abbreviations are also given that are used in figures in rest of the chapter for the purpose of brevity.

10.5.1 Experiment Methodology

The GNU Radio [89] and USRPs [80] are utilized to conduct SDR experiments in the SDR testbed (Section 3.2.3). A Gaussian signal RF waveform of 2 MHz bandwidth is transmitted from an UG dipole antenna, buried at 40 cm depth, by using the transmitter USRP. Signal is received on the receiver USRPs, connected to dipole antennas buried at four different depths (e.g., 10 cm, 20 cm, 30 cm, and 40 cm), with a fixed transmitter-receiver distance of 50 cm. Experiments are repeated for all these depth for the distances of two meter and four meter. For each frequency, transmitter transmits for one second duration, and receivers collect IQ data of four mega samples. Receivers send an acknowledge to the transmitter after finishing the reception, and, accordingly, transmitter starts transmission at the next frequency. This process is repeated for frequency range of 100 MHz to 500 MHz for each depth and distance, and three measurements are taken. Post-processing is done in Matlab [137].

For spectral estimation and path loss analysis, Welch's method [206] is employed. This method is enhanced form of periodogram analysis. By using the computationally efficient Discrete Fourier Transforms, data is divided into fixed blocks to calculate

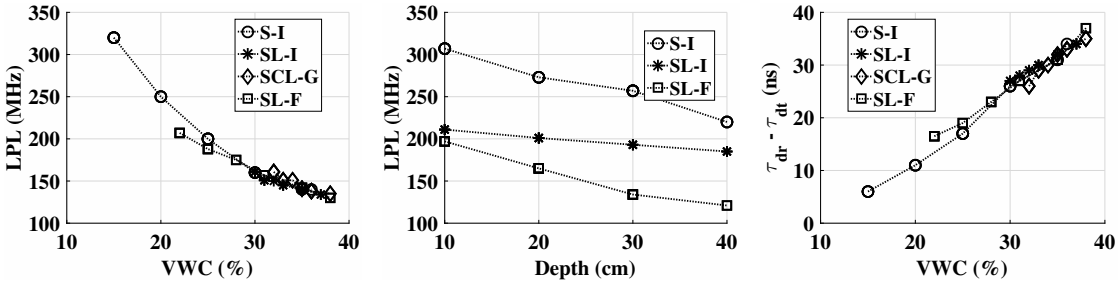

Figure 10.4: (a) Change in lowest path loss frequency of the UG channel at different soil moisture levels in sandy soil, silt loam, and silty clay loam soil, (b) Change in the lowest path frequency over depth, (c) Change in velocity of wave propagation as a function of soil moisture.

periodograms, and modified periodograms. These modified periodogram are averaged to calculate the power spectrum. Details of periodogram method of power spectrum density (PSD) analysis are given in Appendix A.4. In Fig. 10.3(a), PSD of the sent signal is shown.

In Fig. 10.3(b), PSD of received signal at 50 cm distance for 10 cm, 20 cm, 30 cm, and 40 cm, depths is shown. Transmitters's burial depth is 40 Cm. It is clearly evident that with increase in burial depth, PSD decreases significantly.

Pathless with frequency at 10 cm, 20 cm, 30 cm, and 40 cm depths is shown in Fig. 10.3(c). It can be observed that path loss increases significantly with frequency. This indicates that lower frequencies (e.g., less than 500 MHz) are more suitable for wireless UG channel in WUC.

10.5.2 PDP Measurements

In order to determine the velocity of EM wave propagation in soil, PDPs are measured by using the Keysight Technologies N9923A FieldFox VNA. PDP measurements are conducted in the indoor testbed, in sandy, and silt loam soils for dipole antennas buried at 10 cm, 20 cm, 30 cm, and 40 cm depths. Indoor testbed experiments are also done in sandy soil for different soil moisture levels. In the greenhouse testbed,

in silty clay loam soil, an antenna is buried at 20 cm depth. Over-the-air resonant frequency of these dipole antennas in all three soils is also 433 MHz. Channel transfer function and PDP measurement are conducted for different soil moisture levels. To measure PDP, a sinusoidal signal is transmitted by the VNA in frequency domain, from lower to higher frequencies, in an incremental step. The time-domain equivalent impulse response, $h(t)$, is produced from the frequency domain data by using the inverse Fourier transform (IFFT) operation. A total of 401 complex tones are stored in the frequency range of 10 MHz to 4 GHz. To suppress sidelobes, the windowing is done on the measured impulse response of the UG channel. Accordingly, velocity of wave propagation in soil is determined by the process described in Section 10.3.

10.6 Performance Analysis, Model Validation, and Error Analysis

In this section, first, propagation path loss has been measured for different soil types, under different soil moisture levels, at different burial depths using the methods described in Section 10.3. Impact of soil moisture, soil type, and burial depth variations on path loss are presented in Section 10.6.1. Model validation is carried out in Section 10.6.2. Model error analysis is done in Section 10.6.3.

10.6.1 Path Loss in Wireless Underground Communications

In Fig. 10.4(a), change in lowest path loss frequency of the UG channel at different soil moisture levels is shown in sandy soil, silt loam, and silty clay loam soil. It is observed that, in sandy soil, with increase in soil moisture (15% to 36%), lowest path loss frequency has shifted 182 MHz lower from 321 MHz to 139 MHz, which is a 56% decrease. In silt loam soil, as soil moisture decrease from 38% to 22%, lowest path

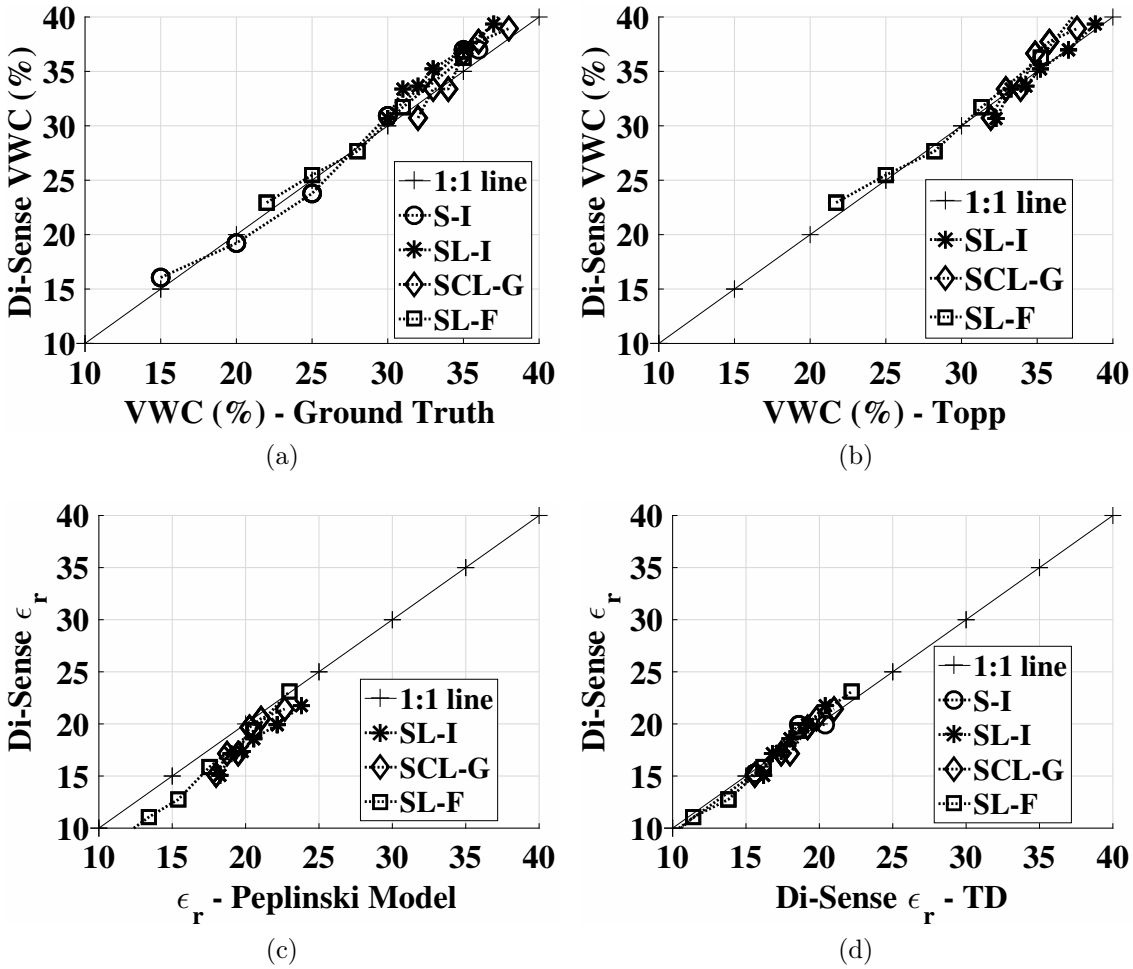

Figure 10.5: (a) Di-Sense VWC compared with ground truth VWC measurements, (b) Di-Sense VWC compared with Topp model (c) Di-Sense permittivity compared with Peplinski model (d) Di-Sense permittivity by time-domain velocity of propagation comparison with Di-Sense path loss propagation permittivity method.

loss frequency has increased from 129 MHz to 207 MHZ (60% increase). Similarly, in silty clay loam soil, with increase in soil moisture (32% to 38%), lowest path loss frequency has shifted 25 MHz lower from 160 MHz to 135 MHz, which is 15.62% decrease. In essence, in these soils, frequency of the lowest path loss decrease with increase in soil moisture, because of the fact that permittivity of soil is greater than the air, and it increases with increase in soil moisture, hence frequency of the lowest path loss shifts to the lower frequency end.

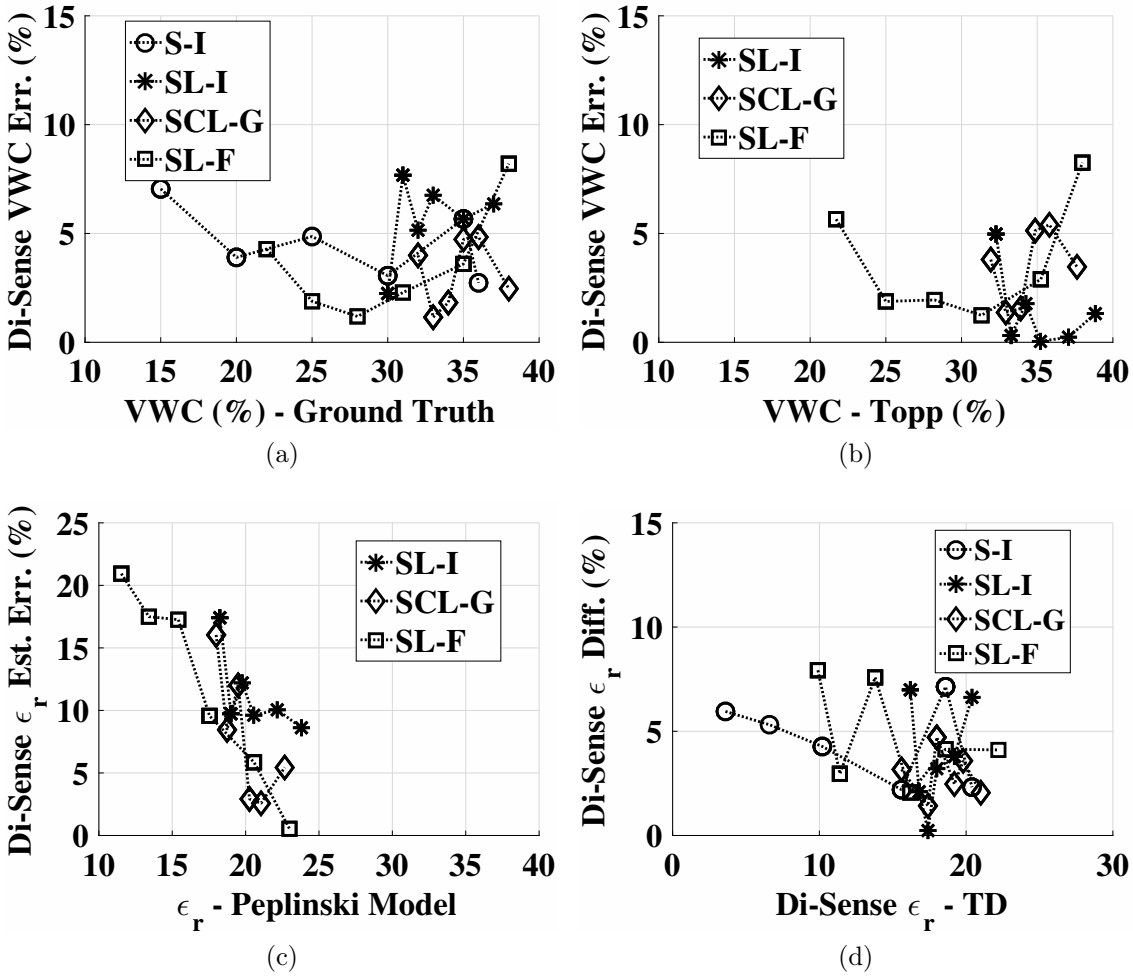

Figure 10.6: Di-Sense error analysis: (a) Di-Sense VWC vs. ground truth VWC measurements, (b) Di-Sense VWC vs. Topp model (c) Di-Sense permittivity vs. Peplinski model (d) Di-Sense permittivity by time-domain velocity of propagation vs. Di-Sense path loss propagation permittivity method.

In Fig. 10.4(b), change in the lowest path frequency over depth in silt loam, silty clay loam, and sandy soil is shown. From 10 cm depth to 20 cm depth, in silt loam soil, a change in lowest path loss frequency from 211 MHz to 201 MHz is observed, and at 40% depth, it has decreased to 185 MHz (which is a 12.32% less as compared to 10 cm depth). Whereas, in silt loam (field), from 10 cm to 40 cm depth, lowest path loss frequency is decreased by 38% from 197 MHz to 121 MHz. Similarly, in sandy soil, lowest path loss frequency, decreases from 308 MHz to 221 MHz when

depth changes from 10 cm to 40 cm. This difference in lowest frequency with depth is caused by the reflected wave from the soil-air interface that induces a current on the antenna and changes the impedance which results in changes in lowest path loss frequency of the wireless UG channel. At higher depths, the distance to the soil-air interface is higher. Hence, the intensity of the reflected wave is less due to higher soil absorption. Furthermore, interaction of antenna fields with the soil causes changes in the lowest path loss frequency of the UG channel.

Moreover, it can also be observed that the change in lowest path loss frequency while going deep in sandy soil is much larger (27.10%) as compared to the 12.32% change in silt loam soil for the same depths. This happens because the relative permittivity of a particular soil depends on its net water content [69], and silt loam has a higher water holding capacity as compared to sandy soil. Therefore, silt loam has a higher relative permittivity, and results in a lower path loss frequency. Whereas sandy soil has low water holding capacity due to large number of pores that leads to lower permittivity, which shifts the lowest path loss frequency to higher spectrum.

In Fig. 10.4(c), time of arrival of the the direct component is shown as a function of change in soil moisture. It can be observed that velocity of wave propagation in soil decrease with increase in soil moisture. In sandy soil, with VWC increase of 15% to 36%, wave velocity is decreased by five times. Similarly, in silty loam soil, it has decreased by three times, as soil moisture increases from 22% to 38%. It can also be observed silt loam has the 11% slower wave propagation velocity at 25% VWC as compared to sandy soil, because of the it higher relative permittivity.

10.6.2 Model Validation

In this section, model validation results are presented. The values of the soil moisture and soil permittivity, over soil moisture, are calculated accordingly by using the (10.5),

(10.6) and (10.7), and results are shown in Figs. 10.5. In Figs. 10.5(a)-10.5(b), Di-Sense VWC is compared with ground truth VWC measurements and Topp model. Di-Sense permittivity is compared with Peplinski model in Fig. 10.5(c). Di-Sense permittivity by time-domain velocity of propagation method is also compared with Di-Sense path loss propagation permittivity method and results are shown in Fig. 10.5(d).

While these graphs clearly show an excellent match of ground truth measurements and the models with Di-Sense, many interesting points are shown in Figs. 10.5. It can be observed that with decrease in lowest path loss frequency, soil permittivity increase rapidly, which also lead to increase in soil moisture. The Di-Sense model estimation error analysis is presented in the next section.

10.6.3 Model Error Analysis

Results of model error analysis are shown in Figs. 10.6. In Fig. 10.6(a), Di-Sense VWC estimation error is shown with measured ground truth soil moisture sensing in different soils. Higher variability of Di-Sense soil moisture estimation error (1% - 8%) is in silt loam soil, and model error variations are less in sandy soil. This highlights the impact of clay contents in soil. Overall, estimation error is less than 8 %.

Di-Sense soil moisture estimation error in comparison to the Topp model is shown in Fig. 10.6(b). It can be observed that estimation error of Di-Sense as compared to the Topp model is also less than 7 %, and higher variability of error is also observed in silt loam soil.

Di-Sense permittivity estimation error as compared to the Peplinski model is shown in Fig. 10.6(c). It can be observed that Di-sense estimation error as compared to the Peplinski model is relatively high (21%) for silt loam (field) as compared to silty clay loam and silt loam (that has error less than 15%). It can also be seen that at higher soil moisture levels, less error is observed as compared to the lower soil

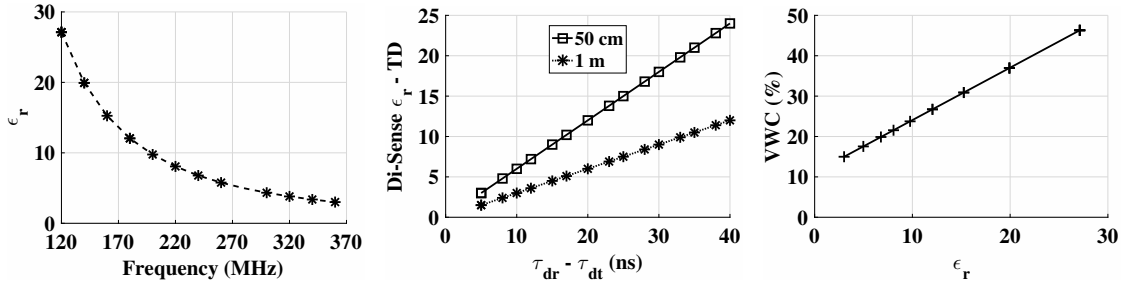

Figure 10.7: Di-Sense transfer functions: (a) soil permittivity, (b) soil permittivity time-domain (c) soil moisture.

moisture levels. Since many factors can affect the permittivity of water, at higher soil moisture level the relationship of soil medium dielectric constant becomes complicated. In addition, different factors (e.g., percentage of clay particles, soil temperature, soil type/texture, bulk density, salinity, porosity, soil bulk density) affect the soil permititivy. However, this effect is less significant on Di-Sense soil moisture estimation model, as still high accuracy in soil water content estimation is achieved in different soil types. Overall, these measured and modeled values are in agreement and the results show that Di-Sense method can be used to measure the soil permittivity and soil water content.

Moreover, it can also be seen that sandy soil permittivity is not compared with Peplinski model in Fig. 10.5(c), because Peplinski model does not work with sandy soil with 86% sand content [144]. Differences in Di-Sense permittivity by time-domain velocity of propagation method with Di-Sense path loss propagation permittivity method are shown in Fig. 10.6(d). Overall, both methods are in good agreement for the testbed soils with less than 8% estimation differences. Therefore, the Di-Sense soil moisture and permititivy models can be used for soil moisture and permititivy estimation in soils that have similar particle size distribution and classification to those used in these experiments.

10.6.4 Di-Sense Transfer Functions

It is worth noting that the results presented here are intended for soil moisture and permittivity estimation, but these can also be used for IOUT communication system design. Moreover, effects of changes in soil permittivity with change in depth are likely to be reduced at higher depths due to the fact that intensity of the reflected wave from soil-air interface is reduced at the deeper depths. For estimation purpose, following procedure would be used:

- Determine the lowest path loss frequency.
- Estimate soil permittivity using (10.5) and (10.6).
- Estimate soil moisture using (10.7).

Di-Sense transfer functions of the soil permittivity and soil moisture are shown in Fig. 10.7. Soil moisture and permittivity of soil medium can be determined using these graphs from measured values of IOUT propagation path loss. Di-Sense measurement technique is simple and easy to use, and no knowledge of type of radios, communication parameters, and antennas, being used in IOUT deployment, is required, as long as propagation path loss can be measured accurately. Moreover, Di-Sense can also be used for different operation frequencies, f_0, because (10.3), (10.4), scale accordingly with respect to the operation frequency. Like other measurement based techniques, there are some limitations for which the Di-Sense method is applicable. The major limitation is that propagation path loss of the soil under test should be measured accurately. For the application of Di-Sense to the application scenarios, where higher accuracy is required, an empirical factor can be used to account for the specific soil properties and soil-water retention capability.

10.7 Di-Sense Applications

Di-Sense approach can be used in applications where a need arises for WUC. In precision agriculture, where IOUTs are already deployed [76], Di-Sense can be utilized for irrigation scheduling. In buildings and bridges structures, Di-Sense measurements can be used to determine the health of the these structures by relating propagation path loss to properties of the communication medium. Another application of the Di-Sense is in the area of the geophysical prospecting, where IOUT can be used simultaneously for sensing, communications, and permittivity estimation of the ice and rocks. Contamination of soils can also be detected by the Di-Sense. It can also be used in meteorology, civil engineering, and geophysics.

10.8 Conclusions

In this chapter, wireless UG channel path loss and velocity of wave propagation in soil medium has been utilized to determine the permittivity and soil moisture. Di-Sense is based on estimation of the frequency of the lowest path loss of the direct communication link between the buried antennas in soil. The soil properties estimated using models developed for different soils compare favorably with experimental and theoretically results presented in the literature, and with ground truth measurements. The Di-Sense models developed in this chapter can be used for soil moisture and permititivy estimation in soils that have similar particle size distribution and classification to those used in these experiments. Di-Sense soil moisture and permittivity estimation approach accompanying fully-connected and reliable IOUT deployment in agricultural fields leads to improvements in precision agriculture practices.

Chapter 11

Conclusions and Future Work

11.1 Research Contributions

In this dissertation, the UG channel is characterized; environment-aware, cross-layer communication solutions are developed to achieve high data rate, long range communications; and applications to agriculture and smart lighting are illustrated. The impulse response of the wireless UG channel is captured and analyzed through extensive experiments. Based on this analysis, multi-carrier modulation and wireless underground channel diversity reception schemes has been developed. Moreover, based on UG antenna analysis, soil moisture adaptive beamforming using underground antenna arrays is also developed. Wide variety of applications potentially can utilize UG communication solutions with diverse requirements. Among these, smart agriculture solutions that highlight long range and high data rate aspects of UG communications are considered to evaluate the developed solutions. The findings of this research are evaluated using computational electromagnetic software simulation and proof-of-concept validations are done using testbed experiments.

11.2 Future Research Directions

The topic of wireless underground communications in Internet of Underground Things (IOUT) provides many research areas for future investigations.

11.2.1 Integration of IOUT with Cloud

Due to limited processing power and energy considerations, data processing and decision making are not generally conducted locally. Depending on privacy considerations, field information can be stored in a private database, provided to the public databases, or shared with other users [214]. There are online marketplaces where big data sets and agricultural apps are used to analyze a region and make decisions to maximize crop yield [161]. Additionally, in-situ SM sensors can be linked to national soil moisture databases for complete, accurate, and comprehensive information of soil moisture [15, 22, 24, 25, 27, 30, 32]. With the support of cloud services, real-time visualization and decision support can be provided. Therefore, Cloud can be used as a hub of data storage and processing applications in precision agricultural. Moreover, Cloud allows the scalability of IOUT paradigm from the field level to bigger geographic areas by forming network of farms.

On the other hand, in the absence of storage or processing constraints, base stations on the fields can pull meteorological data from a weather service or soil information from a national service, fuse this information with in-situ data from UTs, and control the farming equipment. To have a fully automated system, farming equipment should include a controller that can be accessed remotely. The integration of IOUT with creates new avenues to form robust stakeholders in precision agriculture such as growers, industry, and trading companies would result in increased efficiency and sustainability of whole precision agriculture ecosystem. In addition to integration of

farm equipment data to soil and weather databases, other examples include linking UAVs and robotics to precision agriculture paradigm .

Irrespective of in-situ or cloud processing, the main challenge is the integration of heterogeneous systems. Moreover, reliable data transfer from field to cloud, and cloud to farm, will constitute an important functionality of the IOUT cloud architecture. This functionality will not only help connect fields over vast geographical areas to the cloud, but will also facilitate local farms to use this data for assessment and improvement of crop yield. Moreover, there is a need of development of standardized interfaces for seamless connectivity and collaboration between different components of the precision agriculture ecosystem.

11.2.2 Big Data in Precision Agriculture

The IOUT paradigm enables sensing and communications of even minor changes in the field including change in physical properties of the soil and growth of plants. Major sources of big data in precision agriculture are ESA satellite images, NDVI from drones, user maps (yield, electrical conductivity, and others), and soil data. This process generates big data and it becomes very important to extract meaningful information from this huge amount of data. This is also crucial for real-time end user decision making and in evaluation of return on investment. Therefore, it is necessary to develop big data analytics in precision agriculture [210]. It is also essential to analyze the reduction in input cost in water resources, energy consumption and labor cost by adopting precision agriculture practices [46]. Other examples of the big data analytics in precision agriculture are factors affecting crop yield; and demarcation of field zones based on particular application such as productivity, soil moisture, nutrients, harvesting. Farmers, as the biggest stakeholder in the precision agriculture, need to use the technology to see the potential benefits with out being overloaded

with the data. Therefore, the big data analytics to show increase in crop yield and improvement in overall production efficiencies, which can deliver tangible benefits, are vital for success of the whole precision agriculture ecosystem.

11.2.3 Soil Moisture Adaptive Multi-Carrier Protocol Design

Due to availability of different types of SM sensors, their integration with communication equipment is a major challenge. A standard protocol multi-carrier protocol is required for seamless integration of different types of sensors to the communication devices in IOUT. Low-cost and multi-modal soil sensors that can sense soil physical properties in addition to moisture are required. While moisture provides valuable information for irrigation decisions, soil chemicals need to be sensed in-situ for variable rate fertigation applications.

Appendix A

Appendices

A.1 Derivation of Optimal Angle

The effective permittivity of soil-water mixture, which is a complex number, can be modeled as [144]:

$$\epsilon_s = \epsilon_s' - i\epsilon_s'' \ , \tag{A.1}$$

$$\epsilon_s' = \begin{cases} 1.15\Big[1 + \rho_b/\rho_s\left(\epsilon_s^{\delta} - 1\right) + (m_v)^{\nu'}(\epsilon_{fw}')^{\delta} - \\ \quad m_v\Big]^{1/\delta} - 0.68 \qquad 0.3\,\mathrm{GHz} \leq f \leq 1.4\,\mathrm{GHz} \ , \\ \Big[1 + \rho_b/\rho_s\left(\epsilon_s^{\delta} - 1\right) + (m_v)^{\nu'}(\epsilon_{fw}')^{\delta} - m_v\Big]^{1/\delta} \\ \qquad\qquad\qquad\qquad 1.4\,\mathrm{GHz} \leq f \leq 18\,\mathrm{GHz} \ , \end{cases} \tag{A.2}$$

$$\epsilon_s'' = \Big[(m_v)^{\nu''}(\epsilon_{fw}'')^{\delta}\Big]^{1/\delta} \ , \tag{A.3}$$

where f is the frequency in Hz, ϵ_s is the relative complex dielectric constant of the soil-water mixture, m_v is the volumetric water content, ρ_b is the bulk density and ρ_s is the particle density, δ, ν' and ν'' are empirically determined soil-type dependent

constants given by

$$\delta = 0.65 \ , \tag{A.4}$$

$$\nu' = 1.2748 - 0.519S - 0.152C \ , \tag{A.5}$$

$$\nu'' = 1.33797 - 0.603S - 0.166C \ , \tag{A.6}$$

where S and C represent the mass fractions of sand and clay, respectively. The quantities ϵ'_{fw} and ϵ''_{fw} in (A.25) and (A.26) are the real and imaginary parts of the relative permittivity of free water, and are calculated from the Debye model [144]:

$$\epsilon'_{fw} = e_{w\infty} + \frac{\epsilon_{w0} - \epsilon_{w\infty}}{1 + (2\pi f \tau_w)^2} \ , \tag{A.7}$$

$$\epsilon''_{fw} = \frac{2\pi f \tau_w (\epsilon_{w0} - \epsilon_{w\infty})}{1 + (2\pi f \tau_w)^2} + \frac{\delta_{eff}}{2\pi \epsilon_0 f} \frac{(\rho_s - \rho_b)}{\rho_s m_v} \ , \tag{A.8}$$

where $\epsilon_{w\infty} = 4.9$ is the limit of ϵ'_{fw} when $f \to \infty$, ϵ_{w0} is the static dielectric constant for water, τ_w is the relaxation time for water, and ϵ_0 is the permittivity of free space. Expressions for τ_w and ϵ_{w0} are given as a function of temperature. At room temperature (20°C), $2\pi\tau_w = 0.58 \times 10^{-10}$s and $\epsilon_{w0} = 80.1$. The effective conductivity, δ_{eff}, in (A.31) in terms of the textural properties of the soil, is given by

$$\delta_{eff} = \begin{cases} 0.0467 + 0.2204\rho_b - 0.4111S + 0.6614C \\ \qquad\qquad 0.3\,\text{GHz} \leq f \leq 1.4\,\text{GHz} \ . \\ -1.645 + 1.939\rho_b - 2.25622S + 1.594C \\ \qquad\qquad 1.4\,\text{GHz} \leq f \leq 18\,\text{GHz} \ , \end{cases} \tag{A.9}$$

This angle depends on these dielectric properties of the soil and is given as [175]:

$$\theta_{UG} = \frac{1}{2}\tan^{-1}\left(\frac{2Re(n^2-1)^{1/2}}{|n^2-1|-1}\right)rad, \tag{A.10}$$

where n is the refractive index of the soil and is given as

$$n = \sqrt{\frac{\sqrt{\epsilon'^2+\epsilon''^2}+\epsilon'}{2}}\ , \tag{A.11}$$

in which ϵ' and ϵ'' are the real and imaginary parts of the relative permittivity of the soil.

A.2 Wavenumber in Soil

Wavenumber in soil is given as:

$$k_s = \beta_s + i\alpha_s \tag{A.12}$$

where β_s indicates phase shift and α_s indicates propagation losses. Alternatively,

$$k_s = \omega\sqrt{\mu_0\epsilon_s} \tag{A.13}$$

where $\omega = 2\pi f$, and f is the frequency of the wave; μ_0 and ϵ_s are the permeability and permittivity of the soil, respectively.

A.3 Speed of Wave in Soil

Speed of the wave in soil is given as:

$$S = c/n, \tag{A.14}$$

where

$$c = 3 \times 10^8 \ m/s \tag{A.15}$$

is the speed of light, n is the refractive index of soil given by (A.11) with ϵ' and ϵ'' are the real and imaginary parts of the relative permittivity of the soil.

A.4 Periodogram Method of Power Spectrum Density

Collected data X[n], n =0, ... , N -1 is divided into K blocks. Length of these overlapping block is L with a difference of D units from each other. Then

$$\mathbf{X_1}(j) = X(j) j = 0, ...L - 1. \tag{A.16}$$

Similarly,

$$\mathbf{X_2}(j) = X(j + D) j = 0, ...L - 1. \tag{A.17}$$

and

$$\mathbf{X_K}(j) = X(j + (K - 1)D) j = 0, ...L - 1. \tag{A.18}$$

For each L length block modified periodogram is calculated by selecting a data window W(j) j = 0, ... L -1 in order to form the sequence $X_i(j)W(j), ..., X_K W(j)$ Fourier transforms of these sequences $A_i(n), ...A_k(n)$ is taken as follows:-

$$\mathbf{A_k}(n) = \frac{1}{L} \sum_{j=0}^{L-1} X_k(j) W(j) e^{-2kijn/L} \tag{A.19}$$

where $i = (-1)^{\frac{1}{2}}$. K modified periodogram are obtained as following:-

$$\mathbf{I_k}(f_n) = \frac{L}{U} |A_k(n)|^2 \tag{A.20}$$

where

$$f_n = \frac{n}{L} n = 0, ..., L/2 \tag{A.21}$$

and

$$U = \frac{1}{L} \sum_{j=0}^{L-1} W^2(j) \tag{A.22}$$

Power spectral density (PSD) is the average of these periodogram and is given as:-

$$\mathbf{P}(f_n) = \frac{1}{K} \sum_{k=0}^{K} I_k(f_n) \tag{A.23}$$

A.5 Semi-Empirical Dielectric Mixing Model

The effective permittivity of soil-water mixture, which is a complex number, can be modeled as [144]:

$$\epsilon_s = \epsilon_s' - i\epsilon_s'' \ , \tag{A.24}$$

$$\epsilon_s' = \begin{cases} 1.15\Big[1 + \rho_b/\rho_s \left(\epsilon_s^{\delta} - 1\right) + (m_v)^{\nu'}(\epsilon_{fw}')^{\delta} - \\ \quad m_v\Big]^{1/\delta} - 0.68 \qquad 0.3\,\text{GHz} \leq f \leq 1.4\,\text{GHz} \ , \\ \Big[1 + \rho_b/\rho_s \left(\epsilon_s^{\delta} - 1\right) + (m_v)^{\nu'}(\epsilon_{fw}')^{\delta} - m_v\Big]^{1/\delta} \\ \qquad\qquad\qquad\qquad 1.4\,\text{GHz} \leq f \leq 18\,\text{GHz} \ , \end{cases} \tag{A.25}$$

$$\epsilon_s'' = \Big[(m_v)^{\nu''}(\epsilon_{fw}'')^{\delta}\Big]^{1/\delta} \ , \tag{A.26}$$

where f is the frequency in Hz, ϵ_s is the relative complex dielectric constant of the soil-water mixture, m_v is the volumetric water content, ρ_b is the bulk density and ρ_s is the particle density, δ, ν' and ν'' are empirically determined soil-type dependent

constants given by

$$\delta = 0.65 \ , \tag{A.27}$$

$$\nu' = 1.2748 - 0.519S - 0.152C \ , \tag{A.28}$$

$$\nu'' = 1.33797 - 0.603S - 0.166C \ , \tag{A.29}$$

where S and C represent the mass fractions of sand and clay, respectively. The quantities ϵ'_{fw} and ϵ''_{fw} in (A.25) and (A.26) are the real and imaginary parts of the relative permittivity of free water, and are calculated from the Debye model [144]:

$$\epsilon'_{fw} = e_{w\infty} + \frac{\epsilon_{w0} - \epsilon_{w\infty}}{1 + (2\pi f \tau_w)^2} \ , \tag{A.30}$$

$$\epsilon''_{fw} = \frac{2\pi f \tau_w (\epsilon_{w0} - \epsilon_{w\infty})}{1 + (2\pi f \tau_w)^2} + \frac{\delta_{eff}}{2\pi \epsilon_0 f} \frac{(\rho_s - \rho_b)}{\rho_s m_v} \ , \tag{A.31}$$

where $\epsilon_{w\infty} = 4.9$ is the limit of ϵ'_{fw} when $f \to \infty$, ϵ_{w0} is the static dielectric constant for water, τ_w is the relaxation time for water, and ϵ_0 is the permittivity of free space. Expressions for τ_w and ϵ_{w0} are given as a function of temperature. At room temperature (20°C), $2\pi\tau_w = 0.58 \times 10^{-10}$s and $\epsilon_{w0} = 80.1$. The effective conductivity, δ_{eff}, in (A.31) in terms of the textural properties of the soil, is given by

$$\delta_{eff} = \begin{cases} 0.0467 + 0.2204\rho_b - 0.4111S + 0.6614C \\ \qquad\qquad 0.3\,\text{GHz} \leq f \leq 1.4\,\text{GHz} \ . \\ -1.645 + 1.939\rho_b - 2.25622S + 1.594C \\ \qquad\qquad 1.4\,\text{GHz} \leq f \leq 18\,\text{GHz} \ , \end{cases} \tag{A.32}$$

Appendix B

Publications

The work of this research has yielded the following major publications.

- A. Salam and M. C. Vuran. "*EM-based Wireless Underground Sensor Networks*", in *Underground Sensing: Monitoring and hazard detection for environment and infrastructure - 1st edition*, chapter 5. Edited by S. Pamukcu and L. Cheng, Elsevier, in press, Oct 2017.

- M. C. Vuran, **A**. Salam, R. Wong, and S. Irmak "*Internet of Underground Things: Sensing and Communications on the Field for Precision Agriculture*", in Proc. *IEEE 4th World Forum on Internet of Things (**W**F-IOT)*, Singapore, Feb 2018.

- A. Salam, M. C. Vuran, "*Smart Underground Antenna Arrays: A Soil Moisture Adaptive Beamforming Approach*", to appear in Proc. of the *36th IEEE International Conference on Computer Communications (IEEE INFOCOM 2017)*, Atlanta, GA, USA, May 2017.

- A. Salam, M. C. Vuran, "*Wireless Underground Channel Diversity Reception With Multiple Antennas for Internet of Underground Things*", to appear in Proc. of the *IEEE ICC 2017*, Paris, France, May 2017.

- A. Salam, M. C. Vuran, and S. Irmak, "*Towards Internet of Underground Things in Smart Lighting: A Statistical Model of Wireless Underground Channel* ", to appear in Proc. of the *14th IEEE International Conference on Networking, Sensing and Control (IEEE ICNSC)*, Calabria, Italy, May 2017.

- A. Salam, and M. C. Vuran, "*Impacts of Soil Type and Moisture on the Capacity of Multi-Carrier Modulation in Internet of Underground Things*", in Proc. of the *25th International Conference on Computer Communication and Networks (ICCCN 2016)*, Waikoloa, Hawaii, USA, Aug 2016 (**Best Student Paper Award**).

- A. Salam, M. C. Vuran, and S. Irmak, "*Pulses in the Sand: Impulse Response Analysis of Wireless Underground Channel*", in Proc. of the *35th IEEE International Conference on Computer Communications (IEEE INFOCOM 2016)*, San Francisco, CA, USA, Apr 2016.

- M. C. Vuran, A. Salam, R. Wong, and S. Irmak "*Internet of Underground Things in Precision Agriculture: Architecture and Technology Aspects*", *under revision* in Ad Hoc Networks (Elsevier), Aug 2018.

- A. Salam, M. C. Vuran, and S. Irmak "*Di-Sense: In Situ Real-Time Permittivity Estimation and Soil Moisture Sensing using Wireless Underground Communications*", *under review* in Computer Networks (Elsevier), Nov 2018.

- A. Salam, M. C. Vuran, X. Dong, C. Argyropoulos, and S. Irmak, "*Underground Dipole Antennas for Communications in Internet of Underground Things*," *under review* in IEEE Transactions on Antennas and Propagation, 2018.

Bibliography

[1] "365 FarmNet," https://www.365farmnet.com/en/.

[2] "Biosense," www.biosens.rs.

[3] "Cornell Digital Agriculture," https://cuaes.cals.cornell.edu/digital-agriculture.

[4] "Cropx soil monitoring system," https://www.cropx.com/.

[5] "CST Microwave Studio," www.cst.com/products/cstmws.

[6] "CST Simulation Code." [Online]. Available: https://www.dropbox.com/s/sbd92aob9w11ysf/SMABF_simulations.cst?dl=0

[7] "Dynamax SapIP Wireless Mesh Network," http://dynamax.com/products/data-loggers/sapip-wireless-mesh-network.

[8] "Herelab," www.Herelab.io.

[9] "IBM EZ-Farm," https://www.ibm.com/developerworks/community/blogs/dfa2dc54-5a14-4cf8-91e0-978bfd59d0d4/entry/IBM_Research_Africa_Enhancing_the_way_we_farm?lang=en.

[10] "Intellifarms," www.intellifarms.com.

[11] "IoF2020," https://www.iof2020.eu/.

[12] "Iot sensor platform," http://zenseio.com/zenseio-platform.

[13] "Irromesh wireless mesh system," http://www.irrometer.com/loggers.html#975.

[14] "John deere field connect," https://www.deere.com/.

[15] "Ldas land data assimilation systems," https://ldas.gsfc.nasa.gov/nldas/.

[16] "Leaf monitor system," http://www.westernfarmpress.com/tree-nuts/uc-research-explores-continuous-leaf-monitor-system-maximize-irrigation-almonds.

[17] "Plug and sense smart agriculture," http://www.libelium.com/products/plug-sense/models/#smart-agriculture.

[18] "PrecisionHawk Drone Data Platform," http://www.precisionhawk.com/agriculture.

[19] "Purdue's Digital Agriculture Initiative," http://mailimages.purdue.edu/vo/?FileID=ac13556e-8057-487f-a01b-6914f848cc4c.

[20] "Senet," www.senetco.com.

[21] "Sensor network for irrigation scheduling," http://soilphysics.okstate.edu/research/moisst/2017-moisst-workshop/Taghvaeian%20MOISST%202017.pdf/at_download/file.

[22] "Smap soil moisture active passive," https://smap.jpl.nasa.gov/.

[23] "Smart underground antenna arrays: A soil moisture adaptive beamforming approach," Tech. Rep. [Online]. Available: https://www.dropbox.com/s/j4w8nr31jy5w5of/SMABF_Extended.pdf?dl=0

[24] "Smos," www.esa.int/Our_Activities/Observing_the_Earth/SMOS.

[25] "Soil climate analysis network (scan) data & products," www.wcc.nrcs.usda.gov/scan/.

[26] "Symphony link," https://www.link-labs.com/symphony.

[27] "Tamu north american soil moisture database," soilmoisture.tamu.edu.

[28] "Temputech wireless sensor monitoring," http://www.temputech.com/.

[29] "Tule," https://www.tuletechnologies.com/.

[30] "U.s. climate reference network," www.ncdc.noaa.gov/crn/.

[31] "Vri study," http://proceedings.esri.com/library/userconf/proc15/papers/185_435.pdf.

[32] "Web soil survey home," https://websoilsurvey.sc.egov.usda.gov/.

[33] P. Abouzar, D. G. Michelson, and M. Hamdi, "RSSI-based distributed self-localization for wireless sensor networks used in precision agriculture," *IEEE Transactions on Wireless Communications*, Oct 2016.

[34] ——, "Rssi-based distributed self-localization for wireless sensor networks used in precision agriculture," *IEEE Transactions on Wireless Communications*, vol. 15, no. 10, pp. 6638–6650, Oct 2016.

[35] T. E. Abrudan, O. Kypris, N. Trigoni, and A. Markham, "Impact of rocks and minerals on underground magneto-inductive communication and localization," *IEEE Access*, vol. 4, pp. 3999–4010, 2016.

[36] ——, "Impact of rocks and minerals on underground magneto-inductive communication and localization," *IEEE Access*, vol. 4, pp. 3999–4010, 2016.

[37] A. Akdagli, "A closedâĂŘform expression for the resonant frequency of rectangular microstrip antennas," *Microwave and Optical Technology Letters*, vol. 49, no. 8, pp. 1848–1852. [Online]. Available: https://onlinelibrary.wiley.com/doi/abs/10.1002/mop.22572

[38] I. F. Akyildiz and et.al., "Next generation/dynamic spectrum access/cognitive radio wireless networks: A survey," *Computer Networks Journal, (Elsevier)*, vol. 50, pp. 2127–2159, September 2006.

[39] I. F. Akyildiz and E. P. Stuntebeck, "Wireless underground sensor networks: Research challenges," *Ad Hoc Networks Journal*, July 2006.

[40] I. F. Akyildiz, Z. Sun, and M. C. Vuran, "Signal propagation techniques for wireless underground communication networks," *Physical Communication Journal (Elsevier)*, vol. 2, no. 3, pp. 167–183, Sept. 2009.

[41] N. Anand, S.-J. Lee, and E. W. Knightly, "Strobe: Actively securing wireless communications using zero-forcing beamforming," in *INFOCOM, 2012 Proceedings IEEE*, March 2012, pp. 720–728.

[42] V. Arnautovski-Toseva and L. Grcev, "On the image model of a buried horizontal wire," *IEEE Transactions on Electromagnetic Compatibility*, vol. 58, no. 1, pp. 278–286, February 2016.

[43] E. Aryafar and et.al., "Adam: An adaptive beamforming system for multicasting in wireless lans," *IEEE/ACM Trans. on Networking*, 2013.

[44] S. b. Kim, J. D. Ouellette, J. J. van Zyl, and J. T. Johnson, "Detection of inland open water surfaces using dual polarization l-band radar for the soil moisture

active passive mission," *IEEE Transactions on Geoscience and Remote Sensing*, vol. 54, no. 6, pp. 3388–3399, June 2016.

[45] A. Banos, *Dipole radiation in the presence of a conducting halfspace*. Pergamon Press, 1966.

[46] M. Bendre, R. Thool, and V. Thool, "Big data in precision agriculture: Weather forecasting for future farming," in *Next Generation Computing Technologies (NGCT), 2015 1st International Conference on*. IEEE, 2015, pp. 744–750.

[47] A. Bicen, A. Sahin, and O. Akan, "Spectrum-aware underwater networks: Cognitive acoustic communications," *Vehicular Technology Magazine, IEEE*, vol. 7, no. 2, pp. 34–40, June 2012.

[48] A. Biggs, "Dipole antenna radiation fields in stratified antarctic media," *Antennas and Propagation, IEEE Transactions on*, vol. 16, no. 4, pp. 445–448, Jul 1968.

[49] T. S. Bird, "Definition and misuse of return loss [Report of the transactions Editor-in-Chief]," *IEEE Antennas and Propagation Magazine*, vol. 51, no. 2, pp. 166–167, April 2009.

[50] P. Bobrov, A. Repin, and O. Rodionova, "Wideband frequency domain method of soil dielectric property measurements," *Geoscience and Remote Sensing, IEEE Transactions on*, vol. 53, no. 5, pp. 2366–2372, May 2015.

[51] H. R. Bogena, M. Herbst, J. A. Huisman, U. Rosenbaum, A. Weuthen, and H. Vereecken, "Potential of wireless sensor networks for measuring soil water content variability," *Vadose Zone Journal*, Nov. 2010.

[52] H. R. Bogena, J. A. Huismana, H. Meierb, U. Rosenbauma, and A. Weuthena, "Hybrid wireless underground sensor networks: Quantification of signal attenuation in soil," *Vadose Zone Journal*, vol. 8, no. 3, pp. 755–761, August 2009.

[53] K. Boyle, Y. Yuan, and L. Ligthart, "Analysis of mobile phone antenna impedance variations with user proximity," *IEEE Transaction on Antennas and Propagation*, vol. 55, no. 2, pp. 364–372, Feb. 2007.

[54] L. M. Brekhovskikh, *Waves in Layered Media.* New York: Academic Press, 1980.

[55] D. Cassioli, M. Win, and A. Molisch, "The ultra-wide bandwidth indoor channel: from statistical model to simulations," *IEEE JSAC*, vol. 20, no. 6, pp. 1247–1257, Aug 2002.

[56] G. Castorina, L. D. Donato, A. F. Morabito, T. Isernia, and G. Sorbello, "Analysis and design of a concrete embedded antenna for wireless monitoring applications," *IEEE Antennas and Propagation Magazine*, vol. 58, no. 6, pp. 76–93, December 2016.

[57] R. Chandra, R. Mahajan, T. Moscibroda, R. Raghavendra, and P. Bahl, "A case for adapting channel width in wireless networks," *SIGCOMM Comput. Commun. Rev.*, vol. 38, no. 4, pp. 135–146, Aug. 2008. [Online]. Available: http://doi.acm.org/10.1145/1402946.1402975

[58] R. W. Chang, "Synthesis of band-limited orthogonal signals for multichannel data transmission," *Bell System Technical Journal*, vol. 45, no. 10, pp. 1775–1796, 1966.

[59] R. Cheng and S. Verdu, "Gaussian multiaccess channels with ISI: capacity region and multiuser water-filling," *IEEE Trans. Information Theory*, vol. 39, no. 3, pp. 773–785, May 1993.

[60] P. Chow and J. Cioffi, "Bandwidth optimization for high speed data transmission over channels with severe intersymbol interference," in *Proc. GLOBECOM '92*, Orlando, Florida, Dec 1992.

[61] S. T. Chung and A. Goldsmith, "Degrees of freedom in adaptive modulation: a unified view," *IEEE Trans. Communications*, vol. 49, no. 9, pp. 1561–1571, Sep 2001.

[62] D. Comite, A. Galli, S. E. Lauro, E. Mattei, and E. Pettinelli, "Analysis of gpr early-time signal features for the evaluation of soil permittivity through numerical and experimental surveys," *IEEE Journal of Selected Topics in Applied Earth Observations and Remote Sensing*, vol. 9, no. 1, pp. 178–187, Jan 2016.

[63] T. M. Cover and J. A. Thomas, *Elements of Information Theory 2nd Edition.* Wiley-Interscience, July 2006.

[64] CRC Handbook, *CRC Handbook of Chemistry and Physics*, 95th ed. CRC Press, 2014.

[65] J. O. Curtis, "A durable laboratory apparatus for the measurement of soil dielectric properties," *IEEE Transactions on Instrumentation and Measurement*, vol. 50, no. 5, pp. 1364–1369, Oct 2001.

[66] S. Das, E. de Carvalho, and R. Prasad, "Performance analysis of OFDM systems with adaptive sub carrier bandwidth," *IEEE Trans. Wireless Communications*, vol. 7, no. 4, pp. 1117–1122, April 2008.

[67] K. C. DeJonge, S. Taghvaeian, T. J. Trout, and L. H. Comas, "Comparison of canopy temperature-based water stress indices for maize," *Agricultural Water Management*, vol. 156, pp. 51 – 62, 2015. [Online]. Available: http://www.sciencedirect.com/science/article/pii/S0378377415001067

[68] T. Dissanayake, K. Esselle, and M. Yuce, "Dielectric loaded impedance matching for wideband implanted antennas," *IEEE Transactions on Microwave Theory and Techniques*, vol. 57, no. 10, pp. 2480–2487, Oct. 2009.

[69] M. Dobson and et.al., "Microwave dielectric behavior of wet soil—Part II: Dielectric mixing models," *IEEE Trans. Geoscience and Remote Sensing*, vol. GE-23, no. 1, pp. 35 –46, January 1985.

[70] J. Dong, F. Shen, Y. Dong, Y. Wang, W. Fu, H. Li, D. Ye, B. Zhang, J. Huangfu, S. Qiao, Y. Sun, C. Li, and L. Ran, "Noncontact measurement of complex permittivity of electrically small samples at microwave frequencies," *IEEE Transactions on Microwave Theory and Techniques*, vol. 64, no. 9, pp. 2883–2893, Sept 2016.

[71] S. Dong, A. Yao, and F. Meng, "Analysis of an underground horizontal electrically small wire antenna," *Journal of Electrical and Computer Engineering*, vol. 2851, p. 9, 2015.

[72] X. Dong and M. C. Vuran, "Environment aware connectivity for wireless underground sensor networks," in *IEEE/ACM INFOCOM '13*, Turin, Italy, Apr. 2013.

[73] ——, "Exploiting soil moisture information for adaptive error control in wireless underground sensor networks," in *2013 IEEE Global Communications Conference (GLOBECOM)*, Dec 2013.

[74] ——, "Impacts of soil moisture on cognitive radio underground networks," in *Proc. IEEE BlackSeaCom*, Georgia, 2013.

[75] ——, "A channel model for wireless underground sensor networks using lateral waves," in *Proc. of IEEE Globecom '11*, Houston, TX, December 2011.

[76] X. Dong, M. C. Vuran, and S. Irmak, "Autonomous precision agricultrue through integration of wireless underground sensor networks with center pivot irrigation systems," *Ad Hoc Networks (Elsevier)*, 2012.

[77] Y. Du and et.al., "iBeam: Intelligent client-side multi-user beamforming in wireless networks," in *IEEE INFOCOM 2014*, April 2014.

[78] P. Elejoste, I. Angulo, A. Perallos, A. Chertudi, I. J. G. Zuazola, A. Moreno, L. Azpilicueta, J. J. Astrain, F. Falcone, and J. Villadangos, "An easy to deploy street light control system based on wireless communication and led technology," *Sensors*, vol. 13, no. 5, pp. 6492–6523, 2013.

[79] R. S. Elliott, *Antenna Theory and Design*. Prentice-Hall, Inc., 1981.

[80] Ettus Research Website. [Online]. Available: http://www.ettus.com

[81] A. Farid, A. Alshawabkeh, and C. Rappaport, "Validation and calibration of a laboratory experimental setup for cross-well radar in sand," *American Society for Testing and Materials (ASTM) Geotechnical Testing Journal*, vol. 29, no. 2, Mar. 2006.

[82] ——, "Electromagnetic waves in contaminated soils," *Book chapter published in Electromagnetic Waves Propagation in Complex Matter, Ahmed Kishk, ed.*, pp. 117–154, Jul. 2011.

[83] A. Fenn and P. Hurst, *Ultrawideband Phased Array Antenna Technology for Sensing and Communications Systems.* MIT Press, 2015.

[84] R. G. Fitzgerrell and L. L. Haidle, "Design and performance of four buried uhf antennas," *IEEE Trans. Antennas Propagation*, vol. 20, no. 1, pp. 56–62, 1972.

[85] H. D. Foth, *Fundamentals of Soil Science*, 8th ed. John Wiley and Sons, 1990.

[86] J. Galejs, *Antennas in Inhomogeneous Media.* Pergamon Press, 1969.

[87] A.-J. Garcia-Sanchez, F. Garcia-Sanchez, and J. Garcia-Haro, "Wireless sensor network deployment for integrating video-surveillance and data-monitoring in precision agriculture over distributed crops," *Computers and Electronics in Agriculture*, vol. 75, no. 2, pp. 288–303, 2011.

[88] V. Gautam, K. Ray, and P. Haddow, "Hardware efficient design of variable length FFT processor," in *Proc. IEEE DDECS '11*, Cottbus, Germany, April 2011, pp. 309–312.

[89] GNU Radio Website. [Online]. Available: http://www.gnuradio.org

[90] L. C. Godara, "Application of antenna arrays to mobile communications. ii. beam-forming and direction-of-arrival considerations," *Proceedings of the IEEE*, vol. 85, no. 8, pp. 1195–1245, Aug 1997.

[91] A. K. Gopalakrishna, T. Ozcelebi, A. Liotta, and J. J. Lukkien, *Statistical Inference for Intelligent Lighting: A Pilot Study.* Cham: Springer International Publishing, 2015, pp. 9–18.

[92] A. K. Gopalakrishna, T. Ozcelebi, J. J. Lukkien, and A. Liotta, "Relevance in cyber-physical systems with humans in the loop," *Concurrency and Computation: Practice and Experience*, vol. 29, no. 3, 2017.

[93] K. Gosalia, M. Humayun, and G. Lazzi, "Impedance matching and implementation of planar space-filling dipoles as intraocular implanted antennas in a retinal prosthesis," *IEEE Transactions on Antennas and Propagation*, vol. 53, no. 8, pp. 2365–2373, Aug. 2005.

[94] F. Gross, *Smart Antennas with MATLAB*. McGraw-Hill, 2015.

[95] H. Guo and Z. Sun, "Increasing the capacity of magnetic induction communication using mimo coil-array," in *2016 IEEE GLOBECOM*, Dec 2016, pp. 1–6.

[96] ——, "Channel and energy modeling for self-contained wireless sensor networks in oil reservoirs," *IEEE Trans. Wireless Communications*, vol. 13, no. 4, pp. 2258–2269, April 2014.

[97] J. Gutiarrez, J. F. Villa-Medina, A. Nieto-Garibay, and M. A. Porta-Gandara, "Automated irrigation system using a wireless sensor network and gprs module," *IEEE Transactions on Instrumentation and Measurement*, vol. 63, no. 1, pp. 166–176, Jan 2014.

[98] A. Guy and G. Hasserjian, "Impedance properties of large subsurface antenna arrays," *IEEE Transactions on Antennas and Propagation*, vol. 11, no. 3, pp. 232–240, May 1963.

[99] R. Hansen, "Radiation and reception with buried and submerged antennas," *IEEE Transactions on Antennas and Propagation*, vol. 11, no. 3, pp. 207–216, May 1963.

[100] ——, *Phased Array Antennas*. Wiley, 2009.

[101] H. Hashemi, "Impulse response modeling of indoor radio propagation channels," *IEEE JSAC*, vol. 11, no. 7, pp. 967–978, Sep 1993.

[102] R. L. Haupt, "Fitting time delay units in a large wideband corporate fed array," in *2013 IEEE Radar Conference (RadarCon13)*, April 2013.

[103] R. Haupt, *Timed Arrays.* Wiley, 2015.

[104] J. E. Hipp, "Soil electromagnetic parameters as functions of frequency, soil density, and soil moisture," *Proceedings of the IEEE*, vol. 62, no. 1, pp. 98–103, Jan 1974.

[105] G. Hislop, "Permittivity estimation using coupling of commercial ground penetrating radars," *IEEE Transactions on Geoscience and Remote Sensing*, vol. 53, no. 8, pp. 4157–4164, Aug 2015.

[106] J. Hopkins, "USDA ERS - ARMS farm financial and crop production practices: Tailored reports: Crop production practicesl," *ers.usda.gov,*, 2016, Available: http://www.ers.usda.gov/data-products/arms-farm-financial-and-crop-production-practices/tailored-reports-crop-production-practices.aspx.

[107] S. Howard and K. Pahlavan, "Measurement and analysis of the indoor radio channel in the frequency domain," *IEEE Trans. Instrumentation and Measurement*, vol. 39, no. 5, pp. 751–755, Oct 1990.

[108] K. Iizuka, "An experimental investigation on the behavior of the dipole antenna near the interface between the conducting medium and free space," *IEEE Transactions on Antennas and Propagation*, vol. 12, no. 1, pp. 27–35, Jan. 1964.

[109] S. Irmak and et.al., "Large scale on-farm implementation of soil moisture-based irrigation management strategies for increasing maize water productivity," *Transactions of the ASABE*, vol. 55, no. 3, pp. 881–894, 2012.

[110] S. Irmak and D. Haman, "Performance of the watermark. granular matrix sensor in sandy soils," *Applied Engineering in Agriculture*, vol. 17, no. 6, p. 787, 2001.

[111] S. Irmak and A. Irmak, "Performance of frequency-domain reflectometer, capacitance, and psuedo-transit time-based soil water content probes in four coarse-textured soils," *Applied engineering in agriculture*, vol. 21, no. 6, pp. 999–1008, 2005.

[112] S. Irmak, J. O. Payero, D. E. Eisenhauer, W. L. Kranz, D. Martin, G. L. Zoubek, J. M. Rees, B. VanDeWalle, A. P. Christiansen, and D. Leininger, "Ec06-783 watermark granular matrix sensor to measure soil matric potential for irrigation management," 2006.

[113] M. N. Islam, B. J. Kim, P. Henry, and E. Rozner, "A wireless channel sounding system for rapid propagation measurements," in *Proc. IEEE ICC' 2013*, Jun. 2013, pp. 5720–5725.

[114] R. C. Johnson, Ed., *Antenna Engineering Handbook*, 3rd ed. McGraw-Hill, Inc., 1993.

[115] F. Jonard, L. WeihermÃijller, M. Schwank, K. Z. Jadoon, H. Vereecken, and S. Lambot, "Estimation of hydraulic properties of a sandy soil using ground-based active and passive microwave remote sensing," *IEEE Transactions on Geoscience and Remote Sensing*, vol. 53, no. 6, pp. 3095–3109, June 2015.

[116] B. Josephson and A. Blomquist, "The influence of moisture in the ground, temperature and terrain on ground wave propagation in the vhf-band," *IRE Transactions on Antennas and Propagation*, vol. 6, no. 2, pp. 169–172, April 1958.

[117] I. Kalet, "The multitone channel," *IEEE Trans. Communications*, vol. 37, no. 2, pp. 119–124, Feb 1989.

[118] A. S. Kesar and E. Weiss, "Wave propagation between buried antennas," *IEEE Transactions on Antennas and Propagation*, vol. 61, no. 12, pp. 6152–6156, December 2013.

[119] Y. Kim, R. G. Evans, and W. M. Iversen, "Remote sensing and control of an irrigation system using a distributed wireless sensor network," *IEEE Transactions on Instrumentation and Measurement*, vol. 57, no. 7, pp. 1379–1387, July 2008.

[120] R. W. P. King, "The many faces of the insulated antenna," in *Proceedings of the IEEE*. no. 2: vol. 64, February 1976, pp. 228–238.

[121] R. W. P. King, M. Owens, and T. T. Wu, *Lateral Electromagnetic Waves*. Springer-Verlag, May 1992.

[122] R. W. P. King and G. Smith, *Antennas in Matter*. MIT Press, 1981.

[123] S. Kisseleff, I. F. Akyildiz, and W. Gerstacker, "Beamforming for magnetic induction based wireless power transfer systems with multiple receivers," in *2015 IEEE GLOBECOM*, Dec 2015.

[124] S. Kisseleff, I. F. Akyildiz, and W. H. Gerstacker, "Magnetic induction based simultaneous wireless information and power transfer for single information and

multiple power receivers," *IEEE Transactions on Communications*, vol. PP, no. 99, pp. 1–1, 2017.

[125] S. Kisseleff, I. Akyildiz, and W. Gerstacker, "Digital signal transmission in magnetic induction based wireless underground sensor networks," *IEEE Trans. Communications*, vol. 63, no. 6, pp. 2300–2311, June 2015.

[126] S. Lakshmanan, K. Sundaresan, R. Kokku, A. Khojestepour, and S. Rangarajan, "Towards adaptive beamforming in indoor wireless networks: An experimental approach," in *INFOCOM 2009, IEEE*, April 2009.

[127] K. Langendoen, A. Baggio, and O. Visser, "Murphy loves potatoes: Experiences from a pilot sensor network deployment in precision agriculture," in *Parallel and Distributed Processing Symposium, 2006. IPDPS 2006. 20th International.* IEEE, 2006, pp. 8–pp.

[128] J. Ledieu, P. D. Ridder, P. D. Clerck, and S. Dautrebande, "A method of measuring soil moisture by time-domain reflectometry," *Journal of Hydrology*, vol. 88, no. 3, pp. 319 – 328, 1986.

[129] L. Li, M. Vuran, and I. Akyildiz, "Characteristics of underground channel for wirless underground sensor networks," in *Proc. of IFIP Mediterranean Ad Hoc Networking Workshop (Med-Hoc-Net '07)*, Corfu, Greece, June 2007.

[130] S. Lin, I. Akyildiz, P. Wang, and Z. Sun, "Distributed cross-layer protocol design for magnetic induction communication in wireless underground sensor networks," *Wireless Communications, IEEE Transactions on*, vol. 14, no. 7, pp. 4006–4019, July 2015.

[131] G. Liu, Z. Wang, and T. Jiang, "QoS-aware throughput maximization in wireless powered underground sensor networks," *IEEE Transactions on Communications*, vol. PP, no. 99, pp. 1–1, 2016.

[132] ——, "Qos-aware throughput maximization in wireless powered underground sensor networks," *IEEE Transactions on Communications*, vol. 64, no. 11, pp. 4776–4789, Nov 2016.

[133] X. Liu and et.al., "DIRC: increasing indoor wireless capacity using directional antennas," *SIGCOMM Comput. Commun. Rev.*, Aug. 2009.

[134] R. Ma and W. Zhang, "Adaptive MQAM for energy harvesting wireless communications with 1-bit channel feedback," *IEEE Trans. Wireless Communications*, vol. PP, no. 99, pp. 1–1, 2015.

[135] R. Mailloux, *Phased Array Antenna Handbook*. Artech House, 2005.

[136] A. Markham and N. Trigoni, "Magneto-inductive networked rescue system (miners): Taking sensor networks underground," in *Proceedings of the 11th ICPS*, ser. IPSN '12. ACM, 2012, pp. 317–328.

[137] MATLAB. [Online]. Available: http://wwwmatlab.com

[138] R. K. Moore and W. E. Blair, "Dipole radiation in conducting half space," *Journal of Res National Bureau of Standard*, vol. 65, 1961.

[139] E. M. Nassar, R. Lee, and J. D. Young, "A probe antenna for in situ measurement of the complex dielectric constant of materials," *IEEE Transactions on Antennas and Propagation*, vol. 47, no. 6, pp. 1085–1093, Jun 1999.

[140] A. M. Nicolson and G. F. Ross, "Measurement of the intrinsic properties of materials by time-domain techniques," *IEEE Transactions on Instrumentation and Measurement*, vol. 19, no. 4, pp. 377–382, Nov 1970.

[141] T. Nitsche and et.al., "Steering with eyes closed: Mm-wave beam steering without in-band measurement," in *IEEE INFOCOM*, April 2015.

[142] K. A. Norton, "The physical reality of space and surface waves in the radiation field of radio antennas," in *Proceedings of the Institute of Radio Engineers*. no. 9: vol. 25, September 1937, pp. 1192–1202.

[143] D. Paglieroni, C. Pechard, and N. Beer, "Change detection in constellations of buried objects extracted from ground-penetrating radar data," *IEEE Transactions on Geoscience and Remote Sensing*, vol. 53, no. 5, pp. 2426–2439, May 2015.

[144] N. Peplinski, F. Ulaby, and M. Dobson, "Dielectric properties of soil in the 0.3–1.3 ghz range," *IEEE Transactions on Geoscience and Remote Sensing*, vol. 33, no. 3, pp. 803–807, May 1995.

[145] E. Pettinelli, A. D. Matteo, E. Mattei, L. Crocco, F. Soldovieri, J. D. Redman, and A. P. Annan, "Gpr response from buried pipes: Measurement on field site and tomographic reconstructions," *IEEE Transactions on Geoscience and Remote Sensing*, vol. 47, no. 8, pp. 2639–2645, Aug 2009.

[146] M. A. Poletti, "The application of linearly swept frequency measurements," *The Journal of the Acoustical Society of America*, vol. 84, no. 2, pp. 599–610, August 1988.

[147] D. Pompili and I. Akyildiz, "Overview of networking protocols for underwater wireless communications," *IEEE Communications Magazine*, vol. 47, no. 1, pp. 97–102, January 2009.

[148] J. Proakis and M. Salehi, *Digital Communications*, 5th ed. McGraw-Hill, 2007.

[149] F. Quitin and et.al., "A scalable architecture for distributed transmit beamforming with commodity radios: Design and proof of concept," *IEEE Trans. on Wireless Communications*, March 2013.

[150] T. Rappaport, S. Seidel, and K. Takamizawa, "Statistical channel impulse response models for factory and open plan building radio communicate system design," *IEEE Trans. Communications*, vol. 39, no. 5, pp. 794–807, May 1991.

[151] W. Rhee and J. Cioffi, "Increase in capacity of multiuser ofdm system using dynamic subchannel allocation," in *Proc. IEEE 51st VTC 2000-Spring*, Tokyo, Japan, 2000.

[152] C. J. Ritsema and et.al., "A new wireless underground network system for continuous monitoring of soil water contents," *Water Resources Research Journal*, vol. 45, pp. 1–9, May 2009.

[153] F. Rojo, E. Kizer, S. Upadhyaya, S. Ozmen, C. Ko-Madden, and Q. Zhang, "A leaf monitoring system for continuous measurement of plant water status to assist in precision irrigation in grape and almond crops," *IFAC-PapersOnLine*, vol. 49, no. 16, pp. 209 – 215, 2016, 5th IFAC Conference on Sensing, Control and Automation Technologies for Agriculture AGRICONTROL 2016. [Online]. Available: http://www.sciencedirect.com/science/article/pii/S2405896316316020

[154] A. Salam and M. C. Vuran, "Em-based wireless underground sensor networks," in *Underground Sensing: Monitoring and hazard detection for environment and infrastructure - 1st edition*, S. Pamukcu and L. Cheng, Eds. Elsevier, 2017, ch. 5.

[155] ——, "Impacts of soil type and moisture on the capacity of multi-carrier modulation in internet of underground things," in *Proc. ICCCN 2016*, Waikoloa, Hawaii, USA, Aug 2016.

[156] ——, "Smart underground antenna arrays: A soil moisture adaptive beamforming approach," in *Proc. 36th IEEE INFOCOM 2017*, Atlanta, USA, May 2017.

[157] ——, "Wireless underground channel diversity reception with multiple antennas for internet of underground things," in *Proc. IEEE ICC 2017*, Paris, France, May 2017.

[158] A. Salam, M. C. Vuran, and S. Irmak, "Pulses in the sand: Impulse response analysis of wireless underground channel," in *Proc. IEEE INFOCOM 2016*, San Francisco, USA, Apr. 2016.

[159] ——, "Towards internet of underground things in smart lighting: A statistical model of wireless underground channel," in *Proc. 14th IEEE International Conference on Networking, Sensing and Control (IEEE ICNSC)*, Calabria, Italy, May 2017.

[160] A. Saleh and R. Valenzuela, "A statistical model for indoor multipath propagation," *Selected Areas in Communications, IEEE Journal on*, vol. 5, no. 2, pp. 128–137, February 1987.

[161] M. v. Schönfeld, R. Heil, and L. Bittner, *Big Data on a Farm—Smart Farming*. Cham: Springer International Publishing, 2018, pp. 109–120. [Online]. Available: https://doi.org/10.1007/978-3-319-62461-7_12

[162] W. R. Scott and G. S. Smith, "Measured electrical constitutive parameters of soil as functions of frequency and moisture content," *IEEE Transactions on Geoscience and Remote Sensing*, vol. 30, no. 3, pp. 621–623, May 1992.

[163] A. R. Silva and M. C. Vuran, "Communication with aboveground devices in wireless underground sensor networks: An empirical study," in *Proc. of IEEE ICC'10*, Cape Town, South Africa, May 2010, pp. 1–6.

[164] ——, "Development of a Testbed for Wireless Underground Sensor Networks," *EURASIP Journal on Wireless Communications and Networking*, vol. 2010, 2010.

[165] ——, "Empirical evaluation of wireless underground-to-underground communication in wireless underground sensor networks," in *Proc. of IEEE DCOSS '09*, Marina del Rey, CA, June 2009, pp. 231–244.

[166] ——, "$(CPS)^2$: integration of center pivot systems with wireless underground sensor networks for autonomous precision agriculture," in *Proc. of ACM/IEEE International Conf. on Cyber-Physical Systems*, Stockholm, Sweden, April 2010, pp. 79–88.

[167] S. Singh, M. Shahbazi, K. Pelechrinis, K. Sundaresan, S. Krishnamurthy, and S. Addepalli, "Adaptive sub-carrier level power allocation in OFDMA networks," *IEEE Trans. Mobile Computing*, vol. 14, no. 1, pp. 28–41, Jan 2015.

[168] V. Singhvi, A. Krause, C. Guestrin, J. H. Garrett, Jr., and H. S. Matthews, "Intelligent light control using sensor networks," in *Proceedings of the 3rd International Conference on Embedded Networked Sensor Systems*, ser. SenSys '05. New York, NY, USA: ACM, 2005, pp. 218–229. [Online]. Available: http://doi.acm.org/10.1145/1098918.1098942

[169] K. Sivaprasad and R. King, "A study of arrays of dipoles in a semi-infinite dissipative medium," *Antennas and Propagation, IEEE Transactions on*, vol. 11, no. 3, pp. 240–256, May 1963.

[170] E. E. Small, K. M. Larson, C. C. Chew, J. Dong, and T. E. Ochsner, "Validation of gps-ir soil moisture retrievals: Comparison of different algorithms to remove vegetation effects," *IEEE Journal of Selected Topics in Applied Earth Observations and Remote Sensing*, vol. 9, no. 10, pp. 4759–4770, Oct 2016.

[171] G. Smith and J. Nordgard, "Measurement of the electrical constitutive parameters of materials using antennas," *IEEE Transactions on Antennas and Propagation*, vol. 33, no. 7, pp. 783–792, Jul 1985.

[172] G. S. Smith and R. W. P. King, "The resonant linear antenna as a probe for measuring the in situ electrical properties of geological media," *Journal of Geophysical Research*, vol. 79, no. 17, pp. 2623–2628, 1974. [Online]. Available: http://dx.doi.org/10.1029/JB079i017p02623

[173] R. Solimene, A. D'Alterio, G. Gennarelli, and F. Soldovieri, "Estimation of soil permittivity in presence of antenna-soil interactions," *IEEE Journal of Selected Topics in Applied Earth Observations and Remote Sensing*, vol. 7, no. 3, pp. 805–812, March 2014.

[174] A. Sommerfeld, “”uber die ausbreitung der wellen in der drahtlosen telegraphie”. in,” *Ann. Phys*, vol. 28, pp. 665–737, 1909.

[175] D. Staiman and T. Tamir, “Nature and optimisation of the ground (lateral) wave excited by submerged antennas,” *Electrical Engineers, Proceedings of the Institution of*, vol. 113, no. 8, August 1966.

[176] A. Street, L. Lukama, and D. Edwards, “Use of VNAs for wideband propagation measurements,” *IEEE Proc. Communications*, vol. 148, no. 6, pp. 411–415, Dec 2001.

[177] Z. Sun and I. Akyildiz, “Channel modeling and analysis for wireless networks in underground mines and road tunnels,” *IEEE Trans. on Communications*, June 2010.

[178] ——, “Magnetic induction communications for wireless underground sensor networks,” *Antennas and Propagation, IEEE Transactions on*, vol. 58, no. 7, pp. 2426–2435, July 2010.

[179] Z. Sun, I. Akyildiz, S. Kisseleff, and W. Gerstacker, “Increasing the capacity of magnetic induction communications in rf-challenged environments,” *IEEE Trans. Communications*, vol. 61, no. 9, pp. 3943–3952, September 2013.

[180] Z. Sun and et.al., “MISE-PIPE: MI based wireless sensor networks for underground pipeline monitoring,” *Ad Hoc Networks*, 2011.

[181] Z. Sun, P. Wang, M. C. Vuran, M. A. Al-Rodhaan, A. M. Al-Dhelaan, and I. F. Akyildiz, “Border patrol through advanced wireless sensor networks,” *Ad Hoc Networks*, vol. 9, no. 3, pp. 468–477, 2011.

[182] C. T. Tai and R. E. Collin, "Radiation of a hertzian dipole immersed in a dissipative medium," *IEEE Transactions on Antennas and Propagation*, vol. 48, no. 10, pp. 1501–1506, 2000.

[183] X. Tan, Z. Sun, and I. F. Akyildiz, "Wireless underground sensor networks: Mi-based communication systems for underground applications." *IEEE Antennas and Propagation Magazine*, vol. 57, no. 4, pp. 74–87, Aug 2015.

[184] ——, "Wireless underground sensor networks: MI-based communication systems for underground applications." *IEEE Antennas and Propagation Magazine*, vol. 57, no. 4, Aug 2015.

[185] ——, "Wireless underground sensor networks: Mi-based communication systems for underground applications." *IEEE Antennas and Propagation Magazine*, vol. 57, no. 4, pp. 74–87, Aug 2015.

[186] M. J. Tiusanen, "Wideband antenna for underground Soil Scout transmission," *IEEE Anten. and Wireless Prop. Ltrs*, December 2006.

[187] ——, "Wideband antenna for underground Soil Scout transmission," *IEEE Antennas and Wireless Propagation Letters*, vol. 5, no. 1, pp. 517–519, December 2006.

[188] ——, "Wireless Soil Scout prototype radio signal reception compared to the attenuation model," *Precision Agriculture*, vol. 10, no. 5, pp. 372–381, November 2008.

[189] ——, "Soil scouts: Description and performance of single hop wireless underground sensor nodes," *Ad Hoc Networks*, vol. 11, no. 5, pp. 1610 – 1618, 2013.

[190] J. Toftgard, S. Hornsleth, and J. Andersen, "Effects on portable antennas of the presence of a person," *IEEE Transactions on Antennas and Propagation*, vol. 41, no. 6, pp. 739–746, Jun. 1993.

[191] F. Tokan and et.al., "The lateral wave antenna," *IEEE Transactions on Antennas and Propagation*, vol. 62, no. 6, pp. 2909–2916, June 2014.

[192] J. Tooker and M. C. Vuran, "Mobile data harvesting in wireless underground sensor networks," in *Proc. IEEE SECON '12*, Seoul, Korea, June 2012.

[193] G. C. Topp, J. L. Davis, and A. P. Annan, "Electromagnetic determination of soil water content: Measurements in coaxial transmission lines," *Water Resources Research*, vol. 16, no. 3, pp. 574–582, 1980.

[194] J. Toro-Vazquez, R. A. Rodriguez-Solis, and I. Padilla, "Estimation of electromagnetic properties in soil testbeds using frequency and time domain modeling," *IEEE Journal of Selected Topics in Applied Earth Observations and Remote Sensing*, vol. 5, no. 3, pp. 984–989, June 2012.

[195] F. T. Ulaby and D. G. Long, *Microwave Radar and Radiometric Remote Sensing*. University of Michigan Press, 2014.

[196] R. van der Velde, M. S. Salama, O. A. Eweys, J. Wen, and Q. Wang, "Soil moisture mapping using combined active/passive microwave observations over the east of the netherlands," *IEEE Journal of Selected Topics in Applied Earth Observations and Remote Sensing*, vol. 8, no. 9, pp. 4355–4372, Sept 2015.

[197] D. Vasisht, Z. Kapetanovic, J. Won, X. Jin, M. Sudarshan, and S. Stratman, "Farmbeats: An iot platform for data-driven agriculture."

[198] H. Vereecken, A. Schnepf, J. W. Hopmans, M. Javaux, D. Or, T. Roose, J. Vanderborght, M. Young, W. Amelung, M. Aitkenhead *et al.*, "Modeling soil processes: Review, key challenges, and new perspectives," *Vadose Zone Journal*, vol. 15, no. 5, 2016.

[199] M. C. Vuran, X. Dong, and D. Anthony, "Antenna for wireless underground communication," Jun. 25 2015, uS Patent App. 14/415,455. [Online]. Available: http://www.google.com/patents/US20150181315

[200] M. C. Vuran and I. F. Akyildiz, "Channel model and analysis for wireless underground sensor networks in soil medium," *Physical Communication*, vol. 3, no. 4, pp. 245–254, December 2010.

[201] M. C. Vuran, A. Salam, R. Wong, and S. Irmak, "Internet of underground things: Sensing and communications on the field for precision agriculture," in *2018 IEEE 4th World Forum on Internet of Things (WF-IoT) (WF-IoT 2018)*, , Singapore, Feb. 2018.

[202] J. R. Wait, "The electromagnetic fields of a horizontal dipole in the presence of a conducting half-space," *Canadian Journal of Physics*, vol. 39, no. 7, pp. 1017–1028, 1961.

[203] J. R. Wang and T. J. Schmugge, "An empirical model for the complex dielectric permittivity of soils as a function of water content," *IEEE Transactions on Geoscience and Remote Sensing*, vol. GE-18, no. 4, pp. 288–295, Oct 1980.

[204] T. Wark, P. Corke, P. Sikka, L. Klingbeil, Y. Guo, C. Crossman, P. Valencia, D. Swain, and G. Bishop-Hurley, "Transforming agriculture through pervasive wireless sensor networks," *IEEE Pervasive Computing*, vol. 6, no. 2, 2007.

[205] W. B. Weir, "Automatic measurement of complex dielectric constant and permeability at microwave frequencies," *Proceedings of the IEEE*, vol. 62, no. 1, pp. 33–36, Jan 1974.

[206] P. D. Welch, "The use of fast fourier transform for the estimation of power spectra: A method based on time averaging over short, modified periodograms," *Audio and Electroacoustics, IEEE Transactions on*, vol. 15, no. 2, pp. 70–73, Jun 1967.

[207] H. A. Wheeler, "Useful radiation from an underground antenna," *Journal of Research*, vol. 65, pp. 89–91, 1961.

[208] B. Widrow and et.al., "Adaptive antenna systems," *Proceedings of the IEEE*, Dec 1967.

[209] M. Win and R. Scholtz, "Characterization of ultra-wide bandwidth wireless indoor channels: a communication-theoretic view," *Selected Areas in Communications, IEEE Journal on*, vol. 20, no. 9, pp. 1613–1627, Dec 2002.

[210] S. Wolfert, L. Ge, C. Verdouw, and M.-J. Bogaardt, "Big data in smart farming âĂŞ a review," *Agricultural Systems*, vol. 153, p. 69, 2017. [Online]. Available: http://www.sciencedirect.com/science/article/pii/S0308521X16303754

[211] C. Y. Wong, R. Cheng, K. Lataief, and R. Murch, "Multiuser OFDM with adaptive subcarrier, bit, and power allocation," *IEEE JSAC*, vol. 17, no. 10, pp. 1747–1758, Oct 1999.

[212] T. T. Wu, "Theory of the dipole antenna and the twoâĂŘwire transmission line," *Journal of Mathematical Physics*, vol. 2, no. 4, 1961.

[213] A. Xhafa, O. Tonguz, A. Cepni, D. Stancil, P. Nikitin, and D. Brodtkorb, "On the capacity limits of HVAC duct channel for high-speed internet access," *IEEE Trans. Communications*, vol. 53, no. 2, pp. 335–342, Feb 2005.

[214] Q. Yan, H. Yang, M. C. Vuran, and S. Irmak, "Spride: Scalable and private continual geo-distance evaluation for precision agriculture," in *IEEE Conference on Communications and Network Security (IEEE CNS), Las Vegas, NV, USA*, October 2017.

[215] W. Yu and J. Cioffi, "FDMA capacity of Gaussian multiple-access channels with ISI," *In IEEE Trans. Communications*, vol. 50, no. 1, pp. 102–111, Jan 2002.

[216] H. Zemmour, G. Baudoin, and A. Diet, "Effect of depth and soil moisture on buried ultra-wideband antenna," *Electronics Letters*, vol. 52, no. 10, pp. 792–794, 2016.

[217] H. Zemmour, G. Baudoin, C. Hamouda, A. Diet, and M. Biancheri-Astier, "Impact of soil on uwb buried antenna and communication link in ir-uwb wusn applications," in *Radar Conference (EuRAD), 2015 European*, Sept 2015, pp. 353–356.

[218] X. Zhang, A. Andreyev, C. Zumpf, M. C. Negri, S. Guha, and M. Ghosh, "Thoreau: A subterranean wireless sensing network for agriculture and the environment," in *2017 IEEE Conference on Computer Communications Workshops (INFOCOM WKSHPS)*, May 2017, pp. 78–84.

[219] S.-S. Zhong, G. Liu, and G. Qasim, "Closed form expressions for resonant frequency of rectangular patch antennas with multidielectric layers," *IEEE transactions on Antennas and Propagation*, vol. 42, no. 9, pp. 1360–1363, 1994.